QUANTITATIVE OPTICAL IMAGING AND SENSING BY JOINT DESIGN OF POINT SPREAD FUNCTIONS AND ESTIMATION ALGORITHMS

by

SEAN ALBERT QUIRIN

B.A., University of Colorado, 2004

M.S., University of Colorado, 2009

A thesis submitted to the

Faculty of the Graduate School of the

University of Colorado in partial fulfillment

of the requirement for the degree of

Doctor of Philosophy

Department of Electrical, Computer and Energy Engineering

2012

This thesis entitled:
Quantitative Optical Imaging and Sensing by Joint Design of Point Spread Functions and Estimation Algorithms
written by Sean Albert Quirin
has been approved for the Department of Electrical, Computer and Energy Engineering

_____
(Rafael Piestun)

_____
(Kelvin Wagner)

Date_____

The final copy of this thesis has been examined by the signatories, and we find that both the content and the form meet acceptable presentation standards of scholarly work in the above mentioned discipline.

Quirin, Sean Albert (Ph.D., Electrical, Computer and Energy Engineering)

Quantitative Optical Imaging and Sensing by Joint Design of Point Spread Functions and Estimation Algorithms

Thesis directed by Professor Rafael Piestun

The joint application of tailored optical Point Spread Functions (PSF) and estimation methods is an important tool for designing quantitative imaging and sensing solutions. By enhancing the information transfer encoded by the optical waves into an image, matched post-processing algorithms are able to complete tasks with improved performance relative to conventional designs. In this thesis, new engineered PSF solutions with image processing algorithms are introduced and demonstrated for quantitative imaging using information-efficient signal processing tools and/or optical-efficient experimental implementations.

The use of a 3D engineered PSF, the Double-Helix (DH-PSF), is applied as one solution for three-dimensional, super-resolution fluorescence microscopy. The DH-PSF is a tailored PSF which was engineered to have enhanced information transfer for the task of localizing point sources in three dimensions. Both an information- and optical-efficient implementation of the DH-PSF microscope are demonstrated here for the first time. This microscope is applied to image single-molecules and micro-tubules located within a biological sample.

A joint imaging/axial-ranging modality is demonstrated for application to quantifying sources of extended transverse and axial extent. The proposed

implementation has improved optical-efficiency relative to prior designs due to the use of serialized cycling through select engineered PSFs. This system is demonstrated for passive-ranging, extended Depth-of-Field imaging and digital refocusing of random objects under broadband illumination.

Although the serialized engineered PSF solution is an improvement over prior designs for the joint imaging/passive-ranging modality, it requires the use of multiple PSFs – a potentially significant constraint. Therefore an alternative design is proposed, the Single-Helix PSF, where only one engineered PSF is necessary and the chromatic behavior of objects under broadband illumination provides the necessary information transfer. The matched estimation algorithms are introduced along with an optically-efficient experimental system to image and passively estimate the distance to a test object.

An engineered PSF solution is proposed for improving the sensitivity of optical wave-front sensing using a Shack-Hartmann Wave-front Sensor (SHWFS). The performance limits of the classical SHWFS design are evaluated and the engineered PSF system design is demonstrated to enhance performance. This system is fabricated and the mechanism for additional information transfer is identified.

This thesis is dedicated to Amy and Owen.

ACKNOWLEDGEMENTS

The support and patience necessary to complete this research came from influences inside and outside of my work life. I have been very fortunate to make many friends, find amazing mentors and earn a valuable education throughout this experience.

The work contained in this thesis was motivated in part by earlier investigations initiated within Rafael Piestun's research group. Starting with Adam Greengard's initiating demonstrations of depth from diffracted rotation, Sri Rama Prasanna Pavani's work on applying a Double-Helix Point Spread Function to nano-scopy and, most recently, the work of Ginni Grover's application of these methods to biological investigation. All of this research has been guided by Rafael Piestun, an advisor who has educated me on the necessary skills of research and writing as well as provided me with continuous support.

I would like to thank my parents for providing me with the encouragement to continue with college. The memory of a singular educator in my life, Dave Beck, continued to motivate me through these years. The attention and opportunity that he provided for me will always be appreciated and never be forgotten. My primary education in all thing optics (and sometimes chemisty) was courtesy of mentors such as Dr. William Wilson, Dr. Lisa Dhar and Dr. Kevin Curtis during my time at InPhase Technologies and Prof. Rafael Piestun at the University of Colorado.

A special thanks to both Hans-Peter Herzig and Toralf Scharf at Ecole Polytechnique Federale de Lausanne for hosting me as a visiting student in their lab. I received a great education in optical element fabrication from both of them and that knowledge has been directly applied to this thesis.

My research experience at the University of Colorado has been enjoyable due to the daily interaction with my colleagues here. I was fortunate to enter the optics program with not just really intelligent people, but also people who were interesting to be around. Matt Hayman has provided the steady beat of sarcasm and wit necessary to keep me entertained. Tim Gerke and Prasanna Pavani were the two senior members of Rafael's group who helped prepare me for academic research and orient me on lab equipment. Adam Urness and Ginni Grover helped prepare me for the preliminary exam – a very educational experience which I am happy to never repeat. Tony Barsic, Don Conkey and Anurag Agrawal have all been great friends to talk with and learn from.

The sources of funding which have allowed me to focus on research are greatly appreciated. These include the Honda Initiation Grant and the National Science Foundation through the Computational Optical Sensing and Imaging (COSI-IGERT).

My backbone through all of this was provided by the unconditional love and support of my wife Amy. Through this, she has been a best friend, a steady rock, an adventurous traveler and the beautiful mother of our child, Owen. Thank you for

everything that you have done to support me through these times – this would not have been possible without you.

CONTENTS

TABLES

Table

FIGURES

Figure

CHAPTER I

INTRODUCTION

Optical imaging, in its most general sense, is a tool for the collection and storage of an optical signal which has physically interacted with the sample (e.g. emission, scattering, reflection, etc.) and is then used to aid the user in interpreting the object with subsequent display or post-processing. The capture of this information is considered here to be a transfer of data which is utilized in either a qualitative or quantitative sense. The qualitative approach to data evaluation leads to observations which are not measureable. As one example, the common consumer camera will be used to satisfy the capture, storage and display demands which invoke a memory or emotion for the user. In contrast, the quantitative application common to scientific inquiry will use the signal to generate a data point(s) for subsequent analysis – for instance to determine the location of cells in biological tissue. Many available methods exist by which to design a quantitative imaging/sensing system. In particular, the design methodology of computational imaging has focused on exploiting the relationship between object, the scientific question being asked and detected signal in order to focus the system design into a dedicated unit with improved performance at the cost of requisite signal pre- or post-processing. The cheap cost of computational power means that no significant

impediment to this design methodology currently exists. However, the demands then placed on the correct design, manufacture and execution of the joint optical system and signal processing design cannot be dismissed. Therefore, growing interest exists within the scientific community to explore the potential of computational imaging while developing the tools necessary to aid in the current and future design, manufacture and execution of these systems. The use of joint Point Spread Function (PSF) design with matched signal processing as a computational imaging tool is investigated here with application to problems in surveillance and spatial awareness (passive-ranging), 3D biological imaging with resolution beyond the diffraction limit, and optical wave-front measurement.

1.1 Motivation

The earliest forms of imaging used only basic elements such as the mirror and spectacle. Hundreds of years ago, these elements were combined into more complex optical instruments such as the telescope and microscope – thus enabling the study of objects which were previously unknown to mankind or lacked sufficient detail to understand and interpret into new observations. As should be expected, optical system design has increased in sophistication over the original trial-and-error techniques. Today, the propagation of light is understood in terms of Maxwell's equations which treat light as the propagation of electro-magnetic waves. Maxwell's equations natively admit the wave optics solutions which are necessary to understand the phenomena of interference fringes. Alternatively, one is also able to develop an approximate ray-based model of light propagation when the distances

involved are much greater than the size of a wavelength. Today, the availability of both ray-tracing and wave-optics software packages allow for precise optical system design through the definition of optical and mechanical properties for each element in the system to accurately describe the resulting image/signal.

However, it is argued here and elsewhere (1) (2) (3) (4) (5) that despite this precise understanding of light propagation, the advent of digital detectors such as CMOS and Charged-Coupled Devices (CCD) represent additional degrees-of-freedom to optical system design which may not yet be fully exploited. This observation is central to the methodology of computational imaging where the system design is optimized with respect to the signal collected from the digital detector. Within the last 20 years, computational imaging has developed into methods which optimize the form of this digitized, intermediate optical signal to answer a specific scientific question via the use of pre- or post-processing to produce the desired information representation. Through the joint use of optical system design and image processing, example solutions have been studied to characterize/remove/correct optical aberrations (6) (7) (8) (9) (10), extract depth information encoded in the signal (11) (12) (13) (14) (15), improve task-specific optical system performance (2) (16) (17) (18), focus/image through highly-scattering materials (19) (20) (21) (22) and resolve spatial features at resolution beyond the classical diffraction-based limit (14) (23) (24).

From this growing list of successful computational imaging techniques one is of particular interest to this thesis – the joint design of optical Point Spread Functions (PSF) with matched signal-processing algorithms (2) (6) (7) (11) (12) (13)

(14) (15) (16) (17) (18). This method is important because it requires minimal physical modification from the classical optical system layout, is entirely passive and frequently implemented by the addition of only one optical element. This element is designed to functionally alter the fundamental optical response of the system – the PSF – in order to generate a signal at the digital detector which carries more information relevant to the scientific question being asked. Because the new system PSF is no longer the ideal Airy disk which is used in classical imaging applications, the relevant signal may be difficult to interpret directly from the image and will be subject to a post-processing step to generate the final data representation.

1.2 Point Spread Function Engineering in Computational Imaging

The optical concepts applied in the joint design of PSFs and matched post-processing (hence-forth shortened to engineered PSFs) can be understood from the perspective of linear systems theory. This requires that a linear relationship exists between the input (object) and the output (image) such that a transfer function characterizes what happens to the input as it passes through the linear system (here, the optical system). Working in the Fourier domain, where the object is decomposed into a representation of spatial frequency components (or plane-waves), the transfer function assigns a complex coefficient to each spatial frequency of the input to describe what happens at the output of the linear system (Fig. 1.1). To allow that the optical system be modeled in this framework, the assumption of

transverse shift-invariance must be applied (i.e. the optical system response is not dependent upon the transverse position of the object).

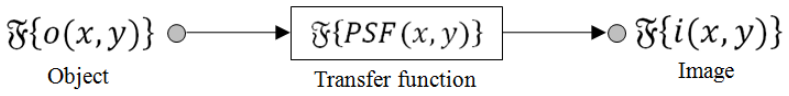

Fig. 1.1: The linear model of an optical system provides a description of the optics in the form of a transfer function, where each component of the transfer function describes the complex coefficient acquired by the spatial frequency components of the input (object) as it passes through the system to form the output (image). Note that $\mathfrak{F}$ denotes a Fourier transform.

Application of the convolution theorem to the model in Fig. 1.1 shows the relationship between the input and output can be written as,

$$i(x,y) = PSF(x,y) \otimes o(x,y) \tag{1.1}$$

where $\otimes$ denotes the convolution operator. Note that most engineered PSF systems operate under incoherent imaging conditions where the object $o(x,y)$ and the image $i(x,y)$ are given in terms of intensity.

To define the PSF for an optical system, a number of assumptions are commonly employed (25) (26):

A. Paraxial assumption: This is the assumption that the maximum propagated spatial frequency is limited to be much less than $1/\lambda$. Note that generally spatial frequencies greater than $1/\lambda$ will attenuate fast due to evanescent decay. Under the wave-optics formulation, this assumption is the approximation that the complex-amplitude emitting from a point-source is a paraboloid,

$$o(x,y;d) \approx e^{-i\frac{2\pi}{\lambda d}(x^2+y^2)} \tag{1.2}$$

instead of a spheroid.

B. Generalized pupil: This assumption is based upon an approximation that the lens may be described with an infinitely thin element. Classically, the most common form of this includes the size and shape of the aperture enclosing the lens with zero phase aberrations (e.g. $p(u,v) = circ\left(\frac{\sqrt{u^2+v^2}}{R}\right)$, where R is the radius of the lens aperture and coordinate system (u,v) is the transverse plane within the pupil). One advantage provided by the application of the generalized pupil function, $p(u,v)$, is that both the lens $(\phi(u,v))$ and system aberrations $(\Psi(u,v;x_0,y_0,z,\lambda))$ can be placed into this plane such that the generalized pupil function becomes,

$$f(u,v) = p(u,v)e^{i\Psi(u,v)} = circ\left(\frac{\sqrt{u^2+v^2}}{R}\right)e^{i\phi(u,v)}e^{i\Psi(u,v;x_0,y_0,z,\lambda)} \qquad (1.3)$$

where the system aberration dependence on object transverse position coordinates x_0 and y_0, axial position z, and color λ are explicitly included. For isoplanatic optical systems, the linear optical system is approximated to be transversely shift-invariant. Therefore the pupil plane aberrations are independent of the object coordinates x_0 and y_0.

C. Scalar wave-functions: This assumption is not critical to the definition of a PSF in general but is instead used to simplify the optical system model. For applications with low Numerical Aperture (NA) the vector behavior of light may be ignored in favor of this simplified description where wave oscillations in 1D are assumed.

With these assumptions in place, the input-output relationship of the incoherent optical system allows the PSF to be defined as,

$$PSF(x, y; z, \lambda) = \left|\Im\{p(u, v)e^{i\Psi(u,v;z,\lambda)}\}\right|^2. \quad (1.4)$$

Therefore the PSF contains all the information about aberration-sensitivities (e.g. defocus, spherical, chromatic) when mapping the input source $o(x, y)$ to the output image $i(x, y)$ in Eq. 1.1.

Returning to the concept of engineered PSFs, these can now be understood as the functional modification of the pupil function $p(u, v)$ in order to enhance the performance with respect to particular aberrations in $\Psi(u, v; z, \lambda)$ or spatial frequency content of the object $o(x, y)$. This now contrasts with classical design parameters where the pupil function was designed to null-out any aberrations in order to retain just the amplitude encoding which describes the shape of the lens aperture and generate the Airy disc as the PSF.

A common on-axis aberration is defocus in the generalized pupil function where,

$$\Psi(u, v; z, \lambda) = \frac{\pi}{\lambda}\left(\frac{1}{f} - \frac{1}{z} - \frac{1}{d_i}\right)(u^2 + v^2) \quad (1.5)$$

and f is the lens focal length, z is the object distance, and d_i is location of the observation plane. Note that when the imaging condition,

$$\frac{1}{z} + \frac{1}{d_i} = \frac{1}{f} \quad (1.6)$$

is satisfied the defocus aberrations are zero and the object and image are considered to be conjugates of each other. The design of engineered PSFs for both 3D imaging and Extended Depth-of-Field (EDOF) applications is principally concerned with the

design of $p(u,v)$ in order to impart specific qualities (e.g. some combination of shape, size, position, orientation, rotation of an object) to the PSF as the amount of defocus, $\Psi(u,v;z,\lambda)$, is varied as a function of z (2) (11) (14) (15).

As one example, in refs. (2) (6) (18), the imaging system is modified by a cubic phase element given by,

$$p(u,v) = e^{-i\alpha(u^3+v^3)} \tag{1.7}$$

which is placed into the pupil of the lens. The result is a modified PSF with a transverse profile approximately invariant to defocus for an extended range of z when $\alpha \gg 20$ assuming that u,v are now in normalized coordinates. Even though the resulting image will be heavily distorted due to the introduction of this phase aberration, the intermediate signal can be deconvolved by this known and axially-invariant PSF to generate a diffraction-limited image within an extended Depth-of-Field relative to the standard optical design. A demonstration of this system is reviewed in Fig. 1.2. This phase element is amenable to fabrication by direct-machining and casting methods due to its smoothly varying spatial profile.

It was noted in ref. (2) that while the resulting PSF had an approximately invariant transverse profile with respect to defocus the centroid position of this PSF will translate as a function of axial position. Recently, this observation has been exploited for use in a line-of-sight spectrometer with application to the generation of plasma channels (27). However, because this transverse translation can be problematic for imaging applications an alternative phase mask was proposed using cylindrical coordinates,

$$p(\rho,\theta) = e^{-i\rho^3 cos3\theta}. \tag{1.8}$$

Despite these advances, the optimum engineered PSF design for restoring defocused object information is still a topic of current research (28).

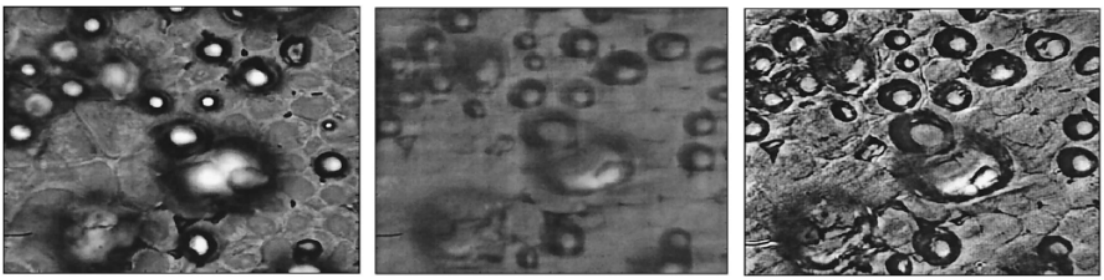

Fig. 1.2: Results comparing the images of an object with extended axial features. In the first image, the classical lens has a characteristic focal plane which captures detailed features of the in-focus object but loses detail for features which are out-of-focus (e.g. blur). In the second image, a lens is encoded with a cubic-phase modulation in the pupil function to generate an image where the level of detail for each axial plane is constant but decreased relative to the focused image with a classical lens. In the final image, restoration of the second image using deconvolution enhances detail of the object for an extended Depth-of-Field compared to the classical system. Images taken from ref. (2).

Alternatively, the choice can be made to enhance the sensitivity to defocus aberration with proper encoding of $p(u, v)$ and subsequent use of signal processing as in (11) (12) (14) (15). In one example (Ref. (14)), the pupil function is encoded with an astigmatic function (via a cylindrical lens) in order to vary the focusing power of the system along the x and y axes of the observation plane and encode the axial position of the source. From the collected signal, the axial position is found from the unique combination of the Full-Width at Half-Maximum (FWHM) along each axes of the detector. This system is reviewed in Fig. 1.3. The axial range sensitivity can also be enhanced via use of a Double-Helix PSF (DH-PSF) which encodes the axial position of the source via a unique rotational orientation of duplicative copies of the object – as shown in Fig. 1.4. The DH-PSF has been

realized via use a hologram (11) or a Spatial Light Modulator (SLM) (13) (29) (30) (31) (32).

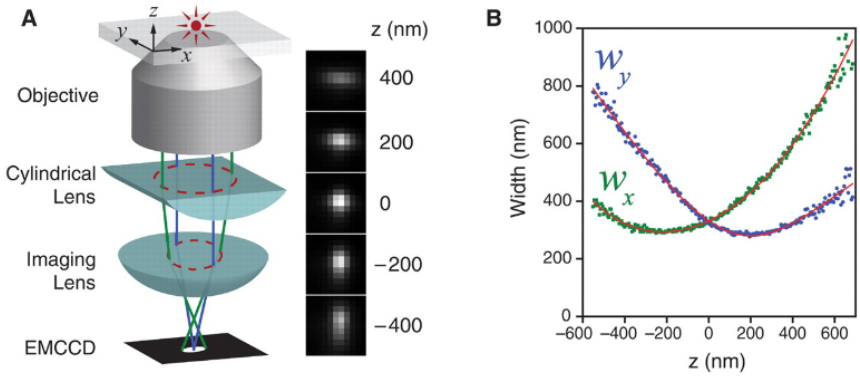

Fig. 1.3: A cylindrical lens is used to functionally encode the generalized pupil function $p(u,v)$ such that the axial position of the source is encoded as a unique combination of the engineered PSF FWHM along the x and y axes of the observation plane. Images taken from ref. (14).

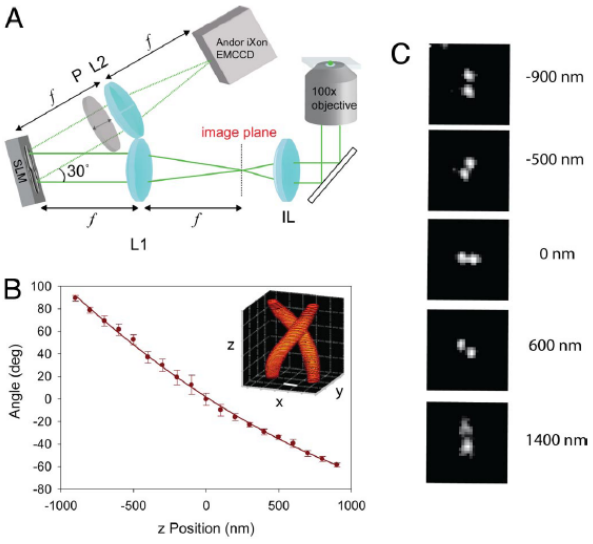

Fig. 1.4: The DH-PSF can be used to encode the axial position of an object by measuring the rotational orientation from duplicative copies of the object. Experimental implementation has required the use of holograms or Spatial Light Modulators (SLM), as shown in A. Using a fluorescent bead as the source, the rotational orientation of the DH-PSF is tracked as the bead is moved axially through focus in B. The experimental DH-PSF images in C show the two lobe characteristic of this engineered PSF. Images taken from ref. (13).

1.3 Evaluation of Optical System Design

While the joint use of engineered PSFs and image processing can enable new functionalities such as 3D imaging and EDOF, methods must be used to evaluate the degree to which performance can be enhanced relative to alternative designs. Common metrics for optical system design include the optical Modulation Transfer Function (MTF), Strehl Ratio, Signal-to-Noise Ratio (SNR), and Signal-to-Background Ratio. In this thesis, this problem is addressed in terms of a task-based performance metric using two quantitative approaches: the Cramer-Rao Lower Bound (CRLB) (33) and the spectral SNR (28).

The use of CRLB as an optical system design metric is ideal because it comprehensively accounts for all elements present in the system – including the pupil function $p(u,v)$, aberrations $\Psi(u,v)$, digital detector properties (e.g. dynamic-range, dark counts and pixel size) and noise properties to generate a theoretical error measure (33). The CRLB is also intuitive as the measure of change in an image with respect to the variable to be measured (e.g. x, y and z position) and is inversely proportional to the amount of noise in the system. Increasing the change in a signal with respect to the variable to be measured will result in better measurement precision. In addition, the intuitive expectation that decreasing the noise in an image will result in improved measurement precision is supported.

Therefore the ideal design of a pupil function $p(u,v)$ and in turn the PSF is the one which generates the most variation with respect to the parameter to be measured.

The second measure used here is the spectral SNR of an optical signal (28). The spectral SNR reports the average SNR for every spatial frequency of the Optical Transfer Function (OTF) across the range of axial object positions which are of interest, where the OTF is defined as,

$$OTF = |\mathfrak{F}^{-1}\{PSF\}|^2. \tag{1.9}$$

The utility of this metric is for evaluating alternative implementations of $p(u,v)$ and finding which carries the most spatial frequency content across the axial range of interest for extended-depth-of-field (EDOF) designs.

1.4 Main Contributions of this Thesis

In this thesis, the joint design of engineered PSF solutions with matched estimation algorithms is investigated and applied to passive-ranging, 3D imaging (including super-resolution microscopy) and optical phase measurement. In general, the space of possible solutions for optical waves and therefore PSFs has been restricted to those which have the property of maintaining their transverse intensity profile, but with a scale- and rotation-transformation, as the wave is propagated (34). In general, the set defined in ref. (34) is further restricted by the requirement that the implementation of these waves must be realizable with a phase-only modulation of the pupil function. Example waves which satisfy these criteria are shown in Fig. 1.5.

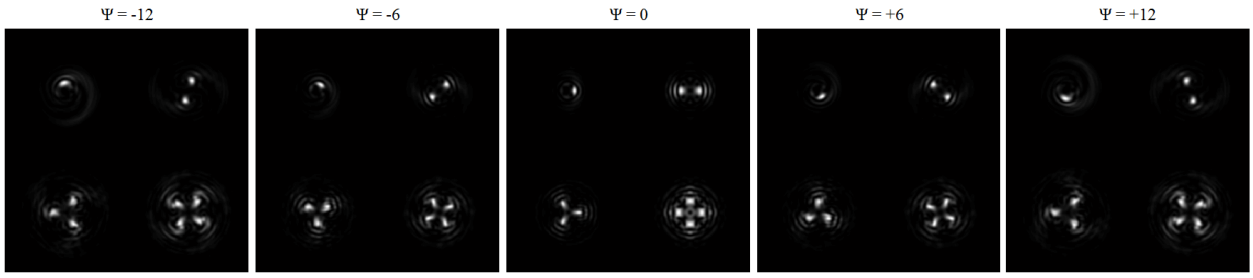

Fig. 1.5: Four examples of engineered Point Spread Functions which rotate and change scale with propagation are presented as a function of defocus given by Ψ. Each example can be implemented with a phase-only modification to the optical pupil function of a lens.

Another example from this set of waves was introduced earlier as the DH-PSF – a PSF which is very similar in origin to that shown in the upper-right of each panel in Fig. 1.5. This PSF has been demonstrated useful in passive ranging (11) and 3D localization-based microscopy (13) (30) (31) (32). However, these DH-PSF implementations have failed to realize the full potential of the engineered PSF because of a mix of inefficient estimation algorithm design and optical system implementation. In this thesis, the DH-PSF is revisited in order to evaluate these shortcomings of prior solutions and find methods which are true to matching the original intent of the DH-PSF proposal. This requires both the information-efficient estimation algorithms which can perform to the limits theorized with the CRLB (demonstrated in Chapter 2) and the development of optical elements for photon-efficient implementation (demonstrated in Chapter 4). These tools are applied simultaneously in Chapter 4 for the first realization of an optical- and information-efficient 3D optical microscopic with diffraction-unlimited resolution of biological samples using the DH-PSF.

Prior work has demonstrated the use of a DH-PSF for passive ranging of extended objects (11). However, this example implemented a hologram for encoding the PSF and therefore required quasi-monochromatic illumination. The passive ranging of extended objects has an additional complication due to the necessary collection or assumption of a signal which provides prior knowledge of the objects being imaged. These problems are revisited here in Chapter 3 where the optical system implementation is designed to allow for operation with broadband illumination. In addition, a dynamic pupil function is introduced to cycle through engineered PSF solutions which will improve the signal available for estimating the object(s) being imaged. The result is an optical system with an improved SNR for both passive-ranging and extended Depth-of-Field imaging relative to prior designs.

However, this passive-ranging design requires the acquisition of at least two images with alternative pupil functions in order to collect enough information for the image processing algorithms to operate correctly. In Chapter 5, an alternative solution is proposed using a Single-Helix PSF (SH-PSF). Under ideal operating conditions, this proposal can collect enough information when using a single pupil function to quantitatively estimate the axial position of an object as well as recover a high-resolution image through an extended Depth-of-Field. Comparison with alternative task-specific designs shows that the SH-PSF can simultaneously improve performance for both of these seemingly different tasks. Using methods developed in Chapters 2 and 4 as well as new estimation algorithms, an optical system is demonstrated which can experimentally generate quantitative passive-ranging data of random, extended objects under broadband illumination and

simultaneously recovers enough information to restore the detail to out-of-focus images.

The final chapters of this thesis are concerned with computational imaging methods which can be used to recover the phase or wave-front of an optical signal. One example of a phase-recovery technique is demonstrated in Chapter 2 and became integral to the development of the estimation algorithm which realizes the limits theorized by the CRLB. An alternative method is known as the Shack-Hartmann Wave-front Sensor (SHWFS). The SHWFS is extensively investigated in Chapter 6 in order to define an optimal system design using conventional components under various experimental conditions. Using the CRLB approach advocated earlier, the optimal SHWFS design is shown for the first time to depend on the number of photons available and the transverse characteristic of the optical wave-front. In Chapter 7, a modified approach to the SHWFS which uses engineered PSFs is proposed and evaluated to demonstrate that the classical system design can be improved using the tools developed earlier in this thesis. The first example of this modified SHWFS design is fabricated and the mechanism for improved information transfer is experimentally demonstrated. A summary of this thesis and future work is suggested at the conclusion in Chapter 8.

CHAPTER 2

MAXIMUM LIKELIHOOD PATTERN MATCHING FOR LOCALIZATION-BASED IMAGING WITH ENGINEERED AND ABERRATED POINT SPREAD FUNCTIONS

2.1 Motivation

The recent application of information theoretic methods to imaging solutions has helped motivate the redesign of optical systems which exploit the concept of information in images. This use of information theoretic tools has been central to recent task-based system designs in microscopy (11) (35) (36) passive-ranging (12), iris recognition (16) and extended depth-of-field (6). Although proven useful, this can lead to improper justification if the associated matched post-processing algorithms do not efficiently meet the limitations shown by this metric. For example, recent work has indicated the optimality of the DH-PSF for volume imaging and localization tasks relative to alternative designs (11) (35) (37). However, none of the proposed algorithms have actually met these fundamental limits. For example, the angle/centroid estimation algorithm originally proposed for the DH-PSF has been documented to deviate from the CRLB by a factor of 2x (37). An improvement to this algorithm proposed fitting the two peak shapes to Gaussians and then calculating the associated angle and mid-point estimate but

this was also shown to deviate from the CRLB (32). Therefore there exists some divide between the theoretical capabilities of engineered PSF designs and actual implementations (algorithms, optics, etc.) that must be addressed in order to realize the full potential. For this reason a Maximum Likelihood Estimator (MLE) is sought to reach these fundamental limits for localization-based imaging.

In this chapter, a MLE is designed which optimally works with engineered PSFs. In addition to the flexibility of including engineered pupil functions, it will also accommodate optical aberrations. Since the ideal pupil function is often known, the MLE could potentially operate with this prior knowledge. However, the optical aberrations inherent to 3D imaging and imaging in biological samples are frequently unknown. Therefore a method is proposed to recover this information in experimental situations and incorporate it into the MLE.

An ideal candidate for demonstrating these methods is localization-based microscopy – where the image of a particle will closely resemble the PSF. Interestingly, the localization of randomly emitting molecules within a sample has recently been demonstrated as a method to yield images which are no longer limited by the diffraction-limit of resolution (24) (38) (39). Because of the general demand for high-resolution images and this link to particle localization, the MLE is demonstrated here experimentally for 3D single-molecule localization. This will serve as the estimation algorithm then used in Chapter 4 to produce 3D super-resolution images with an alternative realization of the DH-PSF.

2.2 Background

Photo-activation localization microscopy is a far-field super-resolution imaging technique based on the localization of single-molecules with sub-diffraction limit precision. Known under acronyms such as PALM (Photo-Activated Localization Microscopy) or STORM (Stochastic Optical Reconstruction Microscopy), these techniques achieve super-resolution by allowing only a sparse, random set of molecules to emit light at any given time and subsequently localizing each molecule with great precision. In this way, the image is not bound by the traditional limit of resolution but rather by the localization precision of the individual molecules.

Ongoing super-resolution microscopy developments are opening up opportunities to explore sub-cellular structure and function as well as to visualize materials at the nanoscale (23) (24) (38) (39) (40) (41) (42). In comparison with other super-resolution microscopy techniques (23) (40) (41) PALM/STORM is attractive because it enables the recording of multiple single-molecules in parallel, with each molecule experiencing limited photo-activation cycles. The technique is also appealing for simultaneously tracking individual molecules over time or measuring the distance between pairs of molecules (43). Recently, such techniques have been extended to three dimensions, opening up unprecedented possibilities to explore the structure and function of cells. Interestingly, proper engineering of the three-dimensional (3D) point spread function (PSF) through additional optics has been demonstrated to theoretically improve 3D position estimation and ultimately resolution. There is a significant current interest in decreasing the data acquisition time by engineering new fluorescent proteins and organic fluorophores (44) along

with optical improvements in photon collection (30) (45). Significant efforts are also underway to reduce systematic errors such as vibrations, drift, and imperfections of the detector (43), as well as bias from asymmetric molecular emission (46). However, existing methods to improve 3D localization use custom estimation algorithms that are not efficient in terms of achieving the fundamental localization limits (13) (14) (31) (32) (47) (48) (49).

Therefore the newly discovered frontiers of optical resolution and functionality - such as quantitative tracking and distance measurement - have not been fully realized yet. Optimal 3D localization procedures are critical to increase resolution for a given number of detected photons and to reduce data acquisition time for a given target resolution. Another practical problem is optical aberrations that distort the single molecule images and negatively affect the localization precision. Accordingly, this chapter addresses the problem of optimal 3D localization for arbitrary 3D PSFs in the presence of noise while providing a solution that rigorously accounts for the inevitable optical system aberrations.

2.3 Current Optical Methods for 3D Single-molecule Localization

Four main techniques are prevalent in far-field 3D single-molecule localization microscopy: bi-plane detection (47), astigmatic imaging (14), double-helix (DH) PSF (13) (29) (30) (48), and interferometric PALM (45). The first three are of particular interest because they require minor modifications of a standard microscope and operate over relatively long depth ranges (up to 2-3 μm for DH-PSF). In contrast,

interferometric PALM offers superb axial resolution but requires more complicated interferometric arrangements and operates over a 200nm range (45) (50).

To evaluate the performance of each system, the fundamental limit to 3D localization precision can be quantified by means of the Cramer-Rao Lower Bound (CRLB) (35) (36) (48). The Cramer-Rao Lower Bound (CRLB) is a measure of the optical system's fundamental limit for precisely estimating a set of parameters (2), in this case, the 3D position of a particle. The CRLB provides the theoretical lower limit of the variance for any unbiased estimator in the presense of noise. It is found from the inverse of the Fisher Information matrix $CRLB \geq FI(\vec{o})^{-1}$ where (33),

$$FI_{j,k} = \sum_{m=1}^{M} \sum_{n=1}^{N} \langle \frac{\partial}{\partial o_j} ln\, pdf(|f(m,n;\vec{o})|^2) \frac{\partial}{\partial o_k} ln\, pdf(|f(m,n;\vec{o})|^2) \rangle \qquad (2.1)$$

pdf is the probability density function, $\vec{o}$ is the object position and $\{j,k\} \in \{\Delta x, \Delta y, \Delta z\}$.

The CRLB also serves as a benchmark for estimator implementations, by which the realized precision of the estimator should approach this fundamental limit. These uses of the CRLB are increasingly relevant in single-molecule imaging, where the number of photons is inherently limited. Estimators based upon simple geometrical interpretations of the PSF (i.e. centroid (14), rotation angle (13) (30) (48), 2D Gaussian-fit (13) (14) (31) (32) (47) (49)) have been implemented and are computationally fast but not optimal because they do not reach the fundamental limit of precision for a given physical system. The reason these methods are sub-optimal is because of the coarse approximation of the PSF spatial profile and also the lack of specific noise statistics. The inclusion of explicit statistics into an estimation algorithm enables the definition of a most-likely 3D position, i.e. a

maximum-likelihood estimator (MLE) (33) (51) (52) (53). Prior demonstrations of 3D MLE's have only included optical systems which can be described with analytical solutions. This represents a limitation for the realizable optical design space that excludes the benefit of numerically optimized solutions. We point to the CRLB analysis demonstrating the 3D performance advantages of one such example, the DH-PSF, relative to the analytical designs, as justification for the necessity to include optimized PSFs (35). In addition, existing MLEs do not explicitly address a method for including inevitable experimental aberrations in the optical system. Inclusion of aberrations is critical in 3D methods because microscopes are in principle corrected for aberrations only across a single transverse plane. Therefore no method has been demonstrated that solves the problems of efficient 3D estimation for generalized optical systems or accurately account for the effects of aberrations induced by both the sample and object. In light of this, an information-efficient algorithm to achieve the CRLB for 3D localization in the presence of aberrations and using arbitrary PSFs is proposed and demonstrated here.

2.4 3D Phase Retrieval for Optimal Estimation

Optimal estimation requires a faithful model which can be matched to experimental calibration. Unfortunately, a detailed and exhaustive calibration of the PSF at single nanometer shifts, if possible, is not always practical because of the required large data acquisition sets (49) (54), which either become less precise or demand longer calibration times. Therefore a phase retrieval (PR) method (8) (55) is introduced to accurately recover the 3D PSF at arbitrary coordinates over a

continuous 3D domain based on only a few calibration measurements. Phase retrieval has been used in microscopy to correct aberrations in classical fluorescent imaging using a single pupil function model (30). This model is an approximation equivalent to a depth-invariant PSF which leads to residual errors even when the vector nature of the fields, the finite size of beads and noise are taken into account (30). While this approach has been shown to provide good results in conventional (diffraction-limited) deconvolution microscopy, its effectiveness is not guaranteed for engineered PSFs and super-resolution imaging, where dimensions are one order of magnitude smaller. Therefore, the PR method proposed here assumes a local, depth-variant model, and is shown below to be effective both for engineered PSFs and for PALM/STORM imaging to improve localization precision and ultimately resolution.

In order to generate a proper model of the imaging system that accounts for the presence of aberrations and the arbitrary optical system design, a set of calibration images,$\{I_{z1}, I_{z2}, \dots, I_{zN}\}$, and a PR algorithm are used to solve for the complex field of the PSF,

$$f_{zn}(x,y) = \left|\sqrt{I_{zn}(x,y)}\right| e^{i\varphi_{zn}(x,y)} \tag{2.2}$$

with zn=$z1 \dots zN$ indicating N axial positions. A diagram of the PR algorithm demonstrating a working example for estimating the complex field at an arbitrary plane z_0 is provided in Fig. 2.1. For any location of the molecule in space, an accurate model of the PSF is obtained from the images $I = |f(\vec{o})|^2$ by continuously propagating along Δz and shifting in Δx, Δy according to the wave equation that governs the evolution of the PSF,

$$f(x,y;\Delta x,\Delta y,\Delta z) \propto \Im\left\{\Im^{-1}\{f_{zn}\}\left(\frac{u}{\lambda f_{4F}},\frac{v}{\lambda f_{4F}}\right)e^{i\frac{2\pi}{\lambda f_{4F}}M(u\Delta x+v\Delta y)}e^{-i\frac{\pi}{\lambda}\left(\frac{u^2+v^2}{f_{4F}{}^2}\right)M^2\Delta z}\right\}. \qquad (2.3)$$

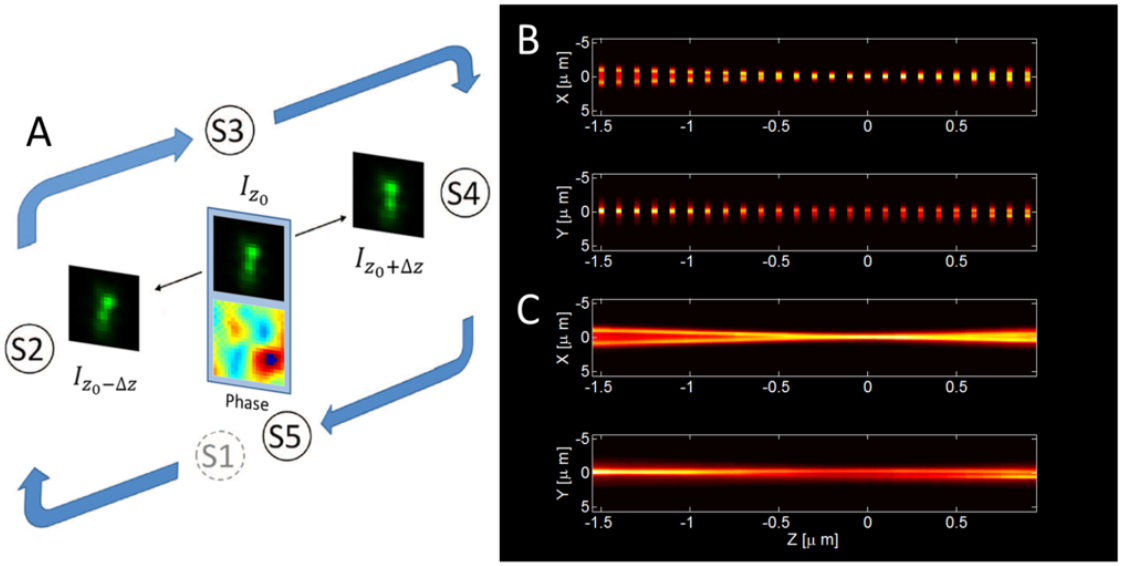

Fig. 2.1: The phase retrieval algorithm for PSF recovery and interpolation. (A) A sequence of three local calibration images ($I_{z0-\Delta z}$, I_{z0}, $I_{z0+\Delta z}$) is used for recovering the local depth-variant complex amplitude PSF of the optical system which is associated with the aberrated and/or engineered point spread function. The search procedure requires five steps (S1 – S5) per iteration until a solution converges at plane z_0, where the local phase is shown below the intensity image. Comparison of the axial dependence for the experimental and interpolated images of the aberrated double-helix PSF are given in panels (B) and (C), respectively. (B) Projections of the experimental images along the x and y axes with axial propagation shows the discrete character of the calibration data. (C) The results from the phase-retrieval algorithm behave smoothly - indicative of proper interpolation of the expected PSF at intermediate image planes to be used for maximum likelihood estimation.

The PR algorithm can be implemented using a minimum of two axial positions for calibration images of the PSF, taken at well known coordinates $\vec{o}_n = \{\Delta x_n, \Delta y_n, \Delta z_n\}$ where $n = 1,2$. However, increasing the number of calibration images for PR has been documented to improve convergence and robustness in the presence of noise (56). Prior methods have assumed that these field estimates can be averaged across the entire depth of focus to provide a best estimate for the

system pupil, but this assumption is overly restrictive for high numerical aperture systems as shown in (30), leading to residual errors in the estimated PSFs. While these errors can be tolerated in applications such as classical diffraction-limited deconvolution imaging, without further modifications they could introduce significant errors in localization-based super-resolution microscopy. Hence, a method that departs from the single-pupil approximation, which implicitly assumes a depth-invariant PSF, is required. It is with this in mind that a depth-variant method is implemented, using the PR algorithm with three local and contiguous axial calibration images to find the complex-field at each of the N depth positions. Hence, in this report we assume each estimate to be the best local representation of the associated field and retain this for later use in the MLE.

Knowledge of the absolute value of the amplitude for $f_{z0-\Delta z}$, f_{z0} and $f_{z0+\Delta z}$ is provided from the calibration images as $\sqrt{I_{z0-\Delta z}}$, $\sqrt{I_{z0}}$ and $\sqrt{I_{z0+\Delta z}}$, respectively and is used to find a unique estimate of f_{z0}. Referring to Fig. 2.1A, the propagation of $-\Delta z$ in step S1 is described by a defocus operation to calculate $f_{z0-\Delta z}$, i.e. a shift in object position of $\vec{o}_{SM} = \{\Delta x = 0, \Delta y = 0, -\Delta z\}$ (see Eq. 2.3). After this numerical propagation, the amplitude constraints of $\sqrt{I_{z0-\Delta z}}$ are enforced and the phase component of $f_{z0-\Delta z}$ is kept in step S2 as this represents an improvement in the estimation of this function. This new estimate is then forward-propagated to provide an updated estimate of f_{z0} as step S3. The forward-propagation is continued to $z0 + \Delta z$, the constraints again enforced as step S4, followed by a subsequent back-propagation to the starting point $z0$ to complete the algorithm with step S5. Steps S1-S5 represent a single iteration of the PR algorithm. Iteration continues until a

measure of convergence such as the sum-squared-error shows asymptotic behavior. Note that in practice, it has been documented that an optimum Δz exists for a given noise level of the calibration images (57). In our experiments, an average of 27 images are taken at each axial position to decrease the noise present in the calibration image (where each axial position is taken at 100nm intervals). The PR can be further refined – if necessary – using known methods that account for under-sampling and broadband emission (58). A generalization of the method presented here is also possible for non-isoplanatic systems.

The result of the PR is a rigorous interpolation of the calibration data that can be used in the MLE process. Note that this process has incorporated the entire optical system into the calibration process without making any significant assumptions about amplitude/phase modulation devices or aberrations. Therefore, optical PSF design and systematic aberrations can be incorporated seamlessly for optimal estimation.

2.5 3D Maximum Likelihood Localization Estimation

The optical system description given by the experimental PSF and, if needed obtained via the PR process, is utilized in the second component of this method. Given an experimental image of a single-molecule I_{exp}, this optimal estimator searches the object space $\vec{o}$ for the most likely PSF match $|f(\vec{o})|^2$ using Eq. 2.4, i.e. the position $\vec{o}(\Delta x, \Delta y, \Delta z)$ of the molecule that maximizes the likelihood function,

$$\hat{o}(\Delta x, \Delta y, \Delta z) = \underset{\vec{o}\in\mathbb{R}^3}{arg\,max}\left\{\mathcal{L}\left(I_{exp}; f(\vec{o})\right)\right\} \tag{2.4}$$

Here, $\hat{o}$ is the estimate resulting from the maximization and $\mathbb{R}^3$ is the set of all 3D positions, $\mathcal{L}$ is a function representing the likelihood of the match at $\vec{o}$ in the presence of random noise processes such as Poisson or Gaussian,

The MLE algorithm is implemented using custom software developed in the MatLab environment (The MathWorks Inc, Natick, MA). The operational details of the algorithm are now introduced to highlight specific contributions of the 3D Phase-retrieval Maximum Likelihood Estimation (PR-MLE). This section assumes the phase retrieval process is complete, and describes how to subsequently use that information for particle localization. The localization occurs in two steps: first, a coarse estimate is made to decrease the computational burden from the iterative MLE search; second, the MLE begins an iterative search for a high-precision 3D localization solution.

The phase retrieval results can be used in the 3D search to begin with an initial guess made on the 3D location of the object of interest. The initial, coarse estimate is required to obtain a first approximation to the solution in the global space to reduce the complexity of the algorithm, accelerate the convergence and avoid local maxima for the optimization required to solve Eq. 2.4. In this case, the initial estimate is obtained in the spatial frequency domain, using the amplitude information of the experimental image and finding the closest match to the phase retrieval result at each calibration image in a sum squared error (SSE) sense,

$$min_{\Delta z\in[-\frac{(N-1)}{2}\Delta z,\ldots,\frac{(N-1)}{2}\Delta z]}\left\{\sum_{m=1}^{M'}\sum_{n=1}^{N'}\left(|\mathcal{F}\{|f^2|\}(m,n;\Delta z)|-\left|\mathcal{F}\{I_{exp}\}(m,n)\right|\right)^2\right\} \qquad (2.5)$$

where N axial calibration images separated by an axial distance Δz = 100nm were used and the image size is MxN. Working in the spatial frequency domain reduces

the initial estimation search from three dimensions to only the axial dimension by ignoring the linear phase responsible for transverse shifts. After this initial estimate is found for the axial location, it is transversely cross-correlated with the experimental image to find coarse x, y coordinates.

Given this set of initial coordinates, an iterative algorithm is then implemented to find the optimum 3D coordinate in the object space $\vec{o} = \{\Delta x, \Delta y, \Delta z\}$ that maximizes the probability of matching the experimental pattern to a rigorously interpolated PSF crossection in the presence of noise (Eq. 2.4),

The likelihood function ($\mathcal{L}$) can be selected to suit the appropriate imaging conditions under consideration. Examples of common likelihoods include both the Poisson and Gaussian distributions,

$$\mathcal{L}\left(I_{exp}(m,n); f(m,n;\vec{o})\right) = \prod_{m=1}^{M'}\prod_{n=1}^{N'} \frac{\left(|f(m,n;\vec{o})|^2\right)^{I_{exp}(m,n)}}{I_{exp}(m,n)!} e^{-|f(m,n;\vec{o})|^2} \tag{2.6}$$

and

$$\mathcal{L}\left(I_{exp}(m,n); f(m,n;\vec{o})\right) = \prod_{m=1}^{M'}\prod_{n=1}^{N'} \frac{1}{\sigma\sqrt{2\pi}} e^{-\frac{\left(I_{exp}(m,n)-|f(m,n;\vec{o})|^2\right)^2}{2\sigma^2}} , \tag{2.7}$$

respectively.

Implementation of the MLE component is realized through maximization of the argument in Eq. 2.4 with the following gradient-descent iterative search algorithm for each axis (33),

$$o_j^{(p+1)} = o_j^{(p)} - \gamma \left(\frac{\partial^2}{\partial j^2}\mathcal{L}\left(I_{exp}; f(\vec{o})\right)\right)^{-1} \frac{\partial}{\partial j}\mathcal{L}\left(I_{exp}; f(\vec{o})\right)\Bigg|_{j=o_j^{(p)}} \tag{2.8}$$

where $j \in \{\Delta x, \Delta y, \Delta z\}$, p is the iteration number and γ is introduced to scale the search step size. Typical values for γ ranged from $0.1 \leq \gamma \leq 1$ (0.1 was used for both

the simulation and experimental results reported). Iteration is continued until the updated localization values are observed to converge. The derivatives along each axis are found numerically using central difference methods for the first-order derivative,

$$\frac{\partial}{\partial j}\mathcal{L}\left(I_{exp};f(\vec{o})\right)=\frac{\mathcal{L}\left(I_{exp};f(\vec{o}+\vec{h})\right)-\mathcal{L}\left(I_{exp};f(\vec{o}-\vec{h})\right)}{2|\vec{h}|} \tag{2.9}$$

and the second-order derivative,

$$\frac{\partial^2}{\partial j^2}\mathcal{L}\left(I_{exp};f(\vec{o})\right)=\frac{\mathcal{L}\left(I_{exp};f(\vec{o}+\vec{h})\right)-2\mathcal{L}\left(I_{exp};f(\vec{o})\right)+\mathcal{L}\left(I_{exp};f(\vec{o}-\vec{h})\right)}{|\vec{h}|^2} \tag{2.10}$$

where $\vec{h}$ is the displacement vector $\{h_x, h_y, h_z\}$ with non-zero values only along the direction that the derivative is taken.

2.6 Performance with Simulation Data

The estimation efficiency of this localization method is quantified by simulating a DH-PSF microscope with NA = 1.3 and M = 91x, imaging a single-molecule with average isotropic emission at λ=515nm. The optical configuration is designed to match that of the typical experimental implementation, as given in Fig. 2.2. The behavior of the DH-PSF image can be approximately described as a pair of intense lobes that rotate about the mutual center of mass as the object translates axially, shown both in the experimental and PR data of Fig. 2.1B and C, respectively, as well as Fig. 2.2.

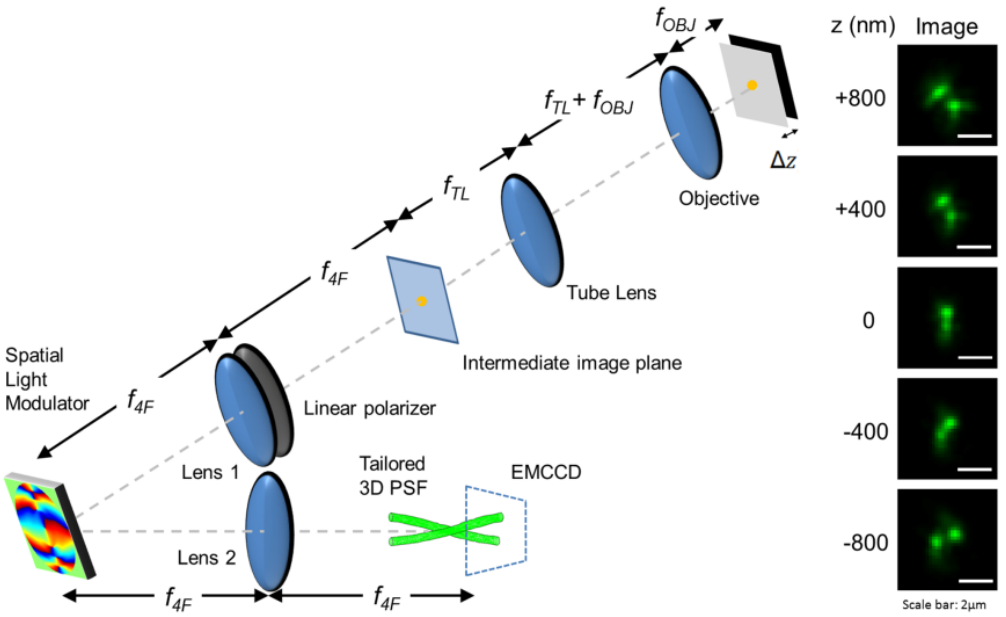

Fig. 2.2: Optical layout of PSF engineered microscope. The double-helix microscope collects the light emitted from the fluorescent sample. A traditional microscope with a 1.3NA objective is appended with a 4F optical setup, used to re-image the intermediate image plane onto the detector. A spatial light modulator (SLM) is placed in the Fourier plane of the 4F setup and is used to code the optical pupil of the microscope. When the double-helix PSF phase mask is present on the SLM, the light emission from the sample is encoded for subsequent imaging onto an electron-multiplying CCD (EM-CCD), located after the second Fourier lens (Lens 2). Experimental images are given in the right pane as a nano-particle is translated axially through focus.

The PR algorithm uses an average of 100 noisy image realizations, taken at three axial positions (z = -100nm, 0nm and +100nm) to form the calibration image set in simulation. Note that the PR algorithm can be run initially for system characterization and then store the recovered optical system pupil function for later use to speed up computation time.

The PR-MLE performance is tracked as the number of photons detected from the emitter is varied across a representative range. Poisson noise is considered the

dominant noise process, consistent with ideal experimental conditions, with a likelihood function given by,

$$\mathcal{L}\left(I_{exp}(m,n); f(m,n;\vec{o})\right) = \prod_{m=1}^{M}\prod_{n=1}^{N} \frac{\left(|f(m,n;\vec{o})|^2+b\right)^{I_{exp}(m,n)}}{I_{exp}(m,n)!} e^{-(|f(m,n;\vec{o})|^2+b)} \quad (2.11)$$

where the image size is MxN and b is a constant background noise level. In order to increase the per-pixel SNR, the DH-PSF was sampled at ½ the Nyquist sampling rate – consistent with our experimental conditions. Note that precise position estimation from a point response does not require full reconstruction of the signal. Further, an optimum sampling rate can be calculated for a given system and noise level. To isolate the performance under the shot-noise limit, no background noise is included in the simulation results presented here. Background noise is included in the experimental results of the appropriate section.

In Fig. 2.3, the MLE performance is compared for two likely scenarios along with the associated system CRLB. The first scenario characterizes the performance of the MLE algorithm when the optical pupil function was known a priori. This establishes the performance limit without introducing any potential errors from the PR algorithm. The second scenario characterizes the PR-MLE method using the PR results from the calibration images to obtain the pupil function and 3D complex-valued PSF. About 20 iterations are necessary for the MLE to converge on each estimate. A measure of the estimator efficiency is provided as $\varepsilon = \frac{\sigma_{est}}{\sigma_{CRLB}}$ - the ratio of the estimator precision (measurement standard deviation) to that of the CRLB. To develop a sense for the performance across a broad range of possible conditions, an average of the estimator efficiency is taken over a photon count range of 300-1100

photons. For a system known a priori, the resulting average efficiency along the x, y and z axes is $\varepsilon_{MLE,ap}(x,y,z) = (1.0 \pm 0.1, 1.0 \pm 0.1, 1.1 \pm 0.1)$. Note that an intrinsic, random error greater than $0.6nm$ is associated with the estimation of σ_{est} due to the finite distribution sample size of $N = 100$ used in the simulation. This random error is responsible for the fluctuations of σ_{est} about the CRLB. Therefore, these results demonstrate that the performance of the MLE is efficient. For the PR-MLE the efficiency is $\varepsilon_{MLE,PR}(x,y,z) = (1.0 \pm 0.1, 1.5 \pm 0.1, 1.1 \pm 0.1)$. The minor loss of precision for the PR-MLE along the y coordinate is due to both the sub-Nyquist sampling conditions and the presence of noise in the calibration images used for the PR estimate. The results of Fig. 2.3 imply that the PR-MLE estimator is efficient in reaching the performance limit in the shot-noise-limited case.

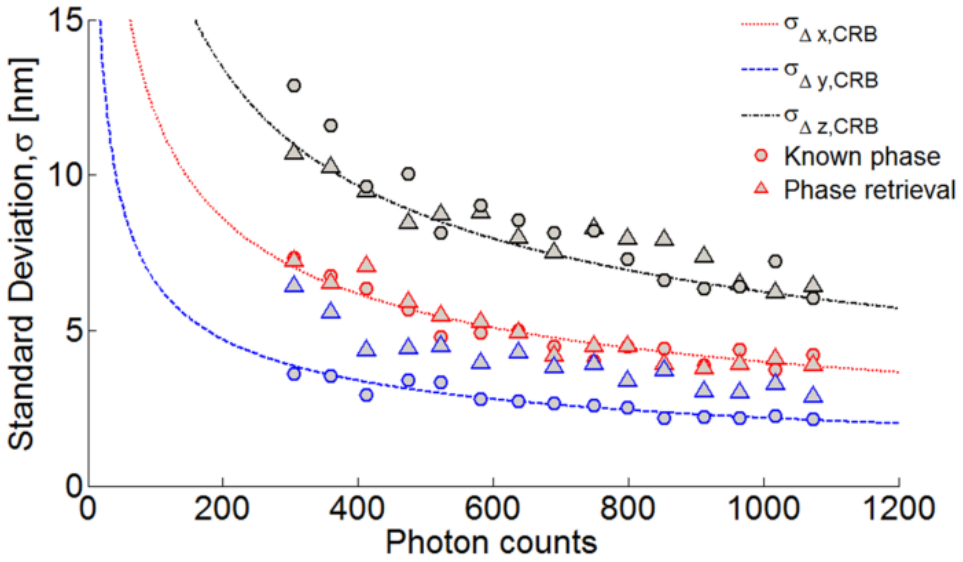

Fig. 2.3: Localization efficiency tests as measured by applying the MLE to 100 simulated, noisy images and varying the number of photon counts. The lines indicate the theoretical lower bound (Cramer-Rao Lower Bound) of the precision for which the x, y and z-axis positions may be localized in the shot-noise limit with an emitter in focus ($z = 0$). The bound increases rapidly as the number of photons collected in the image decreases. The colored circles indicate the associated Maximum-Likelihood (ML) estimation precision when the pupil function of the optical system is well-known and no phase-retrieval is necessary. The colored

triangles indicate the ML precision when the phase-retrieval algorithm is implemented.

In order to test both the quality of the phase-retrieval interpolation and the MLE in the regions not bound by constraints given by calibration images, two tests are proposed. The first test examines the localization accuracy and precision in the axial regions between the calibration planes. The second test examines the precision of the PR-MLE for localization when sub-pixel transverse shifts of the PSF are present.

The results of the first test are presented in Fig. 2.4A, showing that the PR-MLE behaves in a linear fashion between the calibration planes (the vertical shaded regions) and that the accuracy and precision are on par with that given in the calibration planes. Note that any bias present in this algorithm can be found by reference to the known calibration planes. Therefore associated calibration curves can be tabulated from the phase-retrieval step and later used to correct the experimental localizations and improve accuracy.

In Fig. 2.4B, the results of the second test concerning transverse localization are given for a series of non-integer pixel-spacing transverse shifts (integer-valued shifts are highlighted with vertical shaded regions). Again, the PR-MLE results behave both linearly and accurately with sub-pixel shifts in the transverse dimension. The success of these tests again validates the optimality of the PR-MLE procedures highlighed earlier.

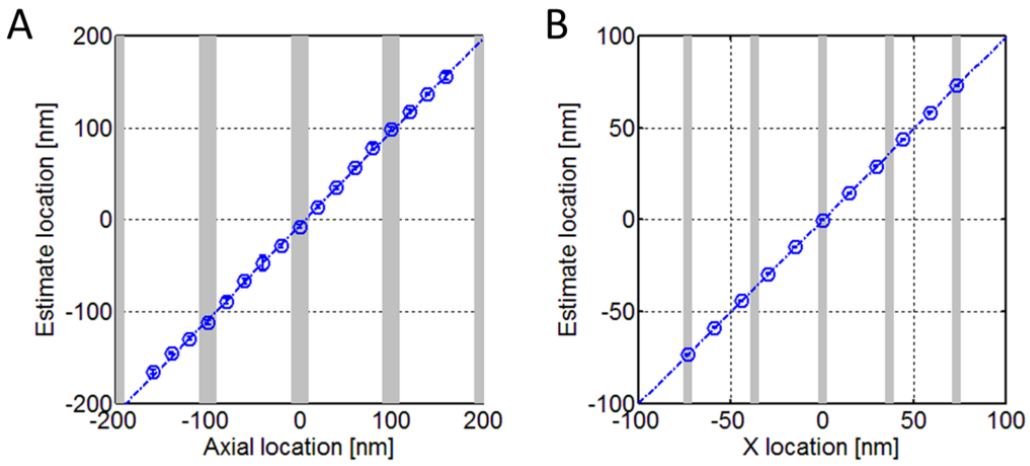

Fig. 2.4: Phase-retrieval MLE (PR-MLE) results for the estimation with interpolated and sub-sampled 3D data. (A) PR-MLE results on simulated data in 20nm intervals through +/- 160nm of axial translation. The gray bands represent the axial planes where the calibration data was taken for phase-retrieval. The interpolation of the PR-MLE is seen to behave linearly between the phase-retrieval calibration planes, thereby demonstrating proper interpolation accuracy and precision in the axial direction. (B) PR-MLE results on simulated data as the source is shifted transversely in sub-pixel intervals. The gray bands represent integer valued pixel shifts. The interpolation of the PR-MLE is seen to behave linearly across multiple pixels thereby demonstrating sub-sampled resolution in the transverse direction.

2.7 Performance with experimental data

The experimental setup shown in Fig. 2.2 was used to image the photo-activatable green fluorescent protein label PA-GFP within a sample of Kangaroo Rat Epithelial cell (PtK1) which was prepared by Prof. Jennifer DeLuca and Keith DeLuca at Colorado State University. The experimental data was collected by Dr. Prasanna Pavani during his Ph.D. study at University of Colorado.

A custom microscope (Zeiss objective Plan-Neo Fluar, 1.3NA) with magnification M=91x is used to image the samples. The tube lens is an achromatic lens of focal length f_{TL} = 150mm. The image conjugate to the focal plane of the objective is named the intermediate image plane. This intermediate image serves as

the focal plane of the 4F optical system located after the microscope stage. The sample mount was attached to a piezo-driven stage (Physik Instrument P-615.3CD).

For the single-molecule imaging in a biological sample, the image acquisition time was set to 500ms. The sample was initially bleached using circularly polarized 488nm illumination (38mW from an Ar+ laser), then re-activated with circularly polarized light from a 405nm diode laser (0.5mW). The re-activation illumination uses a function generator to produce a 500ms pulse at 0.2Hz. Each beam illuminated a 40 micron diameter field on the sample. The data was collected in an epi-fluorescence configuration, with a dichroic mirror placed behind the microscope objective to block/redirect the excitation/activation light and transmit about 90% of the emission from the PA-GFP. Sample prepration is described in Reference (30).

A reflective Spatial Light Modulator (SLM, Boulder Nonlinear Systems XY-P512 SLM) is placed in the Fourier plane of the 4F system to encode the incident wave field with a double-helix PSF transfer function (29). A pair of achromatic lenses (focal length f_{4F}=250mm) and a linear polarizer make up the rest of the 4F system. The linear polarizer is utilized to select polarization parallel to the active axis of the liquid crystal modulated by the SLM and in practice was a broadband polarizing beam splitter (420-680nm, Edmund Optics). The loss of photons in the othogonal polarization state is not necessary and has been solved with the use of additional optics (30) or with the use of phase masks (59). The final image is formed on the electron-multiplying charge-couple device (Andor iXon EM-CCD), with a 16μm pixel pitch, located a distance f_{4F} behind the final 4F lens.

To maximize the light efficiency of the DH-PALM system, the light from the first Fourier lens is obliquely incident on the SLM (at 30 degrees) so that reflected light may pass through the second Fourier lens without the use of additional beamsplitters. This oblique incidence introduces aberration into the optical system from the relative loss in modulation contrast of refractive index seen by the incident light as it is modified by the SLM. Additional sources of aberration include the use of a tilted camera in this system (30) and those inherent to volume imaging such as objectives that are optimized for imaging a single plane with minimal aberration at the cost of volume performance. Lastly, imaging sources at varying depths beyond the cover slip will be subject to spherical and specimen-induced aberrations.

Calibration images were taken using samples prepared with 40nm diameter fluorescent microspheres (Invitrogen yellow-green carboxylate-modified FluoSpheres®). The microspheres were chosen to have similar fluorescent spectrum to the PA-GFP in order to minimize performance differences due to chromatic effects (excitation peak, 405nm; emission peak, 515nm). The 40nm bead size is well below the diffraction limit of the microscope, therefore they were treated as point sources.

The calibration data is generated by images collected as the sample stage is translated in 100nm intervals through the focal plane. A series of images are taken (26 is typical) at each axial location to form an average to be later used as the calibration image for phase retrieval. The axial calibration data was shown earlier in Figure 1.1B and the PR results are given in Figure 1.1C. The exposure time for each image is 273ms and the EM-CCD is cooled to -90°C. The 3D PSF can be

determined by using multiple PSF image planes for Phase-Retrieval (PR) followed by averaging, which implies that a single optical pupil can accurately model the 3D behavior of the optical system (55) (56). This approximation requires depth invariance of the PSF and appropriately describes the behavior of low-NA systems, such as telescopes, to acceptable accuracy. In the new field of precise 3D localization with high-NA systems, the single-pupil approximation introduces errors yielding non-optimal results. Next, the error generated by a single pupil function model is quantified in comparison to the depth-variant model to evaluate which best fits the data.

The calibration images described earlier are used with the PR method described in the main text to generate field estimates for each axial plane of the calibration measurements. A single optical pupil was obtained by averaging these axial estimates (taken here about the typical experimental depth of the single-molecules, $-1000nm \leq \Delta z \leq -400nm$) after transformation into the Fourier domain and addition of the proper phase due to propagation (Eq. 2.3). According to the depth-invariant model, this single pupil suffices to represent the 3D-PSF of the optical system.

The relative merit of the depth-invariant model (single pupil function) is first compared with the depth-variant model in terms of accurately representing the rotational characteristic of the calibration images. The rotation characteristic is provided from the orientation of the two lobes relative to the camera frame of reference (29). I follow the methods developed in Ref. (29) to characterize this orientation. As a review, this method consists of finding the centroid of each of the

two DH-PSF lobes and calculating their subtended angle of orientation where the origin is defined to be parallel to the y-axis of the camera. As rotation is a definitive trait of the DH-PSF, the results in Fig. 2.5A provide one measure of how well the depth-variant and depth-invariant models match the calibration data. It is seen that the depth-variant model tracks the rotational characteristic of the DH-PSF better than the depth-invariant model found from averaging the phase-retrieval results.

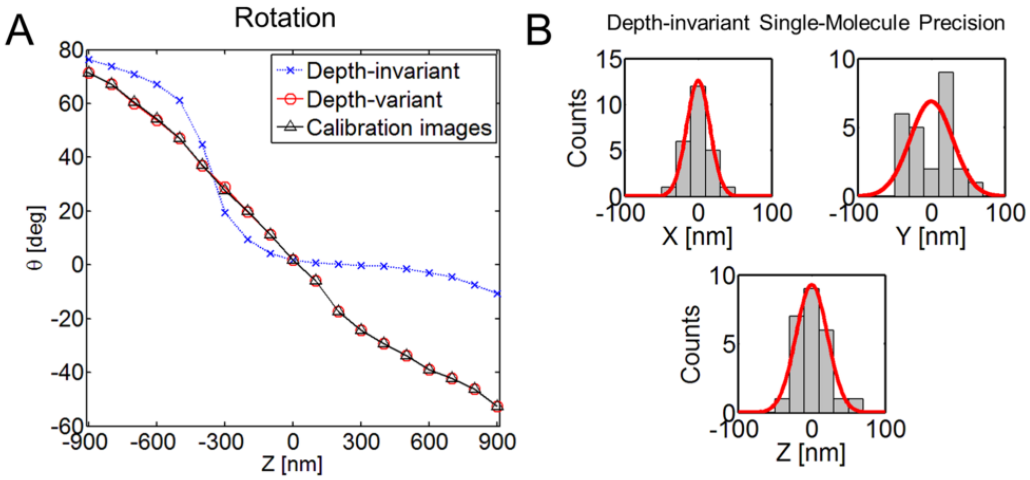

Fig. 2.5: Experimental estimation performance using a depth-invariant model in PR-MLE. (A) Characterizing the predicted rotation of the DH-PSF as a function of depth using the depth-invariant and depth-variant models indicates that the depth-variant model provides better agreement with the calibration data. (B) The depth-invariant model results in a single-molecule localization precision of 16nm, 29nm, 21nm in *x*, *y* and *z*, respectively.

Furthermore, to evaluate the best model for particle localization, we compare the precision obtained with each model for a single-molecule. Fig. 2.5B presents the localization results of the depth-invariant model to be $\sigma_{MLE}^{DI}(x, y, z) = (16,29,21)nm$. Alternatively, the depth-variant treatment in Fig. 2.6 shows that the PR-MLE

localized this molecule to $\sigma_{MLE}^{DV}(x, y, z) = (14,10,13)nm$. This demonstrates again how the depth-variant model is better suited to the experimental data.

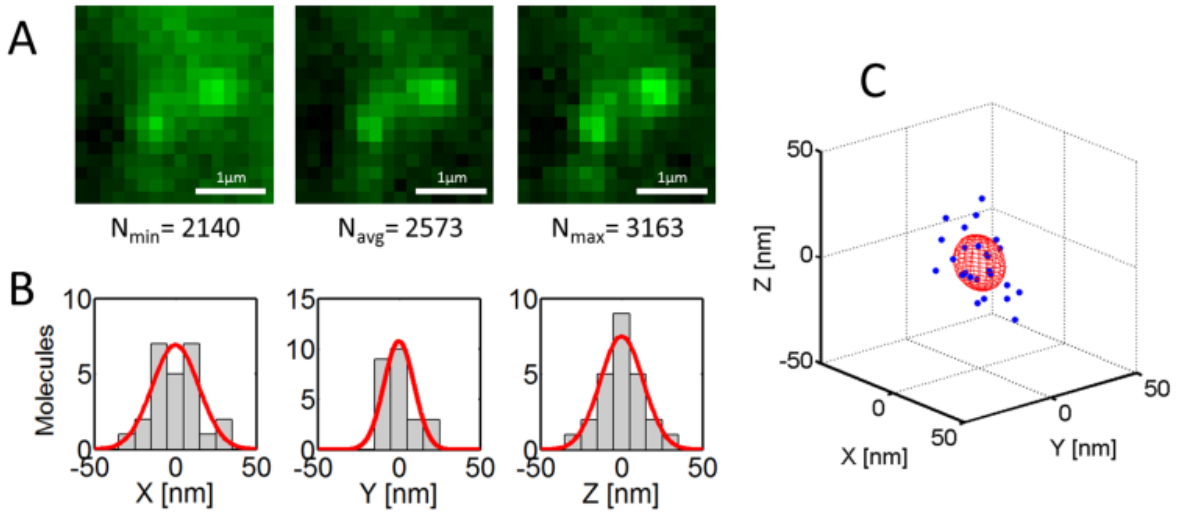

Fig. 2.6: Experimental estimation performance of single-molecule localization. A single molecule is identified with an average of 2574+/-309 photons collected per image over a series of 25 images. (A) Representative images of the experimental data when the minimum, average and maximum number of collected photons are present. (B) Histograms of the *x*, *y* and *z* localization of the emitter, demonstrating localization precision of 14nm, 9nm, 13nm, respectively. (C) Volume visualization of the uncertainty ellipsoid associated with the resulting estimations and the scatter of the individual measurements.

Using the results from the phase-retrieval algorithm (the continuous 2D projection set in Fig. 2.1C) tracking of the beads used for calibration was implemented with the PR-MLE to evaluate performance. Note that the calibration data was taken as an average at each stage position of the images used for this tracking experiment. The plot in Fig. 2.7 shows the estimation results corrected for bias and drift to demonstrate the precision of the MLE, the experimental depth of field, the accuracy of the estimator and the true variability of the calibration sources. The average performance through the 2.2μm axial range was measured to

be $\sigma_{MLE}(x, y, z) = (6.6, 5.0, 5.2)nm$ with an average of $N_\gamma = 8{,}900$ photons collected per image.

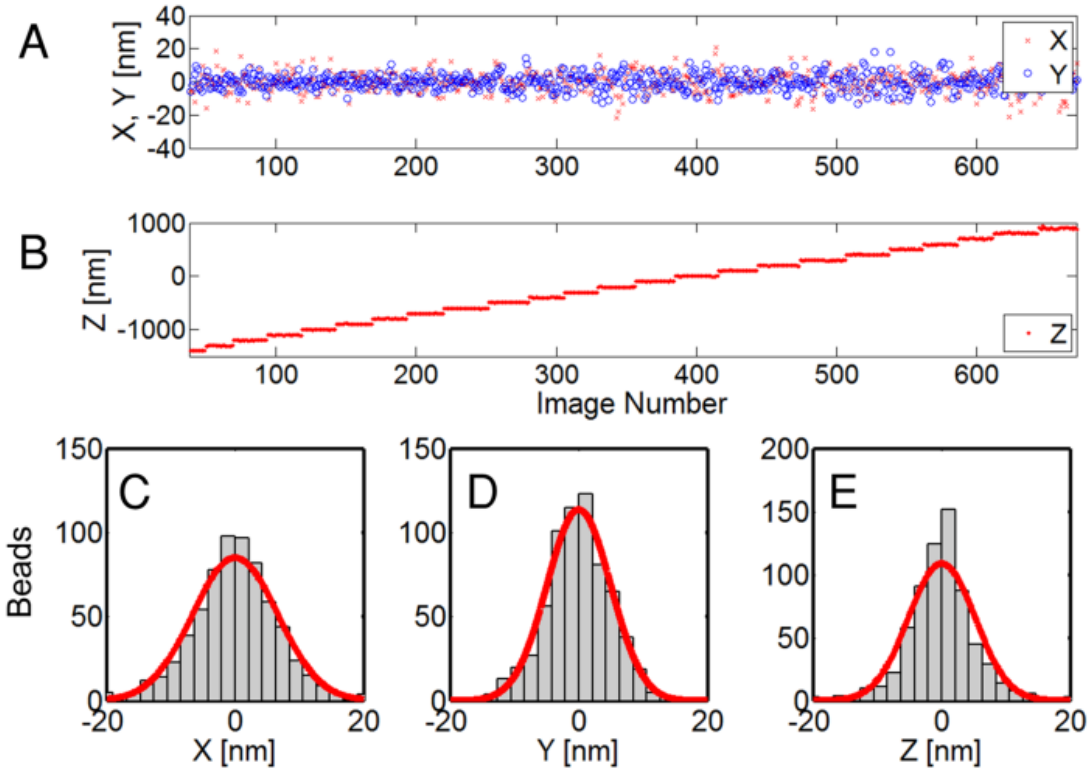

Fig. 2.7: Tracking of fluorescent beads and calibration data. The fluorescent nano-particle calibration images are tracked in x, y (A) and z (B) as the piezo-electric stage is translated in 100nm intervals. The estimation data has been corrected for bias and linear drift. The PR-MLE estimates of the complete data set, centered about the mean for each position, are collected and shown as histograms for x (C), y (D) and z (E). The associated precision (standard deviation) for the complete data set (671 points) through an axial range of 2.2μm is σ *(x,y,z)* = (6.6, 5.0, 5.2) nm.

A Poisson pdf (Eq. 2.11) was utilized for the PR-MLE algorithm and is justified by examination of the image noise statistics shown in Fig. 2.8. A histogram of experimental photo-electron counts generated in an area with approximately uniform intensity is shown to be well described by a Poisson distribution (red curve, Fig. 2.8C).

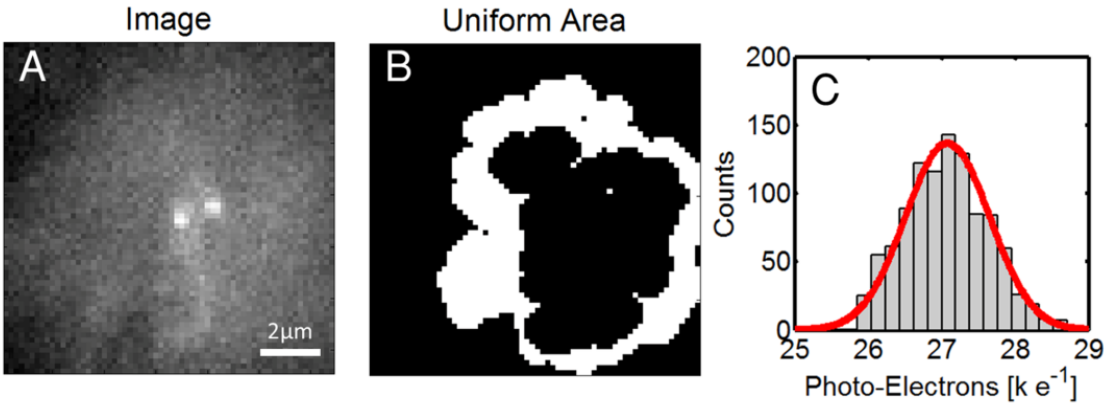

Fig. 2.8: Experimental noise characteristics. (A) An experimental image of a single molecule. (B) Image morphology returns an area of the image with near uniform background level for noise analysis (white region). (C) The distribution of the photo-electrons within the uniform area follows a Poisson distribution (in red).

In order to count the number of photons in a given molecule image, the spatially varying background must be accounted for. The opening image-morphology operation was utilized to analyze the image and estimate the background (60). The process is shown in Fig. 2.9 A-D, where a representative experimental image is given. This image-opening background calculation algorithm searches the image for features that can be approximated as a collection of disk-shaped elements. By setting the size of the disk-shaped element to the dimension of a DH-PSF lobe, the DH-PSF features may be selected out, leaving only the spatially varying background in panel B. The morphological opening operation is implemented using the imopen command of the MatLab Image Processing Toolbox environment (The MathWorks Inc, Natick, MA). As a result, an accurate estimate for both the underlying, average background count and the molecule signal (panel

C) can be made for the input to likelihood functions used in the PR-MLE. An example PR-MLE fit is presented in panel D.

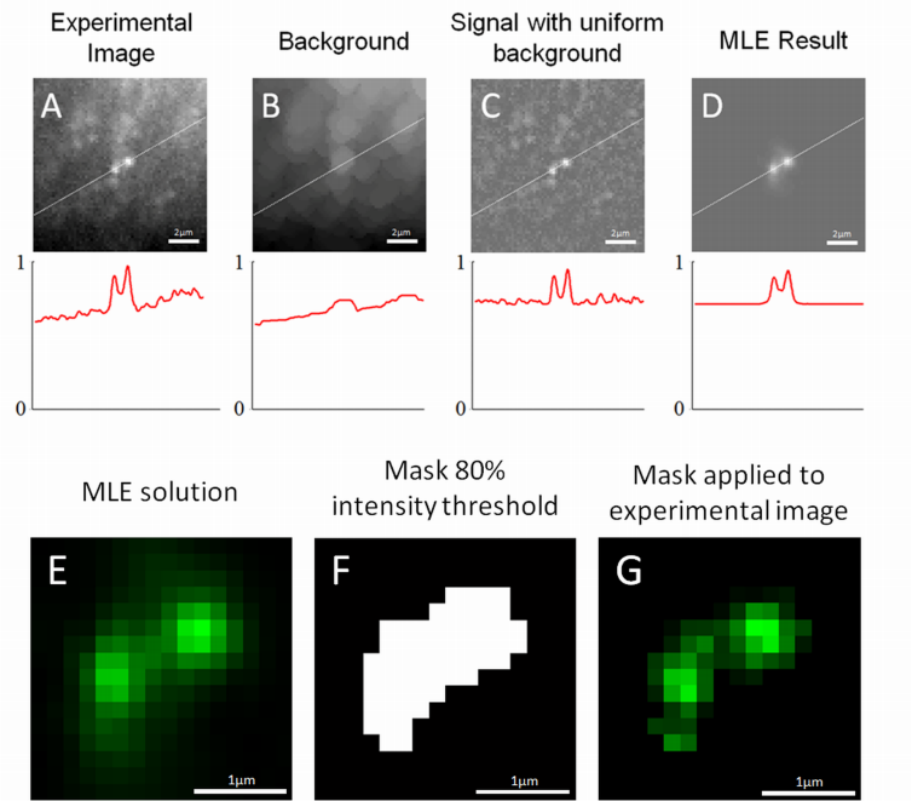

Fig. 2.9: (A-D) Background subtraction algorithm for experimental images. The background of the experimental single-molecule image (A) is estimated using an image morphology operation with the estimated background presented in panel (B). The resulting background subtracted imaged (C) is then treated as the signal used for the PR-MLE with addition of a uniform background which is approximated as the mean value of (B) in the region of the DH-PSF. The result of applying the PR-MLE to this data is presented in panel (D). Line-outs across the DH-PSF region are given below the respective image to aid in visualizing contrast. (E-G) Method for counting the number of photons in an arbitrary PSF. The number of photons collected from a single molecule is quantified as the number of counts within the spatially distributed PSF. First, a most-likely solution is found using the MLE (E). Then a mask is generated representing the regions of the experimental image where the intensity is above threshold (panel F, here 80% threshold). Using the PSF returned from the PR-MLE algorithm (E), the remaining energy of the PSF outside this mask is calculated. The mask is applied to the background-subtracted experimental data (panel G) and the number of contained photon counts is scaled by the amount of energy remaining outside the mask.

The experimental images are collected using an electron multiplying CCD (Andor iXon) and the number of photons incident on the detector is calculated as,

$$N_\gamma = \frac{LG_{AD}}{G_{EM}\eta} \tag{2.12}$$

where L is the ADU (analog-to-digital units) counts output from the A/D converter, G_{EM} is the electron multiplication gain (100 in our experiments), G_{AD} is the number of electrons per A/D count (11.4697), and η is the quantum efficiency of the detector (0.95 @ 515nm).

The number of photons present in the molecule image PSF is then calculated, as shown in Fig. 2.9E-G. Given the most likely match from the PR-MLE, a mask is generated which represents the transverse map thresholding 80% of the intensity of the experimental PSF. The mask is applied to the background-subtracted experimental PSF for an initial photon count. This number is then scaled by the ratio of the remaining energy in an ideal PSF to the energy contained in the 80% threshold mask in order to estimate the total number of photons. The background counts are found by applying the same threshold mask to the background estimate and reporting the average number of photons per pixel within the region associated with the PSF.

The PR-MLE is performed on images from the PALM wide-field microscope dataset of the PA-GFP labeled biological sample. The total accumulation time was over 3.7 hours. Individual molecules were selected from the image by looking for areas of high temporal variance of photon counts, indicating that a photo-activatable source has temporarily fluctuated in intensity. These areas were compared with the calibration images, which serve as templates, to determine

whether the local fluctuation has an intensity pattern which can be associated with the DH-PSF. If the pattern is indeed a match, the PR-MLE is implemented on this local region. A confidence measure was assigned to the estimation results according to the similarity of the estimated PSF and the experimental image. If the transverse overlap of the two patterns contained greater than 45% of the total energy, the measurement was kept. A total of 4689 of these measurements are reported and used to plot the 3D information in Fig. 2.10, visualizing the volume across which the estimator performance has been demonstrated.

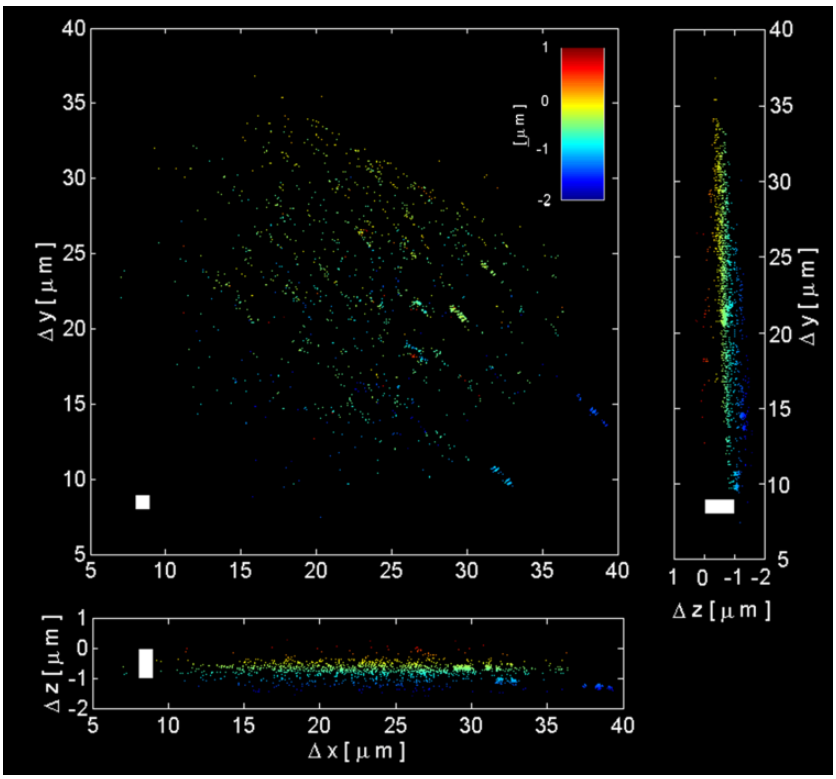

Fig. 2.10: PR-MLE DH-PSF PALM imaging of PtK1 cells expressing PA-GFP-tubulin. The distribution of a sparse set of individual molecules throughout an imaging volume is shown. 4690 individual localization estimations are color coded according to the axial position. Molecules were found to be dispersed within a 25x25x1.9μm volume.

Lastly, from the entire dataset of PA-GFP molecules, a total of 144 individual single molecules are identified under the constraint that each one is present in four sequential images thus yielding 998 total localization measurements. An average collected emission of 2087+/-291 photons per image was collected for this ensemble, shown in Figure 2.11B. The molecules were found to be dispersed throughout a 1.9um axial depth and a 25x25um field of view. The histograms in Figure 2.11C-E show estimation results of the PR-MLE on the data-set of single-molecule measurements, each position shifted to have a mean located at the origin. Significant background is present in the experiment (an average of 349+/-57 photon counts per pixel. The PR-MLE estimation precision (standard deviation) on this collection of molecules is $\sigma_{MLE}(x, y, z) = (17, 10, 19)nm$.

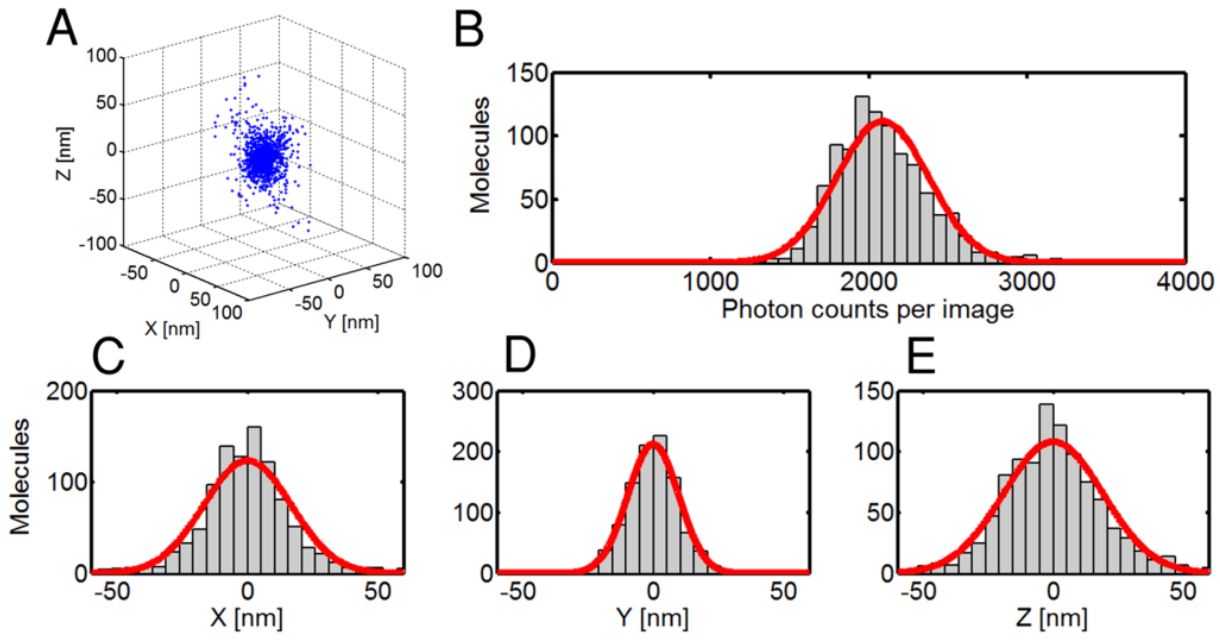

Fig. 2.11: Localization and photon counting results from 998 estimations of single-molecule positions in a PALM experiment with a DH-PSF. (A) The three dimensional scatter plot of these measurements demonstrate localization within a 17nm x 10nm x 19nm volume (standard deviation). (B) The distribution of counts per image reveals a normal distribution with a mean number of 2087 total photons.

(C-E) The individual histograms of the x, y and z-axis estimation from the ensemble used in panel A.

A sense for the experimental estimator efficiency of the PR-MLE is developed by comparison of the reported MLE precision with a representative CRLB by assuming average emitter characteristics found from the data set (i.e. positioned at the mean axial position, emitting the average number of photons with the average background level). This CRLB is found to be $\sigma_{CRLB}(x, y, z) = (12,16,23)nm$. The average estimator efficiency of all three position estimates is therefore 0.95, indicating that, on average, the estimator is indeed efficient at localizing experimental emitters within a volume. Note that this is only an estimate of the performance limitations for the experimental system and that the non-linear relationship with background count levels (~16% measured variation), assumptions of a uniform background, the changes of the signal level from the emitter (~14% measured), as well as the averaging of performance across an extended range of axial depth, all contribute to real deviations from this CRLB estimate, which in this case, should only be taken as indicative of the expected performance of an efficient estimator. During the experiments no significant anisotropic effects were noticed due to the rotational freedom of the fluorescent proteins.

In order to further illustrate the applicability of the methods presented above, a distance measurement is reported here. Two molecules were identified in the PALM experiment and their 3D distance measured as shown in Figure 2.12. The first molecule (right-most) is localized to $\sigma_{SM1}(x, y, z) = (17,16,25)nm$ and the second molecule (left-most) is localized to $\sigma_{SM2}(x, y, z) = (9,19,20)nm$. After

propagating the random error in localization of each molecule, the distance separating them was determined as 778 +/- 22nm. The experimental data points are given as solid dots and each molecule position is visualized as an ellipsoid where the semi-axes are given by the respective standard deviation of each localization measurement.

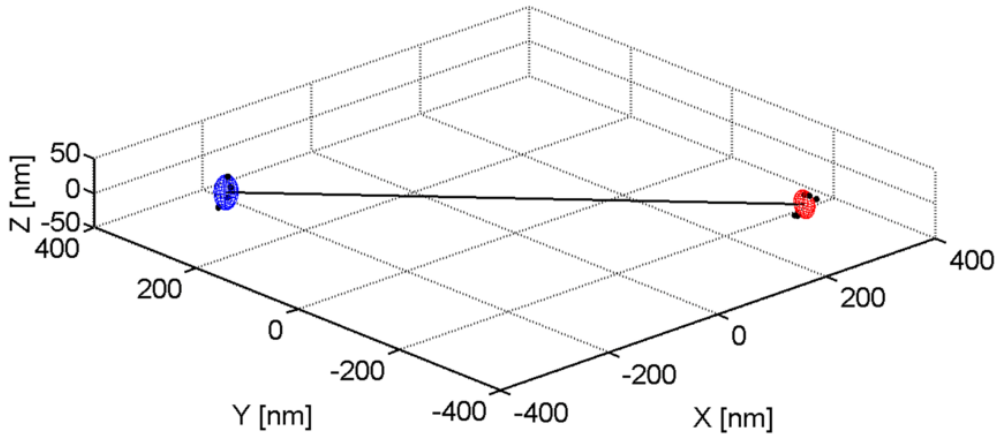

Fig. 2.12: Measurement of the distance between two PA-GFP molecules. Nine total measurements are used to localize the individual molecules. Because each molecule is well-localized a high precision distance measurement can be calculated.

2.8 Discussion

The experimental single-molecule localization performance compares favorably with recent 3D localization experiments in PALM/STORM. A rigorous comparison of the various experimental techniques is difficult because the available reports relate to different samples and fluorophores (13) (14) (30) (45) (47). Furthermore, 3D PALM/STORM reports do not always provide complete data (3D precision, number of detected photons, background noise level, axial range, etc). Besides, many studies use isolated beads rather than single molecules to characterize the system's performance, which, while useful, provide favorable detection conditions with no

background noise from other emitters, no auto-fluorescence, and limited aberrations. One way around this problem is to consider fundamental assessments of the performance limits, which have recently shown the advantages of engineered PSFs (35). Another informative approach is to compare actual experimental single-molecule performances based on quantitative measures of resolution and axial range as explained in what follows.

For the shot-noise limiting case, neglecting for the moment background and pixelation noise, the localization precision follows the $1/\sqrt{N}$ scaling law (36) (61). Hence, one can use the photon-normalized geometric mean precision, $C^{3D} = \sqrt{N}\sqrt[3]{\sigma_x\sigma_y\sigma_z}$, as a resolution metric to compare 3D systems. According to this metric the system demonstrated here achieves about 50% better precision than prior 3D PALM/STORM demonstrations using astigmatic (14) and bi-plane (47) imaging (corresponding to ~3 times smaller minimum resolvable volume) with more than twice the depth range. It thus becomes closer to achieving the axial resolution of interferometric systems (45) while providing one order of magnitude longer axial range with a much simpler system. It should be noted that the current DH-PSF experiment was performed with fluorescent proteins and over a long depth range, both factors which negatively affect the signal to background noise ratio.

The astigmatic method (14) achieved a precision of $\sigma(x,y,z) = (9,11,22)nm$ with 6000 photons, giving $C^{3D}_{Astig} = 1004$. The optimal estimator and the experiments reported here lead to $C^{3D}_{DH} = 614$ and 669 for the individual single-molecule and the ensemble, respectively. Note that this result was obtained with a slightly lower NA, as well as for samples with multiple emitters and lower photon

counts, which increase background noise. Still this metric suggests the dramatic advantage of optimal estimators combined with tailored PSFs. Ref. (47) reports the bi-plane method in a PALM-like experiment with precision of $\sigma(x,y,z) = (30,30,75)nm$ and (apparently) ~500 photons detected, leading to $C_{BP}^{3D} = 910$. Ref. (45) reports resolution tested with beads of $\sigma(x,y,z) = (9.5,9.5,4.1)$nm providing $C_{BP}^{3D} = 250$ but with a range of only 225nm. For Ref. (42) the values on the table are estimated; the main drawback of this method being the limited field of view in one transverse dimension (under 1μm) as opposed to the other methods (>>10 μm). This information is summarized in Table 2.1.

3D PALM/STORM method	Experimental resolution metric (nm) $C^{3D} = \sqrt{N}\sqrt[3]{\sigma_x\sigma_y\sigma_z}$	Axial range (nm)	System complexity (relative to standard microscopes)
Astigmatic STORM (Ref. 6)	1004 *	800	Simple
Bi-plane (Ref. 7)	910 *	1000	Simple
DH-PSF (this report)	669 (ensemble) *, 614 (individual) *	2000	Simple
Interferometric (Ref. 8)	250 †	225	Complex
Virtual volume (tilted mirror) (Ref. 9)	550 †	~900 ‡ (limited in x and z)	Simple (limited sample geometry)

* Measured under PALM/STORM conditions with single molecules
† Measured with beads
‡ Estimated value, field of view limited in one transverse coordinate

Table 2.1: Comparison of resolution and range among 3D PALM/STORM experimental results.

These results show that the integration of PSF engineering, photoactivation-localization imaging, and optimal estimation enables one order of magnitude

improvement in resolution along each spatial direction when compared with classical fluorescence imaging. This translates into three orders of magnitude improvement in the resolvable volume over a wide 3D field of view. In addition, the unknown, systematic aberrations may be completely characterized through comparison of the PR recovered pupil and that of the expected pupil. This data may then be used to provide the user additional information concerning the sources of the aberration (e.g. spherical aberrations due to the distance from cover slip), representing a useful byproduct of the method.

2.9 Conclusion

In conclusion, the optimal estimator based on a (PR-enabled) MLE, tailored to match the conditions found in single molecule imaging, is efficient in reaching the 3D localization performance limits with arbitrary PSFs. The rigorous depth-variant PR interpolation of calibration data takes into account systematic errors caused by unknown and unavoidable 3D optical aberrations. The optimal 3D localization algorithm in conjunction with a DH-PSF shows the best 3D localization precision in PALM/STORM systems with an extended depth range, enabling a ~1000 fold improvement in resolvable volume with respect to classical fluorescence microscopy.

2.10 Appendix A: PR-MLE Algorithm Flowcharts

In the following an explicit enumeration of the PR-MLE algorithm steps is presented for the purposes of reproducing the results presented herein. First, the Phase-retrieval algorithm is presented in Fig. 2.13. This algorithm is followed after

three calibration images have been collected experimentally. The steps enumerated along the right-hand column list the particular equations which are required to complete one iteration of the Phase-retrieval algorithm. Once the PR algorithm is completed, the results can be stored for later use.

The PR results are used in this text as an optical system model to be applied for 3D particle localization. The 3D particle localization is accomplished by following the flowchart in Fig. 2.14 for Maximum Likelihood Estimation (MLE).

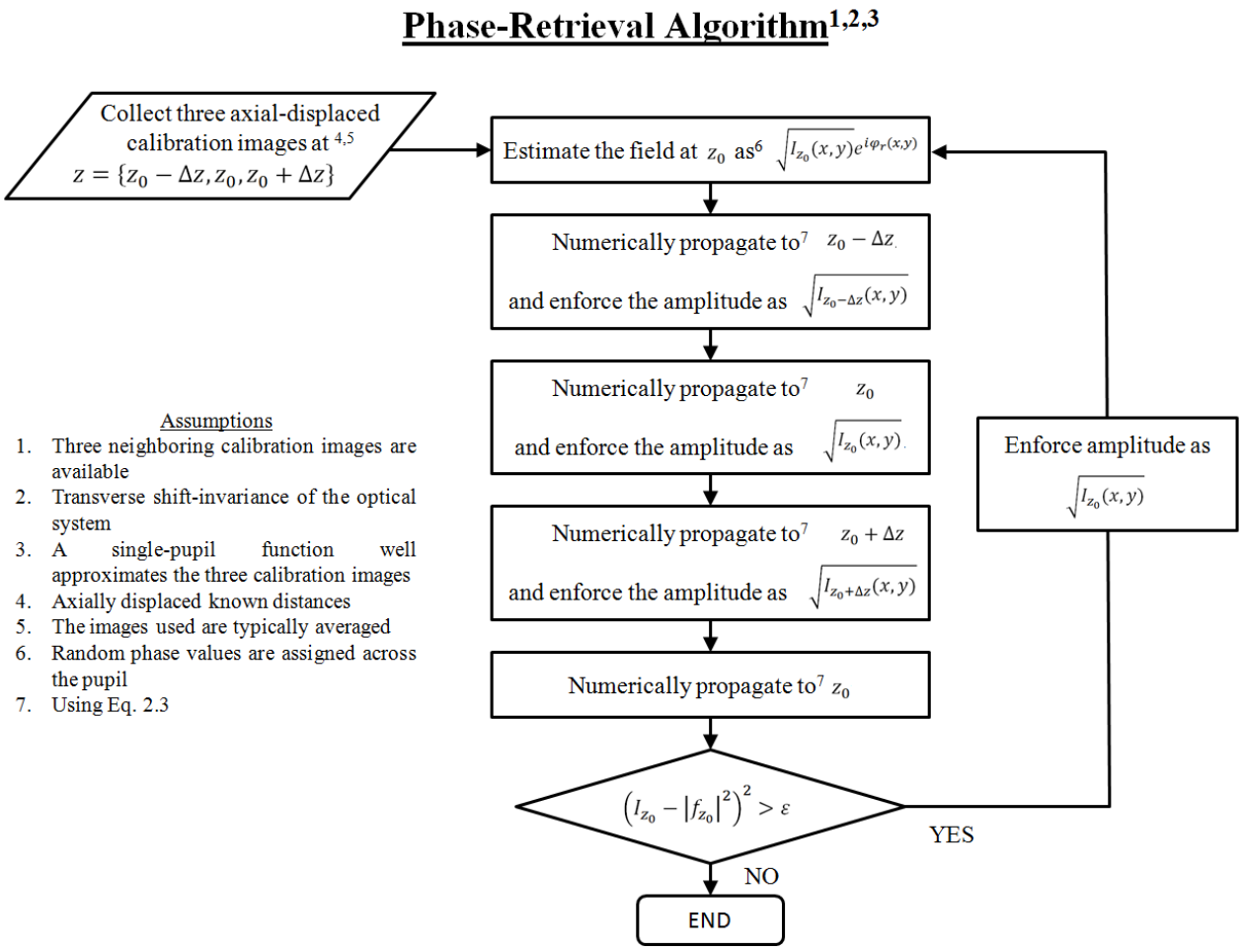

Fig. 2.13: The enumerated steps of the Phase-Retrieval (PR) algorithm used in this text. The steps on the right-hand side are followed in order to complete one iteration. The assumptions used for successful PR are explicitly identified.

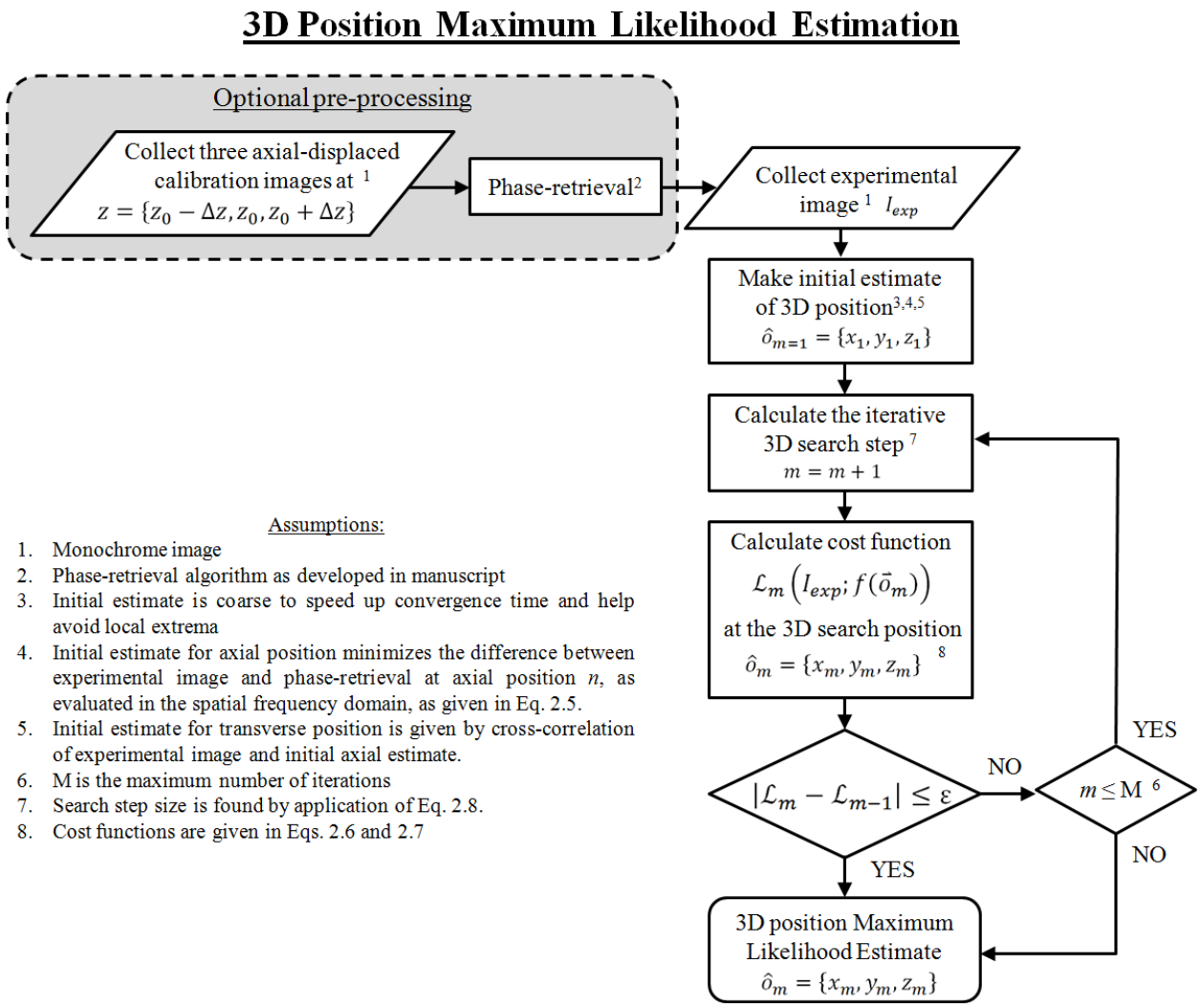

Fig. 2.14: The Maximum Likelihood Algorithm (MLE) which is presented in the main text. After completion of the Phase-Retrieval algorithm reported earlier, the MLE is used to match the 3D location of a point source in an experimental image. The post-processing steps which make up the MLE are identified separately. The assumptions required are explicitly presented in the left-hand side.

CHAPTER 3

2+1D IMAGING WITH ENGINEERED POINT SPREAD FUNCTIONS

3.1 Introduction

The use of a Double-Helix shaped engineered Point Spread Function (DH-PSF) was introduced and demonstrated for application to quantitative 3D microscopy in Chapter 2. In that particular application it was established that the patterned, diffraction-based propagation of the DH-PSF design increased the axial position-related information content in a signal and consequently improved localization precision. Whereas the imaging technique of Chapter 2 relied on the precise localization of individual molecules with a non-linear response to the incident radiation to generate super-resolution images, this chapter will be restricted to objects that exhibit a linear response to the intensity of incident illumination. In addition, the lessons from that prior analysis will now be applied at the other end of the size scale where axial-ranging solutions of macro-sized objects have dominantly been designed using geometrical optics.

Common examples of these geometrical solutions include stereo-vision, which uses the disparity of object position in two images from cameras with known, different viewpoints (62); and depth-from-defocus, which uses the projected size of

the optical pupil in the image plane to estimate depth (63). As opposed to 3D imaging and tomography, these examples, are considered 2+1D and are functionally similar to profilometry. Due to the relative success experienced at the nano-scale with engineered PSF solutions it is worthwhile to examine whether diffraction-based designs can improve axial-ranging for macro-scale problems and if so, develop an intuition on what limits and trade-offs can be expected.

In this chapter, a system is considered for imaging a random collection of objects with extended shape. Therefore one can no longer assume the object being imaged to be known a priori. This is a significant departure from the prior 3D microscopy work in Chapter 2 – where the object remained a single-molecule and was well approximated as a point-like source. For the single-molecule work, this simplified the problem of estimating the PSF, and subsequently the 3D position, from an experimental image,

$$i = h(z) \otimes o + \boldsymbol{n} \tag{3.1}$$

where i is the image, o is the object, $h(z)$ is the axial shift-variant PSF and $\boldsymbol{n}$ is the additive random noise. With a point-like source, the object o can be approximated as a delta function. Therefore the image and the PSF can be considered exact duplicates, i.e. $i = h(z)$, and the estimation problem is reduced to the extreme case where direct estimation of axial position is feasible with a single image.

The passive-ranging problem becomes less straightforward immediately after removing this prior knowledge and admitting random objects as possibilities. Such a scenario will be typical for the application of imaging extended objects found in natural scenes, biological samples and surveillance applications. A solution is

therefore necessary in order to extend the existing work of diffraction-based engineered PSFs to extended object, passive ranging problems. Additionally, it must be evaluated whether engineered PSFs provide improved axial-localization solutions for the macro-scale problems with random objects, and if so, how the localization precision depends upon the specific object under investigation.

Finally, because the localization is determined from $h(z)$ the PSF must be sampled appropriately on the detector for the estimation algorithm to work properly. This places a constraint on the maximum numerical aperture of the imaging lens which then imposes a limit on the Field-of-View (FOV). This relationship between the Field-of-View and Depth-of-Field for engineered PSF solutions is examined in more detail in Appendix A.

For the purpose of this study, the active use of illumination control (for example, time-of-flight and structured-illumination imaging (64) (65)) is excluded from consideration in favor of passive solutions which will only require modification of optical element design. Passive systems are relevant for solutions where data must be collected without leaving any trace of the measurement process in the form of emitted radiation - of paramount importance for surveillance applications. Passive solutions also provide an advantage in terms of power consumption since adequate lighting of a scene is provided from ambient illumination instead of being actively controlled. It should be noted that the current goal of incorporating engineered PSFs into both of these extended object and macro-scale imaging problems will not prevent future solutions from including an active illumination component designed to exploit the prior passive system designs. In fact, this is one

potential avenue for future growth in the engineered PSF domain. In either case, the trade-offs of the passive system design must first be known and demonstrated.

3.2 Background

For passive ranging systems, a sense of depth is provided from defocus modulation of the PSF. This axial-dependence is demonstrated in Figure 3.1A, where the PSF of a standard camera is shown as the image of a point is defocused. The result of defocus is an enlarged transverse pattern, consistent with the observation that out-of-focus objects are blurry and carry limited high-spatial frequency information. Solutions exploiting this axial variation are attractive for macro-scale ranging because they are wide-field imaging solutions which parallelize the data input along the transverse dimension of the image in contrast to point-by-point scanning-based techniques. The axial-position information of the object is then contained in a depth-dependent pattern encoded into the image. Note that in some cases this pattern can be ambiguous, with more than one axial-position producing the same image (6). This is the case for the standard optical pupil which is found in most cameras and reviewed above. For this reason, the depth-from-defocus systems have required the use of more than one image via either the active adjustment of focus across an image series (66) or the use of multiple-fixed focal planes. Either case will provide unique depth discrimination as given by the rate of change of the radius of blur (67) (68) (69). Coded pupil functions represent an alternative which can be utilized to engineer the PSF for increased depth sensitivity/information (11) (12) (15) (70). With suitable coding, it has been demonstrated that these methods can

operate under passive and polychromatic illumination (7) (15) (29), thereby making them useful for a variety of imaging applications.

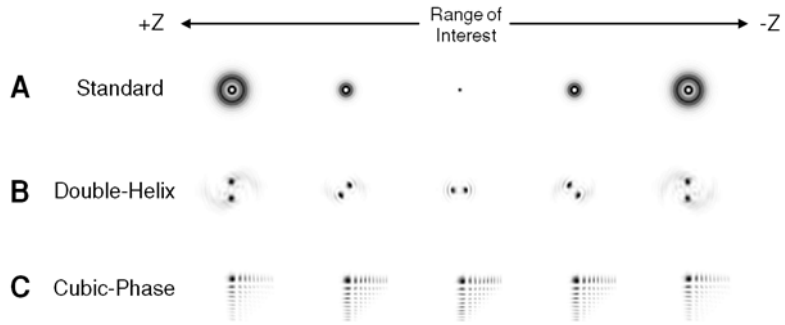

Fig. 3.1: The dependence of three PSFs is presented as a function of the source axial position. The standard camera PSF (panel A) is compared with the Double-Helix PSF (panel B) and Cubic-Phase PSF (panel C) through an equivalent range of defocus. The standard camera PSF is symmetric about focus, the DH-PSF has a unique rotation angle at each position and the cubic-phase PSF has an axially-invariant PSF.

The advantage of the DH-PSF relative to the clear aperture has been its ability to range with enhanced precision when given *a priori* knowledge of the object (11) (35). Rather than encoding with blur, the DH-PSF encodes the axial position of the object with the rotational orientation of duplicative object copies in the image. For point sources, these images will trace a double-helix pattern as the object is moved through focus, as shown in Figure 3.1B. In this chapter, the functionality of using a DH-PSF to passively range random, extended and macroscopic objects under broadband illumination is investigated for the first time. Prior work (11) investigating axial ranging, or alternatively 2+1D imaging, of random, extended objects using the DH-PSF has been limited by use of the following:

A. a second optical channel with limited optical efficiency (the f/# is increased to increase the depth of focus at the cost of reduced aperture size);
B. low efficiency amplitude holograms for optical encoding;
C. the use of quasi-monochromatic illumination.

This chapter expands upon this prior art by addressing each of these effects and their influence on the system design.

3.3 2+1D Imaging with Engineered Point Spread Functions

As discussed earlier, to satisfy the most general imaging applications, one must operate without assumptions on the types of objects present in the scene. Because the PSF applied to encode ranging information is necessarily axial shift-variant, the problem of estimating position from a single image becomes under-determined without additional information about the object. This can be seen from the imaging equation,

$$i(u,v) = \frac{\kappa}{\lambda^2 d_o d_i} \iiint_{-\infty}^{+\infty} h(u-x, v-y; z) o(x,y;z) dx dy dz + \mathbf{n} \tag{3.2}$$

(71) where $h(x,y;z)$ is the axial shift-variant PSF, $o(x,y;z)$ is a planar object or scene, $i(u,v)$ is the image, d_o is the object distance, d_i is the image distance, λ is the wavelength and κ is a constant of proportionality. Noise is addressed in imaging with an additive random variable, $\boldsymbol{n}$, denoted in bold. Here, the measurement $i(u,v)$ contains no unique information to allow disambiguation of the contribution from either the PSF or the object. To address this problem a second optical channel

(camera) is proposed to provide unique object information which will be used to recover partial information about the PSF.

The second optical channel solution will be dedicated to the estimation of object shape. It must therefore provide uniform imaging performance/resolution throughout the same axial working distance as the ranging (DH-PSF) channel. Because the DH-PSF has an operational range well outside the traditional Depth-of-Field (DOF) of a clear circular aperture with equivalent f/# (about a 12x increase as defined by Hopkins allowable defocus criteria in ref. (6)), an extended DOF (EDOF) channel is required to complement the DH-PSF channel. Prior work has utilized a standard optical aperture with higher f/# to accommodate this depth-of-field requirement with an invariant PSF (11). The increased f/# will reduce the aperture size and consequently decrease the optical efficiency. To address this, an alternative is investigated using the Cubic-Phase (CP) pupil function (6),

$$p(u,v) = e^{i\alpha(u^3+v^3)} \tag{3.2}$$

where the CP-PSF is shown in Figure 3.1C. Modulation of the coefficient α is required to find an optimum match to the depth-of-field of the DH-PSF channel (72) but in general $\alpha \gg 20$ (6). The use of a cubic-phase pupil allows the f/# of the two optical channels to be matched – thereby optimizing the optical efficiency of the design.

From the CP-PSF channel, an estimate of the diffraction-limited spatial frequency content of the source is provided via Wiener deconvolution. The Wiener deconvolution filter uses the image i_{EDOF} and the known axial-invariant PSF h_{EDOF} to estimate the object as,

$$\hat{o}(x,y) = \mathfrak{F}^{-1}\left(\frac{\mathfrak{F}\{i_{EDOF}\}}{\mathfrak{F}\{h_{EDOF}\}}\left(\frac{|\mathfrak{F}\{h_{EDOF}\}|^2}{|\mathfrak{F}\{h_{EDOF}\}|^2+SNR(f)^{-1}}\right)\right) \tag{3.3}$$

where $\mathfrak{F}$ denotes a Fourier transform and the carrot denotes an estimate.

The axially-dependent DH-PSF is similarly found from,

$$\hat{h}_{DH}(x,y;z) = \mathfrak{F}^{-1}\left(\frac{\mathfrak{F}\{i_{EDOF}\}^{*}\mathfrak{F}\{i_{DH}\}}{|\mathfrak{F}\{i_{EDOF}\}|^2+SNR(f)^{-1}}\mathfrak{F}\{h_{EDOF}\}\right). \tag{3.4}$$

The solution $\hat{h}_{DH}$ can then be used to estimate z-position through a calibration of the DH-PSF rotation angle to axial position, an example of which is given in Figure 3.2. Note that each of these filtering operations (Eq. 3.3 and 3.4) have been regularized by the spectral SNR in order to account for the presence of noise. In practice, this spectral SNR is assumed to be white and found empirically. An axial position estimation technique based upon the generic geometrical features of the recovered $\hat{h}_{DH}$ is chosen in lieu of an MLE because the centroid/rotation angle algorithm in Fig. 3.2 is expected to be more robust to the noise inherent to deconvolution results.

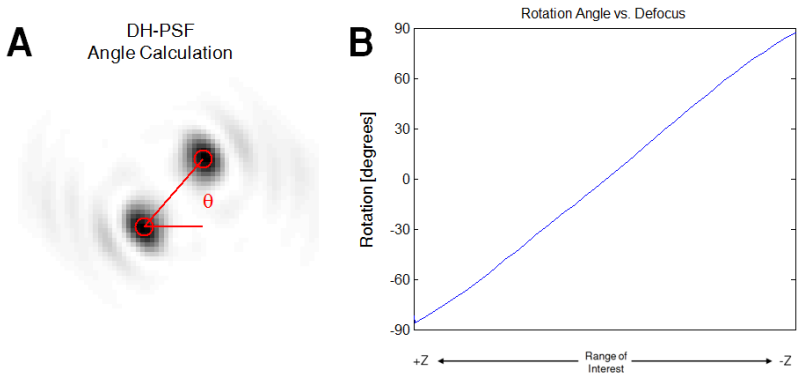

Fig. 3.2: A rotation angle is associated with the DH-PSF image by calculating the angle subtended by the centroids of the two lobes and a frame-of-reference on the detector plane – here the horizontal axis (Panel A). The DH-PSF rotation angle varies as a function of axial position (Panel B).

3.4 Theoretical Performance Limitations

To justify the use of the DH-PSF for this application, the Cramer-Rao Lower Bound (CRLB) is analyzed to quantify the theoretical lower limit of precision for axial ranging and to aid in comparison with alternative designs (33). In contrast to prior analysis (11) (35) (37), the CRLB will also be used to understand the precision dependence on object type. Using the imaging model described in Eq. 3.2, the CRLB is calculated using two input objects; an ideal point source as well as a sample image of a die-cast model car. The sample die-cast model car object is taken from the right-hand portion of the experimental image in Fig. 3.6A. The CRLB is calculated using,

$$\sigma_{CRLB}{}^{-2}(z) = \sum_{m=1}^{M}\sum_{n=1}^{N}\left(\frac{1}{\sigma_N}\left(\frac{\partial}{\partial z} i[m,n]\right)^2\right) \tag{3.5}$$

where $i[m,n] \equiv \int_{\lambda_1}^{\lambda_2} \eta(\lambda) i[m,n;z] d\lambda$ is the broadband, pixilated image, σ_N is the standard deviation of per-pixel Gaussian noise; and σ_{CRLB} is the lower limit to measurement precision (standard deviation) associated with axial estimation (73). Values for the broadband spectrum $\eta(\lambda)$ are selected to match with an experimentally characterized filter used later in the experimental section and shown in Fig. 3.4.

The axial-ranging CRLB performance of a single DH-PSF image is compared with that of a single, clear circular aperture image in Fig 3.3 as a function of the object axial-position. A Gaussian dominated noise process with a SNR of 16 is assumed in the CRLB calculation, where SNR is defined as the ratio of maximum pixel counts to the standard deviation from noise.

These results demonstrate the relative dependence of precision on the object under investigation. This dependence is understood by the fundamental observation that with engineered PSF methods only the spatial frequency content present in an image can be coded. For the point-source, the full advantage of the engineered PSF design can thus be exploited. For a random, extended object, the spatial frequency content is limited and therefore the relative advantage associated with the engineered PSF is decreased. Despite this, the performance of the DH-PSF channel is more uniform over the region of interest and generally improved upon the performance of the standard camera – justifying use of the DH-PSF for axial ranging.

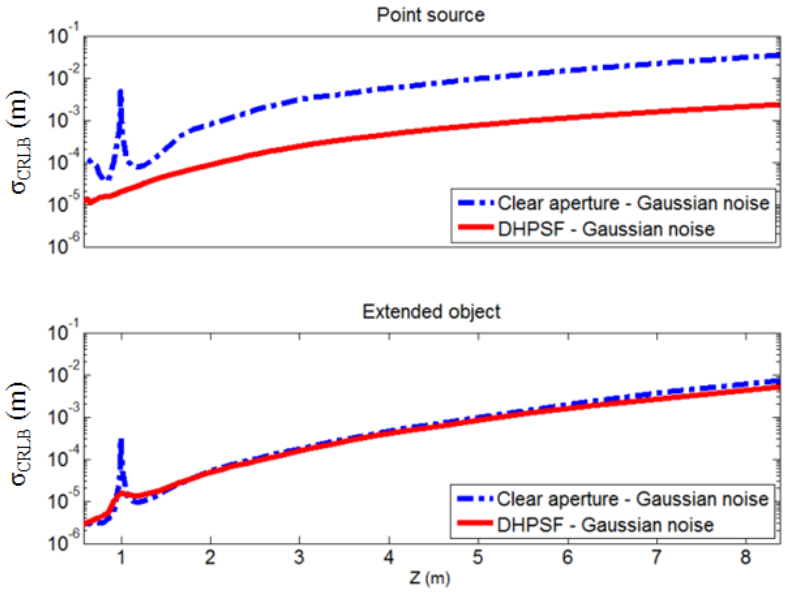

Fig. 3.3: Cramer-Rao Lower Bound (CRLB) analysis of the axial estimation precision for a point source (top panel) and a die-cast car (bottom panel). The performance of the DH-PSF and standard camera is reported.

3.5 Passive Ranging and Extended Depth-of-Field Experiment

The experimental implementation of an engineered PSF 2+1D camera must be able to accommodate the two optical channel design. This can be realized with the serialized engineered PSF imaging system shown in Fig. 3.4 which uses a Spatial Light Modulator (SLM) to cycle through the appropriate pupil functions. This design consists of an imaging lens paired with a chromatic filter ($1/e^2$= 80nm) and linear polarizer, which is then followed with a 4F imaging system. A SLM is placed in the Fourier plane to allow the manipulation of multiple engineered PSF channels as a dynamic, serialized collection of task specific images. The reflective phase-only SLM (Boulder Nonlinear Systems XY-P512) has 8-bit dynamic range which controls the phase within $0 - 2\pi$ on a 512x512 pixel array. This SLM necessitates the use of a polarization analyzer to block the light with polarization orthogonal to the active, modulation axis of the SLM. Because the SLM is chromatic, the color filter is chosen to coincide within the design range of a calibrated SLM. The angle of incidence to the reflective SLM is θ = 18˚. However, the SLM refractive index control is optimized for normal incidence and to compensate for the effect of incidence angle the DH-PSF mask was linearly scaled by a factor of 0.9 to minimize the DC spot observed in the image (Fig. 3.5). The final image is formed a distance f_3 from the last lens. A monochrome detector (Point Grey GRAS-20S4M) with 8-bit dynamic range per pixel and a 4.4x4.4μm pitch pixel is used for capturing images. The lenses have focal lengths f_1 = 60mm, f_2 = 80mm and f_3 = 100mm. The aperture size of the phase mask was limited to $\emptyset$ = 4.19mm by an iris and the object space focal plane was located at d_{OBJ} = 1m. To complement the DH-PSF channel, a cubic phase mask

was implemented for EDOF imaging with a cubic coefficient of α = 166 in normalized coordinates (6). In-focus experimental PSF images from both optical channels are shown in Fig. 3.5. A demonstration scene is created which consists of a pair of die-cast cars located at two different axial distances and illuminated by a halogen bulb. A representative image taken with a clear, circular pupil function is shown in Fig. 3.6A.

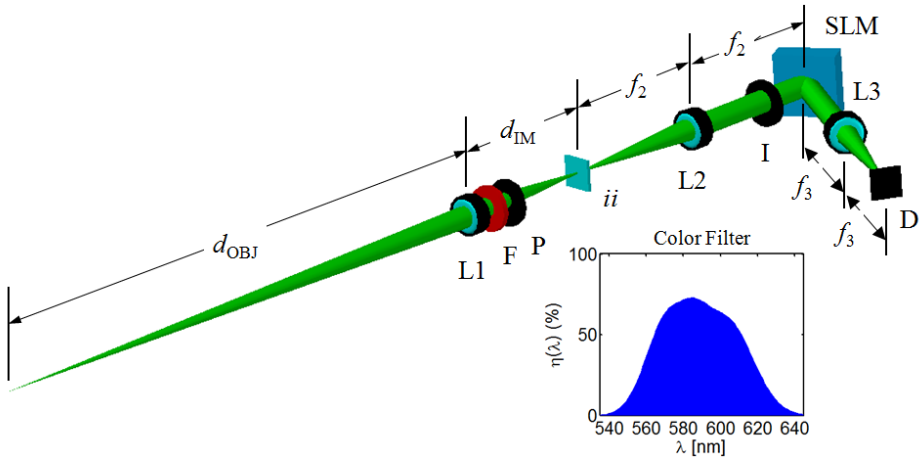

Fig. 3.4: Experimental configuration of serialized engineered point spread function optical imager. The imaging lens (L1) is paired with a color filter (F) and polarization analyzer (P). The intermediate image (*ii*) is re-imaged through a Fourier transform lens (L2) such that the phase of the spatial frequency components can be modulated with the SLM. An iris (I) is placed before the SLM to confine the incident light to the modulated region of the liquid-crystal device. The final Fourier transform lens (L3) is used to complete the optical encoding and form a signal on the detector (D) which is related to the object and encoded with the desired engineered PSF.

Fig. 3.5: The experimental DH-PSF image (panel A) and experimental CP-PSF (panel B) are shown as measured after L3 in the engineered PSF imaging system.

For 2+1D imaging, axial position estimates are required as a function of transverse position. Therefore, a Kaiser window with a damping coefficient $\beta = 5$ is applied to local regions of the image (128x128 pixels) and used to estimate the axial position within the scene by applying Eq. 3.4. A 128x128 pixel window is taken at every 8 pixel interval in the image and deconvolved with the EDOF image in order to create a dense array of axial position estimates. The resulting passive-ranging image therefore sub-samples the original wide-field image by a factor of 8x.

As discussed earlier, engineered PSF methods rely on the spatial frequency content of the scene, therefore a confidence measure for each axial estimate can be made based on the Fourier content within each transverse window. The chosen confidence measure provides a normalized indication of the high-spatial frequency content in the image as,

$$CM = \frac{\int_{\epsilon_u}^{f_{max}} \int_{\epsilon_v}^{f_{max}} |I(u,v)|^2 du dv}{\int_{0}^{f_{max}} \int_{0}^{f_{max}} |I(u,v)|^2 du dv}. \tag{3.6}$$

In practice, the selection of ϵ_u, ϵ_v is found through an iterative search for the best results and f_{max} is determined by the pixel size in the detector plane. The result for

an experimental image is shown in Figure 3.6B. This indicates that the detailed portions from either car should have axial estimates with the highest confidence.

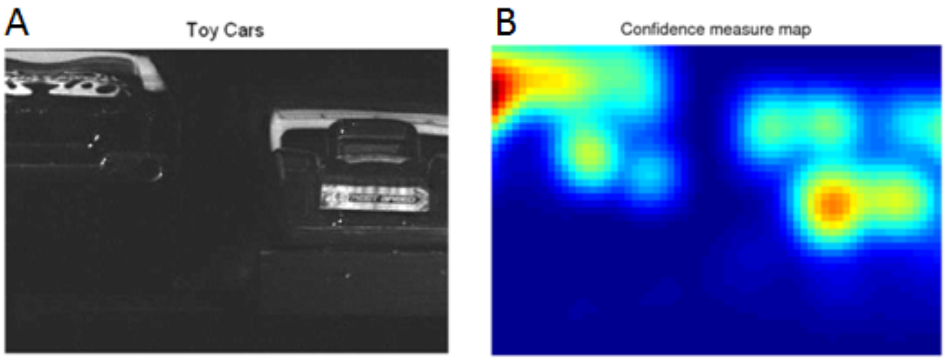

Fig. 3.6: The experimental image (panel A) contains spatial frequency information which is used to provide local confidence measures with regards to the axial estimation (panel B).

Histograms of the estimated axial positions in Fig. 3.7 reveal that the front and back details for each car can be resolved. The mean distance to the front of the cars was $84.15 \pm 0.52\ cm$ and $98.16 \pm 0.26 cm$ for the left and right cars of Figure 3.6A, respectively. The ranging measurement used 169 and 112 independent estimates for the left and right car, respectively, resulting in an error of the mean estimate of $0.04 cm$ and $0.03 cm$. The minimum fractional ranging error is therefore $2.5/10^4$, defined as the ratio of the error of the mean to the mean distance. An image segmentation algorithm is used to identify the individual cars and associate a mean position as shown in Fig. 3.8.

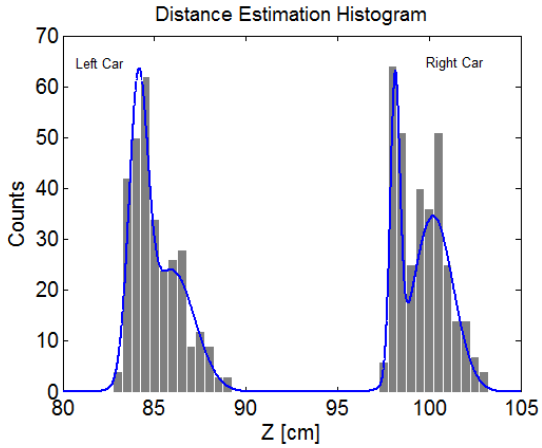

Fig. 3.7: Histograms for the dense collection of axial position estimates. Two broad distributions, indicative of the locations of the two cars are readily apparent.

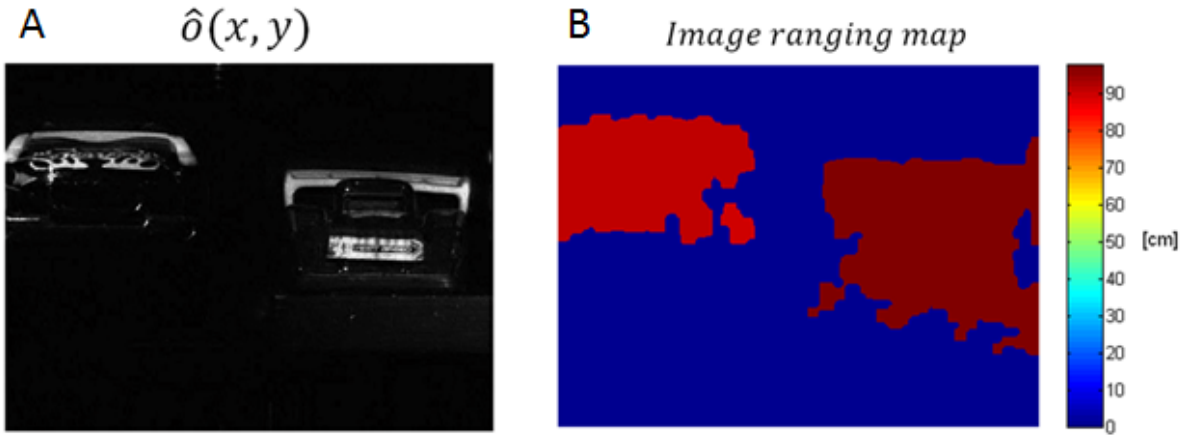

Fig. 3.8: The restored object estimate of the scene from the EDOF channel (panel A) is used for image segmentation. After segmenting the objects within the scene, an average axial distance is assigned to each car (panel B).

Deviation from CRLB performance in this experiment is expected due to three factors:

a) the car has a true three-dimensional profile and not a planar one as assumed in the CRLB calculation;

b) estimators will always trade-off between calculation speed and estimation efficiency - in this experiment, calculation speed was emphasized to achieve faster

throughput. Note that, as discussed in Chapter 2, work on more efficient DH-PSF estimators is also an active area of research (29) (32);

c) an estimate is given for 8x8 neighborhoods of pixels rather than an estimate grid as dense as the pixelated image. This is partially due to the practical difficulty of addressing the influence of the axial position dependent transverse bias of the cubic phase reference image (27). The second factor is related to the computation time required for estimating such dense arrays.

3.6 Digital Refocusing of Experimental Data

Given the estimated z-positions and a digital representation of the restored object, $\hat{o}$, the 3D profile of the scene can now be utilized for synthetically generating images of functional interest. Focus is used as one example because it can be used to emphasize objects with visual cues. It is use of this visual aid that has partially motivated renewed research in the light field or plenoptic camera (74). One drawback of the plenoptic camera design is a sacrifice of transverse resolution necessary to collect the information for refocusing. As an alternative, this system can render re-focused images by defining a synthetic camera with alternative DOFs. In addition, the object space focal plane can be alternatively shifted to either car to generate images which emphasize 3D features of the scene, demonstrated in Fig. 3.9. This system can therefore realistically emphasize details of the scene while requiring minimal user input (only specifying the focal plane is necessary).

Fig. 3.9: Digital refocusing of the scene as a post-processing step. The proposed system returns a grid of axial estimates associated with the diffraction limited information content (panel a) to define function $\hat{\boldsymbol{o}}(\boldsymbol{x},\boldsymbol{y},\boldsymbol{z})$. Images can then be generated synthetically, emphasizing focus to convey visual information. Panels b and c alternatively focus on either object in the scene as a demonstration.

3.7 Conclusions

In summary, a serialized engineered PSF camera was demonstrated to recover the 2+1D function describing the scene. The system performance limits were analyzed theoretically and compared with a classical method, the standard, clear, circular aperture. The experimental implementation was shown to have a fractional ranging error of $2.5/10^4$. The recovered scene function is then used to synthesize functional images which convey particular information to the user.

CHAPTER 4

GRAY-LEVEL LITHOGRAPHIC PHASE MASK FABRICATION FOR ENGINEERED POINT SPREAD FUNCTIONS

4.1 Motivation

In Chapters 2 and 3, it was shown that the introduction of an engineered Point Spread Function (PSF) into the optical system can be used to generate an improved solution for sensing and imaging. This chapter presents a method for manufacturing phase-modulating optical elements that impart aberrations to create an engineered PSF system. Fabrication of the optically-efficient phase masks proposed here will create viable replacements for prior implementations which use amplitude holograms (11) and Spatial Light Modulators (SLM) (13) (30) (31) (32).

4.2 Background

Engineered PSF solutions improve optical system performance in applications where high-precision quantitative measurement is necessary. For example, in demanding scenarios such as single-molecule imaging only a few thousand photons will enter the objective. Recent work has focused on the design of engineered PSFs which enhance the relative information carrying capacity of each photon to improve the theoretical precision in a measurement (35) (75). This was the case in Chapter

2, where the DH-PSF was employed for 3D super-resolution imaging. However, the most photon-efficient DH-PSF implementations have used SLMs and this rejects up to 50% of the incident light due to polarization constraints (13) (29) (48). Unless great care is taken to control and collect all polarization states of emitted light (30), the promised performance gains for applications with limited numbers of photons have not yet been realized.

Alternative engineered PSF designs, such as the astigmatic three-dimensional microscopy system (14) (76), can be implemented with an optically efficient design. For the astigmatic systems, this is realized by incorporating an additional cylindrical lens in the system to change the relative focusing power along the x and y axes. Another option, the bi-focal system, provides a solution which requires a second camera and redirection optics but still operates with minimal optical losses (47). Therefore engineered PSFs which require high-order aberrations, reduced symmetry and/or the presence of phase dislocations (a class which includes the DH-PSF) in the pupil plane of the lens have not been demonstrated with optically efficient implementations. This is an important limitation because as demonstrated in Chapter 2, image processing algorithms such as the PR-MLE can be used to realize the efficient information extraction from photons which arrive at the detector. Thus the remaining hurdle to realizing the full potential for DH-PSF imaging is the limited optical efficiency available in current implementations.

The use of fixed phase masks, realized physically as surface relief modulations in an optical material, is advocated in this chapter as an optically-efficient engineered PSF implementation. The phase mask can be considered a

Diffractive Optical Element (DOE) where the surface profile relates to phase delay of the incident wave by $0 - 2\pi$. In the paraxial and thin-element limit, these masks are approximately insensitive to polarization. They may also be realized using low absorption optical materials such as glass, quartz or polymer. Therefore, lithographic phase masks represent the most optically efficient option while also providing a compact, portable form factor with no power consumption.

The first implementation of a DH-PSF lithographic phase mask is demonstrated in this chapter. This mask will be manufactured using mask-less gray-scale lithography. One representative mask is quantified in terms of optical efficiency and evaluated in an experimental configuration. Enabled by this photon-efficient collection of light from single-molecules, an optical 3D super-resolution microscopy experiment is performed and the results reported here. Later in the thesis, more examples will be given using this lithographic technique to fabricate alternative engineered PSF designs.

4.3 Review of Photo-lithography Techniques

A DOE maps a phase and amplitude transmission function,

$$t(u,v) = A(u,v)e^{i\Psi(u,v)} \tag{4.1}$$

to a pattern of:

a. variably opaque material for amplitude encoding of $A(u,v)$

b. surface height or refractive index modulation for phase encoding of $\Psi(u,v)$

In this chapter, the focus will remain on phase mask fabrication with the amplitude encoding limited to a circular aperture described by,

$$A(u,v) = \ circ\left(\frac{\sqrt{u^2+v^2}}{R}\right) \tag{4.2}$$

where R is the radius of the pupil enclosing the surface relief modulation. The phase profile of the mask can be transformed into a surface relief given by,

$$h(u,v) = \frac{\lambda_0}{n(\lambda_0)-1}\frac{\Psi(u,v)}{2\pi} \tag{4.3}$$

where λ_0 is the wavelength of operation, $n(\lambda_0)$ is the refractive index, the working assumptions of the thin-element approximation, that the phase mask is mounted in an air environment and a low numerical aperture (77).

Phase masks have been realized using fabrication techniques such as direct diamond turning of a reflective/transmissive surface (78) (79), the multi-step exposure sequence of binary mask exposures (77), Ion beam etching (80), excimer or femto-second laser ablation (81), as well as gray-level lithography (82). The particular advantages and disadvantages of these methods are discussed in the following to aid in the selection of a suitable one.

The direct diamond turning method works well with smooth continuous features such as the cubic phase mask (6) and the aspheric surfaces introduced by Polaroid in the 70s (78). A mechanical bit is scanned across the sample and moved vertically in order to remove a pre-determined amount of material and create the desired surface relief. Recent results have demonstrated ultra-precise fabrication of 20μm transverse feature sizes with a minimum of 10nm feature sizes in height; indicating that the technical hurdles of direct-machining small features are

diminishing (83). However, one practical issue remains in that it requires long fabrication run-times and is therefore very expensive.

Multi-level, multi-exposure lithography is the repeated process of applying a binary lithographic mask in order to realize 2^M levels with M masks, outlined in Fig. 4.1 (84) (85) (86). This method is frequently referred to as binary optics. The technique has good transverse resolution – typically limited to ~1 micron. Unfortunately, the method suffers from a propagation of errors due to the tolerances associated with alignment of each mask exposure required in a multi-level structure.

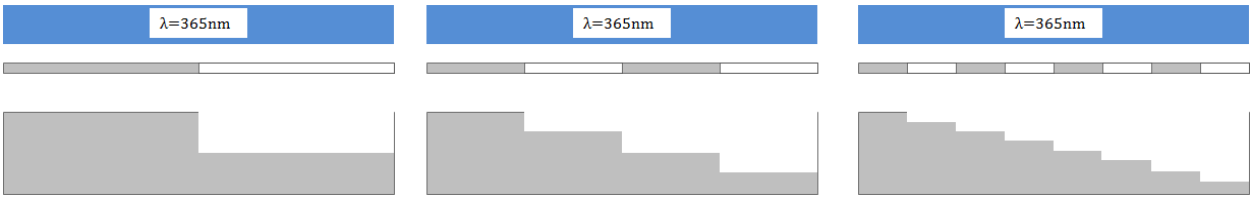

Fig. 4.1: Multi-level lithography as a multi-step process using binary masks. The use of M masks will allow up to 2^M levels.

In addition, only a discrete number of surface heights are realizable and must be used to approximate a continuous surface. This is a known problem and the relationship between the number of discrete steps and the quality of the DOE has already been studied (84) (87). For example, the quality of the mask may be characterized as the diffraction efficiency of a phase grating when using 2^M discrete levels as,

$$\eta(M) = \left(\frac{sin(\pi/M)}{\pi/M}\right)^2 \tag{4.4}$$

where the results given in Fig. 4.2 (25). Based upon this, a minimum of eight levels, or three binary masks, would be required to begin approaching acceptable

performance. However, as mentioned earlier, the problem of aligning three or more binary masks sequentially is not trivial.

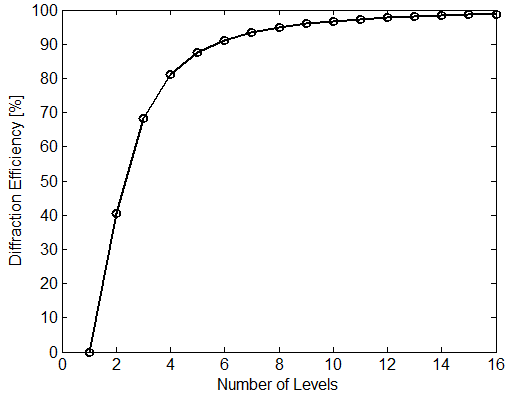

Fig. 4.2: Diffraction efficiency of a phase grating as a function of the number of resolved phase levels. Note that $\mathbf{2}^{\boldsymbol{M}}$ phase levels are achievable with $\boldsymbol{M}$ binary masks.

Direct-write methods such as ion beam etching (80), excimer/femto-second laser ablation (81) and gray-level lithography (82) are options which can avoid the non-trivial alignment associated with binary optics. Of these options, gray-level lithography presents the only option which is not a scanning-based technology and therefore avoids the long fabrications times which are also associated with direct machining (84). The gray-level technique requires only one exposure to transfer a spatially varying intensity pattern and develop the phase mask. Early gray-level lithographic systems were implemented using half-tone masks – where the gray-level characteristic was generated by the varying density of opaque regions on the mask, shown in Fig. 4.3 (84). Alternative gray-level options now exist where the optical transmission is controlled by variation of the optical absorption of the mask. More recently, gray-level lithography has been introduced using mask-less systems

(82). Implementing the same digital micro-mirror device (DMD) which is common to projection illumination systems, the permanently fixed gray-level mask can be replaced with a projection of the two-dimensional, intensity modulated signal from a DMD, illustrated in Fig. 4.4. As with the prior gray-scale methods, the time required to record large structures remains short. This makes gray-level lithography both inexpensive and simple to realize since fewer steps are necessary to fabricate the phase mask. Here, this method is investigated for the first time to fabricate optical phase masks to implement engineered PSFs such as the DH-PSF.

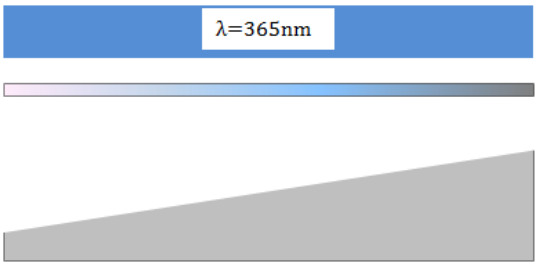

Fig. 4.3: Use of a half-tone or variable absorption mask allows the projection of gray-scale tones for variable surface relief heights.

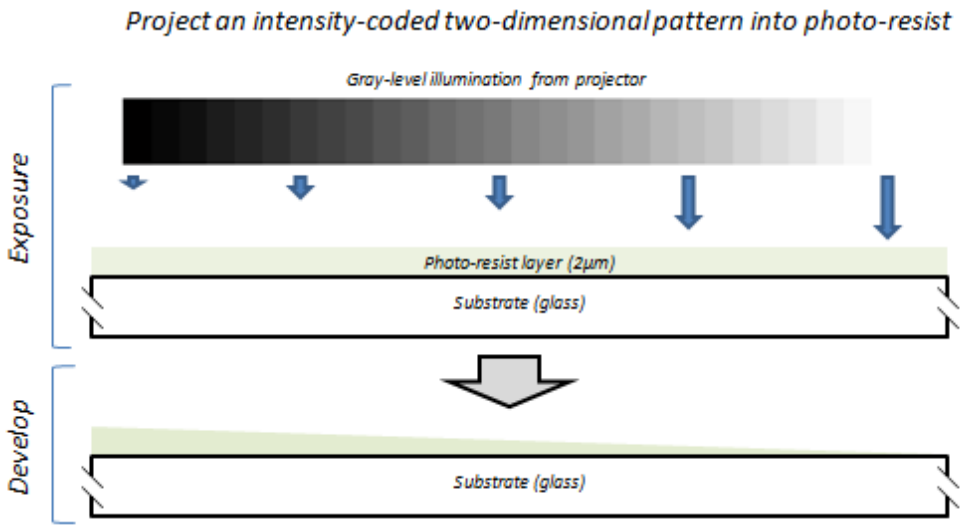

Fig. 4.4: Gray-level, mask-less lithography operates by projecting an intensity-modulated pattern which is representative of the desired surface/phase modulation.

4.4 Methods

Gray-level lithography can be implemented with either positive or negative photo-resist. These two options will develop differently after exposure to light. The positive photo-resist removes only the material which has been exposed to light whereas the negative photo-resist removes the material which has not been exposed – as reviewed in Fig. 4.5. The positive photo-resist Clariant AZ-4210 was selected so that less material will be removed during development of the phase mask (88). This is believed to improve the fidelity of the transfer of intensity information as well as improve the environmental durability of the sample. In addition, this is a common photo-resist used in many laboratories – meaning that the processing developed here would be applicable to other research labs. Finally, AZ-4210 has the beneficial property that it is frequently used as a $2\mu m$ thick film. Since the desired surface

modulation will be on order of $1\mu m$ the AZ-4210 will be able to accommodate phase delays between zero and 2π.

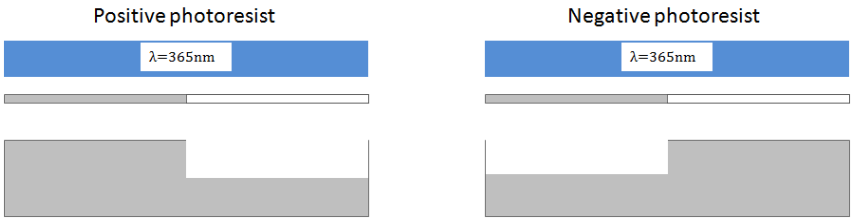

Fig. 4.5: Comparison of the development action of a positive versus negative photo-resist. The positive photo-resist removes material which has been exposed while the negative photo-resist removes the material which has not been exposed.

However, one practical problem is immediately identified. Photo-resist has been traditionally designed to behave non-linearly to incident illumination. This is to allow the production of high-contrast regions when performing the more traditional binary mask exposure. This high-contrast is necessary for the lithographic fabrication of electronic components but not of direct utility for the manufacture of quasi-continuous surface profiles. Therefore, gray-level development will require modification to the typical photo-resist processing parameters in order to calibrate exposure dose to surface relief height.

The gray-level exposure from the DMD will directly contribute to a surface relief modulation in the photo-resist after development. Therefore, the use of the resist is explored as an actual phase-mask implementation. This will allow fewer necessary processing steps to generate a usable mask and represent a rapid-prototyping option. Alternatively and more conventionally (77) (84), the mask may

be etched directly into a quartz substrate from this patterned photo-resist to improve the environmental robustness of the sample.

The gray-scale lithography is performed in the Colorado Nanofabrication Facility (CNL) at University of Colorado, Boulder. A commercial device (Intelligent Micro-Patterning SF-100 Xpress) is identified for gray-level mask-less phase mask fabrication. The necessary processing steps to use this device and manufacture a phase mask are identified as,

A. Manufacture substrate with integrated chrome aperture
B. Spin on optical quality photo-resist layer
C. Alignment of lithographic device to sample
D. Calibrate energy dose to generate gray-level surface relief
E. Photo-resist Development

These steps are discussed individually in the following sub-sections.

A. Manufacture Substrate with Integrated Chrome Aperture

The passage of light through the phase mask must be restricted to the area associated with the surface profile. Therefore a chrome aperture which is integrated into the sample substrate will be necessary to block any unwanted light. The modulation of this chrome mask is required only to have two states: opaque and transparent. Therefore a binary mask writing system is identified as the solution to manufacture the appropriate design.

Commercial substrates, coated with chrome and finished with a layer of photo-resist are readily available in CNL. These are used here for the rapid

manufacture of chrome apertures. The substrate (Nanofilm 4x4", 0.060" thick soda-lime glass with an additional positive photo-resist layer) can be loaded into a binary-mask writing device, here the Heidleberg DWL 66FS available in CNL, and a direct-write, laser patterning algorithm will expose the photo-resist layer in regions which should be transparent.

For the current application, the design in Fig. 4.6A is manufactured. This pattern consists of an array of chrome apertures such that many substrates may be diced out of the sample. The fabrication dimensions of one chrome aperture are given in Fig. 4.6B. After exposure and development of the photo-resist layer to remove the photo-resist and expose the chrome in the 2.7mm diameter pupils, the substrate is placed in chrome etchant to selectively remove the chrome layer and reveal the desired pattern. Following this step, the entire substrate is placed in photo-resist stripper and washed in de-ionized water to provide a clean surface for spin coating the next layer of photo-resist to be used as the phase mask.

The glass substrate can be scribed and cut into the desired form factor, here a 10x10mm unit cell. Each chrome aperture is designed to be 2.7mm in diameter in order to be consistent with the field size of the mask-less lithography equipment (IMP SF-100 Xpress). Note that this aperture size is not a fundamental limitation as in the future stitching capabilities of the SF-100 can allow for larger masks. Tolerances for that production will be analyzed at the end of this chapter. The top left region of the unit cell provides an area where a unique ID is associated with the mask. The 2.7mm diameter aperture is placed in the middle of the unit cell. Four alignment marks are present near the centers of the edges. The alignment marks

are 8mm across from each other and 200 microns in width. These alignment marks are used to map the projected pattern to the chrome aperture such that the mask may easily be centered onto the sample.

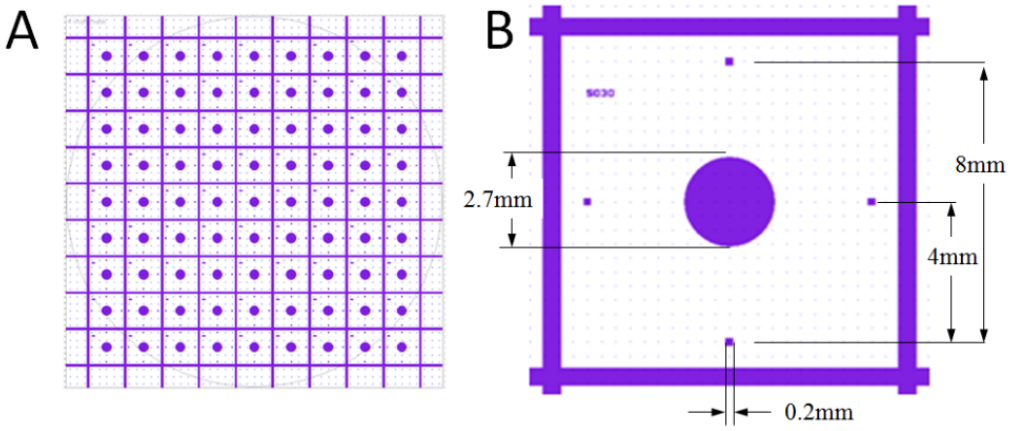

Fig. 4.6: Binary mask layout of 81 2.7mm diameter apertures to be recorded using the Heidelberg direct mask writer. A close up of the unit cell for each mask is shown in panel B.

B. Spin on Optical Quality Photo-resist Layer

To prepare the substrate for photo-resist, the sample is first spun-coat with HMDS (Hexamethyldisilazane) on the side opposite the chrome in order to promote adhesion of the photo-resist to the glass layer. The use of the backside of the chrome is recommended in order to minimize fluid wakes from the etched edges of the chrome/glass interface which were observed when the photo-resist was spun onto the same side as the chrome. The positive photo-resist, AZ-4210 is then spun next into a uniform film.

A study was initiated to search for the optimum spin parameters but found the quality of the film layer to be independent of spin time, as shown in Fig. 4.7. A

slowly-varying surface modulation of up to 50nm was typical of all spin times and will contribute to aberrations in the final mask. The 40 second spin-time was chosen in practice because it resulted in a profile similar to a linear-ramp. When placed in the Fourier plane of an imaging system (a common design), this aberration should result in a transverse shift of the image. The spin-rate is determined by the manufacturer specifications which relate spin-rate to layer thickness. A typical 40 second spin of AZ-4210 results in a 2 micron thick layer.

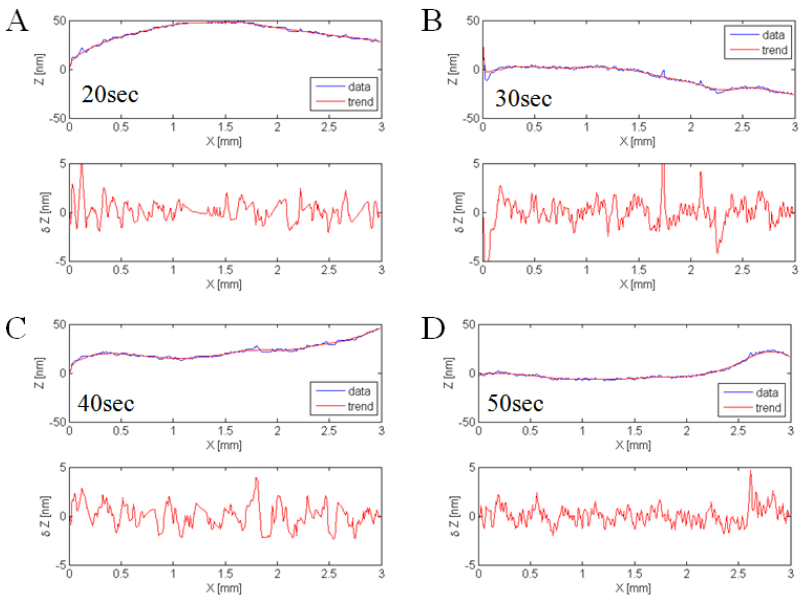

Fig. 4.7: The relationship between the spin time and the resulting surface modulation. The upper panel in A-D is the absolute measurement and the lower panel is the deviation from a smooth fitting of the absolute surface. The standard deviation of the surface roughness was measured to be ±1.0nm, 1.6nm, 1.2nm, 0.9nm as the spin time varied from 20 seconds to 50 seconds, respectively.

C. Alignment of Lithographic Device to Sample

As shown in Figure 4.6B, the unit cell of the phase mask contains a chrome aperture with four, small rectangular windows surrounding it. These windows are

used for aligning the relative position and rotation of the substrate to match that of the projection system. The mask-less lithographic system is set to project a 200 micron diameter circle onto the substrate. The sample stage is then translated axially until the top, photo-resist layer is in focus. Then the sample is translated transversely until the projected circle is centered on one rectangle of the chrome-substrate. Each alignment mark is separated by 8mm, and an appropriate stage translation should yield an aligned projection of the circle to the chrome aperture. The sample is rotated until a 1D translation satisfies this criterion. The center of the chrome optical aperture for the phase mask can then be found with a 4mm 1D translation towards the center of the substrate. The sample is now prepared for exposure of the desired phase mask surface relief profile.

D. Calibrate Energy Dose to Generate Gray-Level Surface Relief

In general, the exposure of the photo-resist to optical radiation has been designed to initiate rapid polymerization of the material. Because of the popularity of binary-step lithography, the photo-resist is optimized to be very sensitive in order to generate features of greater contrast or aspect ratio. Fig. 4.8 is an approximate characterization of the behavior for single-species depletion which causes the polymerization of photo-resist. For gray-scale lithography, the desired outcome is to calibrate the exposure dose such that a number of polymerization levels are discretely addressable and can translate into a variable surface relief profile.

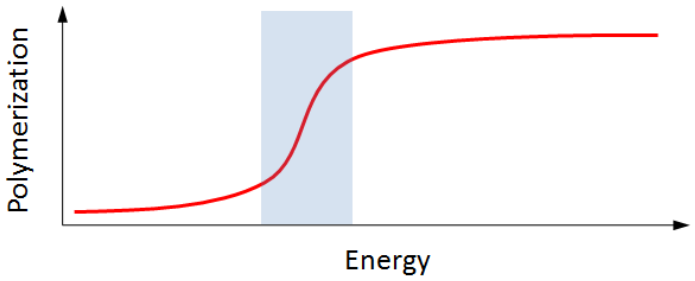

Fig. 4.8: Characterization for the polymerization of photo-resist as a function of input optical energy.

In practice, with the mask-less device used at CNL this calibration is achieved by generating an image with known, gray-scale values in photo-resist. After development, the surface contour can be measured with a profilometer in order to quantify the dependence of surface relief height to exposure energy. For this reason, the area outside the chrome aperture in Fig. 4.6B is utilized for gray-scale exposures which provide a run-time calibration of the relationship between exposure dose and surface relief.

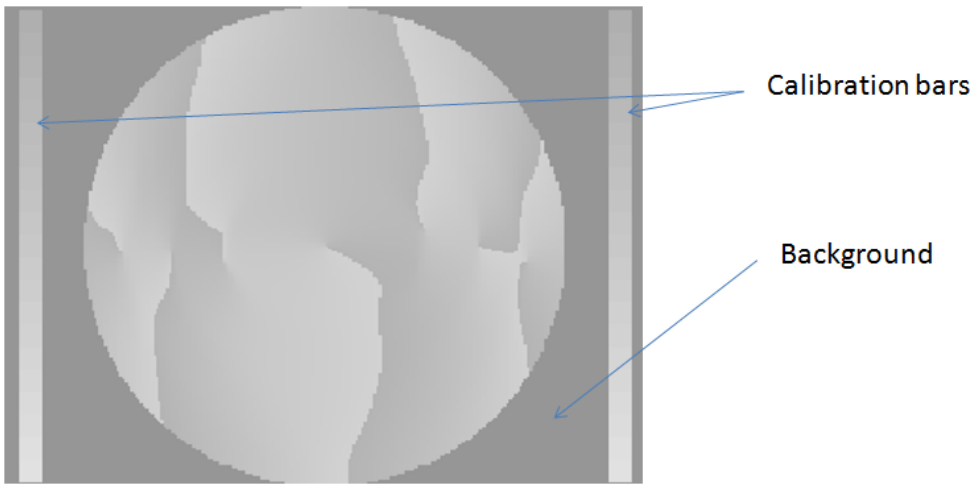

Fig. 4.9: Example gray-level map for phase mask fabrication. The main feature is the desired surface profile and it is accompanied by a linear gradient of illumination levels along each side of the exposure. These outer regions are used for calibration purposes.

One example of the projected gray-scale exposure is shown in Fig. 4.9. The result of these calibrations is shown in Fig. 4.10, where an approximately linear surface profile is generated from variable gray-scale exposure doses within the range on the *x*-axis. The associated energy density of the illumination is measured and given for calibration of future experiments. It has been observed that the characteristic of this profile can vary significantly from day to day or given different batches of photo-resist. Note that with this commercial device 256-discrete illumination levels are addressable. However, because of the non-linear optical response from polymerization, only a subset seems resolvable using single-dose exposure and development procedures.

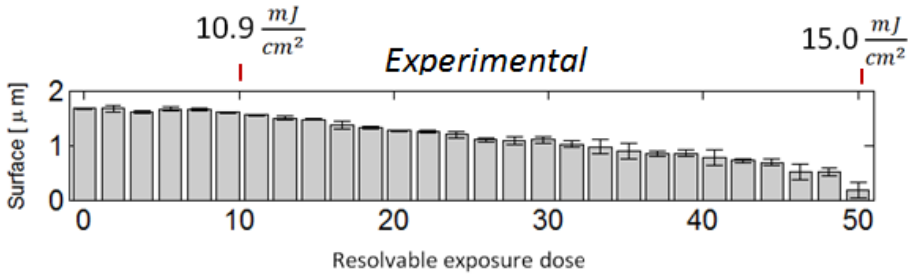

Fig. 4.10: Example calibration of energy dose to surface relief. This relationship can be corrected to the different resolvable levels of the DMD.

The DMD in the mask-less system projects a 1024x768 pixel image onto the photo-resist sample. The exact projected pixel size is measured here in order to match the phase mask pattern to appropriately fill the aperture. To find the feature size, a series of checkerboard exposures of varying sizes were recorded. The feature size of the checkerboard varied from 8x8 to 4x4, 2x2 and 1x1 DMD pixels. A test

sample was prepared, exposed and developed and then examined under a bright-field microscope to compare the fidelity of the features and establish a minimum usable feature size.

Microscope images of the progression of checkerboard patterns are presented in Fig. 4.11. The fidelity of the pattern is seen to fail for the 1x1 pixel checkerboard. The exact cause of this failure mechanism remains unknown. One possibility which was investigated is related to the relative movement (caused by vibration) of the DMD projection and the sample stage. However, one would expect reduced contrast at the 2x2 pixel level as well. A line-scan from the 4x4 region reveals that the average projected pixel size is 3.4 microns, shown in Fig. 4.12.

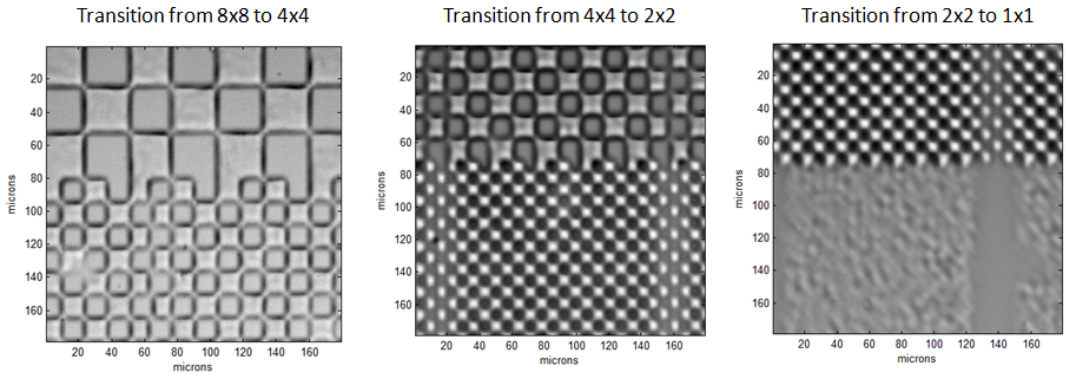

Fig. 4.11: Test of optical resolution size in the photo-resist patterns by projecting checkerboards and imaging with bright-field microscope.

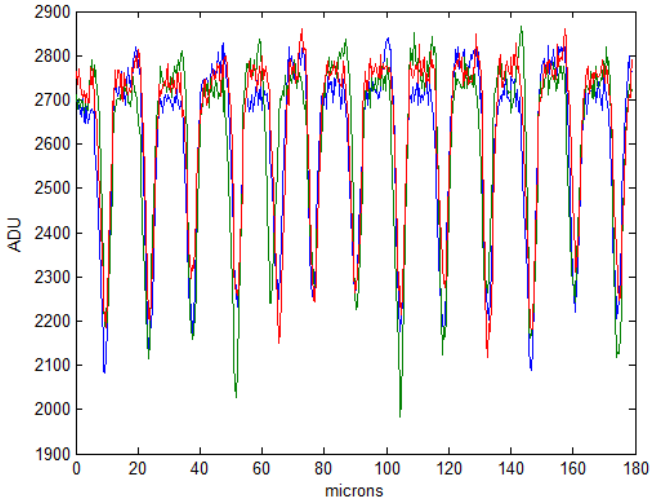

Fig. 4.12: A trio of line-outs across the 4x4 super-pixel region. The periodicity of the scan is used to calculate that the projected pixel size is 3.4 microns.

E. Photo-resist Development

After the photo-resist has been exposed with the gray-level mask dosage, the next process is to develop the resist and remove the exposed regions. Development requires a mixture of Clariant developer AZ-400K with deionized water at a 1:4 ratio. The sample should be mildly agitated in the solution for between 90 and 300 seconds. Then it is rinsed in de-ionized water for 90 seconds.

A characteristic of this mask-less lithographic system is that gray-level surfaces are not smooth. Instead the surface increases in roughness – a result of the discrete, and non-ideal pixels of the DMD which projects a non-uniform incident illumination onto the sample. Surface profilometry of a developed, uniform exposure in photo-resist reveals that after the development process (including exposure and polymerization) the surface roughness of the photo-resist characteristicly adds features ~30nm in height, as shown in Fig. 4.13.

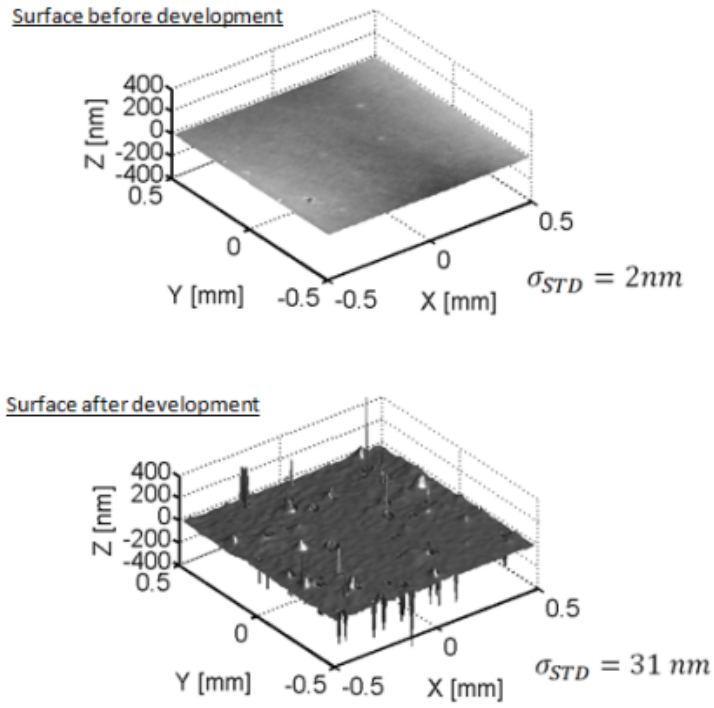

Fig. 4.13: Surface profilometry results of photo-resist before exposure and after development reveals that the mask-less lithographic procedure results in a surface with a distinctly different roughness.

A final step before use is to photo-bleach the resist such that the optical absorption is minimized. A standard UV source is used to bleach the sample in minutes. The result is an optically transmissive layer of photo-resist. The refractive-index of the phase masks after this final step is measured to be $n(633nm) = 1.635 \pm 0.002$ using ellipsometry.

4.5 Fabricated Phase Masks

The procedures developed earlier are followed to manufacture phase masks for direct system implementation. Each mask can be optimized for the specific wavelength required in the experiment through modulating the exposure dose. Two

example phase masks are presented in Fig. 4.14. The surfaces are characterized using white-light interferometery (Zygo New View).

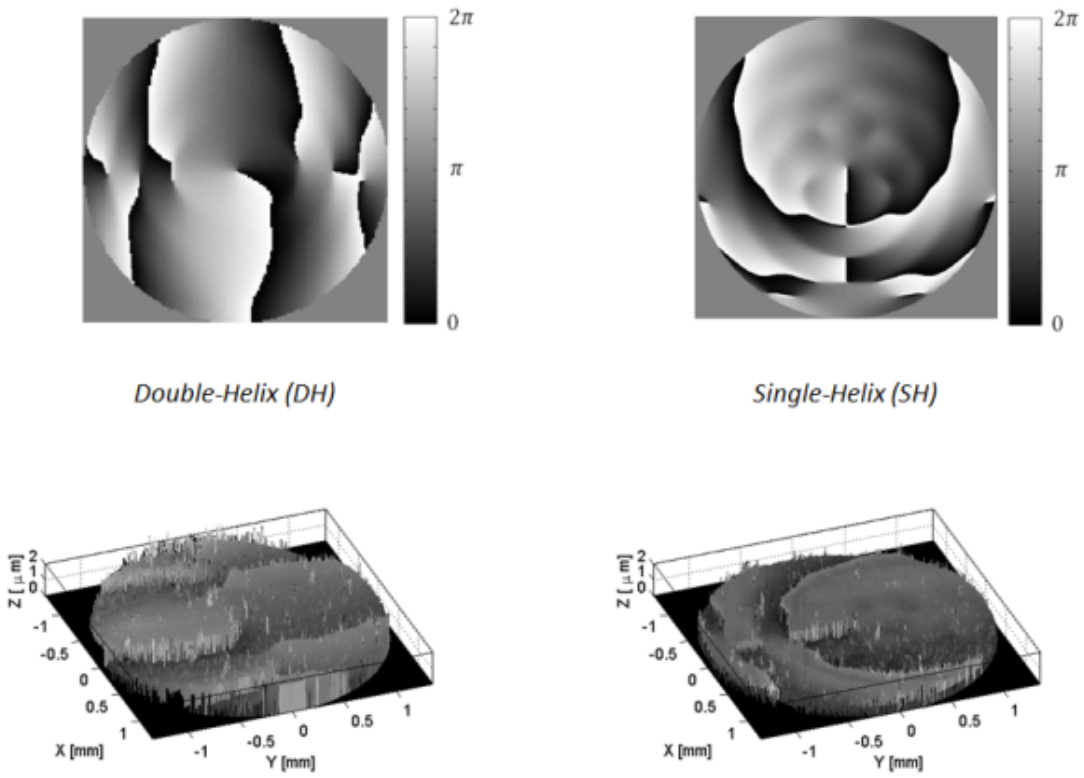

Fig. 4.14: 2D surface profilometry of two example phase masks produced following the recipe discussed in this chapter. The top row is the design mask and the bottom row shows the fabricated surface. The left panels are associated with the Double-Helix PSF. The right panels are associated with the Single-Helix PSF introduced in Chapter 5.

To aid in device integration, interchangeable sample mounts were fabricated for commercial items such as a Zeiss microscope. One example mount is given in Fig. 4.15. Placement of the mount into the DIC (Differential Interference Contrast) slider of a commercial microscope is approximately similar to encoding the pupil plane of the objective to have an engineered PSF profile. The results from imaging a ruled line from a microscope adapted with a DH-PSF phase mask in this way are

presented in Fig. 4.16 as a function of defocus. Two copies of the single line are easily observable and the relative rotation of each line is highlighted with a circle to aid in identifying the rotation orientation.

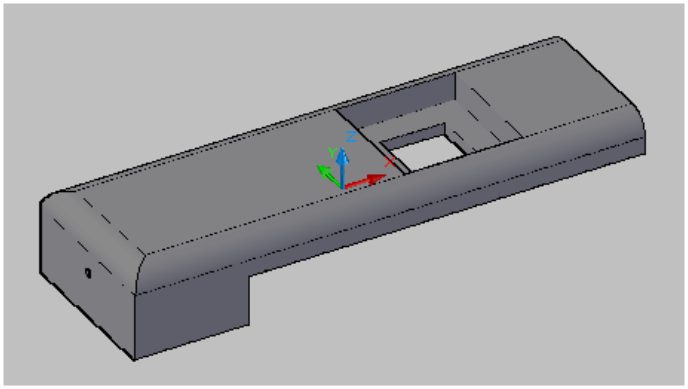

Fig. 4.15: Mount designed to fit a phase mask into the DIC slider port for Zeiss microscopes.

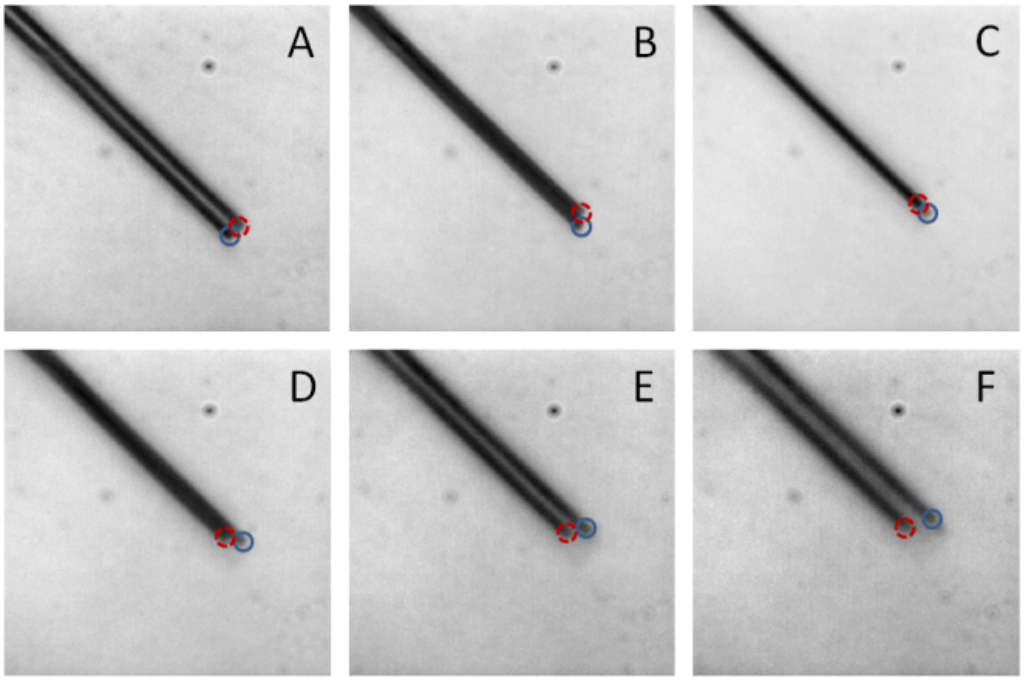

Fig. 4.16: DH-PSF images from a modified Zeiss microscope after placing the phase mask in the DIC slider. The object being imaged is one ruled line from a calibration sample and is demonstrated to rotate as a function of defocus in panels A-F.

The white-light interferometer (Zygo New View) result from an additional DH-PSF phase mask, designed to operate at $\lambda = 514$nm, is given in Fig. 4.17. For the AZ-4210 photo-resist, a 2π phase delay in wavefront corresponds to a thickness of 816 nm. Tests to establish the optical efficiency and PSF performance of this mask are now performed in order to characterize the quality of the phase mask fabrication.

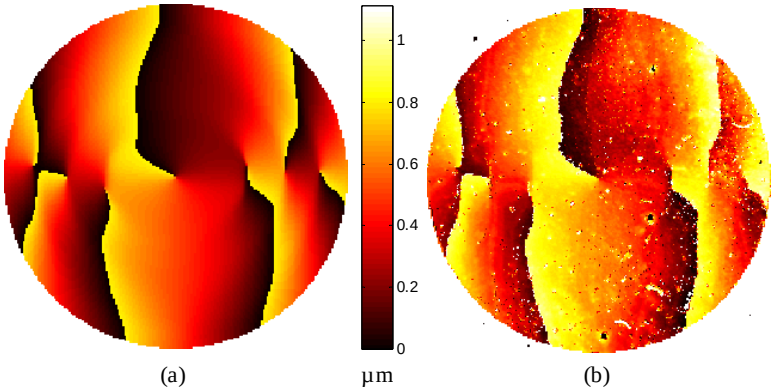

Fig. 4.17: (a) Surface profile of the DH mask design. (b) Measured surface profile of the fabricated phase mask. The colormap corresponds to the height relief. The diameter of the mask is 2.7 mm.

Qualitatively, the fabricated mask matches the design relief in terms of position of phase vortices, phase gradient and location of the extrema. It is important to note that phase vortices and their locations are critical for generating the desired DH-PSF. The imperfections shown in Fig. 4.17B contribute to some scattering, but as shown next, they lead to minor deviations from the ideal DH-PSF design.

The transmission efficiency of this mask and its ability to localize energy into the characteristic DH-PSF pattern was measured to determine the deviation from ideal performance. The testing setup is shown in Fig. 4.18A. The 514 nm

wavelength line of an Ar+ laser (Coherent) is spatially filtered and collimated with a lens of 100mm focal length (L1). The resulting collimated beam is apertured right after the lens to a 2.7 mm diameter. A second lens (L2) of focal length f = 100 mm focuses the beam onto a CCD camera (Point Grey Research, Chameleon CMLN-13S2M-CS). The fabricated mask is placed at the front focal plane of L2 to generate the DH-PSF. The phase mask is mounted on a x,y,z translation stage for alignment. Alignment is determined via observation of the PSF as the stage is adjusted. Images of the standard PSF are acquired by removing the fabricated mask. The camera is adjusted to maximize dynamic range using the standard PSF and these parameters are stored for later testing of the DH-PSF with the fabricated mask in place. Fig. 4.18B and C show the experimental standard PSF and DH-PSF images, respectively. Fig. 4.18D and E show the PSFs numerically simulated with the same system parameters including noise. The dark regions in the experimental PSF images, shown in Fig. 4.18B and C, were characterized and found to have single pixel 0/1 noise with density 0.3. This noise was added to the simulated PSF images so as to make theoretical efficiency calculations consistent with the experimental conditions.

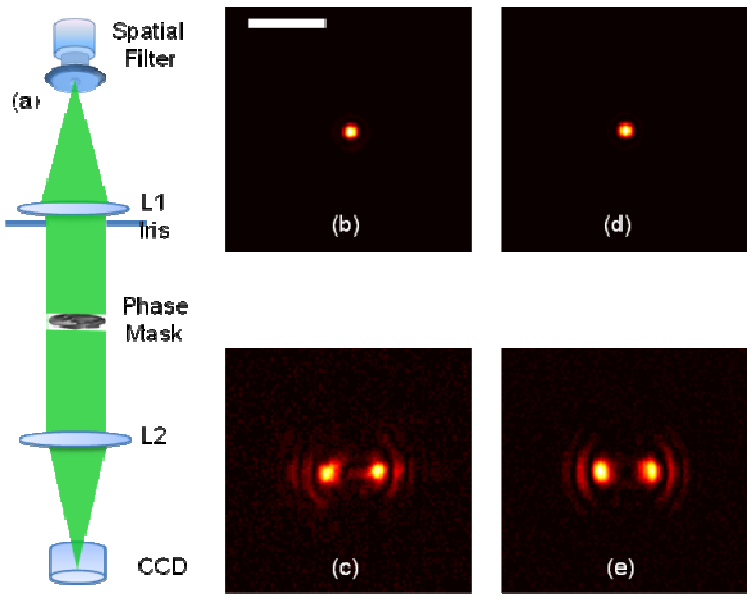

Fig. 4.18: (a) Setup for efficiency measurement of the fabricated DH phase mask. The 514 nm Ar+ laser line is spatially filtered. L1 and L2 are achromatic lenses of focal length f =100 mm. The phase mask is positioned at the back focal plane of L1 (front focal plane of L2) using an translation stage. (b) and (c) show the experimental standard PSF and DH-PSF, respectfully, while (d) and (e) show the corresponding, numerically simulated, PSFs. The scale bar is 150 μm.

One method of measuring the transmission efficiency, η, through the mask is to observe the reading of an optical power meter placed behind the Fourier plane with and without the fabricated mask in the beam path, resulting in = 87%.

Alternatively, the CCD measurements shown in Fig. 4.18B-E were used to determine the transmission efficiency. The relative energy in the DH-PSF image with respect to the energy in the standard PSF image was found to be 83.4% and 95.8%, for the experimental and theoretical cases, respectively. The transmission efficiency of the phase mask is given by the ratio of these numbers leading to = 87%. The theoretical relative energy was used to compensate the experimental

relative energy for the effects of a finite detector. The transmission efficiency found by the two methods described above turned out to be the same.

The remaining 13% of the energy that is not transmitted is lost in reflection, absorption, and scattering. Specular and diffused reflection account for about 11% and can be easily reduced using anti-reflection coatings. Absorption and scattering can be reduced by improving the optical material quality, for instance, by transferring the mask to glass or quartz.

Another measure of the functional efficiency for the fabricated mask is the ratio of the experimental peak intensities for the standard and DH-PSF, $[I_{STD}/I_{DH}]^{EXP}$, as compared to the theoretical value $[I_{STD}/I_{DH}]^{THEO}$. These ratios were found to be 8.7 and 7.2 respectively giving a functional efficiency, $[I_{STD}/I_{DH}]^{THEO}/[I_{STD}/I_{DH}]^{EXP}$ x100=83%. If this efficiency is compensated to take into account the transmission loss, it results in a functional efficiency of 83/.87= 95%.

4.6 Optical 3D Super-resolution Imaging

With this fabrication technique for optically-efficient phase masks available, the full potential of three-dimensional, optical super-resolution experiments using the DH-PSF can now be realized. The results from a localization-based super-resolution experiment are briefly reviewed in order to report the first joint implementation of the new, optically-efficient phase mask and the information-efficient 3D localization algorithm introduced in Chapter 2.

In contrast to the stochastic emission mechanism employed in Chapter 2 which required Photo-Activated Green Fluorescent Protein (PA-GFP) as the

reporting label (24) (89), this experiment is designed to operate in the STORM modality which uses the photo-switchable Alexa 488-Alexa 647 activator/reporter molecule pair for labeling (39). The most significant difference between these two labeling options is that the PA-GFP will typically be photo-activated and emit only once whereas the Alexa 488-Alexa 647 pair can be photo-activated multiple times during the image acquisition cycle.

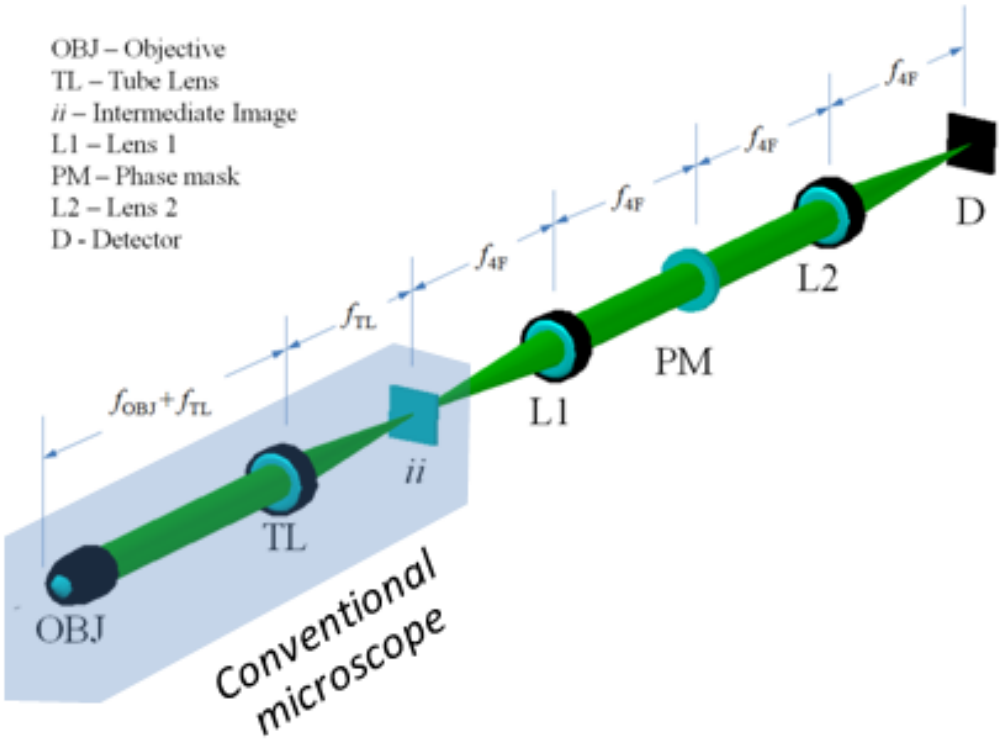

Fig. 4.19: A conventional microscope layout is appended with a 4F optical system for 3D super-resolution imaging. Experimental integration of the optically-efficient DH-PSF phase mask (PM) is realized via placement into the Fourier plane of a 4F optical system.

The biological sample was prepared by Prof. Jennifer Deluca and Keith Deluca at Colorado State University. The experimental setup was aligned and data collection was performed by Ginni Grover. The results reported here have

integrated the gray-level, optically-efficient DH-PSF phase mask into the experimental system shown in Fig. 4.19. This optical system is similar to that used earlier in Chapter 2 but with the Spatial-Light-Modulator replaced by a fixed phase mask.

The analysis of the experimental data uses the information-efficient PR-MLE algorithm of Chapter 2. First, a continuous representation of the 3D-PSF which accounts for the systematic aberrations of the optics must be found for use in the MLE algorithm. To this end, a series of calibration images are recorder for application to the phase retrieval algorithm. This series of axial calibration images are taken in $50nm$ intervals and shown as x, y projections in Fig. 4.20. After analysis by the phase retrieval algorithm, the recovered, continuous representation of the 3D-PSF is estimated and presented in Fig. 4.21. Note that because the signal is assumed to be band-limited, a continuous representation of the 3D-PSF is possible in both the transverse and axial dimensions. This is demonstrated in Fig. 4.21 where the 3D-PSF was interpolated in the x, y and z dimensions using the phase retrieval results.

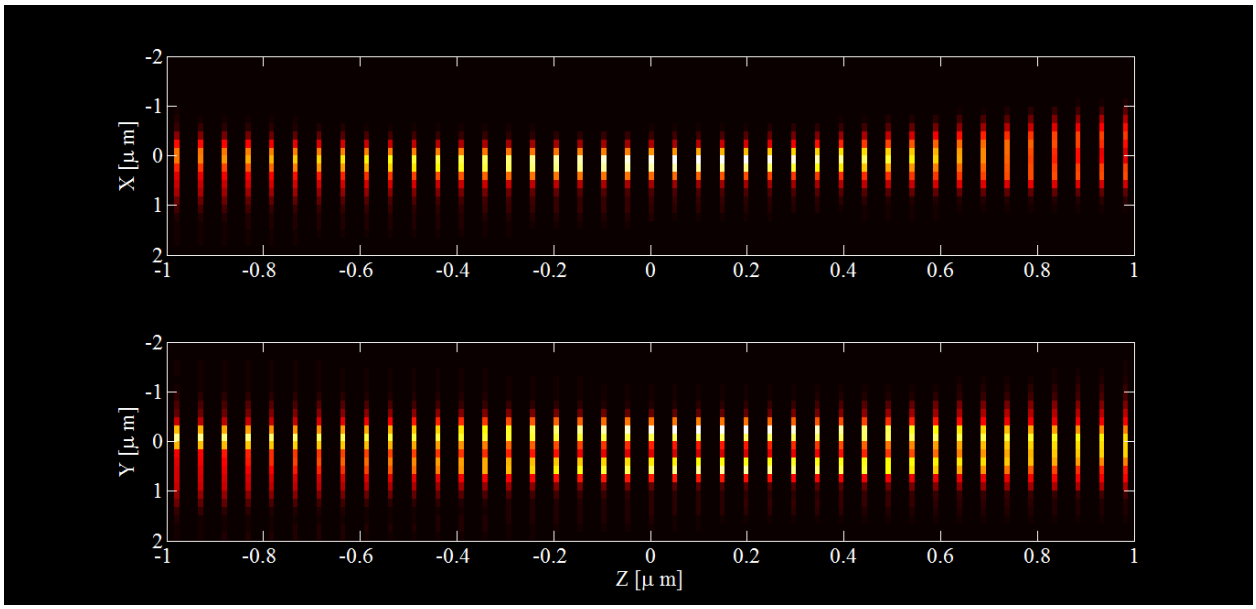

Fig. 4.20: A series of axial calibration images are taken in 50nm intervals from a DH-PSF engineered PSF microscope. The transverse intensity profile at each axial plane is projected along the *x* (top panel) and *y* (bottom panel) axes. The discrete measurement of the 3D-PSF is seen from both the missing axial information and the pixilation of each measurement which is viewable in the transverse projections.

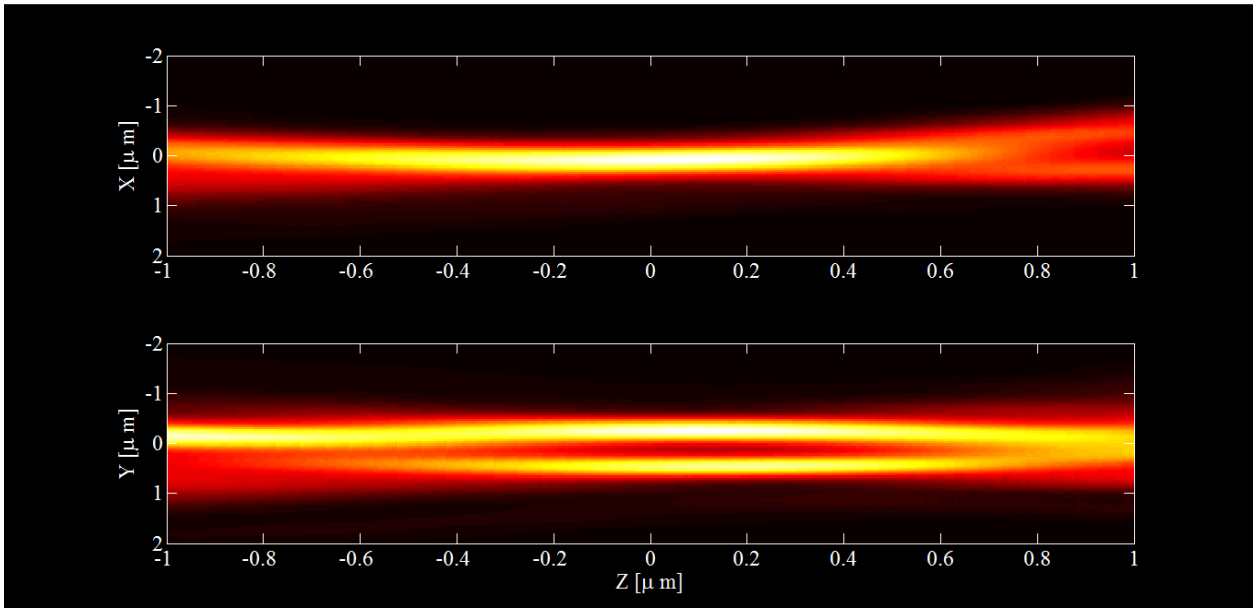

Fig. 4.21: The phase retrieval results (PR) from the calibration data in Fig. 4.20. Because the recovered signal is band-limited, the PR results can be interpolated in both the transverse and axial dimension. This representation of the experimental 3D-PSF is used for maximum likelihood localization estimation of individual molecules in the STORM experiment.

This STORM experiment has labeled the micro-tubules found in a Rat Kangaroo Epithelial Cell. A standard fluorescence image of these micro-tubules is given in Fig. 4.22A. The integrated time-series of stochastic emission and subsequent 3D PR-MLE localization from individual molecules is used to generate the 3D super-resolution image shown in Fig. 4.22B. This is the first reported DH-PSF 3D super-resolution image which uses the simultaneous application of the optical- and information-efficient methods necessary to realize the promised potential predicted by the Cramer-Rao Lower Bound (CRLB).

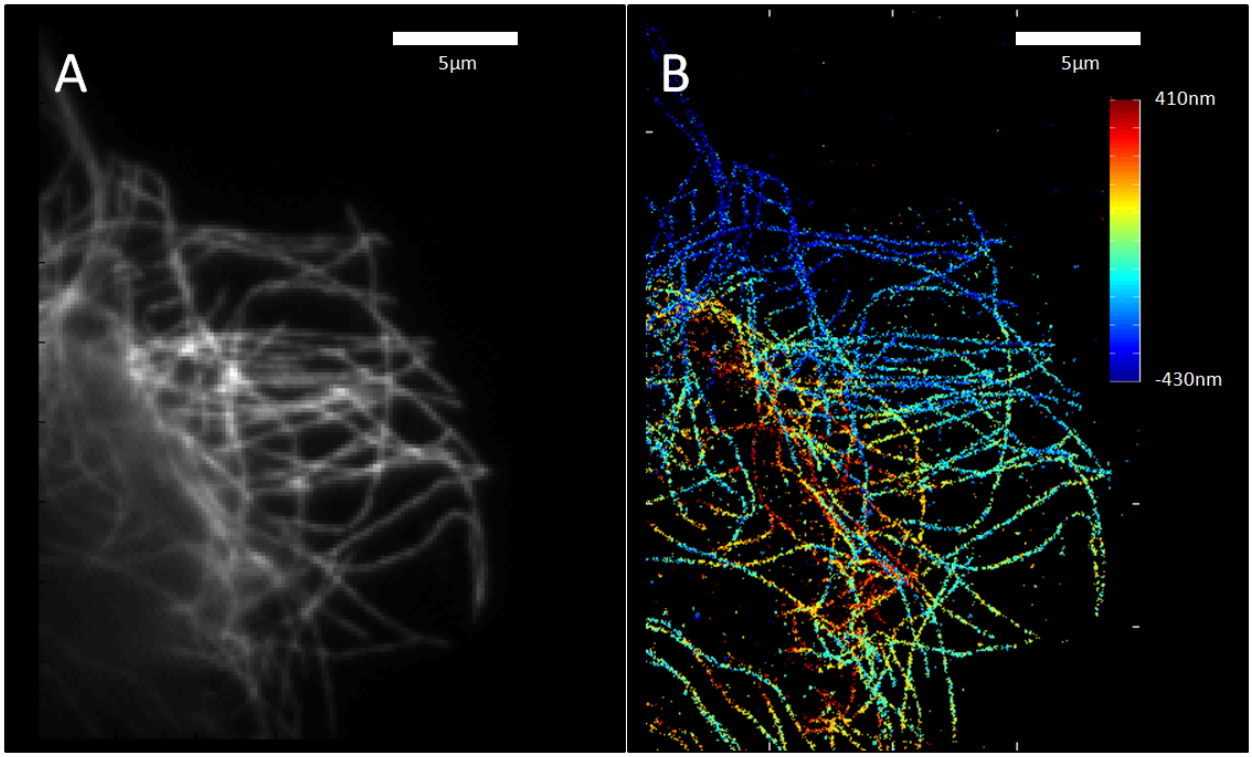

Fig. 4.22: The typical fluorescence image of micro-tubules in panel A is limited by the classical diffraction-limited criteria. A 3D STORM image using a DH-PSF microscope reveals the 3D structure of the object with resolution no longer limited by the classical diffraction limit.

4.7 Photo-stitching Tolerances for Increasing Phase Mask Size

The maximum size of the single-frame exposure from the IMP SF-100 Express mask-less gray-level lithography device is limited to 2.7mm. While this can meet the need of many optical applications, some systems will require masks with larger diameter. Examples include high numerical aperture microscope objectives with large pupil functions and the common, commercially available lenses which have a 1" diameter form-factor. One solution to this problem involves the sequential tiling of the projected lithographic image. In addition, since the projected illumination from the IMP SF-100 Xpress is frequently non-uniform, the use of sequential stitching can be used to tile a region which has uniform illumination properties. Therefore the prospect of stitching multiple frames together into a larger phase mask is investigated here via numerical simulation to identify any fundamental problems with the technique.

The dominant source of error in the stitching algorithm is modeled as positioning accuracy errors of the sample stage. To provide a generous tolerance for stage accuracy – and thereby allow for inexpensive translation-stage equipment - a 4 pixel random positioning error (equivalent to 14μm for the IMP SF-100) is simulated. For the simulation, the phase mask is divided into NxN sub-regions. Each sub-region is randomly offset by $-4 \leq \delta \leq 4$ pixels. The PSF resulting from the ensemble mask of the randomly shifted sub-region is quantified in terms of the efficiency at which energy is concentrated in the two lobes. Using this measure, the phase mask is increasingly divided into sub-regions and the efficiency of the DH-PSF is calculated. Fifty simulations of random translations are simulated for each

NxN phase mask and the average efficiency is given in Fig. 4.23. The results of the simulation indicate that the DH-PSF is tolerant to stitching errors when a low number of tiles are used.

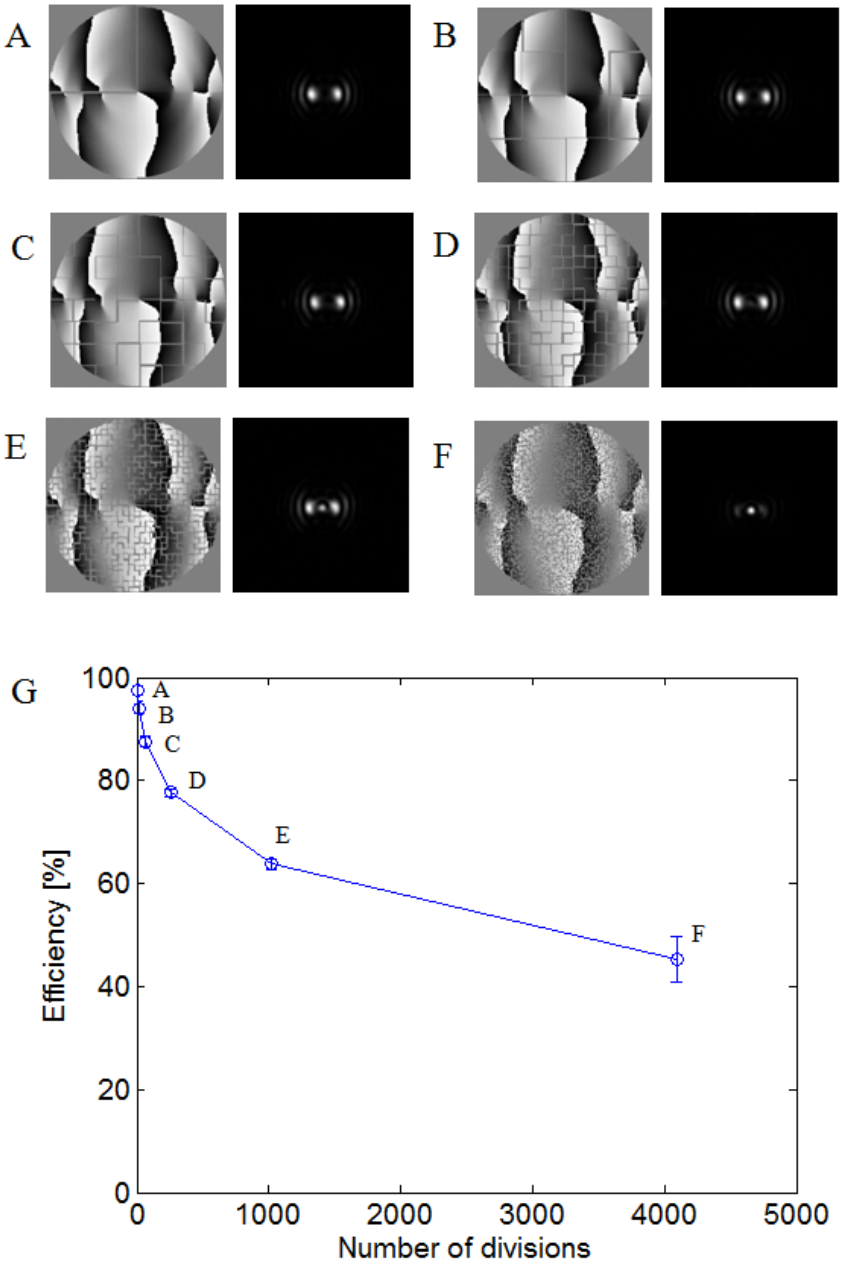

Fig. 4.23: Simulation of the influence that random positioning error will have on the optical efficiency of stitched phase masks. The phase mask is sub-divided into an increasing number of regions with the same range of random position errors (Panels A-F). The resulting DH-PSF is shown next to each respective mask. The efficiency at generating the two lobes characteristic of the DH-PSF is plotted as the number of sub-regions is increased.

4.8 Conclusions

The focus of this chapter was to demonstrate and document a successful method for fabricating the optical elements which are necessary for engineered PSF system implementation. A mask-less gray-level lithography tool (IMP SF-100 Xpress) was identified as a candidate for phase mask manufacturing. The necessary processing and fabrication steps were identified and reported in order to manufacture an optically-efficient phase mask. The first examples of optical phase masks fabricated from this DMD-based lithography tool were provided. These DH-PSF phase masks were implemented in two different systems – first a commercial microscope adaptation and second a custom microscope adaptation. Later in this thesis, this tool will be used to fabricate additional devices.

The efficiency of a representative mask at generating the desired DH-PSF was measured to be 87% - a number that can be increased further with the introduction of Anti-Reflective (AR) coatings onto the surface of the element. Using this fabrication technology, another phase mask was manufactured to demonstrate the first optical- and information-efficient implementation of the DH-PSF microscope. Results of applying this microscope to 3D super-resolution imaging were then reported.

The success of this method will allow for the continued manufacture of engineered PSF phase masks for integration into optical microscopes and cameras both in this thesis and elsewhere. Critically, the optical efficiency of using custom engineered PSF designs is no longer a limitation for system implementation.

CHAPTER 5

A SINGLE-HELIX POINT SPREAD FUNCTION FOR IMAGING AND SENSING APPLICATIONS

5.1 Introduction

The joint optimization of both the optical element and the image processing algorithm has enhanced the task-specific functionality of imaging systems while demonstrating the success of a computational imaging approach. Among the variety of computational imaging techniques, the modification of the Point Spread Function (PSF) has received attention as manufacture of the necessary optical elements has become feasible. Now, with the definition of a clear task, PSF engineering has successfully demonstrated superior solutions for Passive-Ranging (11) (12) (15), 3D super-resolution microscopy (13) (14), Extended Depth-of-Field imaging (6) (7), thermally tolerant infra-red cameras (2) (18) and iris recognition (16).

Here an optical system is presented which is optimized for two simultaneous tasks common in the computational imaging literature, Passive-Ranging (PR) and Extended-Depth-of-Field (EDOF). Whereas prior work (6) (11) (12) (13) (14) (62) (68) (74) has treated each of these tasks independently, this solution seeks to solve these problems jointly. I first address PR, where the objective is to measure the distance to an object without emitting

optical radiation from the system. The second task is to simultaneously provide an in-focus image of the scene to accompany the PR measurement.

The combination of both range and image brightness complement each other to enhance the interpretation of a scene. For this reason, the coupling of solutions which are unique to each task (e.g. the Double-Helix PSF for PR and a cubic-phase PSF for EDOF) has previously been investigated to realize joint functionality in Chapter 3 (90). However in order to maintain a consistent line-of-sight and eliminate image registration issues, that prior solution required a Spatial Light Modulator (SLM) to serially cycle through the requisite phase masks. While effective, that solution may be considered too expensive, power-demanding or optically inefficient (the SLM only encodes one of two, orthogonal linear polarization states) for practical field solutions. In addition, the finite cycle time for the SLM to serially scan through the requisite phase masks may limit the space of relevant applications. Therefore the focus here is on an alternative solution which requires only one mask to realize both functionalities.

This chapter is structured as follows. In Section 5.2 the optical solution is introduced as the Single-Helix PSF which is the enabling contribution for this application. In Section 5.3, the SH-PSF ranging performance is compared with that of the standard optical system. In Section 5.4, the SH-PSF image restorability is compared with the standard optical system for EDOF application. In sections 5.5 and 5.6, two different optical implementations are demonstrated as well as two alternative estimation algorithms to be used for PR and subsequent EDOF. And in Section 5.7, the implications of this system and what opportunities exist for future SH-PSF research are discussed.

5.2 The Single-Helix Point Spread Function

The engineered PSF design for joint PR/EDOF tasks requires a solution which satisfies the following design criteria.

A: The PSF must be axially dependent so that algorithms can search an experimental image for the unique PSF signatures and generate a distance estimate.

B: The PSF must allow a high amount of spatial-frequency (spectral) content relative to noise to be transferred into the image throughout the volume of interest. This will enable the accurate enhancement of image resolution as a post-processing step.

To solve this problem, a solution is identified which is one example of a scale- and rotationally-invariant propagating field (34) and it is implemented as the system PSF.

Scale- and rotationally-invariant propagating waves can be found using select super-positions of Laguerre-Gauss (LG) modes. These super-positions describe the field of a scalar, paraxial beam which remains self-similar up to a transverse scaling function (which increases/decreases the transverse dimension of the beam) and a rotation function (which rotates the transverse profile of the beam as it propagates). One method to realize these beams is by placement of the LG super-position into the pupil plane of a lens, thereby encoding the optical PSF of the system. However, the amplitude modulation of the LG solutions can make these PSFs significantly inefficient to realize in terms of the optical transmission. Fortunately, select solutions do retain their propagation invariance without the LG amplitude modulation and with only the phase encoding present (29).

One such example is found with the superposition of LG modes (m,n) = {(1,1), (2,4), (3,7), (4,10), (5,13)}, where the modes are equally weighted. Placed in the pupil of a lens to encode the PSF, this beam is characterized by a single, intense peak throughout an

extended axial range relative to the clear aperture and therefore has potential for EDOF imaging (91). A unique functional aspect of this PSF is that as a point source is moved through focus, the image of a single peak will shift transversely due to rotation about the optical axis. In 3D, this PSF traces a helical pattern through the focal plane and will be referred to as the Single-Helix (SH) PSF throughout the rest of the text. This unique translational shift encodes the axial position of the object, d_{obj}.

Given this L-G super-position, the phase-mask shown in Fig. 5.1A will be enough to generate the desired PSF characteristic. The associated PSF series is presented in Fig. 5.1B as a function of defocus. For comparison, Fig. 5.1C shows the standard system PSF. The defocus parameter Ψ is used to quantify the amount of defocus and defined as,

$$\Psi(u, v; \lambda, z) = \frac{\pi}{\lambda}(u^2 + v^2)\left(\frac{1}{f} - \frac{1}{z} - \frac{1}{d_{cam}}\right) \tag{5.1}$$

where λ is the wavelength, u, v are the spatial coordinates of the pupil, f is the focal length of the lens, z is the object distance and d_{cam} is the distance to the camera. This quantity represents the quadratic phase aberration present in the pupil and is responsible for defocus effects in the imaging plane (25). The defocus parameter influences the PSF as,

$$h(x, y; \lambda, z) \propto \left|\mathfrak{F}\{p(u, v)e^{-i\Psi(u,v;\lambda,z)}\}\right|^2 \tag{5.2}$$

where h is the PSF, $\mathfrak{F}$ is the forward 2D Fourier transform, and $p(u, v)$ is the pupil function of the optical system and includes any phase modulations included in the mask. Given this PSF the image formation is modeled as,

$$i = h(z, \lambda) \otimes o + \bar{\boldsymbol{n}} \tag{5.3}$$

where o is the object and the random noise variable is denoted with a bar.

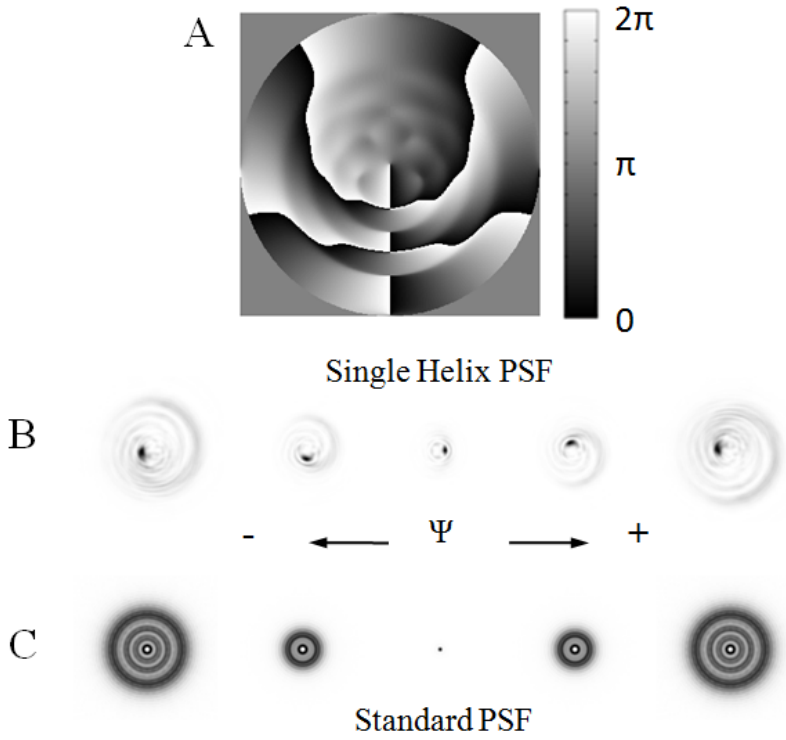

Fig. 5.1: The SH-PSF is generated from the pupil plane phase modulation given in panel A. The SH-PSF and standard PSF are compared as a function of defocus where a point source is translated to generate defocus parameter values of $\boldsymbol{\Psi} = \boldsymbol{-25, -12.5, 0, +12.5, +25}$ waves in panels B and C, respectively.

From the relationship between the transverse position/rotation of the image and the axial position of the source, a variety of techniques can be employed to extract axial information. Here two alternative algorithms are proposed, the first in Section 5.5 where a match is sought of the axially dependent MTF of the PSF and the envelope of the spatial frequency content of the image is used in order to estimate range. This implementation will ignore any chromatic effects of the PSF. As an alternative, the use of an internal reference which will be useful in identification of the axis of rotation and estimating an angle is considered. In Section 5.6, one algorithm is demonstrated for realizing this with a three-color, RGB detector where the color channels serve as the internal references. This

algorithm will exploit the chromatic dependence of the PSF given in Eq. 5.1 and characterized in Fig. 5.2, where for one axial position each color exhibits a unique rotation of the SH-PSF to uniquely code z-position.

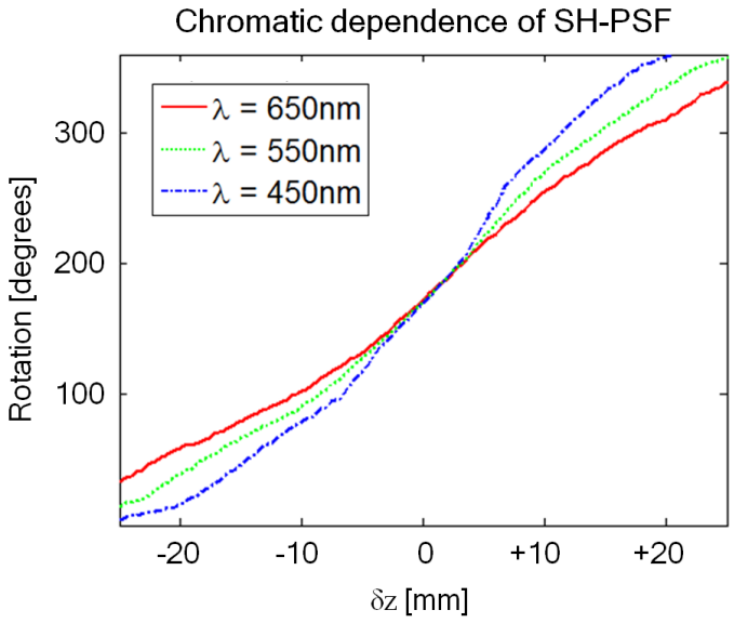

Fig. 5.2: The chromatic dependence on the rotation rate of the SH-PSF as a function of defocusing. Focus is at δz = 0mm and is tracked from $-\mathbf{25}\boldsymbol{mm} \leq \boldsymbol{\delta z} \leq +\mathbf{25}\boldsymbol{mm}$. This is approximately the range of defocus values, $-\mathbf{25} \leq \boldsymbol{\Psi} \leq +\mathbf{25}$.

Yet another single-pupil method exists in the form of the standard optical system. Here one can measure the chromatic dependence of the PSF blur radius to find axial location and use this to properly restore the lost spatial frequency content of the image. Therefore, to justify the use of a SH-PSF for PR and EDOF, a performance comparison of these two systems is required.

5.3 Passive Ranging Performance Comparison

A measure of the performance limit for axial position estimates from noisy measurements can be found using the Cramer-Rao Lower Bound (CRLB) (33) (35). The CRLB has an inverse relationship with the quantity known as Fisher Information (FI) and is written as,

$$CRLB(z) = \left(\sum_{m=1}^{M} \sum_{n=1}^{N} \frac{1}{pr(i(m,n)|z)} \left(\frac{\partial}{\partial z} pr(i(m,n)|z) \right)^2 \right)^{-1} \qquad (5.4)$$

where the quantity in the denominator is the FI, $i(m,n)$ is the discrete image measurement of size MxN and pr is the probability density function for each pixel (33) (73). For the special case that each pixel is statistically independent and the noise is Gaussian, the CRLB is,

$$CRLB(z) = \left(\sum_{m=1}^{M} \sum_{n=1}^{N} \frac{1}{\sigma^2} \left(\frac{\partial}{\partial z} i(m,n;z) \right)^2 \right)^{-1} \qquad (5.5)$$

where σ is the standard deviation from Gaussian noise (73).

For this investigation, the CRLB will measure how sensitive the image is to variation in axial position. Qualitatively, images with greater change will have higher precision, better performance and a lower CRLB. To compare the CRLB across multiple systems a standard object must be selected. A point-source is identified as the standardized object of choice as it may particularly indicative of performance for images with only sparse content. In addition, the point source results will provide a lower-bound for the system CRLB performance and an upper-bound on the spectral SNR improvement because of its maximum spectral frequency content.

For the CRLB evaluation, a 4F imaging system is simulated with two lenses of focal length f = 100mm, pupil diameter D = 2.7mm and three color channels centered at λ = 450, 550 and 650nm. The source is allowed to move within the range –25mm < δz <

+25mm of defocus, where δz = 0 is the focal plane. The CRLB of the two systems is presented in Fig. 5.3. The SH-PSF system is shown to provide improved ranging performance in terms of the theoretical random error from estimation through the entire range of focus. The spike of the estimator standard deviation at the focal position of the standard optical system is due to the image invariance attributable to the depth-of-focus. Because the image is approximately invariant in this region, the measurement precision is poor. As the system is defocused, the SH-PSF remains a well-localized peak, relatively robust to noise, experiencing a near-constant rate of transverse motion. In contrast, the standard PSF slowly increases in blur radius to become relatively sensitive to noise. These differences between the SH-PSF and the standard PSF are responsible for the axial dependence of the ranging precision. These precision limits are a fundamental statement about the ability to measure axial distance. No assumptions are made concerning the actual algorithm used other than it be an unbiased estimator. Note that defocus is defined to be positive when the object is further away from the optical system, $\delta z = z - f$. The in-focus PSF is assumed to use the full dynamic range of the detector (12-bit) and 7.5 micron pixels are assumed. The emitter is assumed constant in intensity as it is moved through focus and a Gaussian noise of σ = 10 counts per pixel is present.

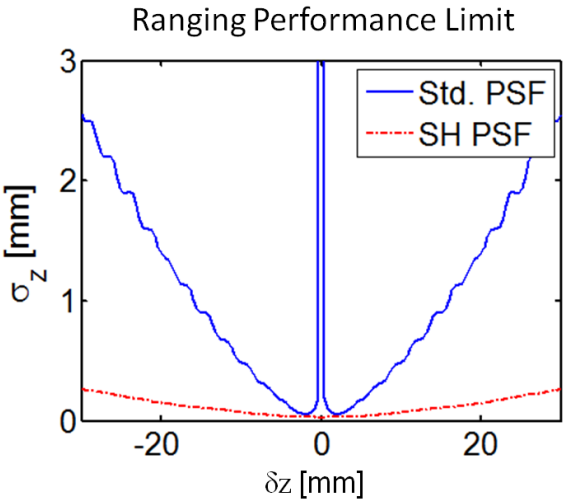

Fig. 5.3: CRLB plot of the ranging precision limit as a function of the axial position of the object. Focus is located at δz = 0mm. The depth precision performance can be seen to improve with application of the SH-PSF.

5.4 Extended-Depth-of-Field Performance Comparison

Spectral SNR is identified as a meaningful measure to evaluate the suitability for EDOF application because it directly quantifies the object related spectral information content in an image with the presence of noise (28). The average spectral SNR is defined across the depth of field as,

$$SNR(u,v) = \frac{1}{2\delta z}\sum_{z=-\delta z}^{\delta z} SNR(u,v;\delta z) \tag{5.6}$$

where δz = 25mm is an application specific selection for the 4F system and

$$SNR(u,v;\delta z) = \overline{SNR}\ \cdot MTF(u,v;\delta z) \tag{5.7}$$

where,

$$\overline{SNR} = \sum_{m=1}^{M}\sum_{n=1}^{N} h(m,n;z)/\sigma(m,n) \tag{5.8}$$

is the average signal to noise and $MTF = |\mathfrak{F}^{-1}\{h\}|$, where $\mathfrak{F}^{-1}$ is the reverse 2D Fourier transform and the MTF is normalized to one at the DC. Note also that the incoherent PSF

$h(m,n;z)$ is scaled to the full dynamic range of the detector. Again, this measure does not provide the user with the optimal means to extract information. It is instead, a fundamental statement about the object-related information available.

For an image to be suitable for restoration, it is required that the spectral SNR remain high throughout the volume of interest. The spectral SNR from a single color channel (λ=550nm) for the SH-PSF and the standard optical system is evaluated and the ratio of the two as a function of spatial frequency is plotted in Fig. 5.4. Relative to the standard PSF, the SH-PSF design provides an increase in spectral SNR capacity, indicated as a ratio greater than one in Fig. 5.4. The spectral SNR performance is for one only channel of the RGB image but this may be considered indicative of the image quality to be found in the additional color channels.

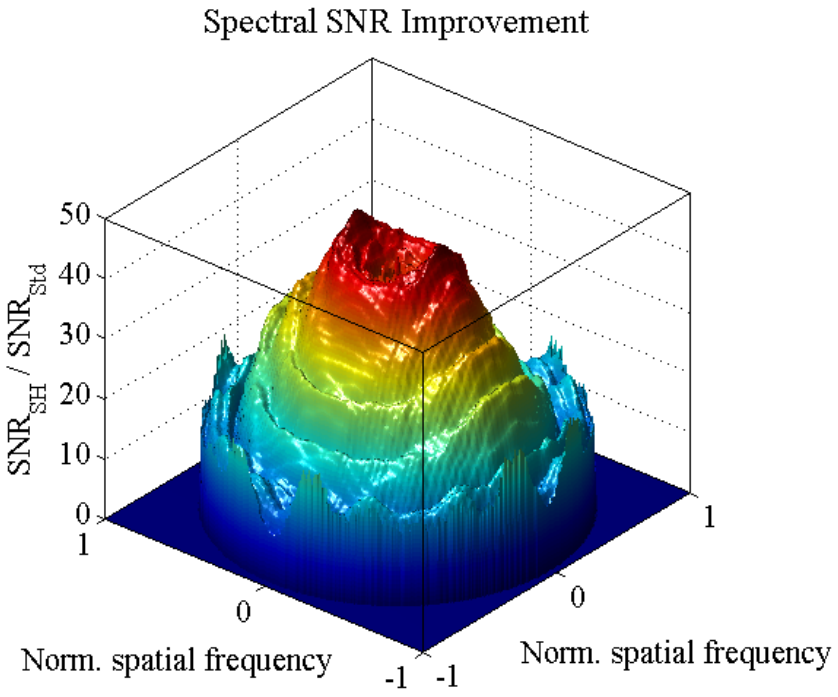

Fig. 5.4: Ratio of the average spectral SNR of the SH-PSF system to the Standard system. A ratio greater-than-one indicates that, on average, an improved spectral SNR is available for that particular spatial frequency. The ratio across the entire 2D spatial frequency plane indicates that the SH-PSF solution can significantly improved spectral SNR.

5.5 Experimental Implementation of EDOF Solution

The first example of SH-PSF imaging is an EDOF imaging solution implemented using a Spatial Light Modulator (SLM) (Boulder Non-Linear Systems XY-P512) to encode the pupil with the optical configuration shown in Fig. 5.5. Because the 2D-OTF of the SH-PSF is axially dependent, an estimation of axial position is proposed using the spatial-frequency domain in order to restore using the correct deconvolution filter, as reviewed in the estimation algorithm flowchart in Fig. 5.6.

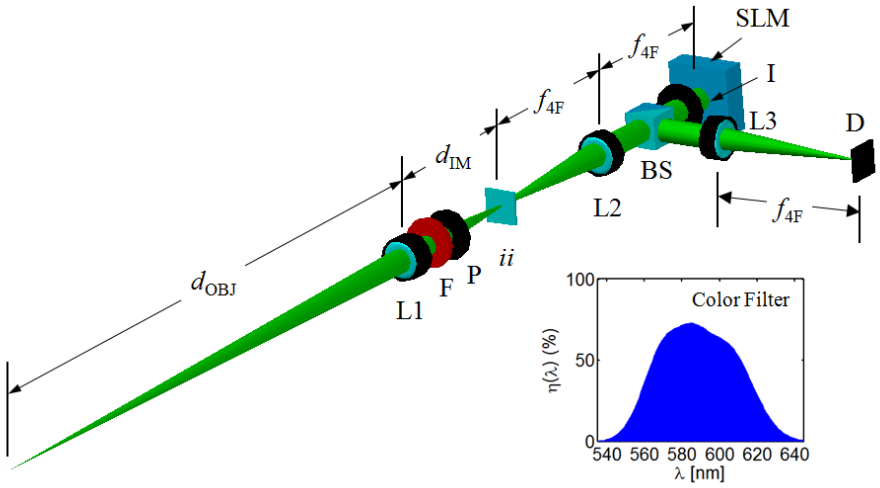

Fig. 5.5: Experimental implementation of EDOF experiment with SH-PSF. L1, imaging lens; F, color filter (inset); P, linear polarizer; ***ii***, intermediate image plane; L2, L3, 4F lenses; BS, 50:50 beam splitter; SLM, spatial light modulator; I, iris; D, detector.

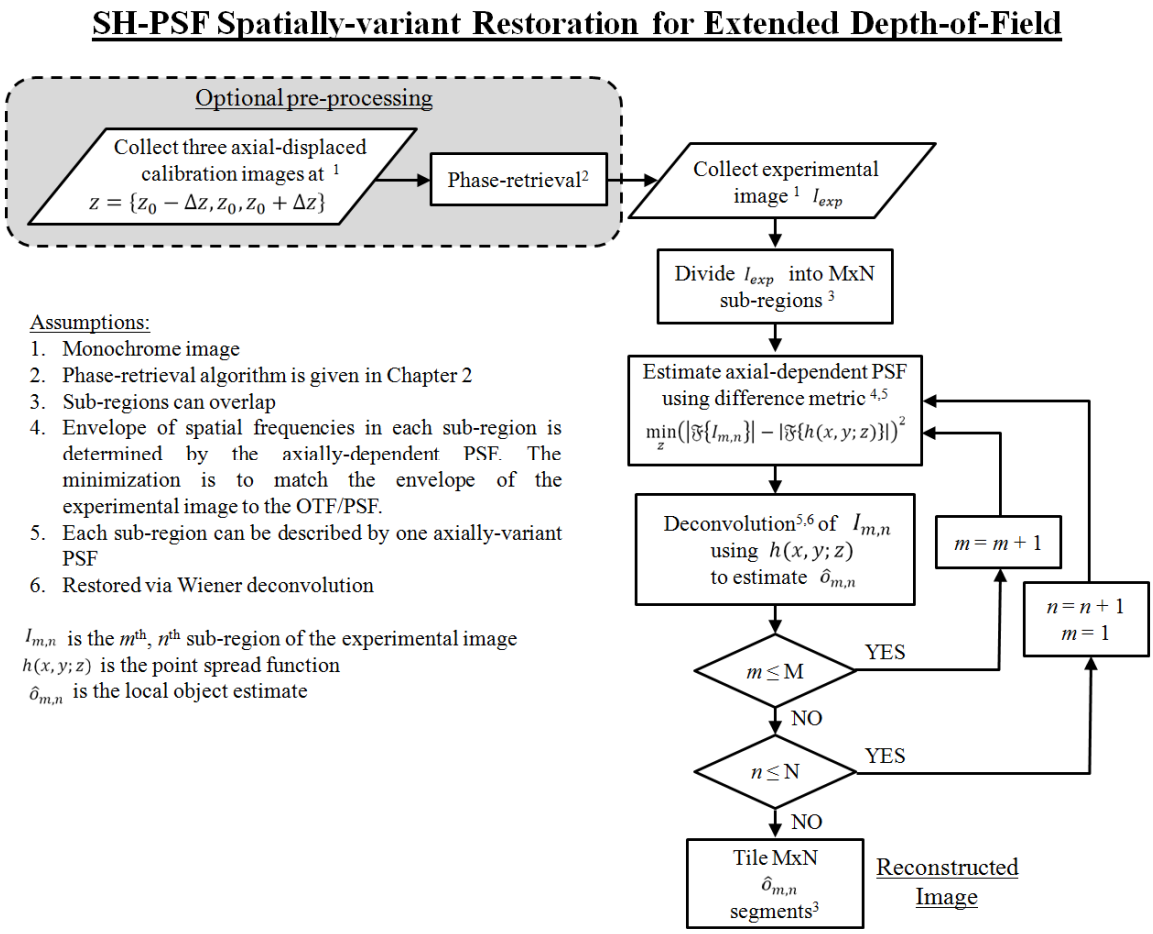

Fig. 5.6: Image reconstruction algorithm details for EDOF solution. Three distinct steps are present; pre-processing, image collection, post-processing.

In the experimental configuration the intermediate image plane, ii, found behind the imaging lens (L1, f_{L1} = 50mm) is optically modified with a 4F imaging system. A color filter, F, is placed in the system to so that the wavelength of operation is matched to the SLM design wavelength. A SLM with a 7.68mm pupil diameter is placed in the Fourier plane to modulate the phase encoding of the optical system. An iris is located before the SLM to make the aperture circular and a polarizer is used to reject the non-modulated polarization state from the SLM. The lenses of the 4F system (L2 and L3) are both f_{4F} = 100mm. A monochromatic detector (Point Grey Chameleon CMLN-1352M) is located in

the new image plane behind the 4F system. The object-space focal plane is located at d_{OBJ} = 72cm. An experimental image is taken of a complex scene consisting of a bouquet of flowers, shown in Fig. 5.7A, to demonstrate the potential for EDOF imaging.

A series of calibration images are first taken in 2mm intervals through focus with the SH-PSF mask loaded onto the SLM. The calibration object was a 15μm pinhole, illuminated from behind with a halogen bulb. A phase-retrieval algorithm (8) (89) is implemented to estimate the field associated with the image at each calibration image.

The image is restored using block processing. A 960x1280 pixel image of the scene is subdivided into 64x64 pixel sub-regions which are repeated in 8 pixel intervals such that the windows overlap. The spatial frequency content of each sub-region is compared with MTFs of the axial-dependent SH-PSF given by the phase-retrieval results. Using Eqs. 5.1 and 5.2, the field is propagated along z to search continuously for the best match of $MTF(z)$ with the envelope of the spatial-frequency content of the image where $MTF(z) = |\Im\{h(m,n;z)\}|$ (89). When the best-matched MTF is identified as,

$$\min_z \left(|\Im\{i(m,n)\}| - MTF(z)\right)^2, \tag{5.9}$$

the sub-region is restored with a Wiener-deconvolution filter,

$$\hat{o} = \Im^{-1}\left\{\frac{\Im\{i(m,n)\}}{\Im\{\hat{h}(m,n;z)\}}\left[\frac{|\Im\{\hat{h}(m,n;z)\}|^2}{|\Im\{\hat{h}(m,n;z)\}|^2 + SNR^{-1}}\right]\right\} \tag{5.10}$$

where $\hat{h}(m,n;z)$ is the solution which minimized Eq. 5.9. The central 8x8 pixel portion of this window is stored, and the algorithm moves to the next processing window. The final image is a composite of the restored 8x8 pixel regions across the image. The use of 8x8 pixel frames taken from 64x64 pixel windows was to minimize the ringing artifacts from window edges in the final image.

The EDOF result is shown in Figure 5.7. An image taken with the standard pupil function is compared with the result of a restored EDOF SH-PSF image. Comparison of the highlighted region demonstrates the restorative capacity and extended axial range of focus available for imaging. Note that this demonstration required only one color channel for full restoration of the image.

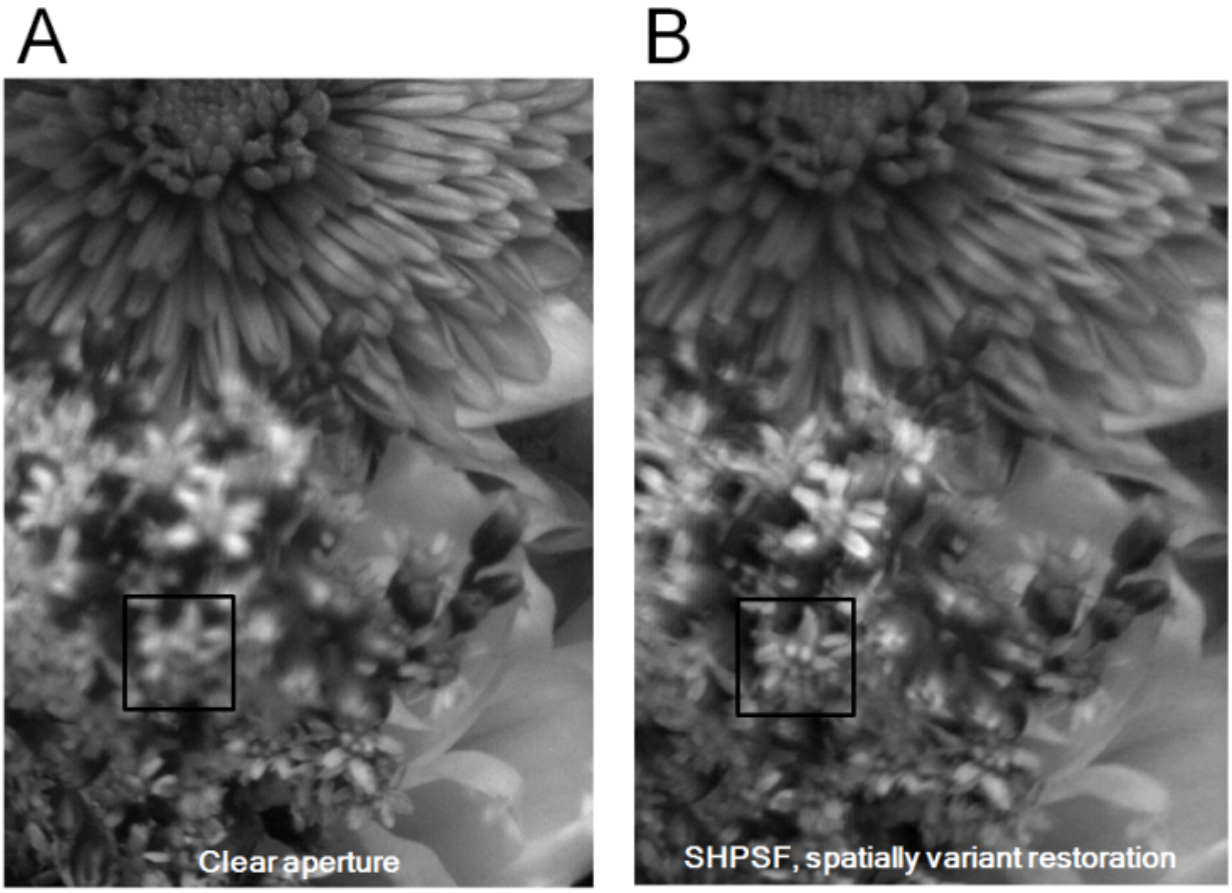

Fig. 5.7: Experimental comparison of the image from a standard system versus the EDOF image from a restored, SHPSF camera.

5.6 Experimental Implementation of Joint Passive-Ranging/Extended Depth-of-Field Device

In this section an experimental realization for the joint PR/EDOF solution is demonstrated by implementation of a lithographically fabricated gray-level SH-PSF phase mask in the 4F system to replace the SLM. By implementing a lithographic phase mask, this system will not require a polarizer for implementation. The mask is manufactured using a commercial gray-scale lithography device (Intelligent Micro-Patterning SF-100 Express). A glass substrate is first prepared with a 2.7mm diameter chrome aperture. This is then spin-coated at 5krpm for 40 seconds with Clariant AZ4210 positive photo-resist (refractive index $n(\lambda = 633nm) = 1.635$). The resist is pre-baked at 90C for 90 seconds. A bit-map of the SH-PSF phase mask is loaded into the software control package for the lithography device and a calibrated dose of 365nm light (i-line) from a Hg source exposes the photo-resist. The sample is then developed in AZ400K diluted with de-ionized water at a 1:4 ratio for 180 seconds. The result is a surface modulation in photo-resist serving as the phase-mask which can be implemented into the compact system of Fig. 5.8.

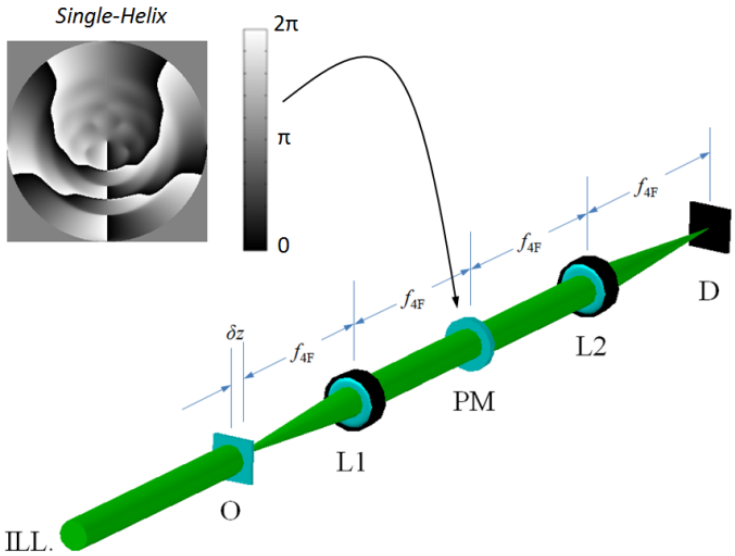

Fig. 5.8: Optical SH-PSF implementation using a lithographic phase mask. ILL is the illumination; O is the object; L1, L2 are the 4F lenses; PM is the phase mask; D is the detector.

A surface profilometry scan (Zygo New View) of the SH-PSF mask is shown in Fig. 5.9, where the profile is related to the phase by

$$\varphi = \frac{2\pi}{\lambda} h(n-1). \tag{5.11}$$

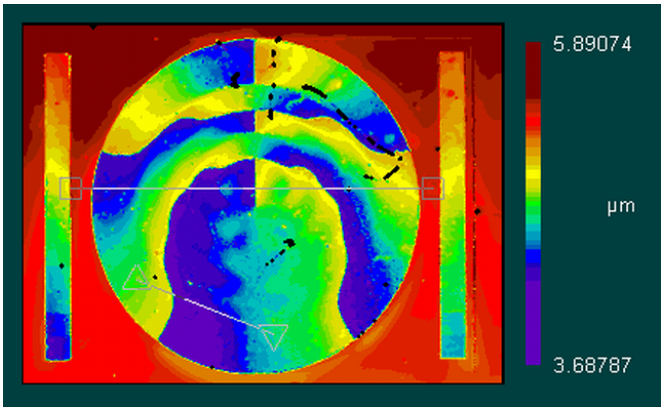

Fig. 5.9: Surface profilometry result of the SH-PSF phase mask. The pair of linear features on either side of the mask are used for calibration purposes.

The optical system is configured to match with that given in the earlier CRLB model. The detector is a color camera (Point Grey Chameleon, CMLN-1352C, 12-bit) with a 3.75μm pixel pitch (alternatively, a 7.5μm pitch for each color in the Bayer pattern). The spectrum peaks for the RGB detector are at 450, 550 and 650nm with a typical band-width of 80nm. The phase mask was fabricated to operate in the middle of this color spectrum spanned by the detector. The experimental PSFs are taken using a 15μm pinhole, illuminated with a halogen bulb and translated in 1mm axial steps through focus. The green channel calibration images of both the standard system and the SH-PSF system are given in Fig. 5.10 for comparison.

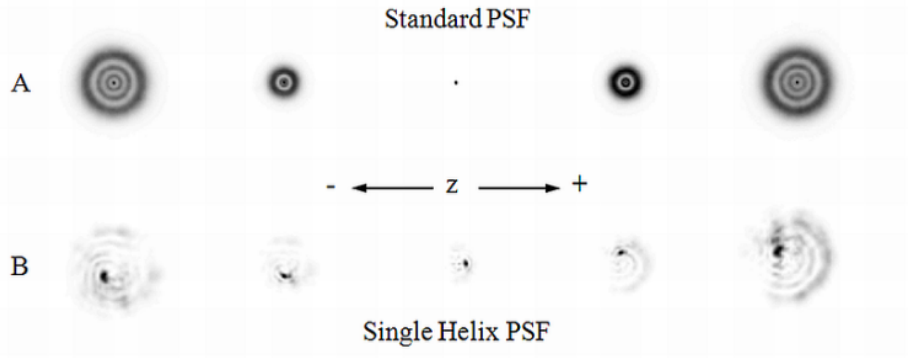

Fig. 5.10: Experimental PSF results of the system in Fig. 5.8 with either no phase encoding present in the phase mask (Standard PSF) or with the Single-Helix PSF mask.

The second joint PR/EDOF restoration algorithm proposed for the SH-PSF treats each RGB image as three independent, registered, information channels but each with the same object and axial position used to encode the image. Because the PSF is chromatic, each color channel can have unique information to use for estimation. These reported

results are for an algorithm which uses just two chromatic channels, and therefore the minimum of two equations exist to estimate two unknowns – object distance z and the object o,

$$im_1 = h(z, \lambda_1) \otimes o + \bar{\boldsymbol{n}}_1 \tag{5.12a}$$

$$im_2 = h(z, \lambda_2) \otimes o + \bar{\boldsymbol{n}}_2 \tag{5.12b}$$

where the random noise variables are denoted with a bar.

The joint PR/EDOF algorithm is outlined in Fig. 5.11 and begins with a guess for axial position, loads the associated SH-PSF (taken from discretely sampled experimental calibration images) and uses Richardson-Lucy (R-L) deconvolution to estimate the object in each color image. A measure of the similarity between the two object estimates is taken (e.g. mean-squared error) and then another axial position is guessed and the algorithm repeats. This continues until a maximum for the similarity for the two color channels is found and associated with a detection of the axial position. This detection occurs when the proper z position is found and the two images are perfectly registered after deconvolution, minimizing the mean-squared error. Implicit in this algorithm is the assumption that the object is spectrally white in the temporal domain and therefore the deconvolved result is independent of the color used.

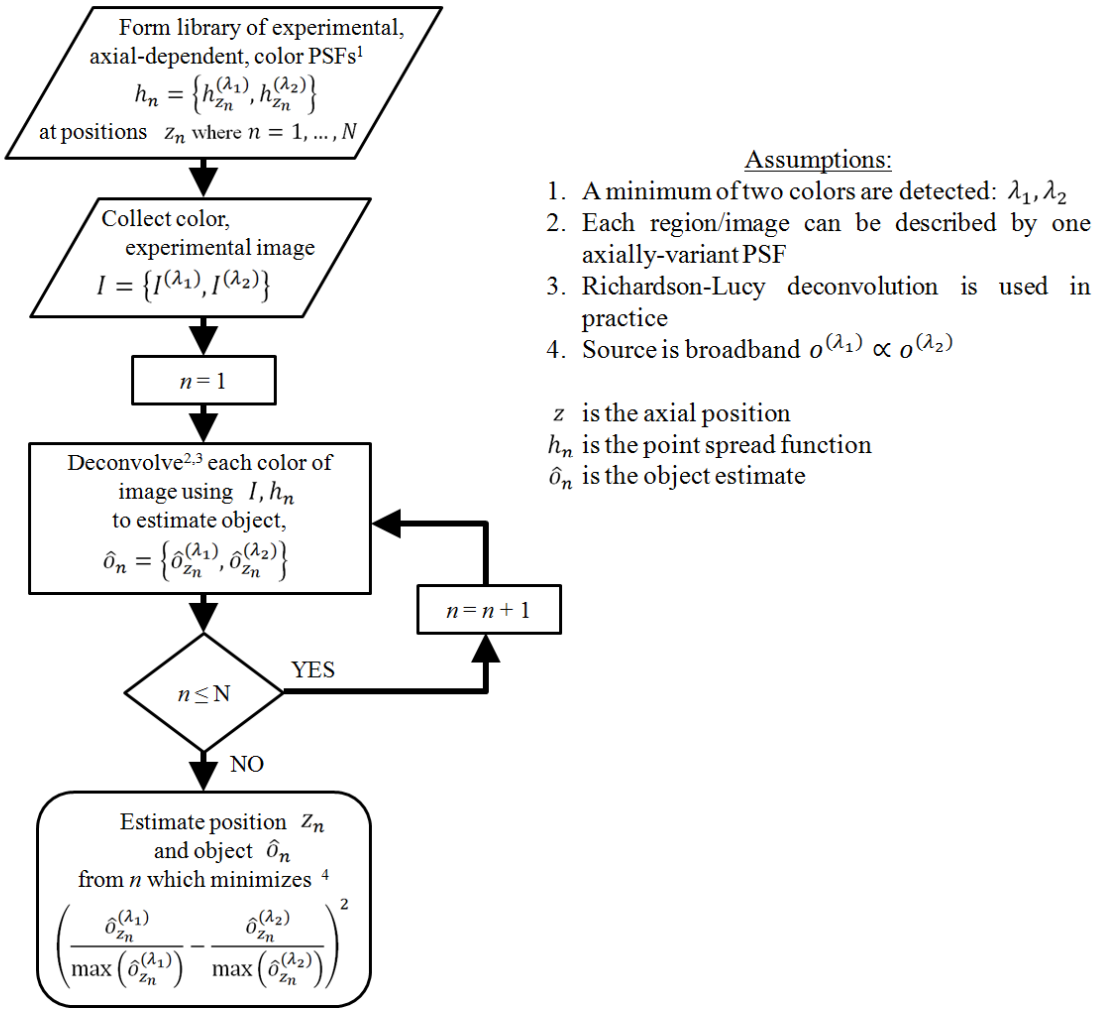

Fig. 5.11: Flowchart outlining the processing steps of the joint ranging and image restoration algorithm used in Section 5.6

A standard pattern is selected to serve as a test target (Edmund Optics, Negative USAF 1951 Resolution Test Pattern on glass). The sample is back illuminated with a halogen bulb and diffuse glass is located between the target and the bulb to make the illumination uniform. The red and green color images are used for the estimation algorithm since they had the highest SNR given the source and spectral filters of the camera. Experimental EDOF results are presented in Fig. 5.12A for an object located at

three axial positions responsible for moderate defocus and focused imaging. To aid in the evaluation of image quality, a vertical line-out of the left-most bar patterns is presented to the left of the two images. The PR detection results are given in Fig. 5.12B. Ten images/estimates were taken at each axial position. It is seen from the figures that the image restoration improves the available detail significantly. In addition, the PR is demonstrated to work within an error consistent with the minimum step size of the experimental PSFs used. Although the objects are assumed to be spectrally white, this can be relaxed and chromatic objects may be treated using alternative methods such as matching between the object boundaries.

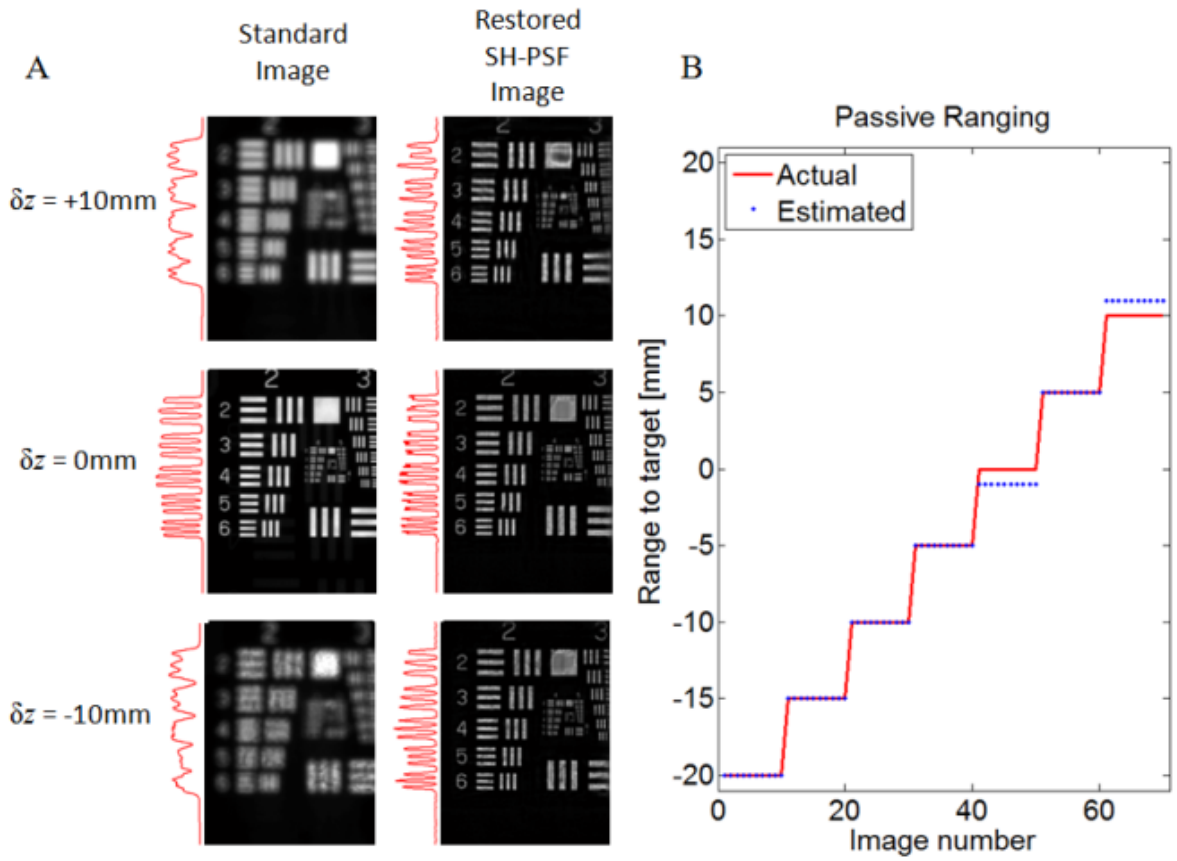

Fig. 5.12: The restored images are compared to the standard images at different ranges of defocus in panel A. The passive ranging results are presented in panel B. 10 measurements are taken at each position.

5.7 Discussion

One limitation of both algorithms introduced here is that each has required an assumption that the object remain at one axial distance for a greater than 1x1 pixel area. In fact, the minimum area for which this assumption was applied to was a 64x64 pixel area. Much as the sophisticated algorithms for spatially-variant restoration have developed for standard pupil systems (e.g. depth-from-defocus, depth-from-diffusion), it is believed possible that additional algorithms may be developed to accommodate engineered PSFs such as the SH-PSF.

One important outcome which was demonstrated here is that alternative approaches exist for EDOF image restoration. While the approach advocated by users of the cubic-phase mask requires only one deconvolution filter for all axial positions is both sound and attractive, the SH-PSF represents the unique opportunity to recover higher-spatial frequency content while simultaneously extracting depth information. The additional processing steps are considered to be a trade-off for the increased information available about the scene being queried.

5.8 Conclusions

An engineered PSF solution is reported to jointly solve two task-specific problems, both of general utility. The proposed SH-PSF solution is justified in terms of the theoretical performance limits for each task. Two system implementations were demonstrated as well as two estimation algorithms, each particularly suited for different constraints. A compact realization of a SH-PSF system was realized and demonstrated to operate for both PR and EDOF. The chromatic behavior of the phase mask was exploited here in order to provide

an algorithm which simulaneously estimates the range to an object as well as restore the image spatial-frequency information.

CHAPTER 6

PERFORMANCE BOUNDS OF WAVE-FRONT SENSING USING CONVENTIONAL MICRO-LENS ARRAYS

6.1 Introduction

In this chapter the information theoretic bounds of the Shack-Hartmann optical phase recovery technique is evaluated in order to find the associated performance limitation of wave-front sensing and to identify areas for improvement. It will be shown that when the space of possible phase modulations is restricted to a finite set of Zernike polynomials, performance trade-offs exist between the number of photons in the signal, the number of unknown Zernike polynomial aberration coefficients to estimate and the size of the micro-lens array. The implications of these limits are discussed as well as whether an optimum number of apertures in the Shack-Hartmann geometry can exist under specific scenarios.

The precise measurement of optical phase aberrations has enabled the development of transformative technology across disciplines such as astronomy (92), biology (55) (93) and medicine (94). Solutions including interferometry (95) (96), Phase-Retrieval (PR) (8) (56) and the Shack-Hartmann Wave-front Sensor (SHWFS) (97) have been utilized to circumvent the temporal sampling limitations of optical waves by transforming this phase information into spatial distributions.

Here, the focus of attention will remain on one technique particularly suited for applications which operate with broadband illumination, does not require environmental stability, remain light-weight and is commonly implemented for measuring phase aberrations (92) (94). The SHWFS satisfies all these operational criteria by using of an array of micro-lenses to transversely sample an incident wave-front into localized segments and uses the resulting signal for estimating the amplitude/phase modulation (73) (97).

The system performance is investigated in terms of how much aberration information is transferred from the wave-front,

$$u(\rho,\theta) = A(\rho,\theta)e^{i\frac{2\pi}{\lambda}W(\rho,\theta)} \tag{6.1}$$

into the final measurement. This problem is further restricted to wave-front sensing where the quantitative measurement of the coefficients for Zernike polynomials (an orthonormal basis set defined over the unit circle) are sought, w_n^m. When assuming uniform illumination, the optical phase may therefore be represented as,

$$W(\rho,\varphi) = \sum_{m,n} w_n^m \, Z_n^m(\rho,\varphi) \tag{6.2}$$

where the phase modulation is,

$$Z_n^m(\rho,\varphi) = \frac{(1+\delta_{m,0})(n+1)}{\pi} R_n^m(\rho) \begin{Bmatrix} cos\, m\varphi & m > 0 \\ sin\, m\varphi & m < 0 \end{Bmatrix} \tag{6.3}$$

the radial polynomial is given by,

$$R_n^m(\rho) = \sum_{k=0}^{(n-m)/2} \frac{(-1)^k (n-1)!}{k!\left(\frac{(n+m)}{2}-k\right)!\left(\frac{(n-m)}{2}-k\right)!} \rho^{n-2k} \tag{6.4}$$

and $0 \le \rho \le 1$, $0 \le \varphi \le 2\pi$, $|m| \le n$, $n - |m|$ is even (98).

Note that this investigation focuses on the finite set of what will be considered the lower-order aberrations (considered here to be $n \le 5$, where n limits

the modulation of the radial component and puts an upper limit to the azimuthal variation in Eq. 6.3 and 6.4) as these are easiest to correct with addressable, adaptive optics such as deformable mirrors or laser correction surgery and are considered in most applications (94) (99) (100) (101) (102). The performance of this limited set of aberrations is shown later to be sufficient for understanding the performance trends of higher-order aberrations ($n > 5$). Alternatively the high-order aberrations may be included as an extension of this work.

An Information Theoretic analysis of the wave-front sensing experiment will determine the fundamental precision limits to be associated with estimation of each Zernike polynomial coefficient when a measurement is made in the presence of noise. This analysis can be used to tease out the mechanisms which limit realizable precision and identify, when possible, areas of further research to improve system performance. The analysis contained herein also reveals whether an optimum configuration, such as the number of micro-lenses, exists and how to find it.

Two typical application scenarios are addressed with numerical simulations to understand how the relationship between design parameters such as the number of micro-lenses will affect performance. First, the available precision is investigated when the full dynamic-range of the detector is utilized. This is named the Dynamic-Range (DR) limited scenario and implies that as the size of the micro-lens array increases, the number of photons in the system will correspondingly increase. The second case addresses the performance limitations of a system with only a finite number of photons, specifically that the total number of photons is conserved regardless of the micro-lens density. This situation is named the Photon-Limited

(PH) scenario. The results for these two extremes of system operation effectively characterize the limiting capabilities of the optical system design.

In Section 6.2 of this chapter, the Fisher Information (FI) metric is re-introduced as applied to investigating estimation and system performance limits for the SHWFS. In Section 6.3, the performance of the SHWFS is analyzed under both the above operating scenarios. Results for non-ideal conditions which the SHWFS may encounter in an adaptive optics setup are provided in Section 6.4. The feasibility of realizing the CRLB with a SHWFS is demonstrated by simulation in Section 6.5. A side-by-side comparison with an alternative technique known as Phase-Retrieval (PR) is evaluated (8) (56) and presented in Section 6.6. A discussion of these results and an outline of some future directions for research are given in Section 6.7.

6.2 Information content of a wave-front

The sensitivity to aberration of a phase-recovery solution will depend on factors including the design of the optical system, limitations of the electronics (e.g. dynamic range, dark-counts, etc.) as well as the implemented estimation algorithm. Of these, only the optical system and the associated electronics are considered here to make fundamental contributions to the realizable precision bounds. The performance using different estimation algorithms can vary greatly and should, in practice, be chosen to accommodate user constraints such as computational power, time, required precision, and sophistication of the algorithm. Therefore, it is argued that in order to determine the performance trade-off of the different system designs,

a careful evaluation should omit the effects of algorithm selection, which can be sub-optimal, and instead seek to determine how sensitive the optical measurement itself can be to the sought-after parameters.

An objective measure which accounts for the information transfer of multi-parameter systems (e.g. the measurement of more-than-one Zernike polynomial) in the presence of noise is the Fisher Information (FI) matrix. Here the incorporation of aberration-related information transfer of the SHWFS into a FI framework is sought. A successful model for the FI will provide a statistical measure which quantifies the amount of knowledge available in the measured optical signal which is useful for estimation of the Zernike polynomial coefficients.

FI analysis has been successfully applied elsewhere in optics to demonstrate the measurement insensitivity/sensitivity to aberrations responsible for extended Depth-of-Field imaging (6) as well as three-dimensional localization-based microscopy (11) (35). In fact, all these aberrations can be associated with the Zernike polynomials $Z_1^{-1}, Z_1^{+1}, Z_2^0$ – aberrations which are responsible for transverse and axial object shift. Analysis of the current wave-front sensing application will require an expansion of this prior work to include a greater number of Zernike polynomials in a different optical system configuration. The application of similar statistical methods to wave-front sensing has been considered previously however these have focused on optimal information extraction instead of quantifying performance limitations (73).

The diagonal values of the FI matrix quantify the degree of influence a particular Zernike aberration mode will have on the final measurement, here an

image formed by a micro-lens array, as shown in Fig. 6.1. Aberrations which have greater impact on the image will have higher FI. This information matrix is found from,

$$FI(\theta_{i,j}) = \sum_{u=1}^{U}\sum_{v=1}^{V}\frac{1}{p(u,v)}\frac{\partial}{\partial\theta_i}p(u,v;\boldsymbol{w})\frac{\partial}{\partial\theta_j}p(u,v;\boldsymbol{w}) \tag{6.5}$$

where this form has assumed ideal imaging conditions (i.e that the random variation of the signal can be described as a Poisson process from photon-counting noise) (73). θ_i and θ_j are elements from the set of parameters to be measured, here $\theta \in \{Z_n^m; n \leq 5, |m| \leq n, n-|m| \; is \; even\}$, $p(u,v;\boldsymbol{w})$ is the signal and $\boldsymbol{w}$ is the vector of Zernike polynomial coefficients describing the pupil function of the optical system. Note the i^{th} index is used here as a unique identification for each Z_n^m. U,V are the number of pixels along the horizontal and vertical axes of the detector plane which incorporates the signal from the entire micro-lens array. The individual pixels are each considered as independent measurements (i.e. the noise is not correlated) and therefore add linearly to the FI of the system. Off-diagonal terms capture the correlated influence of the Zernike polynomials. Omission of the Zernike polynomials with $n \geq 6$ assumes that these aberrations are identically zero. Note that this is not overly restrictive because the dominant phase terms for applications in adaptive optics can, in some cases, be reduced to a finite set of lower-order aberrations with the higher-order terms deemed insignificant (94) (102). If however, higher-order aberrations are present, significant and unaccounted for this can lead to different CRLB performance as investigated in Appendix 6A.

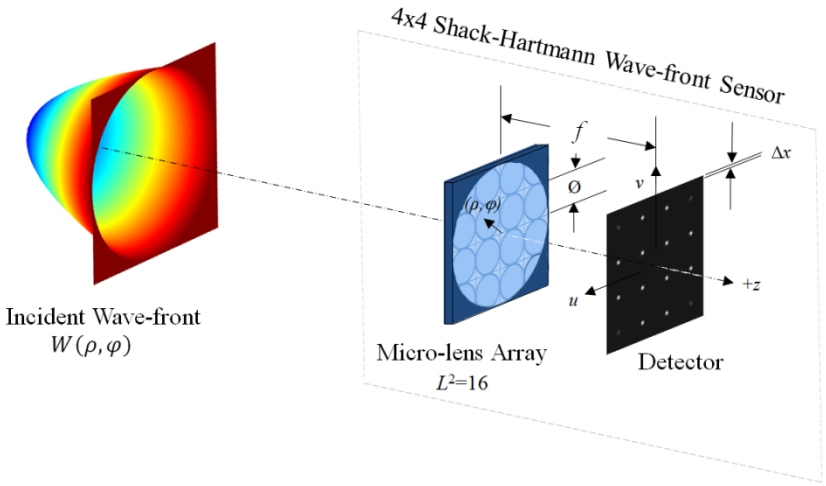

Fig. 6.1: The imaging system for a Shack-Hartmann Wave-front Sensor (SHWFS). An incident wave-front is sampled with micro-lenses distributed spatially in the transverse dimension. The resulting image can be used to estimate the incident amplitude/phase profile.

Image formation for an individual lens is modeled as,

$$p(u, v; \boldsymbol{w}) \propto \left| \mathfrak{F}\left\{ e^{i\frac{2\pi}{\lambda}W(\rho,\theta)} \right\} \right|^2 \tag{6.6}$$

where (u, v) is the coordinate system of the detector and $\mathfrak{F}$ is the two-dimensional Fourier transform. For a micro-lens array size of *LxL* lenses, this incident wave-front is sub-divided accordingly and each micro-lens forms an image from the sub-sampled optical pupil. The ensemble of these sub-images is then used in Eq. 6.5.

The FI provides additional insight because of its inverse relationship with the bound on achievable precision, known as the Cramer-Rao Lower Bound (CRLB) (33). The CRLB is a fundamental quantity and when given knowledge of the noise processes in the system is used to quantify the lower limit on the system estimation precision (given as a variance) for the parameter set θ. Therefore use of the CRLB allows for precise statements to be made about the comparison of optical

performance between different systems. The form presented here assumes only that an unbiased estimation algorithm be used. The CRLB is the inverse of the Fisher Information matrix,

$$CRLB(\theta) = FI^{-1}(\theta) \tag{6.7}$$

where the elements of FI are given in Eq. 6.5 and the lower bound for each Zernike polynomial is given by the diagonal values of this matrix. The square root of the CRLB provides the lower-bound of the standard deviation for each estimated parameter (e.g. the coefficient estimation error of each Zernike polynomial) and this quantity will be quoted throughout the rest of the chapter.

6.3 Phase recovery from Shack-Hartmann Wave-front Sensors

FI analysis is applied to the SHWFS in order to understand how performance will scale with the micro-lens array density. A model SHWFS system is shown in Fig. 6.1, where an incident wave-front is divided into L^2 non-overlapping samples. The most common algorithms for recovering phase information from SHWFS data have focused on treating the non-overlapping sampling as a piece-wise linear approximation to the incident field and to then measure the transverse shift of the PSF image in order to calculate the local tip/tilt and reconstruct the wave-front (97) (103). However, it is well documented that optical aberrations other than tip/tilt will influence the image, here the PSF of a micro-lens, but often these higher-order modes are ignored in computational algorithms (73) (97). To reinforce this, a pyramid of the images resulting from each additional aberration is presented in Fig. 6.2, shown for the complete set $\theta \in \{Z_n^m; n \leq 3, |m| \leq n, n - |m| \; is \; even\}$. It is therefore

observed that an opportunity exists for additional information extraction if the proper algorithm existed. This is one justification for why a strict comparison of system designs must exclude the particular estimation algorithm implementation.

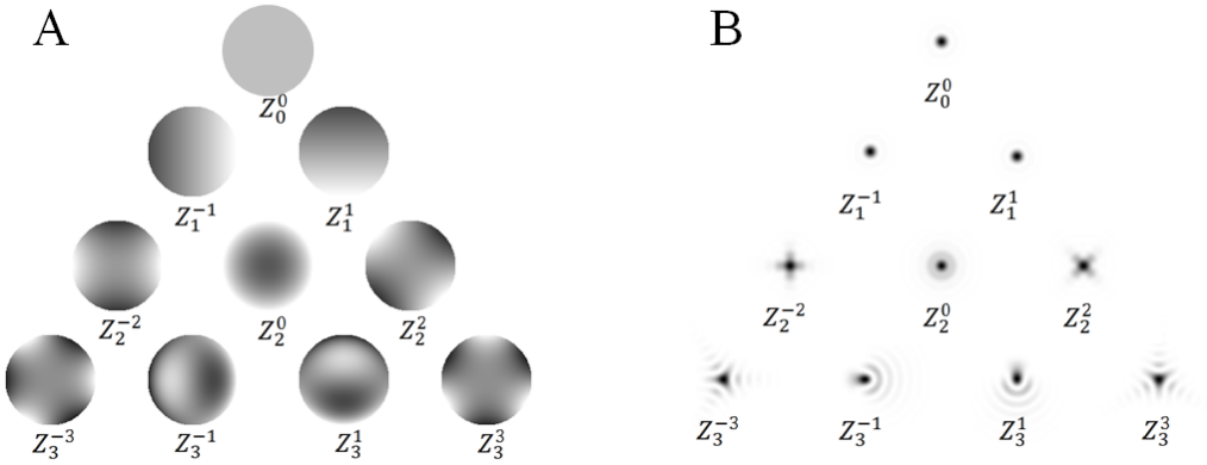

Fig. 6.2: The first ten Zernike polynomials ($n \leq 3, |m| \leq n, n - |m|$ *is even*) are shown in panel A. The associated PSF for a quarter-wave amplitude aberration is shown for each aberration of a clear, circular aperture in panel B.

The SHWFS is considered here as an increase in the array size of lenses (with the numerical aperture of each lens held fixed), L^2, which transversely sample the wave-front. The diameter of each aperture is fixed at $\varnothing = 300\mu m$, with a micro-lens NA = 0.03, and the total area of the sensor will scale accordingly with larger micro-lens array densities. The physical dimensions of the micro-lens array and camera simulated here are selected to be consistent with what will be easily realizable for practical systems. The unknown field incident to the SHWFS is assumed to be band-limited with an associated Nyquist sampling period in the detector plane of $5.3x5.3\mu m$ when given the micro-lens parameters above. This field is sampled in the far-field with a $5x5\mu m$ pixel pitch detector in the simulation -

slightly greater than Nyquist sampling. Since the choice of pixel size can be arbitrary, the dependence of estimation performance versus sampling period was investigated in Appendix 6B. There it is demonstrated that the CRLB-related estimation error will scale an increased/decreased amount as the signal is sampled at a decreased/increased rate and therefore all trends established at a $\Delta x = 5\mu m$ pixel pitch will be applicable within the investigated range of $0.5x$ to $2x$ the Nyquist sampling period. Monochromatic illumination is assumed ($\lambda = 633nm$) and the images are simulated with an 8-bit detector. Uniform illumination is also assumed across the transverse dimension of the pupil.

Because most adaptive optics applications attempt to reach a steady-state performance which corrects all input aberrations to be nulled, an incident plane-wave is assumed to quantify the characteristics of this idealized design state. The DR-limited performance is given in Fig. 6.3 where the number of photons collected is scaled for each micro-lens array size to match the dynamic range of the sensor. Note that as documented in prior literature, a single, focused image from one lens is relatively insensitive to particular Zernike modes (35) (e.g. defocus from depth-of-focus invariance of a standard PSF) but that increasing the sampling density from $L = 1$ to $L = 2$ will rapidly improve the estimation precision for these modes. However, further increases in the micro-lens array density are seen to yield little improvement and approach an asymptotic value. This statement is analyzed using separate arguments in Appendix 6C to independently support the conclusions of this simulation analysis. An understanding of this behavior is provided from the observation that given a fixed aberration at the entrance to the LxL array and as the

array size is increased, each micro-lens will witness a smaller total aberration. Perfectly balancing this loss of local sensitivity is the increase in the signal due to the additional micro-lenses across the aperture using the full camera dynamic-range. Together, these effects are coordinated such that as L increases, an asymptotic, non-zero limit is reached.

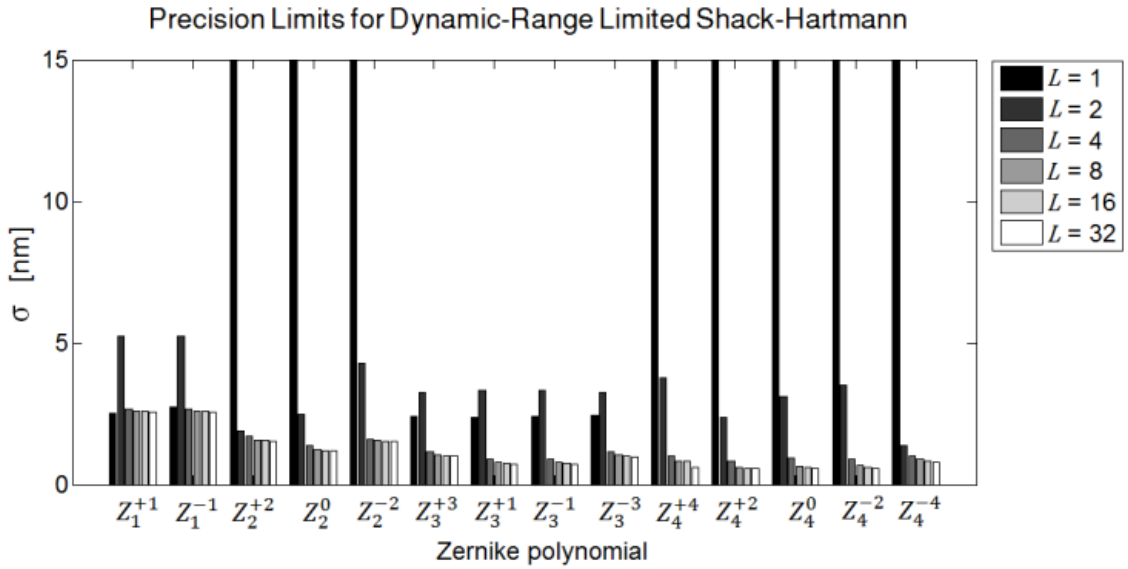

Fig. 6.3: The CRLB limited wave-front precision for the first 14 Zernike polynomials using the SHWFS dynamic-range limited geometry. As the sampling density of the wave-front is increased, $\boldsymbol{L^2}$, the precision of the wave-front estimation for each aberration polynomial approaches an asymptotic limit.

This observation indicates that with the implementation of an efficient, unbiased estimation algorithm, similar precision results can be realized with fewer micro-lenses. It is anticipated that current estimation algorithms may be tolerant to this diminishing return because they apply an approximation that only linear phase aberrations are present at each micro-lens. This piece-wise linear approximation to the incident wave-front will result in increased reconstruction errors for systems with low micro-lens density (97). However increasing the micro-lens density to

compensate for inefficient estimation algorithms is unacceptable for the photon-limited scenario because, as will be demonstrated next, an optimum micro-lens density does exist. These implications are also relevant because a smaller array of high-quality micro-lenses will typically have higher fabrication yields than larger arrays of high-quality micro-lenses. This may result in decreased costs and/or more ideal performance per micro-lens.

The CRLB precision limits for the photon-limited (PH) SHWFS are given in Fig. 6.4 for each of the first 14 Zernike polynomials ($n \leq 4$). In this scenario the signal is limited to P total photons, which is determined by the maximum number of photons in a dynamic-range limited image from an individual micro-lens (L=1). Again, the character of this performance is uniquely interesting because it does not reach an asymptotic limit but instead depends on the number of micro-lenses L^2.

Comparison of the two limits (dynamic-range vs. photon-limited) is evaluated by using the average estimation precision of each case,

$$\sigma_{avg}(K) \equiv \frac{1}{T}\sum_{j=1}^{T} \sigma_{\theta_j}(K) \tag{6.8}$$

where $T = 14$ is the total number of Zernike polynomials. For the PH-case an optimal SHWFS can be defined for average wave-front performance from the minimum seen to exist between the limits of $1 \leq L \leq 32$ in Fig. 6.4. Here, the optimum number of micro-lenses is $L = 4$ with $\sigma_{avg}^{PH}(L = 4) = 5.4nm,$ found when estimating the set of Zernike polynomials with $n \leq 4$. This performance is justified again in Appendix 6C to separately verify the scaling behavior with respect to L.

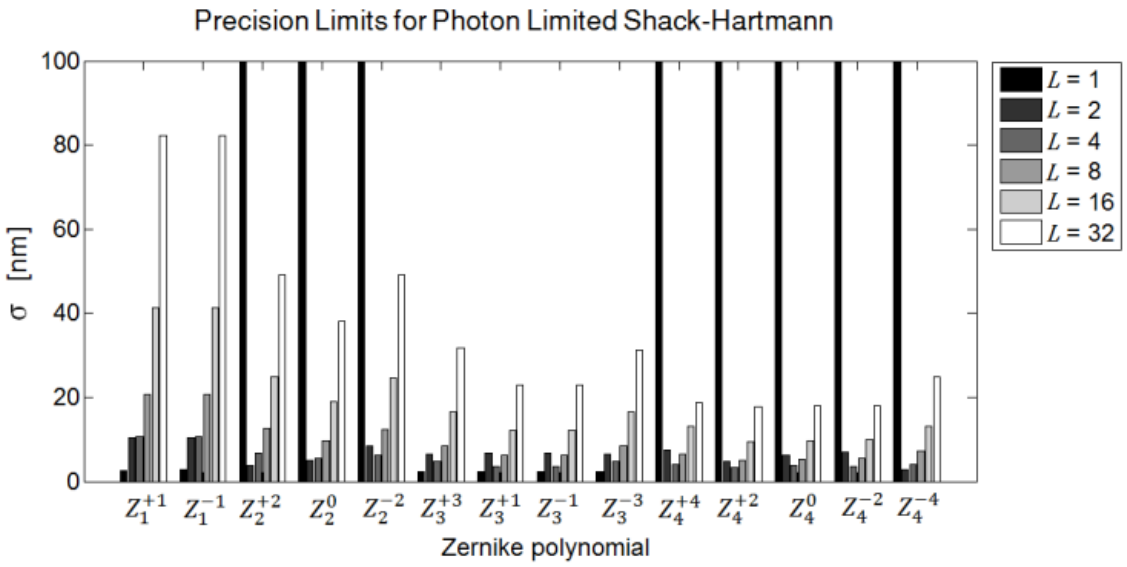

Fig. 6.4: The CRLB limited wave-front precision for the first 14 Zernike polynomials in a photon-limited SHWFS configuration. As the number of micro-lenses increases past a critical value, the precision declines. An optimum performance is seen to exist at $L = 4$.

Further examination reveals that the photon-limited SHWFS optimum at $L = 4$ can be attributed to the maximum spatial modulation of the Zernike phase functions present and to be estimated. Fig. 6.5 presents the average SHWFS performance, σ_{avg}, for both the DR and PH cases (panel A and B, respectively) as the number of micro-lenses is increased. The index n is associated with the radial component of the Zernike polynomial given in Eq. 6.4 - acting to limit both the radial and azimuthal spatial modulation frequency. In the simulation, as n is increased, m takes all allowed values such that the total number of polynomials being present and to be estimated will be increasing. For the DR limited scenario, performance similar to Fig. 6.3 is observed but here the rate at which the system approaches asymptotic performance is shown to depend on the frequency of spatial modulation for the polynomials being estimated. In summary, the higher the spatial

modulation frequency, the more micro-lenses it will take to reach the asymptotic value. This statement is consistent with requiring a minimum sampling frequency for signal reconstruction. A similar trend is associated with the PH scenario where the optimum number of micro-lenses is shown to scale with the spatial modulation of the Zernike polynomials. Again, as the spatial-frequency modulation of the incident aberration increases, the optimum density of micro-lenses for the photon-limited scenario will increase accordingly.

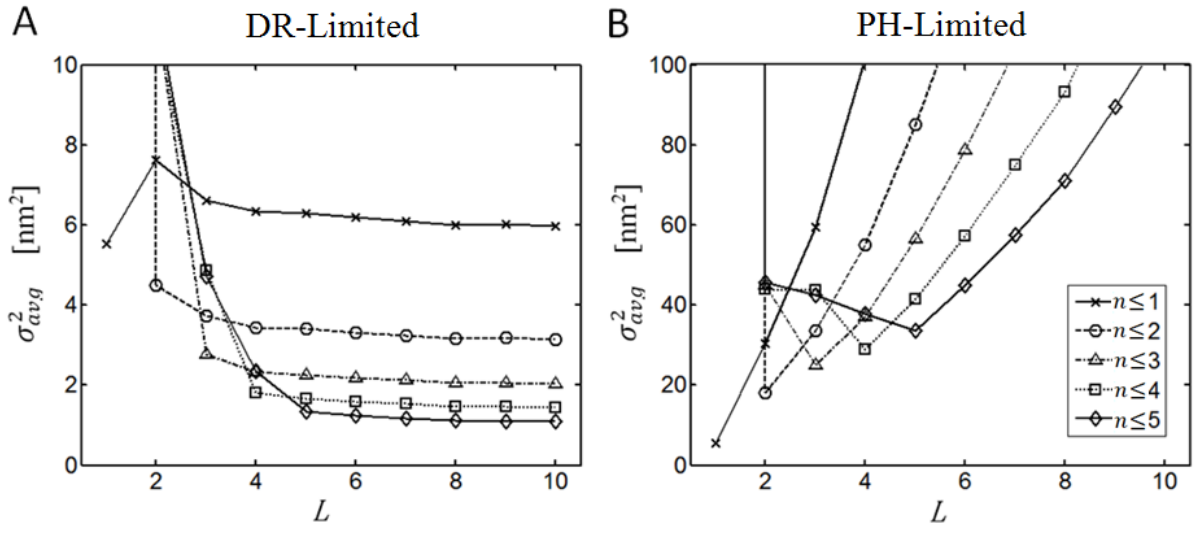

Fig. 6.5: The average performance bounds of the SHWFS are shown as the number of micro-lenses in the array, L, is increased for the DR (panel A) and PH (panel B) scenarios. The performance is reported as estimator variance to aid in visual clarity. For both the dynamic-range and photon limited cases, the performance varies depending on the number of Zernike polynomials present and to be estimated, given by the maximum order of the radial coeffient n.

6.4 CRLB of SHWFS for Random Input Aberrations

The performance limits of a non-ideal wave-front sensing state (i.e. a wavefront different from a plane wave) are now investigated to verify that the prior observations are useful under alternative circumstances. Non-ideal wave-front

sensing states are meant to address the uncorrected wave-front which is invariably present at the start of an adaptive optic feedback algorithm. This case also arrises in application of SHWFS to uncorrected optical systems for manufacturing and measuring aberrations of the human eye. To test this, the CRLB performance is found as above but now with ten random samplings of Zernike aberration coefficients taken to represent incident wave-fronts instead of assuming a planar wave-front. The Zernike aberration coefficients were randomly selected from a uniform distribution limited by $-\lambda \leq w_n^m < \lambda$. In general, similar trends to those reported earlier are observed in Fig. 6.6 – except with the optimum micro-lens density potentially shifted upwards.

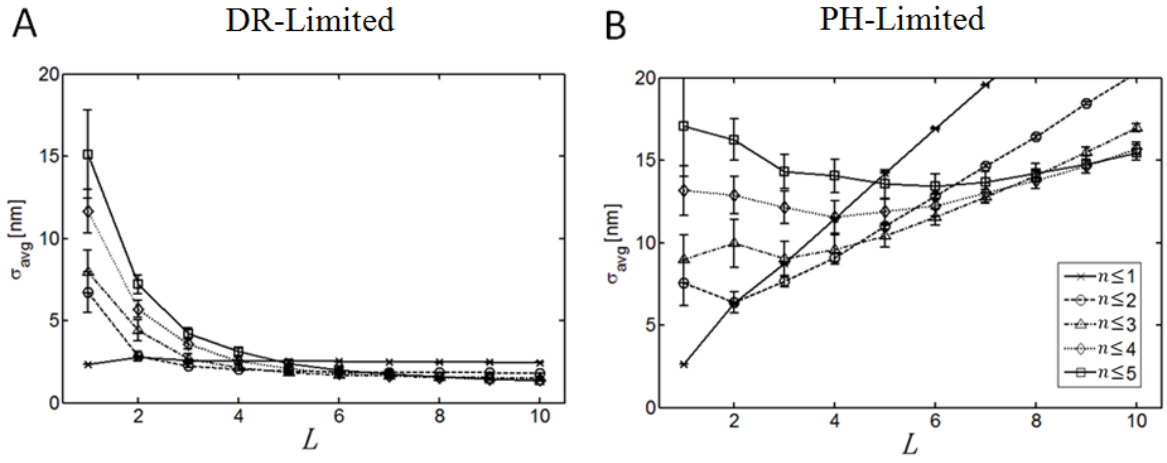

Fig. 6.6: Average CRLB results for random input wave-fronts as a function of the number of micro-lenses. The input wave-front is allowed to have random aberrations for all Zernike polynomials limited by n of each line-series. The dynamic range limited performance is given in Panel A, the photon-limited performance in panel B.

Less significant variation of the average CRLB is present with higher density micro-lens arrays because the input wave-front becomes better approximated by similar looking patterns (e.g. translated Airy patterns) across the array. The lower

density micro-lens arrays will see more variation in the individual PSFs of the micro-lens which leads to the greater variability of performance. One random input wave-front is taken from the simulation of Fig. 6.6 where $n \leq 5, |m| \leq n, n - |m|$ *is even* and presented in Fig. 6.7 to visualize what example phase aberrations are present at the input (panels A and B) of the SHWFS and what the associated image will look like (panel C). It is apparent in panel B that the micro-lens density of 8x8 does not always sample the wave-front at a fine enough frequency in order to accurately approximate the phase at each lens as purely a linear phase. The resulting image consists of individual PSFs which may not be well-approximated by a translated Airy disk. Note that the contrast was adjusted in panel C to aid in visualization by presenting the amplitude of the field in the detector plane rather than the intensity.

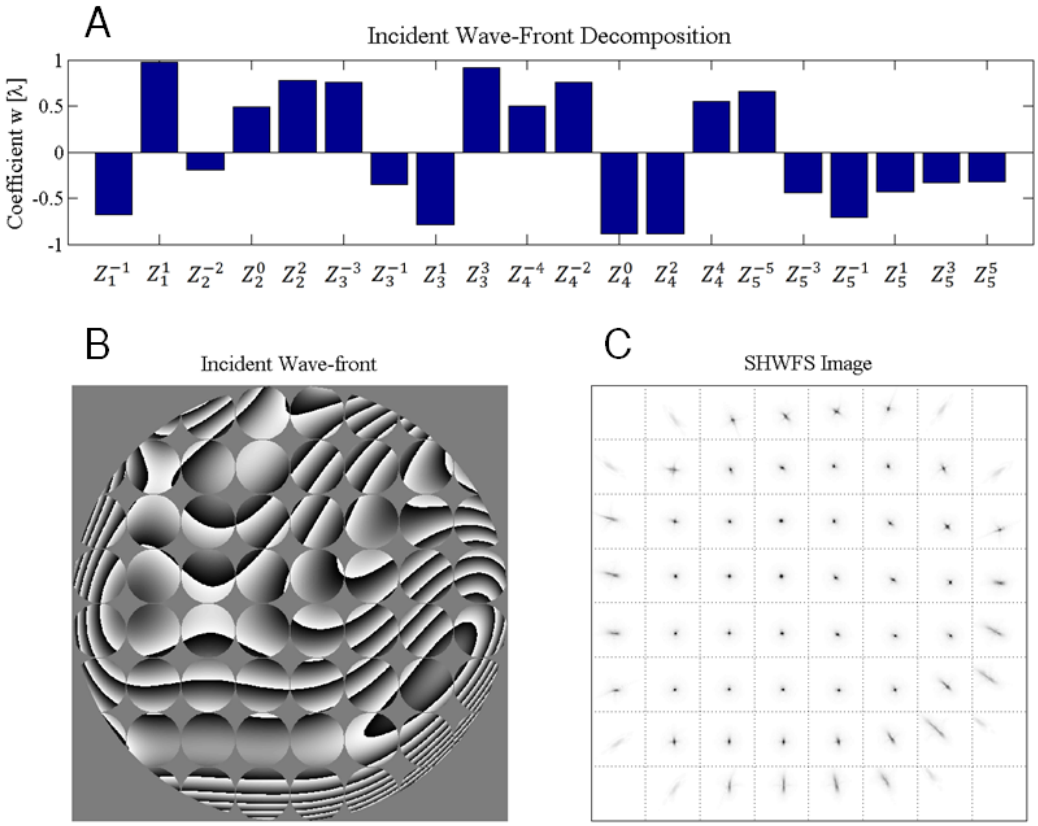

Fig. 6.7: One example of the random input wave-fronts with $n \leq 5$ used in the simulation is given in panel A in terms of the coefficients of the Zernike polynomials. This wave-front is shown in panel B when input to an 8x8 micro-lens array where each micro-lens has a circular aperture. The resulting field in the image plane is given in panel C.

6.5 Simulated Verification of CRLB

To demonstrate that the inclusion of higher-order aberration terms into an estimation algorithm can yield estimator performance similar to the CRLB and therefore realize the trends discussed above, a multi-parameter direct search algorithm (104) is implemented on a simulated SHWFS system where the micro-lens density is limited to the regime with most performance variation, $1 \leq L \leq 5$. The flowchart associated with this algorithm is provided in Fig. 6.8. For each micro-lens

array size, the direct-search algorithm simulates the signal from a shot noise limited system and implements a grid-based search in order to find the aberrations which minimize a Poisson cost function. Two-hundred noisy images were simulated for each array size.

To reduce computational complexity and aid in visualization, only the results for estimation of the Zernike terms $n \leq 2, |m| \leq n, n - |m| \; is \; even$ are presented in Fig. 6.9, for both the dynamic-range and photon limited scenarios. The top panels show the CRLB performance of each Zernike polynomial as the size of the micro-lens array is increased. The bottom panels show the direct-search estimation results from the simulated images. One failure is noted in that the direct-search algorithm seems to have a false precision estimate for parameters to which the image is invariant – here the terms associated with $n = 2$ when $L = 1$. This failure is due to insensitivity of the search algorithm to these parameters and therefore any search along these dimensions will not be explored (the direct-search algorithm searches near an initial guess and finds the step direction which minimizes the cost function – if no benefit to the cost function is found then steps along invariant dimensions will not be explored). It is shown here that the same trends reported earlier are observable in the Direct-Search estimation results and also that the fundamental precision limit can be realized for SHWFS systems through the inclusion of higher-order aberration terms to the image processing algorithm.

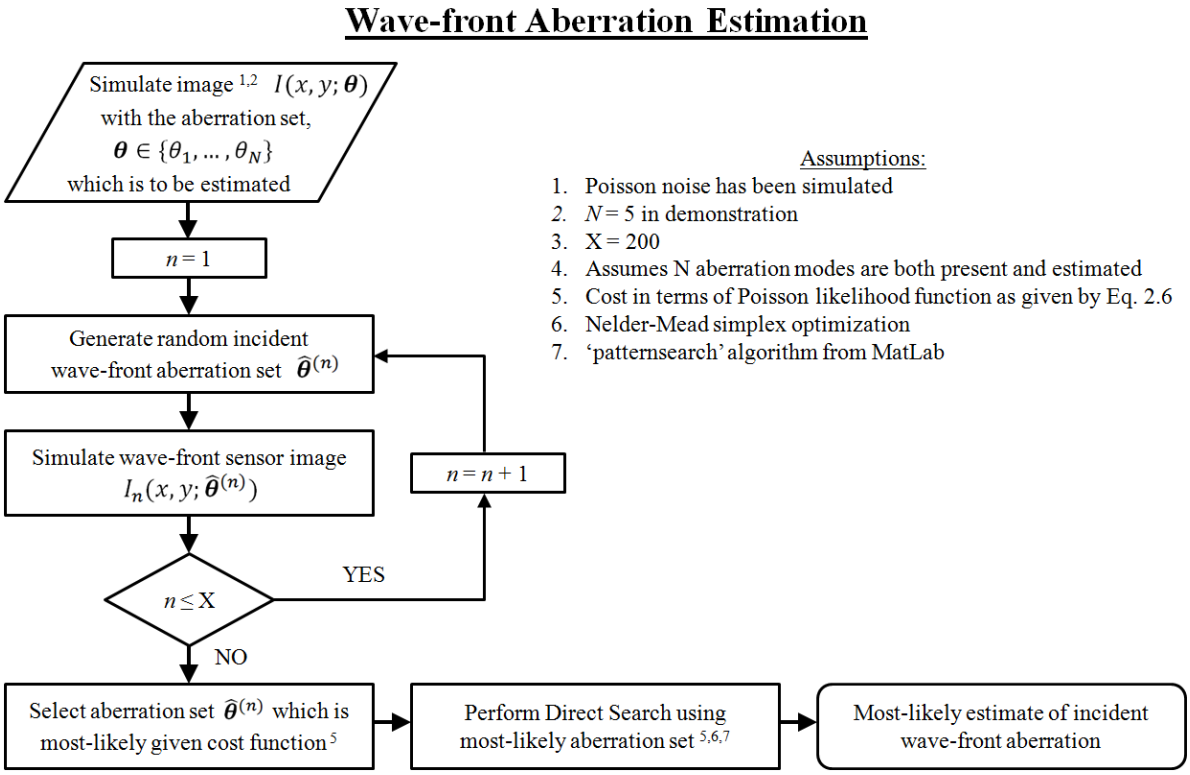

Fig. 6.8: Algorithm flowchart for estimating the incident wave-front to a SHWFS array. The algorithm begins with a random number of wave-front guesses and picks that which possesses the best fitness for further iterative evaluation. Note that local assumptions of incident linear phase are never applied to any micro-lens and instead the complete wave-front with all local variation is included.

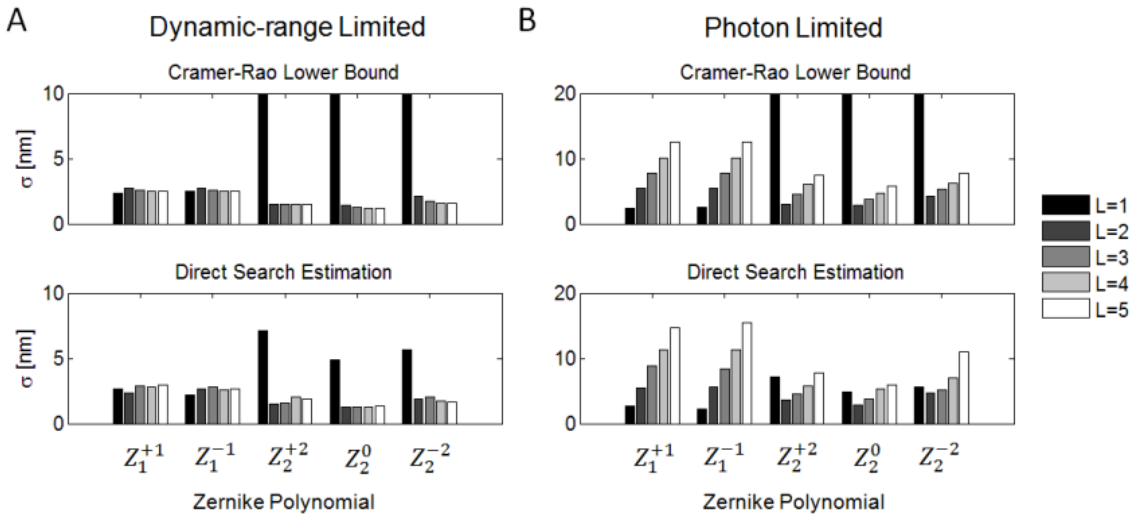

Fig. 6.9: The dynamic-range (panel A) and photon- (panel B) limited performance given by the CRLB (top row) and from simulated estimation results when given Poisson noise limited images (bottom row). The results are tracked as the number of micro-lenses increases with L. The estimation results are seen to closely track the CRLB performance for each of the Zernike polynomials. The exception is for estimation of the $\boldsymbol{n} = \mathbf{2}$ Zernike polynomials with a single lens, L=1.

6.6 Comparison of SHWFS and Phase-Retrieval methods

An alternative but common phase-recovery method is investigated to give an idea of the relative merits of either technique. We identify the Phase-Retrieval (PR) technique as a particularly relevant comparison since the optical system is degenerate with a SHWFS when only one micro-lens is assumed. Key, however, to the PR technique is the use of one or more images located at different axial planes in the far-field. Shown in Fig. 6.10, this technique uses multiple, axially-displaced images, and places assumptions on the band-limit of the signal in order to measure the amplitude and phase modulations of large telescopes, high numerical aperture

microscopes and phase/amplitude objects (8) (55) (56) (57) (89) (105) (106). Some algorithms, such as the Gerschberg-Saxon or Fienup (8), will iteratively solve for the amplitude/phase function. On the other hand, alternative implementations, such as the Transport-of-Intensity Equation (TIE) are available to solve for the phase function directly (57) (106). An important characteristic of the PR method is that under proper constraints, the solution can be guaranteed to converge and be unique.

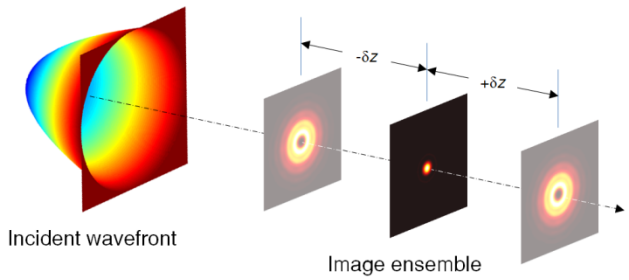

Fig. 6.10: Signal formation model for Phase-Retrieval algorithm. An incident wavefront is measured in the far-field by one or more image planes to make up an ensemble used later for processing. The defocused images are shown with a defocus of $\boldsymbol{w_2^0 = \pm 0.5\lambda}$.

Image formation in the PR system is modeled by,

$$p_k(u, v; \boldsymbol{w}) \propto \left| \Im \left\{ e^{i\frac{2\pi}{\lambda} \Sigma_m \Sigma_n w_n^m Z_n^m} \right\} \right|^2 \tag{6.9}$$

where k denotes the k^{th} image of the ensemble. Axial translation from the focal plane is simulated by increasing the coefficient of the Z_2^0 polynomial which is associated with defocus. If multiple image planes are used $(k > 1)$, the axial translation is arbitrarily chosen to be of uniform intervals between $-0.5\lambda \leq w_2^0 \leq +0.5\lambda$.

The FI of the PR system, comprising a total of K images in the ensemble is,

$$FI(\theta_{i,j}) = \sum_{k=1}^{K}\sum_{m=1}^{M}\sum_{n=1}^{N}\frac{1}{p_k(m,n)}\frac{\partial}{\partial\theta_i}p_k(m,n;\boldsymbol{w})\frac{\partial}{\partial\theta_j}p_k(m,n;\boldsymbol{w}) \quad (6.10)$$

where the only change from Eq. 6.5 is that a summation is taken over all K images. As in the case of individual pixels, each image is considered a random, independent measurement and therefore adds to the total FI. In all simulations, the incident field is assumed to be a perfectly planar wave-front and it is the deviations from this ideal that are to be measured.

The estimation precision limits (CRLB) of the Zernike polynomials for the case of a DR limited measurement are given in Fig. 6.11 as a function of the size of the image ensemble, K. The precision limit of the wave-front coefficient estimation error, $\sigma(nm)$, for each Zernike polynomial approaches zero as the number of images increase. This can be understood by associating the number of images with the total signal available for estimation. In the PR method, an increase in the number of images results in a directly proportional increase in the signal. As opposed to the SHWFS scenario, the wave-front is never divided into smaller samples and therefore the sensitivity never decreases per image. In these simulations, a scaling law dependence is observed to go approximately as $K^{-0.5}$. The significant improvement of precision noticed at $K = 2$ is again due to the loss of invariance to aberrations such as defocus and typical for a single lens.

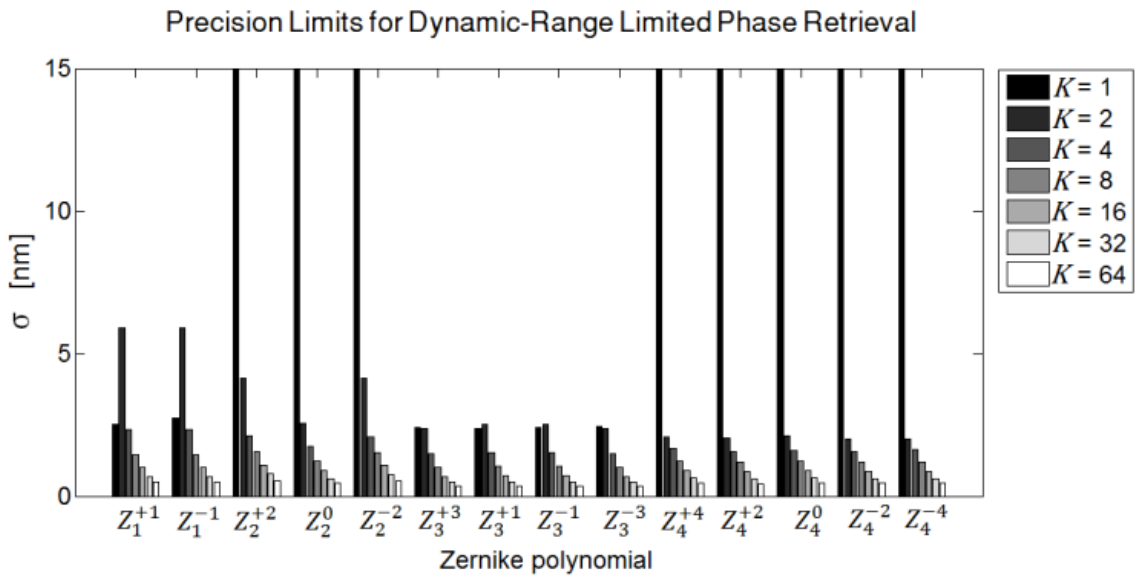

Fig. 6.11: The CRLB limited wave-front precision for the first 14 Zernike polynomials of the PR, dynamic-range limited system. The precision improves as the number of images, K, in increased.

Justification of this CRLB performance with respect to K is given in Appendix 6D, where it is shown under the weak assumptions that the K^{th} image contain finite energy and that its derivative with respect to an aberration mode is non-zero that the FI will increase indefinitely, yielding a diminishing estimation error.

An examination of the PH scenario reveals significantly different characteristics. We analyze the CRLB for the case of P total photons, determined by the dynamic-range limited single-image. These P photons are evenly distributed across the ensemble of K measurements. The resulting performance, shown in Fig. 6.12, demonstrates that as K increases, the gains in performance rapidly diminish until an asymptotic limit is reached for the measurement precision, independent of K.

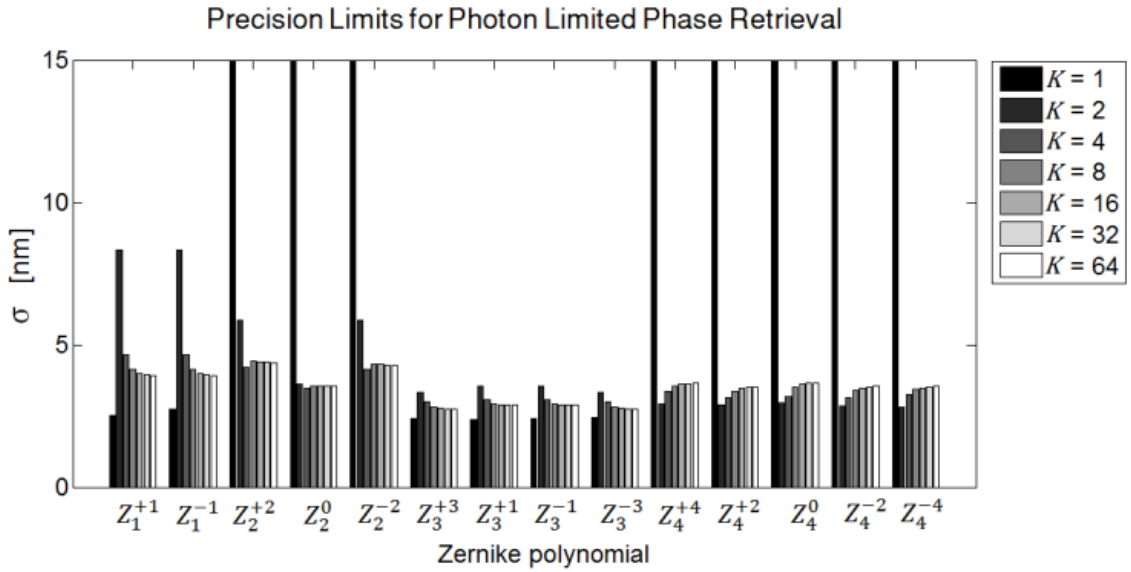

Fig. 6.12: The CRLB limited wave-front precision for the first 14 Zernike polynomials of the PR, photon-limited system. The precision approaches a constant value as the number of image planes, K, increases.

Comparison of the two limits (dynamic-range vs. photon-conserved) is again evaluated by the average estimation precision of each case. This comparison reveals that the photon-limited performance of $lim_{K\to\infty}\sigma_{avg}^{PH} = 3.5nm$ diverges from the dynamic-range limited performance after only 2 image planes are used $(\sigma_{avg}^{DR}(K = 2) = 3.0nm)$.

Having systematically characterized the SHWFS and PR and wave-front sensing techniques according the CRLB of Zernike polynomial estimation, a definitive comparison between the two is now possible. Fig. 6.13 and 6.14 compare the average wave-front precision from estimating the first 14 Zernike polynomials $(n \le 4, |m| \le n, n - |m| \; is \; even)$ in the dynamic-range limiting and photon-limited scenarios, σ_{avg}^{DR} and σ_{avg}^{PH}, respectively. This comparison is significant because it serves to reveal the relative limits which may be approached as one reaches the

manufacturing tolerances of micro-lenses and must evaluate the trade-off to a PR system. In other words, when limited by manufacturing tolerances to a particular NA for a micro-lens, what is the SHWFS performance relative to a PR method using the same lens characteristics?

In Fig. 6.13, the asymptotic, DR limited SHWFS is seen to provide an improved precision, relative to the PR method, if $K \leq 9$. If greater than 9 PR images are available, the PR method can out-perform the SHWFS regardless of micro-lens array density.

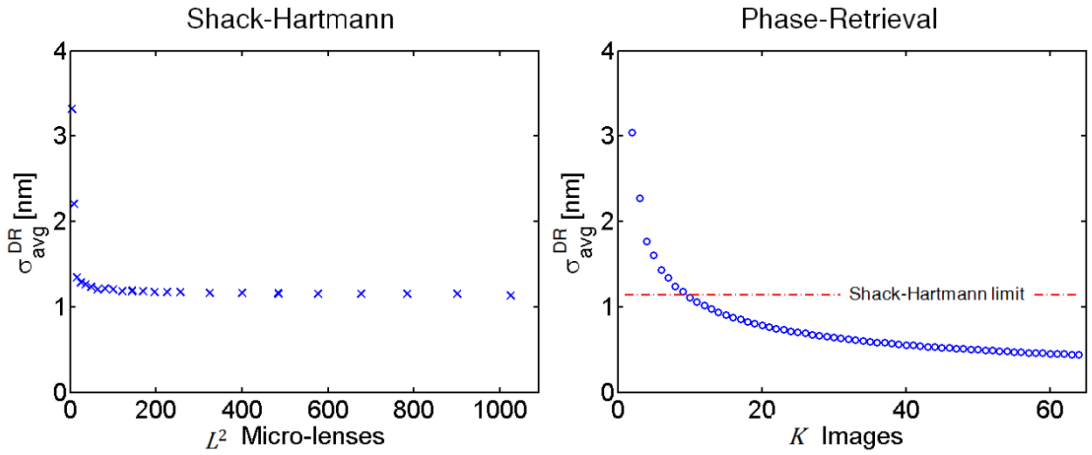

Fig. 6.13: Comparison of the average CRLB limited wave-front precision for both the SHWFS and the PR technique when the systems are dynamic range limited. The asymptotic value of the SH-WFS outperforms the PR method if the number of PR image planes is less than 10.

In Fig. 6.14, the average precision of the two methods is compared for the PL scenario. It is seen that the SHWFS is unable to perform better than the PR technique for any K. The bend of the SHWFS precision curve discussed earlier is easily identified and shows that the optimum L for the micro-lens array is 4 given the photon-conserved scenario and estimation of Zernike polynomials of order $n \leq 4$.

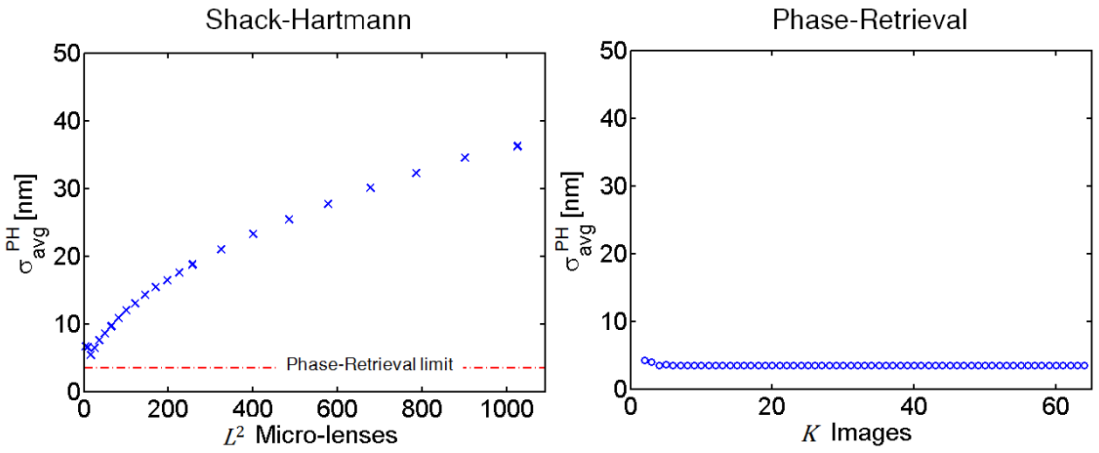

Fig. 6.14: Comparison of the average CRLB limited wave-front precision for both the SHWFS and the PR techniques when the number of collected photons is conserved. The PR method always out-performs the SH-WFS. However, if one chooses to use a SH-WFS, an optimum number of micro-lenses exists for the best precision.

6.7 Discussion

The application of information theoretic tools such as Fisher Information and the Cramer-Rao Lower Bound has demonstrated utility for the selection of wave-front sensing options. While work has focused on the optimal estimation of linear tip/tilt phase at each micro-lens of the SHWFS (73) (103), the incorporation of higher-order modes into the estimation/image-processing algorithm is needed in order to optimally extract all wave-front information when using lower density micro-lens arrays. As demonstrated for the photon-limited scenario, the optimum performance is at low micro-lens density and therefore those algorithms will have immediate application.

The most salient point is the surprising potential sensitivity of the SHWFS with fewer micro-lenses. To improve system performance along these lines, work on

higher-order estimation algorithms and implementing specialized micro-lens arrays which highlight particular aberrations would be an area of promising research (107). One particular proposal has identified the benefit of using additional aberrations for wave-front sensing, specifically those associated with astigmatism, and developed a modified SHWFS geometry optimized to increase the computational efficiency for extracting these higher-order modes (107). Additionally, when characteristics of the complete adaptive optical system are included, such as the use of bi-morph mirrors, it may turn out that the linear tip/tilt is not as useful of a measurement as local curvature (108). Therefore, we propose that the design of specialized micro-lens arrays be thought as a form of task-based sensing – where the systems are optimized to sense a particular number of phase aberrations. Given the recent successes of the task-based sensing/imaging paradigm, it may be reasonable to conclude that using these tools, further improvements may be found for the SHWFS – a proposal which is investigated next in Chapter 7.

This analysis has ignored any measurement to address the spatial modulation of intensity profiles other than uniform. This was a simplification to aid in the analysis – however it ignores an important practical constraint. For the scenario when the illumination cannot be considered uniform across the pupil, the possibility exists for further important trade-offs between the SHWFS and PR methods. In addition, the SHWFS may have a different optimal micro-lens density – for example, one which is related to the expected spatial frequency modulations of the intensity profile.

6.8 Conclusions

The relative trade-offs of the PR and SHWFS phase recovery techniques have been established. Most surprisingly, the SHWFS has asymptotic behavior which acts to limit the available precision while the PR technique is limited only by the number of images used under the dynamic-range limited scenario. A method was presented for choosing the best design for a SHWFS when given particular constraints such as a fixed signal level or a finite number of Zernike aberrations. The CRLB limits and performance curves were matched with a Direct-Search algorithm which did not place a constraint of linear phase at each micro-lens and instead accounted for all possible aberrations at the wave-front sensor input. A discussion accompanied this analysis which introduced steps towards improving the SHWFS design from an information theoretic perspective.

6.9 Appendix A: Lower-Order Aberration Estimation in the Presence of Higher-Order Nuisance Aberrations

The CRLB values reported in the main text for $n \leq N_{max}$, where N_{max} limits the maximum radial spatial frequency modulation, had required the assumption that any higher-order aberration modes ($n > N_{max}$) were identically zero. Although this may be an appropriately approximate solution for some applications (94) (102), an investigation is undertaken here in an attempt to gain insight into how relevant the

presence of higher-order, nuisance aberrations are when only lower-order aberrations are to be estimated.

Prior investigation had predicted that if these nuisance aberrations are present, the statistics of the wave-front coefficients are important for considering the impact on CRLB (73). The statistics used here assume that the set of wave-front coefficients are random processes described by a uniform distribution between $-\lambda \leq w_n^m < \lambda$. Ten random instances of the set of coefficients for Zernike polynomial aberrations with $n \leq 5, |m| \leq n, n - |m| \; is \; even$ are simulated. One example instance was shown earlier in Fig. 6.7. The results of the numerical investigation are shown in Fig. 6.15 and present different behavior than that reported in Fig. 6.6. The performance of these curves is dominated by the maximum radial spatial frequency term (here $n = 5$) of the nuisance aberrations which can be verified by examination of the $n \leq 5$ curve in Fig. 6.6.

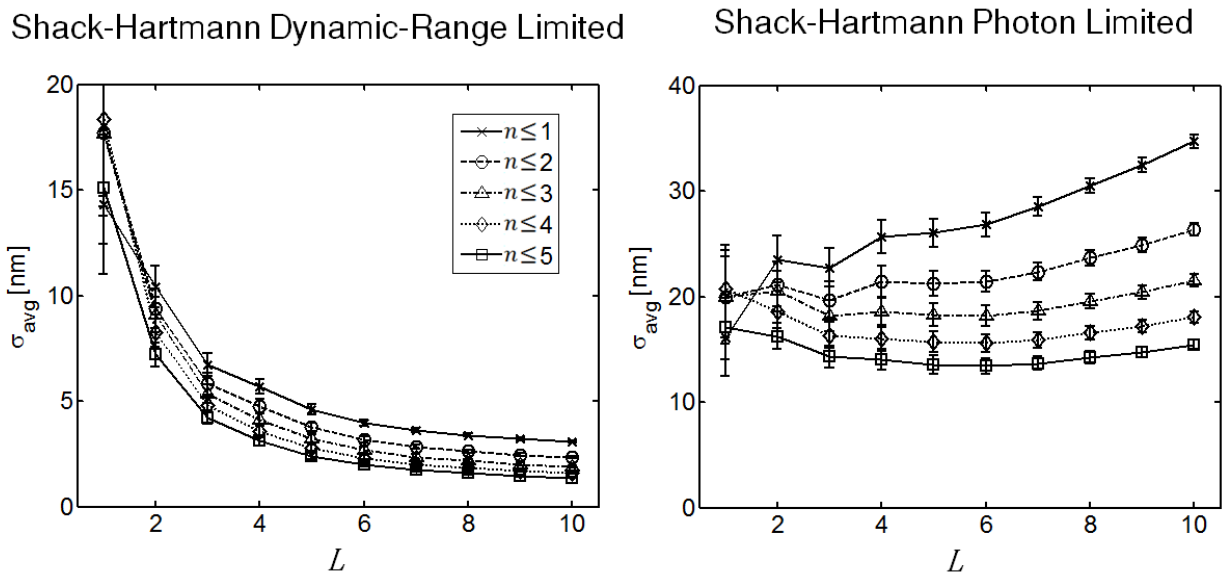

Fig. 6.15: The SHWFS CRLB performance is shown when estimating lower-order aberrations in the presence of nuisance aberrations. The number of Zernike coefficients to be estimated is limited by n for each line series of each plot. The maximum radial spatial frequency modulation of the nuisance aberrations in each scenario is limited by $n \leq 5$.

6.10 Appendix B: SHWFS Performance Bound versus Pixel Size

The trends reported for the SHWFS in the main text are supported by the insight provided in Appendix 6C and 6D as well as the simulated estimator performance presented in Section 6.5. However, the remaining question regarding fundamental performance bounds as a function of the camera pixel size and therefore the PSF sampling rate must be addressed. According to the work of Appendix 6C and 6D, the expected behavior should follow similar trends but at a different scale – uniquely given by the respective CRLB inherent to a single lens. This is now verified by computation of the CRLB as a function of different pixel sizes – assuming a fill-factor of unity. The chosen pixel sizes (2.5μm, 5.0μm and 10.0μm) are associated with Nyquist sampling the intensity PSF at a rate of 0.53x, 1.06x and

2.11x. The results are presented in Figure 6.16, demonstrating that the CRLB behavior as the density of micro-lenses has scale-similarity regardless of whether the system is DR or PL limited. The maximum order of the Zernike polynomials was assumed to be limited to $n \leq 3$ in this simulation and the critical sampling density is seen to be at $L = 3$ for both the dynamic-range and photon-limited scenarios – regardless of spatial sampling of the PSF.

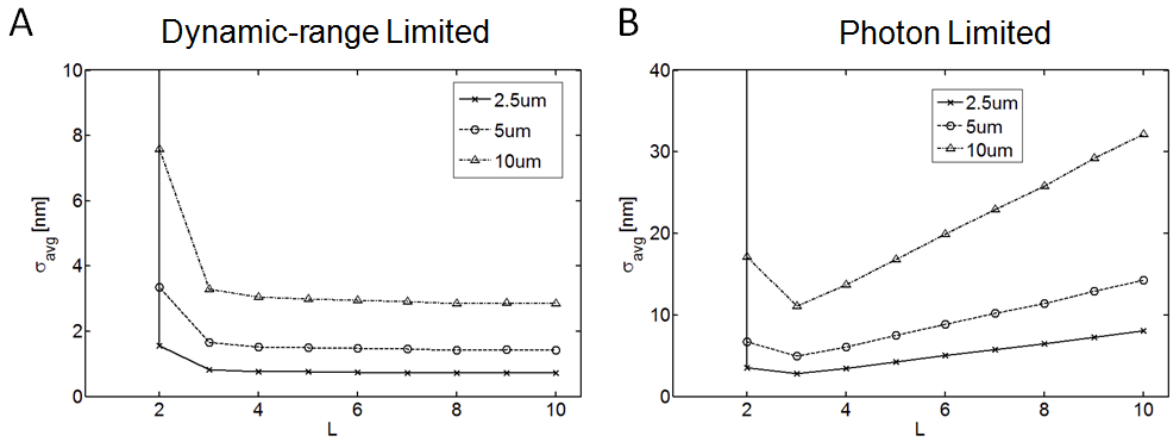

Fig. 6.16: The CRLB performance of the SHWFS as the density of micro-lenses is increased. (A) The dynamic-range limited scenario approaches a limit asymptotically at a similar rate - regardless of the camera pixel size. (B) The photon-limited scenario has an optimum number of micro-lenses which is held fixed and associated with the maximum order of the Zernike polynomial, regardless of the camera pixel size.

6.11 Appendix C: Asymptotic behavior of SHWFS with linear tip/tilt

For a SHWFS, assuming that the number of photons in a DR limited aperture is *N*,

$$FI_L(\theta_i; L) = N \sum_{l=1}^{L^2} \sum_{m=1}^{M} \sum_{n=1}^{N} \frac{1}{f_l(m,n;\theta_i,L)} \left(\frac{\partial}{\partial \theta_i} f_l(m,n;\theta_i,L) \right)^2$$

where $f_l(m,n;\theta_i)$ is the sub-image of the SHWFS for microlens l and is normalized to have unit energy, i.e. $\sum_{m=1}^{M}\sum_{n=1}^{N} f_l(m,n;\theta_i) = 1$. In general, as L is increased, $f_l(m,n;\theta_i,L) \neq f_l(m,n;\theta_i,L+1)$ and $\frac{\partial}{\partial\theta_i} f_l(m,n;\theta_i,L) \neq \frac{\partial}{\partial\theta_i} f_l(m,n;\theta_i,L+1)$ as each pupil (or micro-lens) will see a different portion of the incident wave-front. However, when examining the two linear phase Zernike polynomials, Z_1^{-1} and Z_1^{+1}, a few coarse approximations may be allowed to demonstrate the validity of the limiting behavior in Fig. 6.3.

In what follows, it is assumed that the NA of each micro-lens is fixed. Therefore as L is increased the Zernike polynomial is divided into L^2 subdivisions and, ignoring edge effects from the circular aperture, each image $f_l(m,n;\theta_i)$ is the same for all L, where $\theta_i \in \{Z_1^{-1}, Z_1^{+1}\}$. The second approximation, again ignoring the effects from the circular aperture, is that the derivative is scaled by the number of apertures along one dimension, $\frac{\partial}{\partial\theta_i} f_l(m,n;\theta_i,L) = \frac{1}{L}\frac{\partial}{\partial\theta_i} f_l(m,n;\theta_i)$. This is a statement that as a fixed amount of linear tilt is distributed across more apertures, the amount of local tilt is scaled and generates a correspondingly scaled, transverse shift of the PSF in the image. Applying this scaling behavior of the derivative to the diagonals of the Fisher Information matrix results in,

$$FI(\theta_i;L) = N\sum_{l=1}^{L^2}\sum_{m=1}^{M}\sum_{n=1}^{N}\frac{1}{f_l(m,n;\theta_i)}\left(\frac{\partial}{\partial\theta_i} f_l(m,n;\theta_i,L)\right)^2 =$$

$$\frac{N}{L^2}\sum_{l=1}^{L^2}\sum_{m=1}^{M}\sum_{n=1}^{N}\frac{1}{f_l(m,n;\theta_i)}\left(\frac{\partial}{\partial\theta_i} f_l(m,n;\theta_i)\right)^2.$$

Then applying the assumption that all micro-lens images are equal and are influenced by the same amount of input aberration (i.e. the linear phase is constant across the micro-lens array) the summation over L^2 lenses can be found as,

$$FI(\theta_i; L) = \frac{N}{L^2}\sum_{l=1}^{L^2}\sum_{m=1}^{M}\sum_{n=1}^{N}\frac{1}{f_l(m,n;\theta_i)}\left(\frac{\partial}{\partial\theta_i}f_l(m,n;\theta_i)\right)^2 =$$

$$N\sum_{m=1}^{M}\sum_{n=1}^{N}\frac{1}{f_l(m,n;\theta_i)}\left(\frac{\partial}{\partial\theta_i}f_l(m,n;\theta_i)\right)^2,$$

proving that the Fisher Information becomes independent of the number of micro-lenses. This result can be compared with that given in Fig. 6.3 to verify the numerical accuracy of the model and the asymptotic behavior of the Fisher Information.

The scenario for a conserved number of photons is addressed by scaling the energy of $\sum_{m=1}^{M}\sum_{n=1}^{N} f_l(m,n;\theta_i,L) = 1/L^2$ (energy conservation) and $\frac{\partial}{\partial\theta_i}f_l(m,n;\theta_i,L) = \left(\frac{1}{L}\right)^3\frac{\partial}{\partial\theta_i}f_l(m,n;\theta_i)$ (to account for the dependence of wave-front slope on micro-lens l). Therefore following the previous treatment will yield,

$$FI(\theta_i; L) = N\sum_{l=1}^{L^2}\sum_{m=1}^{M}\sum_{n=1}^{N}\frac{1}{f_l(m,n;\theta_i,L)}\left(\frac{\partial}{\partial\theta_i}f_l(m,n;\theta_i,L)\right)^2 =$$

$$\frac{N}{L^2}\sum_{m=1}^{M}\sum_{n=1}^{N}\frac{1}{f_l(m,n;\theta_i)}\left(\frac{\partial}{\partial\theta_i}f_l(m,n;\theta_i)\right)^2,$$

which describes the limiting photon-limited case behavior for the tip/tilt terms as σ being proportional to L.

6.12 Appendix D: Asymptotic behavior of PR based phase recovery

As given in Equation 6.9, the Fisher Information for the PR method using Kimages is,

$$FI(\theta_{i,j}; K) = \sum_{k=1}^{K}\sum_{m=1}^{M}\sum_{n=1}^{N}\frac{1}{p_k(m,n)}\frac{\partial}{\partial\theta_i}p_k(m,n)\frac{\partial}{\partial\theta_j}p_k(m,n).$$

For the dynamic-range limited scenario, let $p_k(m,n) = Nf_k(m,n)$, i.e. the k^{th} image is normalized to have Nphotons and therefore finite energy. Then

$$FI(\theta_{i,j};K) = N\sum_{k=1}^{K}\sum_{m=1}^{M}\sum_{n=1}^{N}\frac{1}{f_k(m,n)}\frac{\partial}{\partial\theta_i}f_k(m,n)\frac{\partial}{\partial\theta_j}f_k(m,n).$$

Under the condition that $\sum_{m=1,n=1}^{M,N}\frac{\partial}{\partial\theta_i}f_{K+1}(m,n) \neq 0$, then

$$FI\big(\theta_{i,j};K+1\big) > FI\big(\theta_{i,j};K\big)$$

This is a statement that as long as additional image(s) contain information then,

$lim_{K\to\infty} FI(\theta) = \infty$,

which validates the limiting behavior shown in Fig. 6.11.

CHAPTER 7

ENGINEERED POINT SPREAD FUNCTION MICRO-LENS ARRAYS FOR IMPROVED WAVE-FRONT SENSING

7.1 Introduction

In this chapter, the information theoretic bounds of a new wave-front Sensor based on phase mask arrays of engineered Point Spread Functions (PSF) are evaluated. The individual micro-phase mask/micro-lens characteristic is now investigated for the particular task of improving aberration sensitivity. It is shown that when the space of possible phase modulations input to the wave-front sensor (WFS) is restricted to include a finite set of Zernike polynomials, performance can be improved relative to the classical Shack-Hartman wave-front sensor (SHWFS) design. The use of an array of Double-Helix Point Spread Functions (DH-PSF) is evaluated specifically as one implementation of this proposal. An example array is fabricated and tested to demonstrate one operational mode and algorithm which exploits the additional aberration sensitivity of individual micro-lenses with phase-masks.

7.2 Background

The SHWFS has been established as a valuable tool for recovering optical amplitude and phase information in applications spanning from biological imaging (109) (110) (111) to astronomy (112) as well as manufacturing (113) (114) and vision (94) (115). The SHWFS configuration is simple, it consists of only a micro-lens array paired with the image detection device shown in Fig. 7.1. Relative to interferometric methods, the SHWFS is a convenient technique for measuring optical amplitude/phase due to its relatively small form-factor; limited number of components; simplicity to align and robustness to external environmental factors such as vibration. A description of the imaging process is given in Chapter 6.

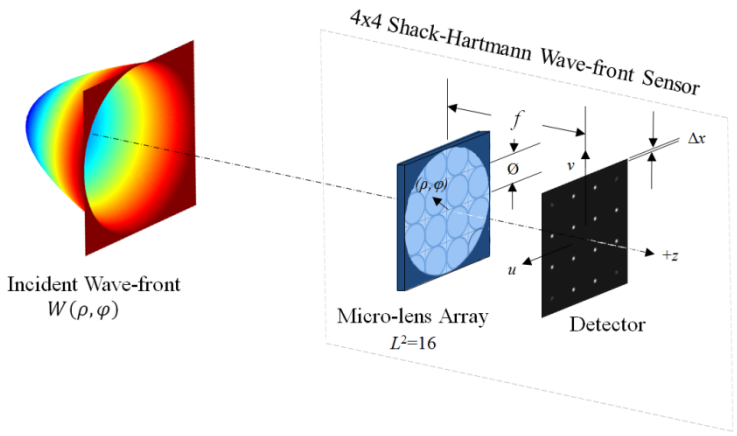

Fig. 7.1: The operational principle of the Shack-Hartmann Wave-Front Sensor. An incident wave-front is transversely sampled in segments using a micro-lens array. The image formed is used to estimate the wave-front from the ensemble of local measurements.

However, as demonstrated in Chapter 6, fundamental bounds exist which limit the measurement precision of the SHWFS geometry. An investigation into how these bounds may be lowered is merited in order to improve the performance of

the SHWFS relative to alternative phase recovery techniques. Additionally, it may be possible to improve the device dynamic range of the SHWFS by increasing the maximum resolvable phase aberration before the PSF becomes ambiguous with a neighboring micro-lens. This device dynamic range is classically considered to be $\delta = \frac{1}{2} D$, as shown in Fig. 7.2, since all the neighboring PSFs are identical.

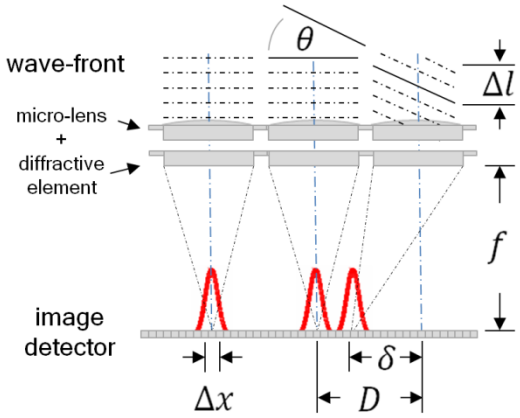

Fig. 7.2: The micro-lens array locally samples the incident wave-front and translates the PSF according to the average amount of linear tilt across the pupil. The micro-lenses are separated by a pitch equal to D and have a focal length $\boldsymbol{f}$. A tilt of angle θ or peak-to-valley aberration $\Delta \boldsymbol{l}$ results in a shift of the PSF, $\delta = \theta \boldsymbol{f}$. The dynamic range of the classical SHWFS device is typically considered to be limited by the micro-lens separation/diameter, D.

Two limiting scenarios capture the SHWFS performance across a variety of applications. The first situation involves applications where the only limit to the number of available photons is the dynamic range of the detector for sensing the wave-front. For this application scenario, the prior chapter has revealed that under practical constraints the SHWFS design will asymptotically reach a bounding precision limit and any increase of the number of micro-lenses in the array will leave this bound unperturbed. The second limiting situation addresses the case

where the number of photons available in the system is fundamentally limited. An example of this scenario exists in Astronomy, where the use of adaptive optics is employed to maximize the efficiency at forming a diffraction-limited spot in the image plane of the telescope. Again, the prior chapter has shown that the theoretical limit to this performance is bound by the maximum spatial frequency modulation of aberration modes present in the system.

Therefore in order to improve the measurement sensitivity and device dynamic range for quantifying microscopic visual or macroscopic telescope aberrations, the concept for an alternative micro-optical element design is investigated. This design of the micro-lens pupil must result in an engineered PSF which is particularly sensitive to aberrations described with Zernike polynomials (107) (116) (117). This investigation will focus on the measurement of phase aberration (assuming uniform illumination conditions) and be limited to include no more than the lower order Zernike aberrations (considered here to be $n \leq 5$, where n limits the modulation of the radial component and puts an upper limit to the azimuthal variation) as these are easiest to correct with addressable, adaptive optics such as deformable mirrors or laser correction surgery (94) (102). The material is presented here such that higher order terms ($n > 5$)may be included as a simple extension of this work.

This chapter develops as follows. In Section 7.3, the exact engineered PSF for this application is introduced. The theoretical tool used to quantify the performance limitations of an individual micro-lens design is reviewed and results reported in Section 7.4. Evaluation of the engineered PSF micro-lens array under the two

illumination conditions highlighted earlier is given in Section 7.5. A discussion of these results and future directions of investigation is given in Section 7.6. Fabrication and test of a demonstration device is presented in Appendix 7A.

7.3 Engineered Point Spread Function Micro-lens Arrays

The classical micro-lens array has enabled the development of many new applications and opened up the possibility for realizing new imaging modalities (74). However, the actual design of an individual micro-lens has traditionally focused on reducing the presence of aberrations in order to generate a diffraction-limited spot in the focal plane. Despite the vast potential already provided from traditional micro-lens arrays, it is now apparent that the design can be improved to expand the scope of applications. Alternative solutions to increase estimation precision include improving the transverse resolution of the image via super-resolution pupil filters (116) (117). The introduction of diffractive optical elements (Fig. 7.2) or intentional aberrations to the micro-lens array is discussed next in order to simultaneously increase the device dynamic range and improve the aberration mode estimation precision. It is anticipated that such adaptations, which may be directly integrated onto the micro-lens, will be useful for alternative applications which have also benefitted from micro-lens array implementation. This potential will be revisited in the final discussion section.

To motivate the use of engineered PSFs, the recent activity aimed at increasing localization precision in microscopy is highlighted. In particular, the

design of optical elements optimally suited to increase three-dimensional localization precision has been particularly rich (13) (14). Those designs are relatable to the task considered here since they have focused on maximizing the information in an image for measuring parameters for transverse location (Z_1^{-1}, Z_1^1) and defocus (Z_2^0). Examples, such as the use of astigmatism via cylindrical lenses, have been demonstrated both theoretically and experimentally. To further justify the similarity of the two tasks, recently a proposal has been made to employ arrays of cylindrical lenses in order to increase the curvature sensitivity of the SHWFS and optimize the matching of the system response to bi-morph mirrors (107). An example which particularly motivates study is research using propagating waves with rotation- and scale-invariance (34). From this solution space, the Double-Helix Point Spread Function (DH-PSF) is identified. In 3D localization-based super-resolution microscopy, the DH-PSF has become an important contribution due to its enhanced sensitivity to quadratic phase for scenarios with limited numbers of photons (35).

The use of propagating scale- and rotation-invariant waves is promising for micro-lens array coding because a) the array of coded apertures may be such that each aperture is a rotated or otherwise unique version from neighboring apertures thereby increasing the dynamic range of the maximum wave-front aberration (introduced later), b) the resulting PSF may natively improve fast estimation algorithm precision by including second-order aberration sensitivity through measured rotation (11) and c) enhanced first-, second- and higher-order aberration

sensitivity may be possible for use with information-efficient estimation algorithms to reach a lower CRLB.

The numerically optimized DH-PSF (29) is analyzed here as one possible solution for engineered PSF micro-lens arrays. The DH-PSF is manifest as a transverse pattern with two dominant peaks which work in concert to exhibit a rotation and scale change as quadratic phase (Zernike polynomial, Z_2^0) is added to the pupil. The 3D-PSF traces out a double-helix pattern in space. Because the sensitivity of this mask to defocus has already been documented, we examine the sensitivity to higher order aberrations for the first time.

Because of this documented sensitivity to one second-order Zernike aberration, the DH-PSF is investigated as an initial design for estimating higher-order terms as well. The DH-PSF can be realized via proper coding of a diffractive element placed properly with respect to a micro-lens, as shown in Fig. 7.2. The Zernike polynomials under investigation here are summarized in Fig. 7.3A. The associated PSFs for $¼\lambda$ aberration with a DH-PSF are shown in Fig. 7.3B. Each polynomial produces a pattern indicative of the particular aberration present. One can see from the aberration pyramid that the DH-PSF provides a distinct advantage in that Zernike polynomials on either half of the vertical axis of the Zernike pyramid (corresponding to a rotation of the Zernike aberration) look quite similar for the classical micro-lens aperture (see Fig. 6.2 in Chapter 6), whereas the DH-PSF produces a more unique transverse intensity distribution due to the non-rotationally symmetric pupil function.

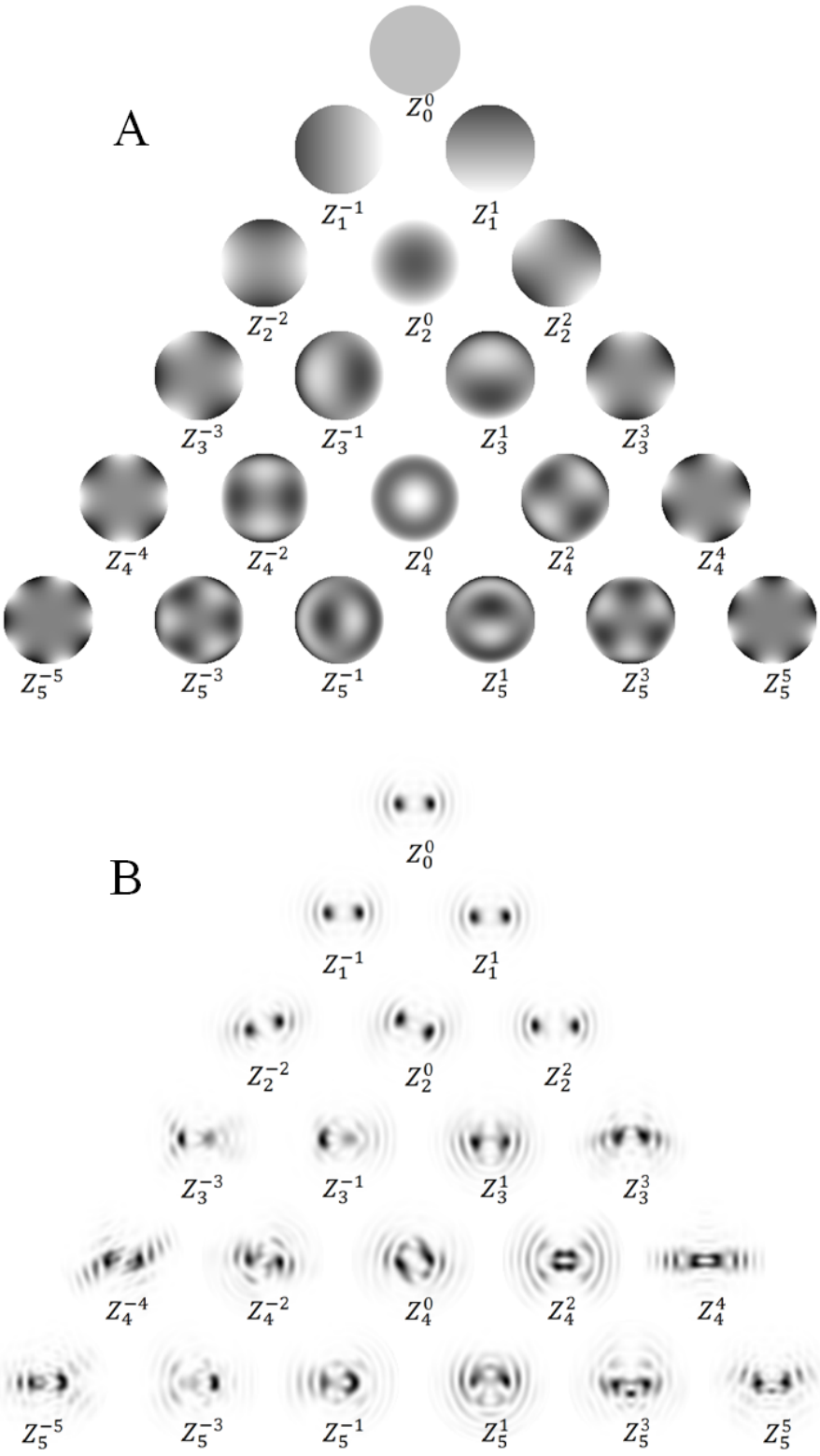

Fig. 7.3: Aberration pyramid of Zernike polynomials and the respective influence on Double-Helix Point Spread Functions. The Zernike polynomials (panel A) influence the Double-Helix PSF uniquely and in a non-rotationally degenerate way.

Another important quantity is found by determining the number of resolvable phase levels from an incident wave-front due to the individual micro-lens. This is a function of two variables: the device dynamic range (maximum aberration tolerance) and the localization precision. The ratio of the dynamic range to the localization precision provides the number of resolvable levels for the micro-lens. This metric is introduced to provide a measure which accounts for both the increased measurement precision and the device dynamic range. Notice that with a classical micro-lens array, the device dynamic range can only be increased by decreasing the number of local wave-front samples (i.e. micro-lenses). In contrast the use of arrays with non-rotationally symmetric point spread functions is of interest because the array of coded apertures can be such that each aperture is a rotated or otherwise unique version from neighboring apertures. This allows the impulse response to overlap with a neighboring group of pixels and be separated with signal processing. Whereas the classical dynamic range can be seen from Fig. 7.2 to be of order ½ the micro-lens pupil size, the introduction of non-symmetric PSFs means that neighboring micro-lenses can be distinguishable by introduction of a rotation to each pupil function. This rotation of neighboring pupils will scale the dynamic range by the number of rotations. It will also be shown to be necessary for improving aberration sensitivity performance in Section 7.5A

7.4 Performance Quantification with Information Theoretic Bounds

The Cramer-Rao Lower Bound (CRLB) is used to compare aberration estimation performance. As implemented here, the CRLB is the lower limit to the variance of the estimated quantity (e.g. the aberrations in the Zernike polynomials) when using an unbiased estimator. The measurement standard deviation associated with the CRLB will be reported for the first 15 Zernike coefficients when the pupil coding is present. Note that the CRLB with no pupil coding is reported in Chapter 6. The reported values are from estimating the deviation from an ideal plane wave incident upon the device. Using this quantity, it is shown in Fig. 7.4 that the theoretical limit to measurement precision is improved with the DH-PSF coded pupil function, relative to the classical pupil. The DH-PSF is therefore investigated to determine whether it can provide a better solution for lens design when implementing an array configuration.

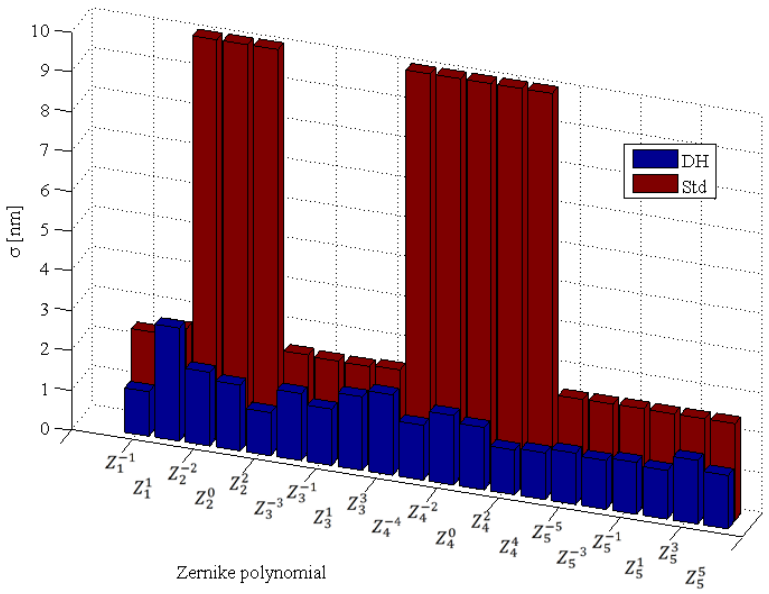

Fig. 7.4: Single-lens Cramer-Rao Lower Bound (CRLB) of aberration sensitivity.

7.5 Analysis of Performance Bounds

In what follows, a systematic evaluation of the optimum system design is first presented in Section 7.5A. It is shown that simply stamping out a series of DH-PSF micro-lenses may not lead to the optimum result. Using a more desirable configuration the performance bounds are analyzed when the input wave-front may be restricted to be a plane-wave (as explained in Chapter 6) in Section 7.5B. Finally, bounds are analyzed when prior knowledge of the input phase is removed and a random set of wave-fronts are allowed for measurement with the DH-PSF WFS in Section 7.5C to compare with the results of Chapter 6. The dependence of the performance of the SHWFS and DHPSF WFS on photon-counts is analyzed in Section 7.5D and demonstrates that the DH-PSF can improve performance relative to the classical design – even when accounting for photon-limited situations.

A. CRLB for DH-PSF Arrays

Based upon the relative performance gains of a DH-PSF system for Zernike polynomial estimation shown in Fig. 7.4, it is proposed to implement an array of these pupils into a wave-front sensing system. As seen in Fig. 7.3C, the DH-PSF with zero aberrations is not a rotationally symmetric pattern and therefore the x and y precision are not equal – as also seen from the CRLB in Fig. 7.4. In order to minimize this bias of tip versus tilt, an array of alternating DH-PSF rotations is investigated as a micro-lens array, where every other pupil will consist of a 90-degree rotated version of the original – thereby also increasing the device dynamic range by 2x. Note the difference of using a DH-PSF versus two smaller micro-lenses pupils - the DH-PSF produces two points which shift in concert to avoid any loss in the dynamic range. This is not true when a pupil is simply divided into two. Fig. 7.5 shows the results of an 8x8 micro-lens array, where the numerical aperture of each micro-lens is 0.03 and diameter is 300 microns – the same specifications used in Chapter 6. A detector is placed in the focal plane of the array with 5x5 micron pixels. The bit-depth of the camera is assumed to be 8-bit. A micro-lens array where the DH-PSF mask is sampled discretely with 150x150 pixels (i.e. a pixel pitch of 2um) is simulated. The mask has 8 discrete levels to modulate a phase delay between $0 - 2\pi$, optimized for the operational wavelength $\lambda = 633nm$. It is seen that by alternating the DH-PSF mask, the CRLB performance becomes more symmetric about aberrations along the *x* and *y*-axes.

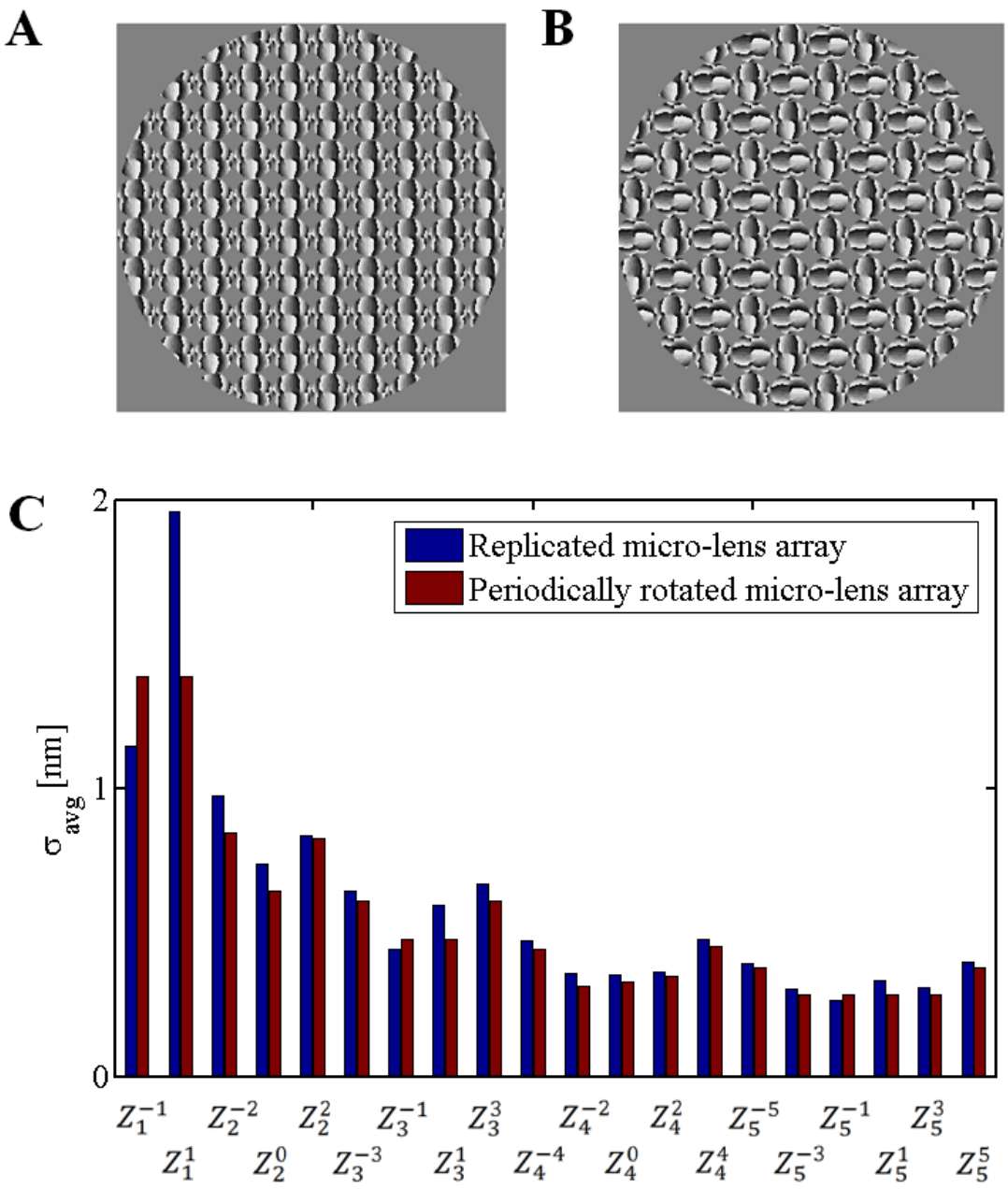

Fig. 7.5: The first micro-lens array design is shown in panel A. An alternative design with rotated versions of the mask is shown in panel B. The performance bounds, as quantified by the CRLB, are given in panel C.

B. CRLB for Planar Incident Wave-fronts

To address performance specifically related to the application of adaptive optics, an ideal scenario is assumed in which an incident wave has been corrected to null-out

any aberrations – resulting in an incident plane-wave. The two limits of signal level regimes (DR and PH) which were previously described are applicable here and therefore investigated. The simulation parameters (e.g. camera pixel size, wavelength, etc.) are kept constant with the prior simulation work. The precision bounds are analyzed as a function of the density of micro-lenses L^2 as well as the number of unknown aberration terms to be estimated (given by n).

Comparison of the two limits (dynamic-range vs. photon-limited) is evaluated by using the average estimation precision of each case,

$$\sigma_{avg}(K) \equiv \frac{1}{T}\sum_{j=1}^{T}\sigma_{\theta_j}(K) \tag{7.1}$$

where $T = 14$ is the total number of Zernike polynomials and shown in Fig. 7.6. It can be seen that the DH-PSF DR-limited design approaches an asymptotic value as L is increased. This is similar to the trends observed with the classical array. However, all things equal, the classical SHWFS array has a bound of $\sigma_{avg}^{DR}(n \leq 5) = 1.0nm$ as $L \to \infty$, as shown in Chapter 6. In constrast, the DH-PSF WFS micro-lens array is able to improve the average precision bound by 67% to $\sigma_{avg,DH}^{DR}(n \leq 5) = 0.6nm$ in the DR scenario.

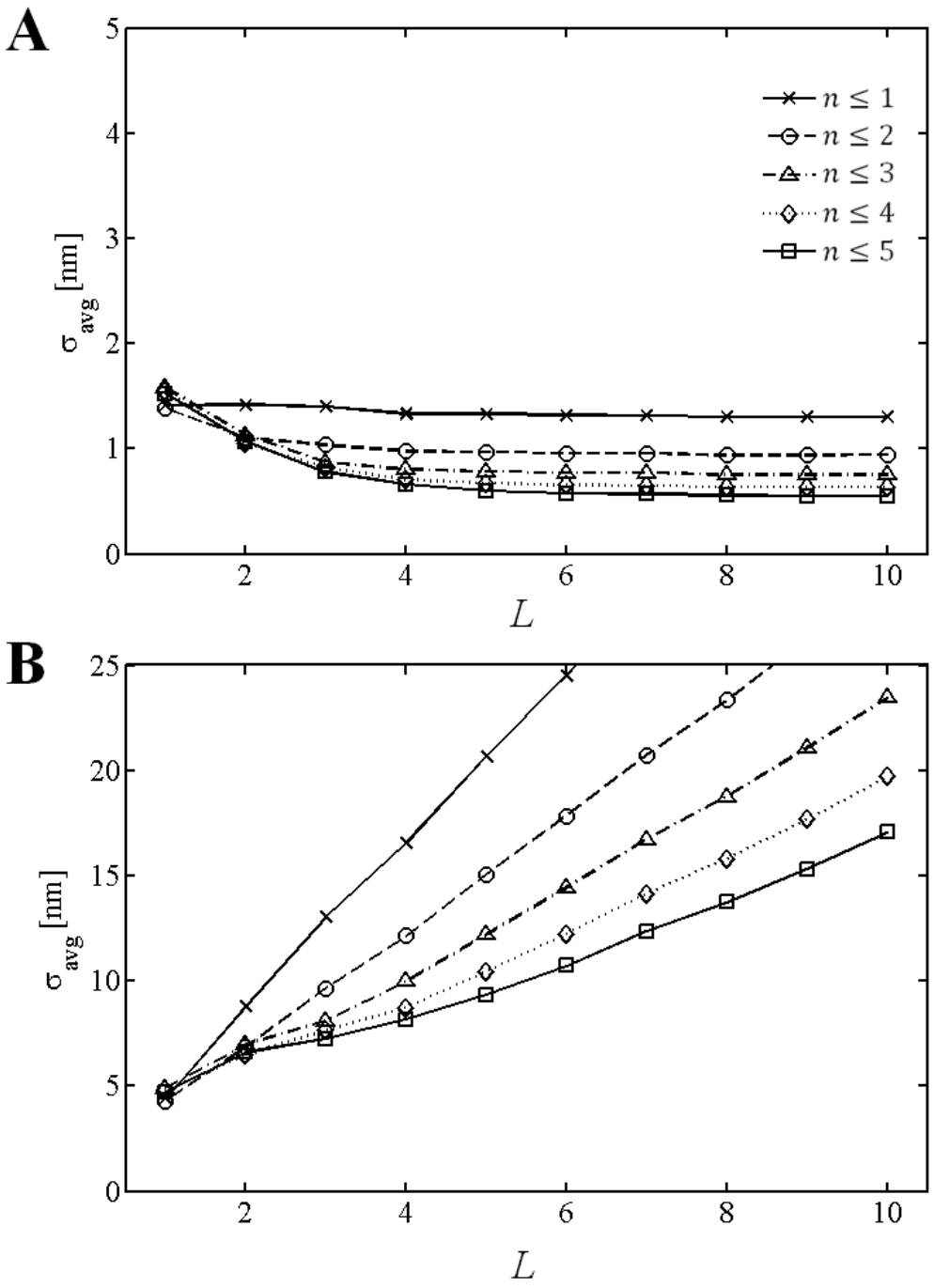

Fig. 7.6: The DR performance is plotted as a function of increasing micro-lens density, given by L in panel A. The PH-limited performance is plotted as a function of L in panel B. For both cases, the number of estimated aberration modes is allowed to vary from $1 \leq n \leq 5$. The analogous case for a classical SHWFS is reported in Fig. 6.5.

For the PH case a surprising observation is made with respect to the optimum micro-lens size to measure wave-front aberrations. It is seen that regardless of the number of unknown Zernike polynomial aberration modes to estimate that a single lens will be the best use of photons. The key difference in performance between the DH-PSF and the classical optical pupil is readily apparent here. The classical pupil can be relatively insensitive to particular aberrations – shown specifically in Fig. 7.4. The DH-PSF does not have particular modes with poor precision and instead is uniformly sensitive the first 21 Zernike polynomials, therefore improving the average precision at low *L.*

C. CRLB for Random Incident Wave-fronts

For applications such as clinical vision quantification for laser correction, the measurement device must be able to sense a large number of possibly aberrated wave-fronts since these will represent the common distribution of aberrations in the eye. In order to evaluate system performance, ten random incident wave-fronts are simulated for each micro-lens array density. Additionally, the number of possible aberrations in these random incident wave-fronts is increased from $n \leq 1$ to $n \leq 5$. The statistics of these wave-fronts is exactly the same as that used in Chapter 6. An example random wave-front is given in Fig. 7.7 along with the associated image behind the DH-PSF micro-lens array.

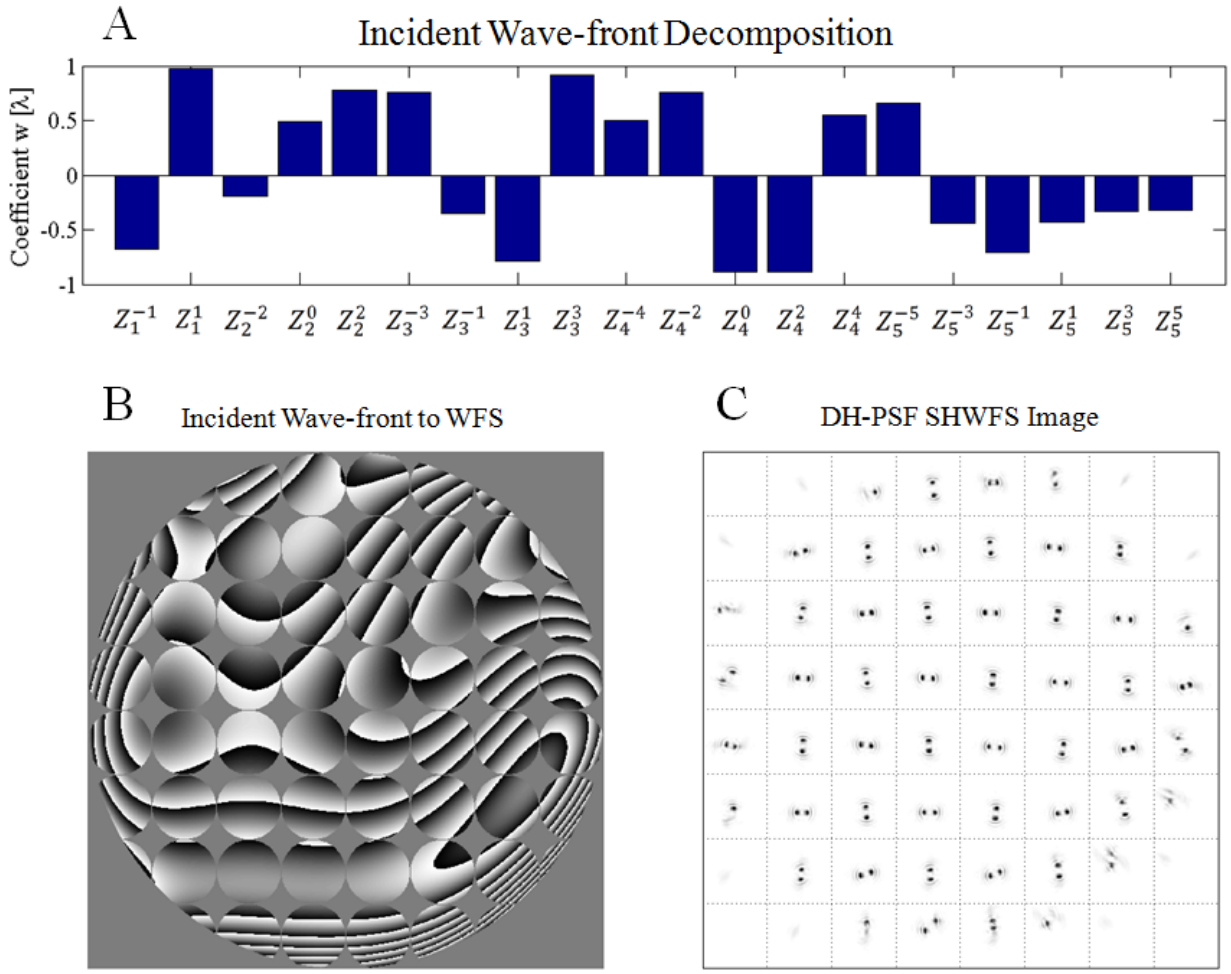

Fig. 7.7: A random super-position of Zernike polynomials is present to the input of the wave-front sensor. The particular modes and their respective coefficients are given in Panel A. The local distribution of the wave-front aberration is seen to be poorly approximated with tip/tilt phase aberrations in panel B. The wave-front sensor image for an 8x8 DH-PSF micro-lens array to be used for estimating the incident phase.

The average performance bounds (CRLB) are presented in Fig. 7.8 for all ten instances as a function of micro-lens density. When compared with the results for the plane-wave incident CRLB, it is observed that for higher micro-lens density, the two results approach the same values.

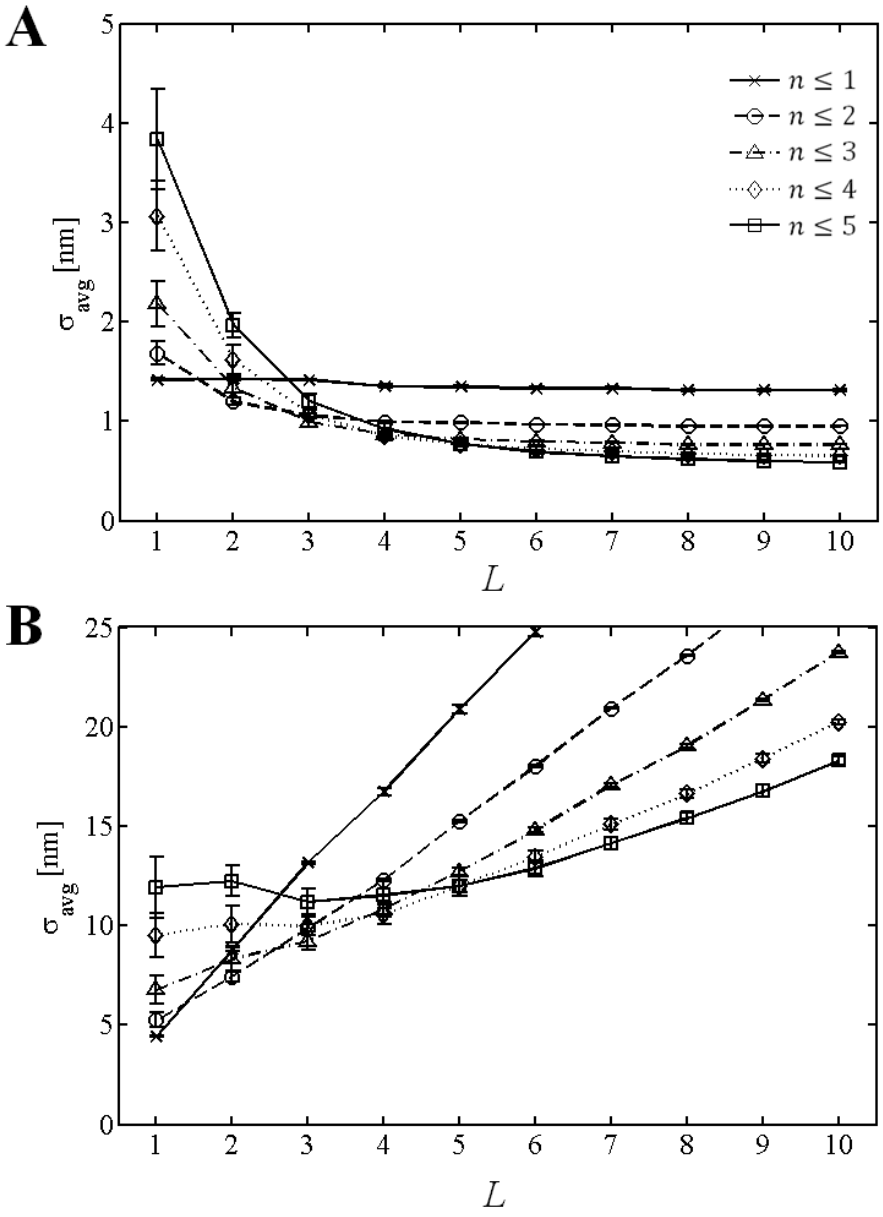

Fig. 7.8: The performance bounds of the DH-PSF SHWFS when random incident wave-fronts are measured. The camera dynamic-range limited scenario is presented in panel A. The photon-limited scenario is presented in panel B.

D. The Significance of Available Photons

Because the behavior of the CRLB showed qualitatively similar behavior with simulation of an incident plane-wave versus the average behavior of random

incident wave-fronts as L is increased past a threshold ($L \geq 5$), only the plane-wave scenario is investigated further in this section. For the dynamic-range limited scenario, the SHWFS has been demonstrated in Chapter 6 to asymptotically approach a limiting value as the micro-lens array density is increased – regardless of the particular pupil encoding. The CRLB for each Zernike polynomial is given in Fig. 7.9 at micro-lens densities of 8x8 and 16x16 for the classical SHWFS micro-lens array to reinforce this conclusion. With DH-PSF pupil encoding, the asymptotic CRLB value can be decreased relative to the classical micro-lens design in the dynamic-range limited scenario – shown in Fig. 7.9 for 8x8 and 16x16 micro-lenses. As seen earlier in Fig. 7.7 and 7.8, the photon-limited performance exhibits precision loss relative to the DR case. However, one can show that the DH-PSF can still be advantageous.

As an example of this, two systems will be evaluated. First, a 16x16 classical SHWFS micro-lens array is used in the DR-limited regime with the performance reported earlier. The second system is evaluated using an equivalent number of photons but instead with a DH-PSF WFS at a 5x5 micro-lens density. This effectively increases the SNR relative to the scenarios evaluated earlier in Fig. 7.7 and 7.8. Because the DH-PSF is more sensitive to aberrations, the 5x5 array is able to improve upon the SHWFS performance of a classical design when using the same number of photons. This important conclusion demonstrates that encoded micro-lens arrays can provide improved performance relative to the classical SHWFS across all operational conditions if the incident beam is expanded/contracted to be used optimally.

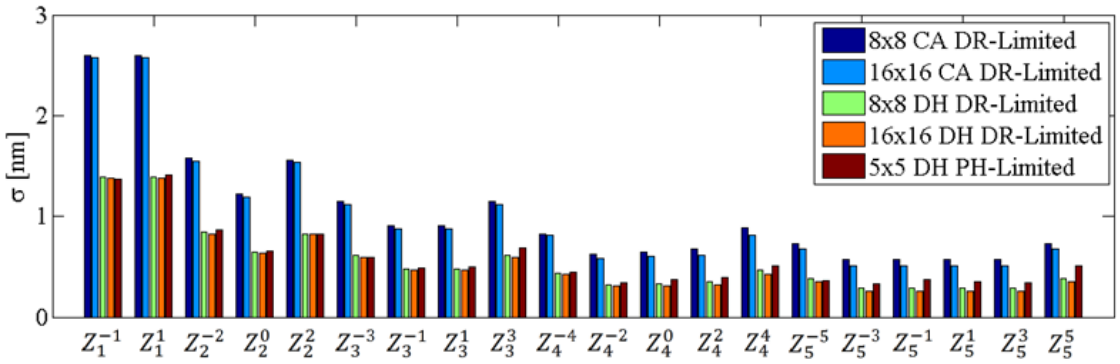

Fig. 7.9: The performance bounds are analyzed for a variety of micro-lens configurations. The classical, clear aperture (CA) micro-lens array performance bounds are shown side-by-side with the DH-PSF micro-lens array (DH). It is seen that the classical design also approaches an asymptotic value but that the DH-PSF system can improve the performance relative to this in the dynamic-range limited regime. When conserving the number of photons in a 16x16 dynamic-range limited classical micro-lens array, a reduced array of 8x8 DH-PSF micro-lenses can out-perform the classical system – in the dynamic-range and photon-limited scenarios.

7.6 Discussion

The micro-lens array is a key enabling device for application solutions such as the Shack-Hartmann Wave-Front Sensors (SHWFS). Outside of this specialty, it has also directly contributed to the development of light-field or plen-optic cameras (74), compact imaging systems (118) and parallelized sensors (119). With regards to the design and manufacture of the micro-lenses, most research has focused on fabrication techniques and the useful application of these classical micro-lens arrays (77) (95). However, recently optimal design of micro-lens pupils for particular task-specific imaging/sensing applications has received more attention (16) (107) (116) (117).

This recent work has verified that modification of the individual pupil function for the micro-lenses may be beneficial for performing specific tasks. Much

of the prior work has focused on wave-front sensing, where estimation precision and dynamic range are the prevailing metrics for sensor performance. It was argued here that the estimation precision may be dependent upon the following parameters: dynamic range of the image capture device; the number of photons collected; the point spread function (PSF) of the associate pupil; the type of noise and signal-to-noise ratio. In this work, an engineered PSF solution was evaluated using a non-uniform array of DH-PSF masks which addresses how to optimize both the device dynamic range and estimation precision for the first time. The wave-front sensing application was an interesting candidate to test the proposal of engineered PSF micro-lens arrays because it is expected to be sensitive to a larger domain of possible aberrations relative to all the prior systems which have been considered (11) (35).

Possible scenarios were simulated which would be typical for specific SHWFS applications with/without a DH-PSF pupil to verify that the Cramer-Rao Lower Bound (CRLB) can indeed be improved over the documented, classical performance limitations. Using the alternating sequence of DH-PSF masks, it is shown that the DH-PSF coded pupil micro-lens array can represent up to a 2x improvement in device dynamic range and almost a 2x improvement in estimation performance. Together, this represents a 4x improvement in the number of resolvable phase levels relative to the performance of the clear pupil scenario. This would be advantages for applications such as aberration measurement of the eye, where aberrations may be large but precision must remain very good.

Since the design of the individual pupil function for each micro-lens array is similar to the optimal designs for 3D microscopy (35) and passive ranging applications (11), it is expected that an engineered PSF array would provide advantages in applications where only a subset of wave-front aberrations are present. Possible applications include use in a TOMBO configuration to extract additional depth resolution information (118); applying to a micro-fluidic device for 3D sensing of particles in each channel; and finally, since the aberrations are inherently chromatic, using a DH-PSF micro-lens array as a parallelized spectral imaging device.

As discussed in Appendix 7A, future work is necessary to reduce the aberrations present in the fabrication of these diffractive optical elements when coupled with traditional micro-lens arrays. Since the potential applications can be rapidly found this represents a fertile opportunity for further research.

7.7. Appendix A: DH-PSF Mask Array and Micro-lens (Fresnel) Fabrication

A demonstration of this system is provided by combining a mix of lithographic techniques for manufacturing the array. The phase mask was numerically optimized using an established method (29) but for use with a rectangular pupil instead of a circular pupil. This was to accommodate the possibility of extreme light sensitive applications where the use of chrome circular apertures must be avoided as this decreases the optical efficiency of the device.

Fig. 7.10: Lithographic design of 8-level phase mask for DH-PSF micro-lens array. The first three masks are used sequentially as binary lithographic development processes. The result is the 8-level diffractive optic shown in the last panel.

The DH-PSF array is fabricated using three steps of binary mask exposures to generate the 8-level diffractive optic in Fig. 7.10. This fabrication technique was reviewed in Chapter 4. The mask was manufactured at Ecole Polytechnique Federale de Lausanne in Neuchatel, Switzerland in collaboration with Toralf Scharf and Hans-Peter Herzig in a micro-optic fabrication lab which has no access to the gray-level techniques used earlier in this work. The manufacturing process included the coating of a 4x4" quartz substrate with photo-resist, followed by alignment and exposure to the first binary mask in Fig. 7.10. The sample is then developed and processed using a Reactive-Ion Etch (RIE) in order to transfer the pattern into quartz. Then the sample is again coated with photo-resist and the procedure repeated for the second and third masks of Fig. 7.10. A white-light interferometric surface profilometry scan (Zeiss New View) of the phase-mask is presented in Fig. 7.11 to verify the pattern transfer and alternating rotations of the phase-mask. The optimum wavelength for this mask is 546nm as given by the maximum difference in the surface relief height and assuming that the refractive index of the quartz is n=1.4548.

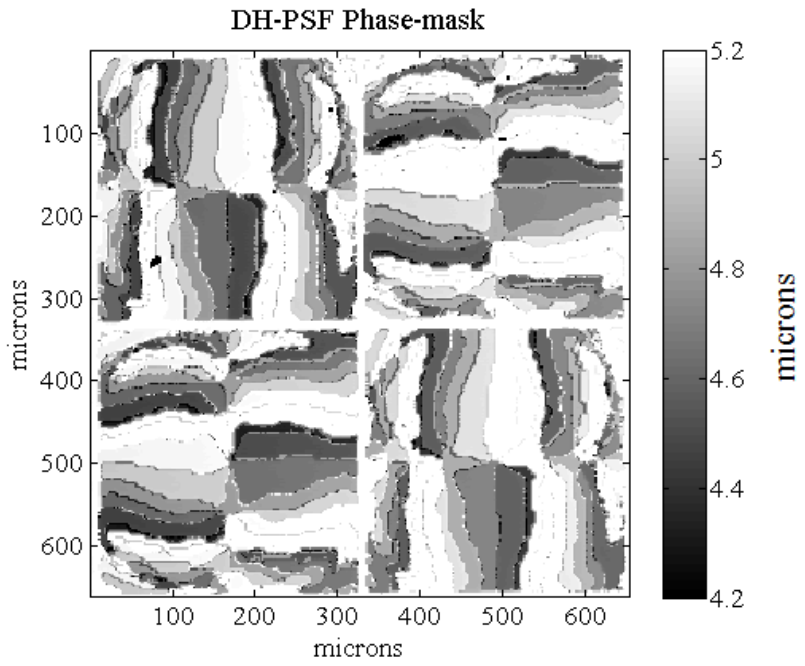

Fig. 7.11: Surface profilometry of a 2x2 sub-region from the DH-PSF phase mask array.

The focusing element of the micro-lens was fabricated at CNL as a Fresnel lens with the same pitch size as the DH-PSF mask. The mask was fabricated on the mask-less lithography device (IMP SF-100 Xpress). The processing steps included loading the phase mask array onto the spin chuck for spin-coating with the mask side down. The top side was coated with an AZ-4210 layer at 5krpm for 40 seconds. This sample is then transferred to the lithography device where a binary pattern of periodic disks was projected on the sample. This allowed for the proper transverse translation and rotation alignment to be set in order to generate an 8x8 micro-lens array on the opposite side of the DH-PSF array in quartz. The sample is then developed and processed according to the procedures outlined in Chapter 4. The resulting surface is shown in Fig. 7.12. The Fresnel lenses are clearly observed however significant noisy surface modulation is also present – as earlier

documented. The optimum wavelength is calculated to be 700nm – as given by the maximum surface relief variation and assuming the photo-resist refractive index to be n = 1.635.

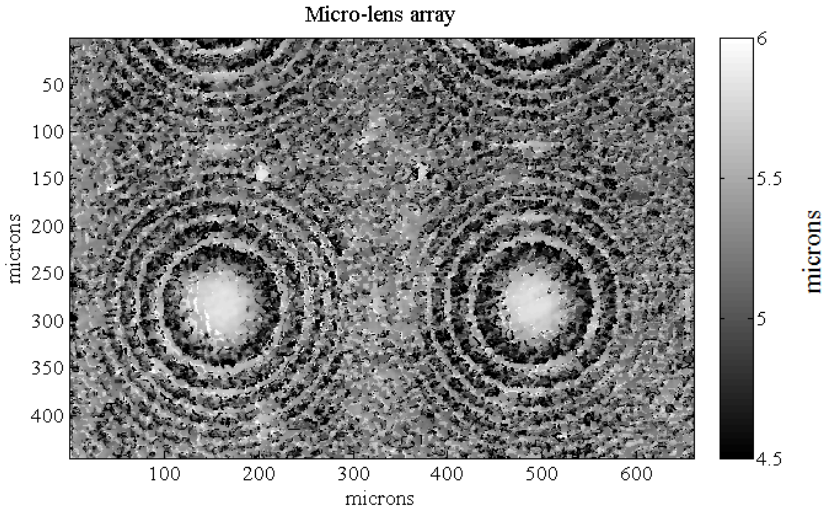

Fig. 7.12: Surface profilometry of Fresnel lenses on the backside of the phase mask array.

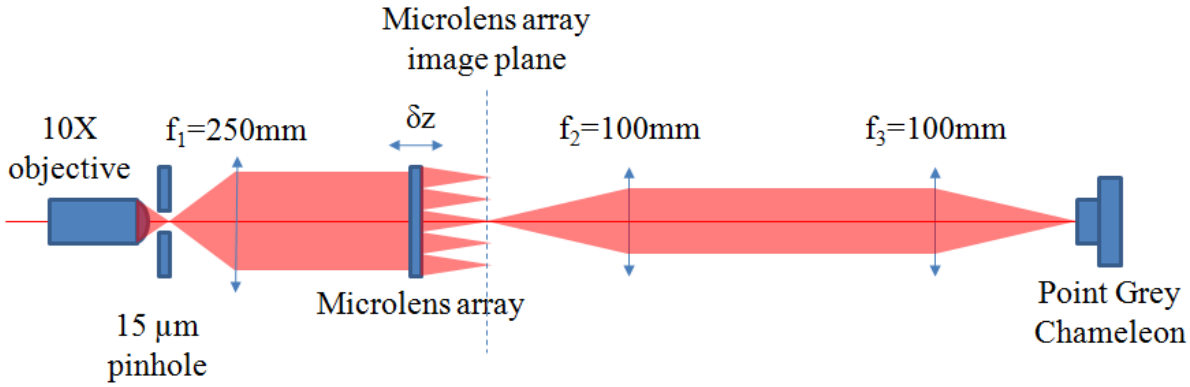

Fig. 7.13: Experimental test configuration. An incident beam from a HeNe source is spatially filtered using an objective and pinhole. The resulting diverging beam is collimated with a lens of focal length f_1. The collimated beam is incident to the micro-lens array element with the DH-PSF array side facing the beam. The array of beams is re-imaged onto a detector with a 4F system.

A wave-front sensing experiment is employed to test the ability of the DH-PSF micro-lens array for sensing aberrations beyond tip/tilt. The test measures a

quadratic phase term by defocusing the collimation lens in Fig. 7.13 by 10cm. This additional quadratic phase results in both translation and rotation of the DH-PSF in the micro-lens image plane which can be easily measured (11) (32). Note the use of a 4F system to relay the image from the micro-lens image plane to the detector plane. This was necessary as the focal length of the micro-lens was much shorter than the length of the distance between the camera detector plane (Point Grey Chameleon CMLN-I3S2M) and its IR filter.

The focused image is shown in Fig. 7.14. Once the collimation lens is translated, a simple estimator is proposed here to increase the local accuracy beyond just tip/tilt by measuring the relative rotation change of the DH-PSF in each micro-lens (as done in Chapter 3). The tip/tilt terms are still provided from the familiar transverse translation of the PSF – exactly as with the classical micro-lens. Both the calculated translation and rotation are shown in Fig. 7.15 showing the direct sensing of higher-order aberrations locally at each micro-lens. As an alternative estimation implementation, a multi-variate search algorithm (such as direct-search or genetic algorithm optimization) can be utilized to solve for the aberrations globally present across the micro-lens array instead of concentrating on using the local measurements.

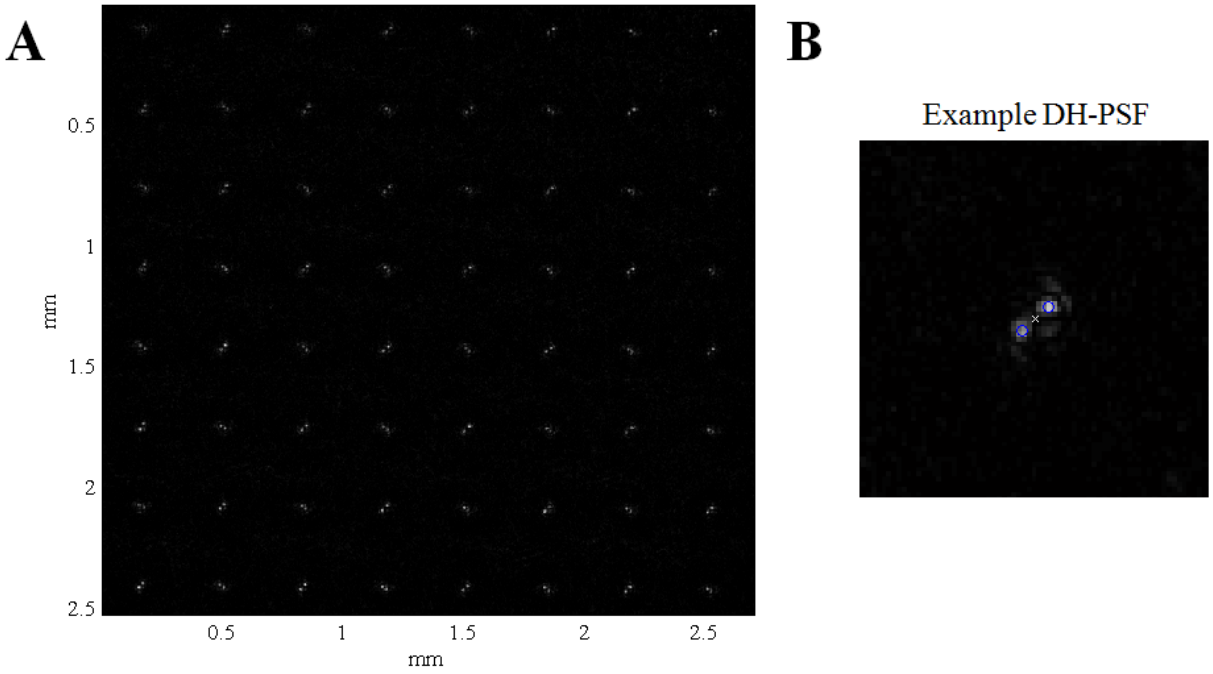

Fig. 7.14: Experimental images from the DH-PSF micro-lens array. The 8x8 array which is used for wave-front sensing shows alternating patterns of DH-PSFs (panel A). An example DH-PSF is used to demonstrate that the centroid can be easily found for measuring transverse shifts (centroid is given with white cross) and that the two peaks can be identified to calculate an angle which is related to defocus aberrations (panel B).

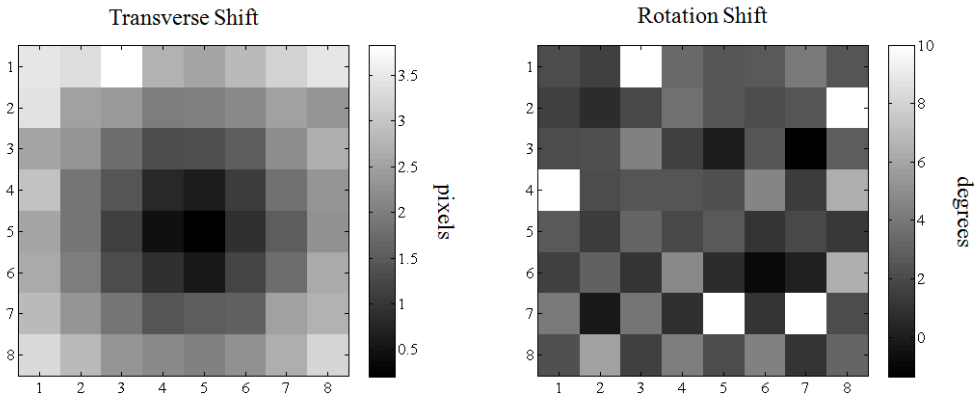

Fig. 7.15: Measurement of quadratic phase aberration with the DH-PSF micro-lens array in terms of transverse shift (linear tip/tilt) as well as higher-order local aberrations which are quantified locally in terms of the DH-PSF rotation.

CHAPTER 8

CONCLUSION

A review of prior literature firmly establishes the utility of optimization criteria such as Fisher Information and the Cramer-Rao Lower Bound (CRLB) as well as the capabilities of encoding the pupil function for optical system design. However, despite the advantages of these systems, in some cases, missing pieces were still necessary to form a complete solution. This was observed with existing techniques for scale- and rotation-invariant propagating wave solutions, where two failures had stood out:

a. The lack of estimation algorithms which reach the promised advantages of engineered PSF design in 3D super-resolution microscopy
b. The lack of optical elements which efficiently encode the designed PSF in terms of photons

Therefore tools to satisfy these demands were developed early in thesis and each applied individually. For the first time, a comprehensive implementation of the two was later demonstrated for 3D super-resolution microscopy in Chapter 4.

Based upon this, it is believed that 3D localization based super-resolution imaging techniques using engineered PSFs can finally realize their full-potential.

To this end, a full system should be manufactured which incorporates the tools necessary from the point-of-view of biologists. Such tools would include an inverted microscope design with tip/tilt control and automatic feedback of the sample stage as well as a convenient eye-piece for viewing/alignment. To facilitate rapid signal processing and super-resolution image development, the parallel computing capabilities of Graphic Processing Units (GPUs) can be paired with the PR-MLE.

The single-molecule work in this thesis had assumed isotropic emission from each fluorophore. While accurate for the 3D super-resolution microscopy studies undertaken here, additional physics can be found from measuring how the orientation of a dipole changes in different environments (120) (121). Image-based techniques have been explored as one solution to estimating dipole orientation from the far-field emission pattern (46) (120) (122) (123). Recently, these proposals have been characterized in terms of their respective Information theoretic limits (124). Additional work is warranted to search whether an improved solution using engineered PSFs exists. If so, an extension to the PR-MLE model could be explored for application to this class of imaging.

Subsequent work was demonstrated here to further exploit the suite of tools developed for engineered PSFs. First, a system was demonstrated which can realize the promised goals of two individual tasks. This required the use of multiple engineered PSFs – each ideal for one of the two tasks. To realize these tasks simultaneously, a new pupil-encoding was proposed – the Single-Helix PSF which allows for a single-lens/camera implementation. The means to realize this encoding

was discussed and the requisite mask was fabricated. The proposed utility of the design was also demonstrated in experiment.

However, the gains of exploiting the pupil-function have now been demonstrated for only a limited set of tasks – tasks which are associated with three particular phase aberrations: linear phase tip/tilt (object transverse translation) and quadratic phase (object axial location). In order to explore and demonstrate the potential of engineered PSFs for new areas, the application of wave-front sensing is explored. This application is of particular interest because it involves the direct sensing of an arbitrarily larger set of new and additional aberrations. The classical Shack-Hartmann Wave-front Sensing design was analyzed in terms of the CRLB, quantifying the limiting performance. Using the same tools, a proposal was analyzed to use engineered PSFs for wave-front sensing micro-lens arrays. The subsequent design was shown to be of theoretical value for most scenarios applicable to wave-front sensing applications. The proposed micro-lens device was fabricated as a demonstration that such systems are realizable and a straight-forward algorithm was demonstrated to extract enhanced aberration information relative to the classical micro-lens design.

The analysis of a wave-front sensor with engineered PSF design demonstrates the improvement available to all passive imaging techniques which plan to exploit the information transmitted in aberration modes. Additional modes included in this analysis have direct applications outside of wave-front sensing. One example is the use of spherical aberration in microscopy to estimate the distance of a source from the cover slip of a microscope sample.

With the demonstrated success of these tools for engineered PSF design, the ability to move forward on finding successful applications should improve. An interesting avenue for future work would be to focus on the exploitation of the chromatic dependence of optical aberrations in order to develop dense arrays of chromatic sensors. Exploitation of chromatic aberrations was already introduced in Chapter 5 through the application of SH-PSFs for a joint ranging/extended Depth-of-Field solution. The advantage of such a design for chromatic sensing is that in contrast to the use of diffraction gratings and prisms, the pattern matching algorithms and optical elements demonstrated here can be used to reach the information theoretic limits for small form factors and engineered PSFs which are simple to estimate. One example system can potentially be demonstrated using the DH-PSF micro-lens array in Chapter 7 however since aberrations were present in the image due to errors in the mask/micro-lens surface, better fabrication techniques must be developed. Such a system could be fixed to a micro-fluidic device where the fluidic channels are each matched to a micro-lens. When placed at a fixed axial distance (any distance which is out-of-focus will do) from the micro-lens, the chromatic behavior of the DH-PSF will encode the chromatic content of the fluidic channel into a unique rotation of the PSF.

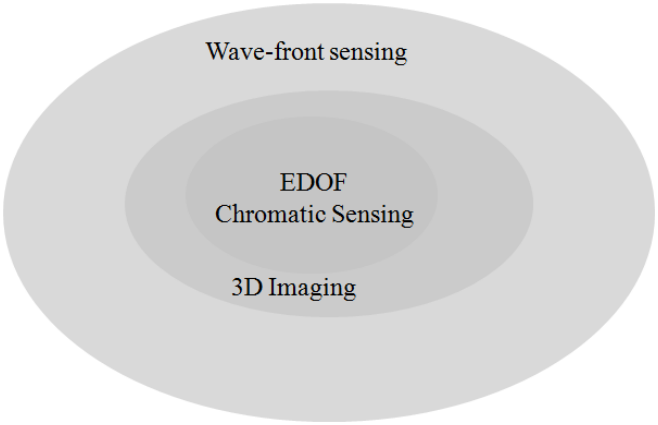

Fig. 8.1: A Venn diagram showing the nested relationship between different optical sensing/imaging applications in terms of the aberrations necessary for that application.

Each of the applications in this thesis can be traced to the targeted exploitation of specific aberration functions. As the task becomes more complicated, a greater number of aberrations are necessary to infer the inverse relationship between the image and the parameters to be estimated. This nested relationship between particular tasks and the set of aberrations necessary to complete them is given in Fig. 8.1. The shape of the Venn diagram is not directly indicative of the relative difficulty or significance of each particular task. For instance, only three aberrations are responsible for the sensing associated with 3D imaging. However it does emphasize the relatively small domain of existing applications relative to the available number of aberration modes and provide some additional motivation for the future study of the ideas investigated here.

APPENDIX A

TRADE-OFF OF DEPTH-OF-FIELD VERSUS FIELD-OF-VIEW FOR ENGINEERED POINT SPREAD FUNCTION CHANNELS

A.1 Optical system design

The prior geometrical optic designs discussed in Chapter 3 will operate with a different operational axial-depth range and sensitivity than the diffraction-based methods. This is because the classical geometrical optics approaches have traditionally defined the Depth-of-Field (DOF) by an acceptable increase in the transverse spot size of the PSF before image blur become unacceptable. The practical reason behind this is to define an axial range where the imaging system will approximately behave with invariance. In contrast, the diffractive optics approaches described in this thesis have an operational range which is typically associated with a range of allowable rotation. In addition, the use of a diffractive optics approach will account for the wave-nature of light - particularly relevant for when high-accuracy and precision is necessary. Therefore, the diffractive engineered Point Spread Function (PSF) design should benefit the application where 3D precision within the short range where geometrical optics fails is paramount as well as to increase the operational DOF. However, the use of an

engineered PSF (such as the Double-Helix PSF) requires trade-offs between the necessary spatial sampling of the PSF for estimation purposes and important characteristics such as the system Field-Of-View (FOV). This particular trade-off is investigated here in order to select the proper system design and understand its limits.

A.2 Depth-of-Field versus Field-of-View

The usable Depth-of-Field (DOF) is defined here as,

$$DOF \equiv d_{o,max}(f, d_i, \Psi_{\min}) - d_{o,min}(f, d_i, \Psi_{\max}) \tag{A.1}$$

and the Field-of-View (FOV) as,

$$FOV \equiv atan\frac{N_p \Delta_c}{d_i} \tag{A.2}$$

where d_o is the (variable) object distance and will be developed in more detail later, f is the lens focal length, d_i is the (static) focused image position, N_p is the number of pixels on the camera, Δ_c is the pixel size and $\Psi_{\min}$, $\Psi_{\max}$ are the minimum and maximum defocus parameter values associated with the operational axial range. These defocus values are the number of waves of defocus aberration in the optical pupil which is associated with the extremes of the object location and defined as (25),

$$\Psi_{\min} = \frac{\pi}{\lambda}(u^2 + v^2)\left(\frac{1}{d_{o,max}} + \frac{1}{d_i} - \frac{1}{f}\right) \tag{A.3}$$

$$\Psi_{\max} = \frac{\pi}{\lambda}(u^2 + v^2)\left(\frac{1}{d_{o,min}} + \frac{1}{d_i} - \frac{1}{f}\right) \tag{A.4}$$

where λ is the wavelength of operation, $d_{o,min}$ and $d_{o,max}$ take the minimum and maximum object positions and u, v are the pupil plane coordinates to define the

aperture size of the optical system. An example of this defocus dependence on the object distance is given in Fig. A.1 where an example system with $\lambda = 633nm, 0 \leq u, v \leq 2.5mm, d_i = 55mm$ and $f = 50mm$.

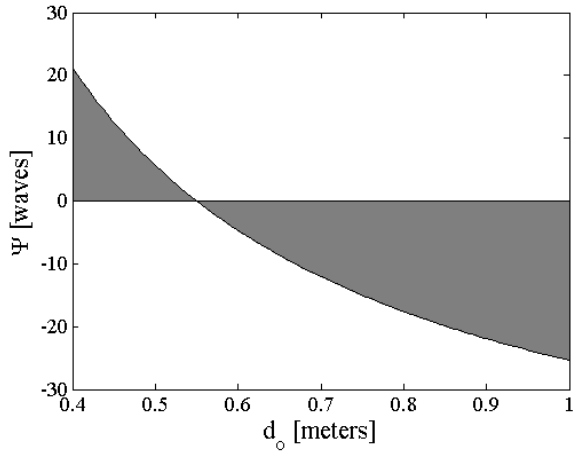

Fig. A.1: The non-linear dependence of the number of waves of defocus, Ψ, as a function of object distance for a representative system. The allowable values of Ψ are in the shaded region associated with the maximum values being present at the edge of the optical pupil.

This parameter Ψ influences the Point Spread Function (PSF) of the system through the addition of quadratic phase to the pupil function (25),

$$PSF(x,y) = \left(\frac{1}{\lambda d_o d_i}\right)^2 \left|\Im\{p(u,v)e^{-i\Psi(u,v)}\}\right|^2 \quad \text{(A.5)}$$

where $p(u,v)$ describes the potential complex-valued pupil function of the lens and $d_{o,min} \leq d_o \leq d_{o,max}$.

The operational limits of Ψ (e.g. Eqs. A.3, A.4) are chosen to accommodate the functional range of the PSF. For example, as previously mentioned, the classical definition for the acceptable defocus ranges in a standard optical system can correspond with an increase of the Airy disk width (i.e. the transverse distribution of the standard PSF shape) by $\sqrt{2}$ from the focal plane PSF size. Therefore, the

choice of $\Psi_{\min}, \Psi_{\max}$ will coincide with this constraint on the spatial feature of the PSF. In contrast, the DH-PSF has a functional range associated with the 180° rotation of its characteristic lobes. It is found that this rotation occurs within the range $-12 \leq \Psi \leq +12$ waves of defocus aberration at the pupil perimeter, the same range used to plot the images in Fig. 3.1.

The aperture size in Eq. A.5 can be constrained by definition of a required sampling rate in the detector plane to have a maximum resolvable spatial frequency of,

$$f_{incoh} = 2f_{coh} = \frac{4}{N_{ss}} \frac{r_{max}}{\lambda d_i} \tag{A.6}$$

where N_{ss} is a Nyquist sub-sampling factor to account for non-ideal detector pixel-pitch, f_{coh} is the coherent optical system cut-off frequency, f_{incoh} is the incoherent optical system cut-off frequency and $p(u,v) = 0$ if $u, v > r_{max}$. The necessary sampling rate here is dictated by the performance and capabilities of the specific algorithm being implemented for range estimation with the PSF. For the DH-PSF, this has ranged experimentally in the range between $1 \leq N_{ss} \leq 2$. Using these constraints the maximum aperture size can be re-written in terms of the detector pitch Δ_c as,

$$r_{max} = \frac{\lambda d_i}{4\Delta_c} N_{ss}. \tag{A.7}$$

This can be rewritten again using familiar optical parameters such as the numerical aperture (NA) as,

$$NA = \frac{\lambda \varepsilon}{4\Delta_c} N_{ss} \tag{A.8}$$

where the focused image distance $d_i \equiv \varepsilon f$ and $\varepsilon \geq 1$. Using common system values for $N_{ss} = 1$ and $\Delta_c = 4\mu m$, the relationship between the allowable NA to realize the minimum spatial sampling constraints is given in Fig. A.2.

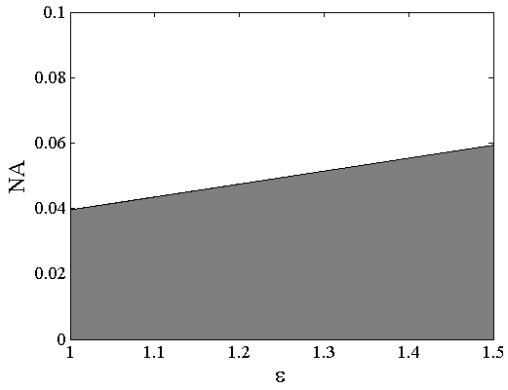

Fig. A.2: The dependence of the maximum allowable numerical aperture (NA) versus a scaling factor for the imaging distance given by ε. Shaded regions signify allowable values which are constrained by requiring the PSF to be sampled at no less than 1x Nyquist frequency ($N_{ss} \leq 1$).

Using Eq. A.3 and A.7, the object distance satisfying these constraints can be found,

$$d_{o,max} = \left[\frac{16\Psi_{min}}{\pi\lambda}\left(\frac{\Delta_c}{N_{ss}d_i}\right)^2 + \frac{1}{f} - \frac{1}{d_i}\right]^{-1} \tag{A.8}$$

and subsequently used to find the DOF defined in Eq. A.1. Implementing the use of a scaling factor definition of the focused image distance for convenience, (i.e. $d_i \equiv \varepsilon f$), Eq. A.8 is rewritten,

$$d_{o,max} = \frac{\epsilon f}{\frac{16\Psi_{min}}{\pi\lambda\varepsilon f}\left(\frac{\Delta_c}{N_{ss}}\right)^2 + \epsilon - 1} \tag{A.9}$$

In addition to this constraint for object distance, other parameters may be used to further define the parameter space. For example, the non-linear, monotonic relationship between object distance and defocus in Eq. A.9 and explicitly

demonstrated in Fig. A.1, will translate to a variation in object space axial precision as a function of position. This is because the variable Ψ is what directly influences the rotation of the PSF, as defined by Eq. A.5, and as the object distance increases the influence on Ψ wanes - thus resulting in decreased axial estimation precision. As a result, a gain factor γ is defined for a single-lens imaging system that will limit the variation in this object space precision as,

$$\gamma = \frac{d_o(\Psi_{min}) - d_o(\Psi_{min}+\delta\Psi)}{d_o(\Psi_{max}-\delta\Psi) - d_o(\Psi_{max})} \tag{A.10}$$

where $\delta\Psi$ is an expected minimum resolvable defocus step of the rotating PSF and is dependent on factors such as estimation algorithm, Signal-to-Noise Ratio (SNR), the sampling rate N_{ss}, etc.. Using the parameters already defined for an optical system, a representative gain dependence contour is given in Fig. A.3. Note that one must be careful in understanding the role of NA on the gain performance. Here the NA scales according to ε (Eq. A.8) and not f as would typically be expected. Instead as f is varied for a fixed ε, the radius of the aperture is scaled in order to maintain a constant NA to satisfy the sampling constraints.

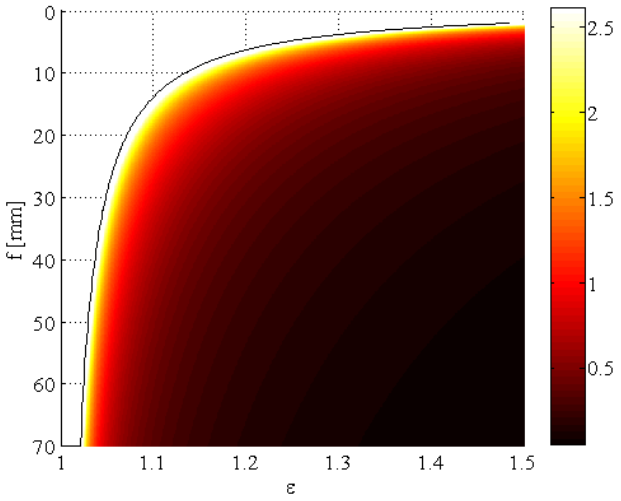

Fig. A.3: The gain dependence of an optical system (color coded) as a function of the focused image position and focal length of the imaging lens. An increase of ε is equivalent to an increase in NA (Eq. A.8) and it is observed that as the NA increases, the DOF decreases. Note that the gain is displayed in a $\log_{10}$ scale in order to increase the information conveyed visually. The invalid solution space is not color coded in the image (e.g. where a value of f and ε yield a negative d_o).

In order to begin mapping the relationship between DOF and FOV, a numerical study between the two is provided using the same optical configuration assumed previously. Using the object space resolution gain criteria of Eq. A.10, a solution for the allowable lens focal length given the parameter set $\mathbb{S} \in \{\gamma, \varepsilon, \Psi_{\text{lim}}, \lambda, \text{N}_{\text{ss}}, \Delta_{\text{c}}, \text{N}_{\text{p}}\}$ is found where,

$$f = -\frac{B}{2A} + \frac{\sqrt{B^2 - 4AC}}{2A} \tag{A.11}$$

and

$$A = (\varepsilon^2\gamma - 2\varepsilon\gamma + \gamma) - (\varepsilon^2 - 2\varepsilon + 1) \tag{A.12A}$$

$$B = (\varepsilon - 1)\frac{16}{\pi\lambda\varepsilon}\left(\frac{\Delta_c}{N_{ss}}\right)^2 (\delta\Psi\gamma - 2\Psi_{lim}\gamma - 2\Psi_{lim} + \delta\Psi) \tag{A.12B}$$

$$C = \left(\frac{16}{\pi\lambda\varepsilon}\left(\frac{\Delta_c}{N_{ss}}\right)^2\right)^2 ((-\Psi_{lim})^2\gamma - \delta\Psi\Psi_{lim}\gamma - (\Psi_{lim})^2 + \delta\Psi\Psi_{lim}). \tag{A.12C}$$

With this solution for f, the relationship between DOF and FOV can be found using equations,

$$FOV \approx \frac{N_p\Delta_{\text{c}}}{\varepsilon f} \tag{A.13A}$$

and

$$DOF = \frac{\varepsilon f}{\frac{16\Psi_{\min}}{\pi\lambda\varepsilon f}\left(\frac{\Delta_c}{N_{ss}}\right)^2 + \varepsilon - 1} - \frac{\varepsilon f}{\frac{16\Psi_{\max}}{\pi\lambda\varepsilon f}\left(\frac{\Delta_c}{N_{ss}}\right)^2 + \varepsilon - 1}. \tag{A.13B}$$

Constraining the parameter set defining the system to be $\mathbb{S} \in \{100, 1 \leq \varepsilon \leq 1.5, \Psi_{\text{lim}} = 12, \lambda = 633\text{nm}, \text{N}_{\text{ss}} = 1, \Delta_{\text{c}} = 4\mu\text{m}, \text{N}_{\text{p}} = 1024\}$, the relationship between

DOF and FOV is numerically solved in Fig. A.4 and fit to a power law with the solution,

$$DOF = (0.04549)FOV^{-2}$$

where DOF is in units of length (meters) and FOV is in units of angle (degrees). This relationship follows the inverse square law expected from classical optics.

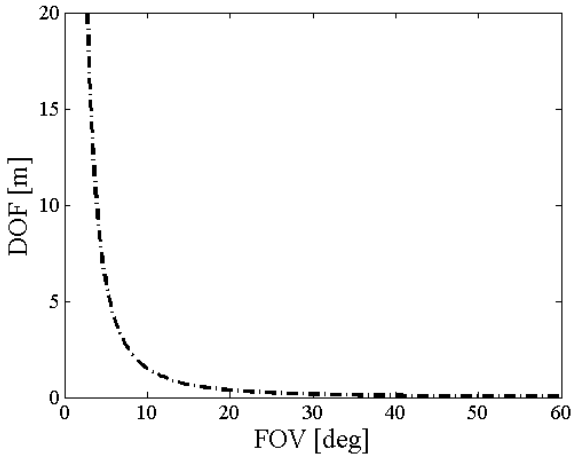

Fig. A.4: The relationship between Depth-of-Field and Field-of-View for an Engineered PSF system is seen to obey the inverse square law. The coefficient of the inverse relationship is determined by the required sampling conditions, operational defocus parameters, etc.

APPENDIX B

FISHER INFORMATION MATRICES FROM NUMERICAL OPTICAL SYSTEM SIMULATION

B.1 Numerical Calculation

The use of Fisher Information (FI) matrices and their inverse, the Cramer-Rao Lower Bound (CRLB), is prevalent throughout this text. In what follows, an introduction into the methods employed for numerically calculating the FI is presented for those interested in reproducing existing results or applying FI analysis to new problems.

The FI is used to quantify the amount of information contained in the measurement I which is related to the unknown set of random variables, $\boldsymbol{\theta}$. The generalized, multi-parameter matrix form is written as (33),

$$FI(\theta_i, \theta_j) = E\left[\frac{\partial}{\partial\theta_i} ln\, f(I;\boldsymbol{\theta}) \frac{\partial}{\partial\theta_j} ln\, f(I;\boldsymbol{\theta})\right] \qquad \text{(B.1)}$$

where N unknown parameters are assumed in $\boldsymbol{\theta} \in \{\theta_i, \ldots, \theta_N\}$, E is the expectation value, f is the probability density function and the FI matrix is NxN.

In optical applications, the measurement is typically the experimental image and examples for the unknown set of random variables can include the object being imaged, the intensity of the source, the 3D location of the source, the particular

wavefront aberration, etc. Information is transferred to the measurement via a change in the signal as the unknown variable is modulated, as seen by the partial derivative in Eq. B.1. An example form of the FI matrix for 3D localization is presented in Fig. B.1.

The generalized FI form of Eq. B.1 can be reduced to an approximate form for joint Gaussian and Poisson processes in an imaging system as (73),

$$FI(\theta_i, \theta_j) \approx \sum_{m=1}^{M} \sum_{n=1}^{N} \frac{R^2}{\sigma^2 + R^2 I(m,n;\boldsymbol{\theta})} \frac{\partial I(m,n;\boldsymbol{\theta})}{\partial \theta_i} \frac{\partial I(m,n;\boldsymbol{\theta})}{\partial \theta_j} \tag{B.2}$$

if $\sigma/R > 0.5$, where σ is the standard deviation from Gaussian noise in units of [Volts] and R is the pixel responsivity in units of [Volts/photon] and $I(m,n;\boldsymbol{\theta})$ is the number of photons in the image from pixel m,n. Note that when reduced to pure Gaussian ($\sigma^2 \gg R^2 I$) or pure Poisson ($\sigma = 0$) noise processes, this expression is exact (73). Assumptions used to derive this form are that each pixel is an uncorrelated, independently random event and that a uniform standard deviation is applicable across the detector array such that the FI will add across all pixels.

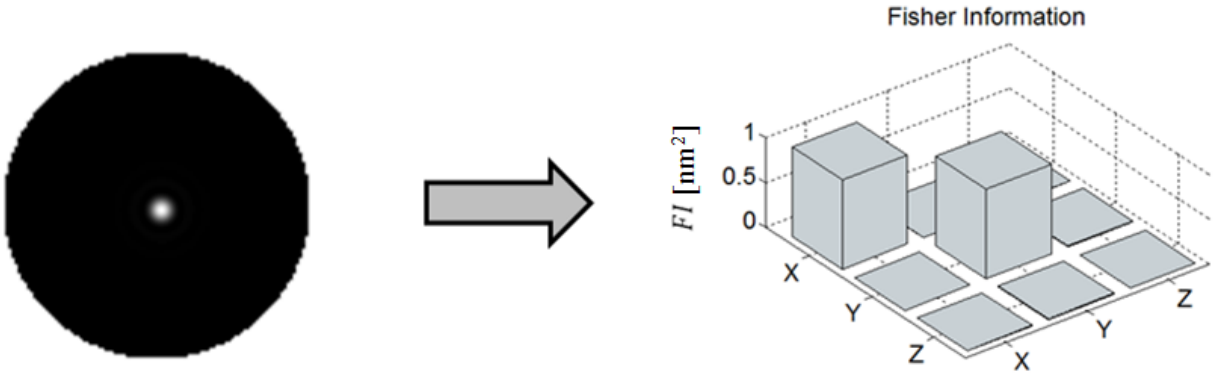

Fig. B.1: Example of the optical point spread function (left) used for estimating 3D localization. Application of the FI yields the 3x3 matrix shown to the right with $\theta \in [X, Y, Z]$. Note the matrix values have been normalized. The transverse coordinates (X,Y) are shown to have relatively high FI relative to the axial coordinate (Z) – indicating that the amount of change in the image is higher for transverse shifts. The transverse shift-invariance is responsible for the low cross-

terms between the parameters *X, Y*. The axial-invariance of the PSF due to the depth-of-focus is responsible for the low FI content of the *Z* parameter.

When given the Fisher Information matrix, the Cramer-Rao Lower Bound (*CRLB*) can be found from the matrix inverse,

$$CRLB \geq FI^{-1} \tag{B.3}$$

where the *CRLB* is a matrix providing the lower limit of the realizable estimation variance for parameter set $\boldsymbol{\theta}$.

The *CRLB* values along the diagonal provide the estimator variances of each independent parameter and are frequently quoted when analyzing system performance. In practice, the off-diagonal, correlated terms are left unreported. However, these values are relevant as indications of the relationship between particular parameters. For example, in 3D localization the cross-correlated terms of the x, y axes should indicate that the precision is independent of the location of the transverse location, i.e. transverse shift-invariance as shown in Fig. B.2.

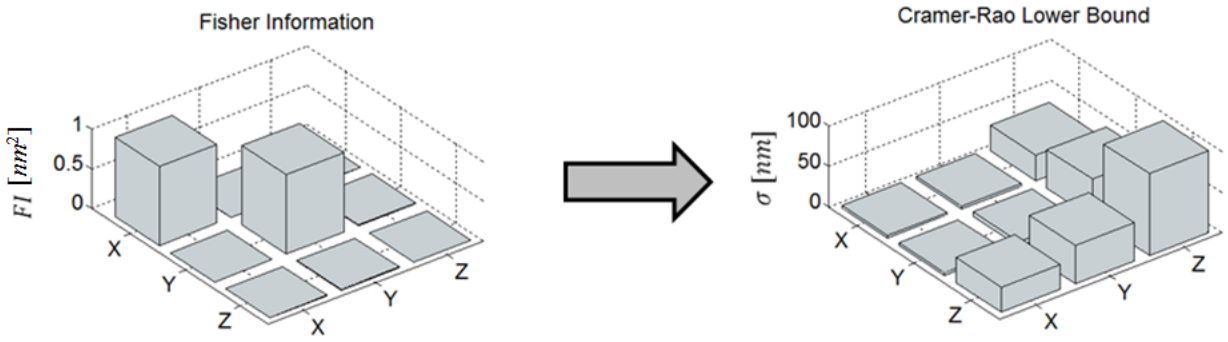

Fig. B.2: The FI (left) is utilized to provide the lower-limits of estimation precision, via the Cramer-Rao Lower Bound (right). The inverse relationship between the two matrices means that parameters with higher FI will yield improved estimation variances. The axial-invariance from depth-of-focus is responsible for the high estimation variance of the *Z* parameter and its cross-terms.

A flowchart for calculating the Fisher Information matrix is given in Fig. B-3. In panel (A), the FI matrix calculation algorithm is presented for a generalized form of unknown parameters, $\boldsymbol{\theta}$. In panel (B), the FI matrix is found for the example of 3D localization imaging.

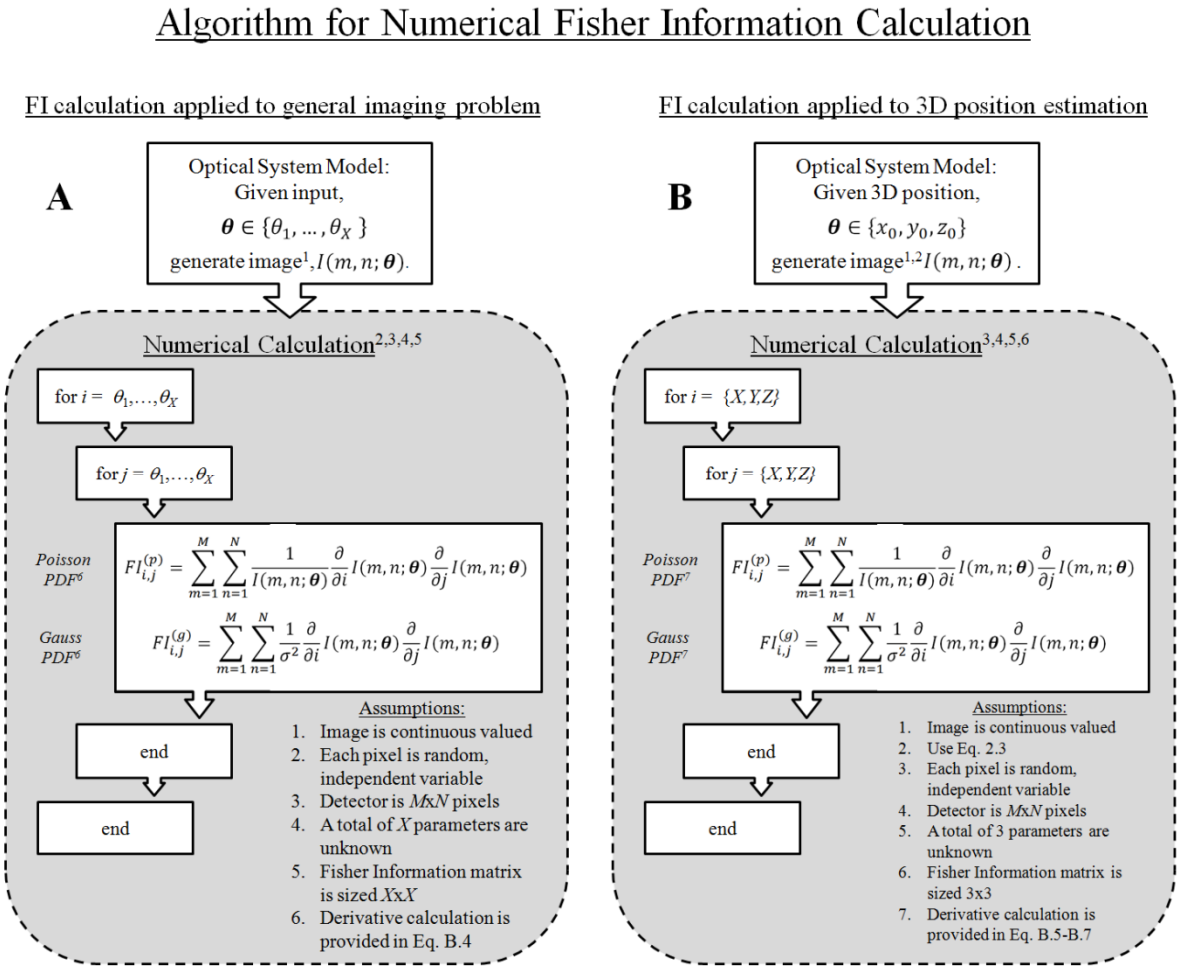

Fig. B.3: Example flowcharts for calculating Fisher Information matrices. The flowchart for creating a FI matrix for a general set of parameters, $\boldsymbol{\theta}$, is presented in panel A. A specific example of FI analysis for the case of 3D localization analysis is presented in panel B. Forms of the FI matrix elements are provided for the assumption of either Poisson or Gaussian noise.

Calculation of the FI matrix requires an accurate system model to generate the image $I(m,n;\boldsymbol{\theta})$. Given this, the partial derivatives can be found using central difference methods,

$$\frac{\partial}{\partial x} I = \frac{I(x+h)-I(x-h)}{2h} \tag{B.4}$$

where h is the numerical step size. To make this formula more explicit for a representative task, the following is an example for calculating the partial derivatives for the 3D localization of a target at the position x_0, y_0, z_0,

$$\frac{\partial}{\partial X} I(m,n;x_0,y_0,z_0) = \frac{I(m,n;x_0+\Delta x,y_0,z_0)-I(m,n;x_0-\Delta x,y_0,z_0)}{2\Delta x} \tag{B.5}$$

$$\frac{\partial}{\partial Y} I(m,n;x_0,y_0,z_0) = \frac{I(m,n;x_0,y_0+\Delta y,z_0)-I(m,n;x_0,y_0-\Delta y,z_0)}{2\Delta y} \tag{B.6}$$

$$\frac{\partial}{\partial Z} I(m,n;x_0,y_0,z_0) = \frac{I(m,n;x_0,y_0,z_0+\Delta z)-I(m,n;x_0,y_0,z_0-\Delta z)}{2\Delta z} \tag{B.7}$$

where care must be taken to chose a value for $\Delta x, \Delta y, \Delta z$ which accurately provides the derivative. In practice, this is achieved by calculating the derivative for many values of step size and selecting the step size where the derivative has asymptotically approached a limit. Utilizing all the tools now developed an algorithm for calculating only the axial Fisher Information of a three-dimensional imaging system is presented as an example in Fig. B.4.

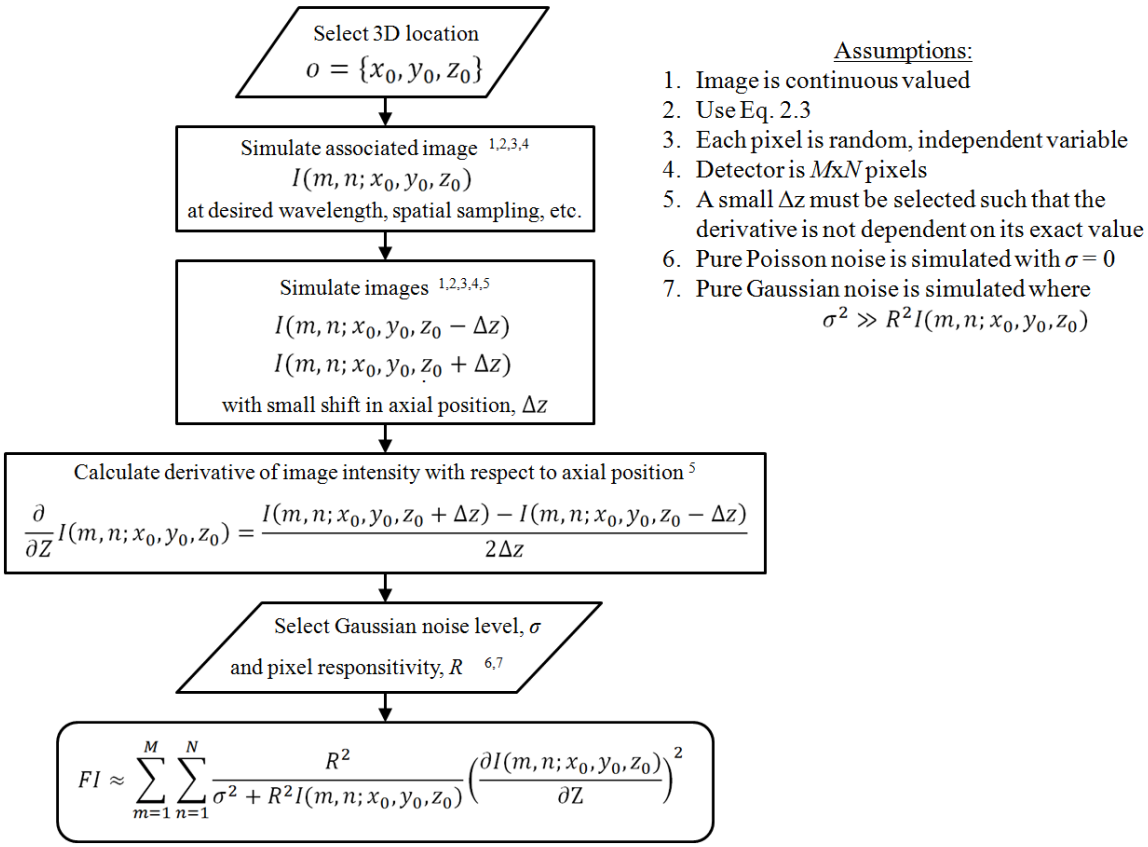

Fig. B.4: Flowchart for calculating the Fisher Information content in a general imaging system to be used for localizing the axial position of the source being imaged.

BIBLIOGRAPHY

1. Brady, D. J., *Optical Imaging and Spectroscopy* (Wiley-OSA, 2009)

2. Cathey, W. T., and Dowski, E. R., "New paradigm for imaging systems," Appl. Opt. **41**(29), 6080-6092 (2002)

3. Testorf, M., et al., "Signal Recovery and Computational Sensing and Imaging: introduction to the feature issue," Appl. Opt. **49**(34), SRC64-SRC65 (2010)

4. Awwal, A., et al., "Convergence in Optical and Digital Pattern Recognition: introduction to the feature issue," Appl. Opt. **49**(10), DPR1-DPR2 (2010)

5. Brady, D. J., et al., "Computational optical sensing and imaging: introduction to the feature issue," Appl. Opt. **47**(10), COSI1-COSI2 (2008)

6. Dowski, E., and Cathey, W. T., "Extended depth of field through wave-front coding," Appl. Opt. **34**(11), 1859-1866 (1995)

7. van der Gracht, J., et al., "Broadband behavior of an optical-digital focus-invariant system," Opt. Lett., **22**(13), 919-921 (1996)
8. Fienup, J. R., "Phase retrieval algorithms: a comparison," Appl. Opt. **21**(15), 2758-2769 (1982)

9. Ji, N., Milkie, D. E., and Betzig, E., "Adaptive optics via pupil segmentation for high-resolution imaging of biological tissues," Nat. Meth. **7**, 141-147 (2010)

10. Jesacher, A., et al., "Adaptive harmonic generation microscopy of mammalian embryos," Opt. Lett. **34**(20), 3154-3156

11. Greengard, A., Schechner, Y. Y., and Piestun, R., "Depth from diffracted rotation," Opt. Lett. **31**(2), 181-183 (2006)

12. Dowski, E. R., and Cathey, W. T., "Passive ranging through wave-front coding: Information and Application," Appl. Opt. **39**(11), 1700-1710 (2000)

13. Pavani, S. R. P., et al., "Three-dimensional, single-molecule fluorescence imaging beyond the diffraction limit by using a double-helix point spread function," Proc. Natl. Acad. Sci. USA **106**, 2995-2999 (2009)

14. Huang, B., et al., "Three-dimensional super-resolution imaging by Stochastic Optical Reconstruction Microscopy," Science **319**, 810-813 (2008)

15. Levin, A., et al., "Image and depth from a conventional camera with a coded aperture," SIGGRAPH 2007 (2007)

16. Ashok, A., and Neifeld, M., "Point Spread Function engineering for iris recognition system design," Appl. Opt. **49**, B26-B39

17. Plemmons, R. J., et al., "Computational imaging systems for iris recognition," Proc. SPIE 5559, 346 (2004)

18. Muyo, G., et al., "Infrared imaging with a wavefront-coded single lens," Opt. Express **17**(23), 21118-21123 (2009)

19. Vellekoop, I. M., and Mosk, A. M., "Focusing coherent light through opaque strongly scattering media," Opt. Lett. **32**(16), 2309-2311 (2007)

20. Popoff, S. M., et al., "Measuring the transmission matrix in optics: An approach to the study and control of light propagation in disordered media," Phys. Rev. Lett. **104**(10), 100601(1-4) (2010)

21. Barsi, C., Wan. W., Fleischer, J. W., "Imaging through nonlinear media using digital holography," Nat. Photon. **3**, 211-215 (2009)

22. Fujimoto, J. G., et al., "Optical Coherence Tomography: An emerging technology for biomedical imaging and optical biopsy," Neoplasia **2**(1-2), 9-25 (2000)

23. Gustafsson, M. G. L., "Nonlinear structured-illumination microscopy: Wide-field fluorescence imaging with theoretically unlimited resolution," Proc. Natl. Acad. Sci. USA **102** (2005)

24. Betzig, E., et al., "Imaging intracellular fluorescent proteins at nanometer resolution," Science **313** (2006)

25. Goodman, J. W., *Introduction to Fourier Optics, 3rd Edition* (Roberts & Company Publishers, 2004)

26. Saleh, B. E. A., and Teich, M. C., *Fundamentals of Photonics* (John Wiley & Sons, 1991)

27. Polynkin, P., et al., "Curved plasma channel generation using ultraintense Airy beams," Science **324**, 229-232 (2009)

28. Bagheri, S., Silveira, P. E. X., Barbastathis, G., "Signal-to-noise-ratio limit to the depth-of-field extension for imaging systems with an arbitrary pupil function," J. Opt. Soc. Am. A **26**(4), 895-908 (2009)

29. Pavani, S. R. P., and Piestun, R., "High-efficiency rotating point spread functions," Opt. Express **16**, 3484-3489 (2008)

30. Pavani, S. R. P., DeLuca, J. G., and Piestun, R., "Polarization sensitive, three-dimensional, single-molecule imaging of cells with a double-helix system," Opt. Express **17**, 19644-19655 (2009)

31. Thompson, M. A., et al., "Three-dimensional tracking of single mRNS particles in Saccharomyces cerevisiae using a double-helix point spread function," Proc. Natl. Acad. Sci. USA **42**, 17864-17871 (2010)

32. Thompson, M. A., et al., "Localizing and tracking single nanoscale emitters in three dimensions with high spatiotemporal resolution using a double-helix point spread function," Nano Lett. **10**, 211-218 (2010)

33. Kay, S. M., *Fundamentals of Statistical Signal Processing, Volume 1: Estimation Theory* (Prentice Hall, 1993)

34. Piestun, R., Schechner, Y. Y., Shamir, J., "Propagation-invariant wave fields with finite energy," J. Opt. Soc. Am. A. **17**(2), 294-303 (2000)

35. Grover, G., Pavani, S. R. P., and Piestun, R., "Performance limits on three-dimensional particle localization in photon-limited microscopy," Opt. Lett. **35**, 3306-3308 (2010)

36. Ober, R., Ram, S., and Ward, E. S., "Localization accuracy in single-molecule microscopy," Biophys. J. **86**, 1185-1200 (2004)

37. Pavani, S. R. P., Greengard, A., and Piestun, R., "Three-dimensional localization with nanometer accuracy using a detector-limited double-helix point spread function system," Appl. Phys. Lett. **95**(2), 021103 (2009)

38. Hess, S. T., Girirajan T. P. K. and Mason, M. D., "Ultra-high resolution imaging by fluorescence photoactivation localization microscopy," Biophys. J. **91**, 4258-4272 (2006)

39. Rust, M. J., Bates, M., Zhuang, X., "Sub-diffraction-limit imaging by stochastic optical reconstruction microscopy (STORM)," Nat. Meth. **3**, 793-796 (2006)

40. Egner, A., et al., "Fluorescence nanoscopy in whole cells by asynchronous localization of photoswitching emitters," Biophys. J. **93**, 3285-3290 (2007)

41. Hell, S. W., and Wichmann, J., "Breaking the diffraction resolution limit by stimulated emission: stimulated-emission-depletion fluorescence microscopy," Opt. Lett. **19**(11), 780-782 (1994)

42. Tang, J., et al., "Near-isotropic 3D optical nanoscopy with photon-limited chromophores," Proc. Natl. Acad. Sci. USA, dio:10.1073/pnas.1004899107 (2010)

43. Pertsinidis, A., Zhang, Y., and Chu, S., "Subnanometre single-molecule localization, registration and distance measurements," Nature **466**, 647-651 (2010)

44. Lord, S. J., et al., "Azido push-pull fluorogens photoactivate to produce bright fluorescent labels," J. Phys. Chem. B **114**(45), 14157-14167 (2010)

45. Shtengel, G., et al., "Interferometric fluorescent super-resolution microscopy resolves 3D cellular ultrastructure," Proc. Natl. Acad. Sci. USA **106**, 3125-3130 (2009)

46. Aguet, F., et al., "Super-resolution orientation estimation and localization of fluorescent dipoles using 3-D steerable filters," Opt. Express **17**, 6829-6848 (2009)

47. Juette, M. F., et al., "Three-dimensional sub-100nm resolution fluorescence microscopy of thick samples," Nat. Meth. **5**, 527-529 (2008)

48. Pavani, S. R. P., and Piestun, R., "Three dimensional tracking of fluorescent microparticles using a photon-limited double-helix response system," Opt. Express **16**, 22048-22057 (2008)

49. Mlodzianoski, M. J., et al., "Experimental characterization of 3D localization techniques for particle-tracking and super-resolution microscopy," Opt. Express **17**, 8264-8277 (2009)

50. von Middendorff, C., et al., "Isotropic 3D nanoscopy based on single emitter switching," Opt. Express **16**, 20774-20788 (2008)

51. Aguet, F., van de Ville, D., and Unser, M., "A maximum-likelihood formulism for sub-resolution axial localization of fluorescent nanoparticles," Opt. Express **13**, 10503-10522 (2005)

52. Mortensen, K. I., et al., "Optimized localization analysis for single-molecule tracking and super-resolution microscopy," Nat. Meth. **7**, 377-381 (2010)

53. Smith, C. S., et al., "Fast, single-molecule localization that achieves theoretically minimum uncertainty," Nat. Meth. **7**, 373-375 (2010)

54. Shaevitz, J. W., and Fletcher, D. A., "Enhanced three-dimensional deconvolution microscopy using a measured depth-varying point-spread-function," J. Opt. Soc. Am. A **24**(9), 2622-2627 (2007)

55. Hanser, B. M., et al., "Phase-retrieved pupil functions in wide-field fluorescence microscopy," J. Microscopy **216**, 32-48 (2004)

56. Allen, L. J., and Oxley, M. P., "Phase retrieval from series of images obtained by defocus variation," Opt. Comm. **199**, 65-75 (2001)

57. Waller, L., Tian, L., and Barbastathis, G., "Transport of Intensity phase-amplitude imaging with higher order intensity derivatives," Opt. Express **18**, 12552-12561 (2010)

58. Fienup, J. R., "Phase retrieval from undersampled broadband images," J. Opt. Soc. Am. A **16**(7), 1831-1837 (1999)

59. Grover, G., Quirin, S., Fiedler, C., and Piestun, R., "Photon-efficient Double-Helix Point Spread Function microscope for 3D Photo-activation Localization Microscopy," Bio. Opt. Express **2**(11), 3010-3020 (2011)

60. Gonzalez, R. C., and Woods, R. E., *Digital Image Processing 2nd Edition* (Prentice Hall, 2002)

61. Thompson, R. E., Larson, D. R., Webb, W. W., "Precise nanometer localization analysis for individual fluorescent probes," Biophys. J. **82**(5), 2775-2783 (2002)

62. Schechner, Y. Y. and Kiryati, N., "Depth from defocus vs. Stereo: How different really are they?," Inter. J. Comp. Vis. **39**(2), 141-162 (2000)

63. Chaudhuri, S., and Rajagopalan, A. N., *Depth from Defocus: A real aperture imaging approach* (Springer-Verlag, 1999)

64. Medina, A., Gaya, F., and del Poza, F., "Compact laser radar and three-dimensional camera," J. Opt. Soc. Am. A **23**(4), 800-805 (2006)

65. Shaffer, M., et al., "High-speed three-dimensional shape measurements of objects with laser speckles and acousto-optic deflection," Opt. Lett. **36**(16), 3097-3099 (2011)

66. Nayar, S., and Nakagawa, Y., "Shape from Focus," IEEE PAMI **16**(8), 824-831 (1994)

67. Pentland, A. P., "A new sense for depth of field," IEEE PAMI **9**(4), 523-531 (1987)

68. Favaro, P., and Soatto, S., *3-D Shape Estimation and Image Restoration – Exploiting Defocus and Motion Blur* (Springer-Verlag, 2007)

69. Ram, S., et al., "A novel approach to determining the three-dimensional location of microscopic objects with applications to 3D particle tracking," SPIE 6443 (2007)

70. Zhou, C., Lin, S., and Nayar, S., "Coded aperture pairs for Depth from Defocus and Defocus Deblurring," Int. J. Comp. Vis. **93**(1), 53 (2011)

71. Blahut, R. E., *Theory of Remote Image Formation* (Cambridge University Press, 2004)

72. Bagheri, S., et al., "Analytical optical solution of the extension of the depth of field using cubic-phase wavefront coding. Part II. Design and optimization of the cubic phase," J. Opt. Soc. Am. A **25**(5), 1064-1074 (2008)

73. Barrett, H., Dainty, C., and Lara D., "Maximum-likelihood methods in wavefront sensing: stochastic models and likelihood functions," J. Opt. Soc. Am. A 24(4), 391-414 (2007)

74. Ng, R., et al., *Light field photography with a hand-held plenoptic camera* Stanford University Computer Science Tech Report CSTR 2005-02 (2005)

75. Badieirostami, M., et al., "Three-dimensional localization precision of the Double-Helix Point Spread Function versus Astigmatism and Biplane," Appl. Phys. Lett. 97(16), 161103 (2010)

76. Kao, H. P., and Verkman, A. S., "Tracking of single fluorescent particles in three dimensions: use of cylindrical optics to encode particle position," Biophys. J. 67, 1291 (1994)

77. Herzig, H.-P., *Micro-Optics: Elements, Systems and Applications* (CRC Press, 1997)

78. Plummer, W. T., "Unusual optics of the Polaroid SX-70 Land camera," Appl. Opt. **21**(2), 196-202 (1982)

79. Rhorer, R. L., and Evan, C. J., *Chapter 10: Fabrication of Optics by Diamond Turning. Handbook of Optics, Volume II 3rd Edition* (McGraw-Hill, 2010)

80. Shank, S. M., et al., "Multi-level phase gratings fabricated using focused ion-beam milling and electron-beam lithography," J. Vac. Sci. Technol. B. **12**(6) (1994)

81. Zimmer, K., and Bohme, R., "Precise etching of fused silica for micro-optical applications," Appl. Surf. Sci. **243**, 415-420 (2005)

82. McKenna, C., et al., "Maskless direct write grayscale lithography for MEMS applications," Micro/Nano Symposium (UGIM), 2010 18th Biennial University/Government/Industry (2010)

83. Li, L., et al., "Fabrication of diffractive optics by use of slow tool servo diamond turning process," Opt. Eng. **45**(11) (2006)

84. O'Shea, D. C., et al., *Diffractive Optics: Design, Fabrication and Test* (SPIE Publications, 2003)

85. Spektor, B. I., "Methods for synthesizing the phase structure of kinoforms," Avtometriya **6**, 34-38 (1985)

86. Swanson, G. J., *Binary optics technology: the theory and design of multilevel diffractive optical elements*, MIT Lincoln Laboratory Tech. Rep. No. 854 (1989)

87. Erteza, I. A., *Diffraction efficiency analysis for multi-level diffractive optical elements* Sandia National Laboratories, Report SAND95-1697, UC-910 (1995)

88. Photoresists. AZ Electronic Materials [Online] [Cited: January 16th, 2011] http://www.az-em.com/en/Products/Litho-technology/Photoresists.aspx

89. Quirin, S., Pavani, S. R. P., and Piestun, R., "Optimal 3D single-molecule localization for super-resolution microscopy with engineered point spread functions," Proc. Natl. Acad. Sci. USA doi:10.1073/pnas.1109011108 (2011)

90. Quirin, S., Pavani, S. R. P., and Piestun, R., "Broadband three-dimensional imaging using a Double-Helix Point Spread Function," in Computational Optical Sensing and Imaging, OSA Technical Digest (CD), paper CTuD3 (2009)

91. Quirin, S., and Piestun, R., "3-D Imaging using Helical Point Spread Functions," in Imaging Systems, OSA Technical Digest (DC), paper IWC1 (2010)

92. Roddier, F., *Adaptics Optics in Astronomy* (Cambridge University Press, 2004)

93. Booth, M. J., "Adaptive optics in microscopy," Phil. Trans. R. Soc. A **365**, 2829-2843 (2007)

94. Thibos, L. N., and Hong, X., "Clinical applications of the Shack-Hartmann Aberrometer," Opt. and Vis. Sci. **76**(12), 817-825 (1999)

95. Kim, M.-S., Scharf, T., and Herzig, H.-P., "Small-size microlens characterization by multiwavelength high-resolution interference microscopy," Opt. Express **18**, 14319-14329 (2010)

96. Schwertner, M., et al., "Measurement of specimen-induced aberrations of biological samples using phase stepping interferometry," J. Microscopy **213**(1), 11-19 (2003)

97. Southwell, W. H., "Wave-front estimation from wave-front slope measurements," J. Opt. Soc. Am. **70**(8), 998 (1980)

98. Born, M., and Wolf, E., *Principles of Optics, 7th Edition* (Cambridge University Press, 2005)

99. Debarre, D., et al., "Adaptive optics for structured illumination micrscopy," 16(13), 9290-9305 (2008)

100. Huang, D., and Arif, M., "Spot size and quality of scanning laser correction of higher order wavefront aberrations," J. Refr. Surg. **17**, S588-S591 (2001)

101. Liang, J., and Williams, D. R., "Aberrations and retinal image quality of the normal human eye," J. Opt. Soc. Am. A **14**(11), 2873-2883 (1997)

102. Fried, D. L., "Statistics of a geometric representation of wavefront distortion," J. Opt. Soc. Am. **55**(11), 1427-1431 (1965)

103. Sallberg, S. A., Welsh, B. M., and Roggemann, M. C., "Maximum a posteriori estimation of wave-front slopes using a Shack-Hartmann wave-front sensor," J. Opt. Soc. Am. A **14**(6), 1347-1354 (1997)

104. Optimization Toolbox, Matlab. Natick, MA: The MathWorks

105. Fienup, J. R., et al., "Hubble Space Telescope characterized by using phase-retrieval algorithms," Appl. Opt. **32**(10), 1747-1767 (1993)

106. Teague, M. R., "Deterministic phase retrieval: a Green's function solution," J. Opt. Soc. Am. **73**(11), 1434-1441 (1983)

107. Paterson, C., and Dainty, J. C., "Hybrid curvature and gradient wave-front sensor," Opt. Lett. **25**(23), 1687-1689 (2000)

108. Roddier, F., "Curvature sensing and compensation: a new concept in adaptive optics," Appl. Opt. **27**(7), 1223-1225 (1988)

109. Kner, P., et al., "High-resolution wide-field microscopy with adaptive optics for spherical aberration correction and motionless focusing," J. Microsc. **237**(2), 136-147 (2010)

110. Olivier, N., Debarre, D., and Beaurepaire, E., "Dynamic aberration correction for multiharmonic microscopy," Opt. Lett. **23**, 3145-3147 (2009)

111. Cha, J. W., and So, P. T., "A Shack-Hartmann wavefront sensor based adaptive optics system for multiphoton microscopy," in Biomedical Optics, OSA Technical Digest (CD), paper BMD52 (2008)

112. van Dam, M. A., Le Mignant, D., and Macintosh, B. A., "Performance of the Keck Observatory adaptive-optics system," Appl. Opt. **43**, 5458-5467 (2004)

113. Pfund, J., Lindlein, N., and Schwider, J., "Non-null testing of aspherical surfaces by using a Shack-Hartmann sensor," in Optical Fabrication and Testing, OSA Technical Digest, paper OTuC5 (2000)

114. Neal, D. R., Armstrong, D. J., and Turner, W. T., "Wave-front sensors for control and process monitoring in optics manufacture," in Lasers as Tools for Manufacturing II, SPIE 2993, 1-10 (1997)

115. Yoon, G., Pantanelli, S., and Nagy, L. J., "Large-dynamic-range Shack-Hartmann wavefront sensor for highly aberrated eyes," J. Biomed. Opt. **11** (2006)

116. Paeder, B., et al., "Microlenses with annular amplitude and phase masks," J. Eur. Opt. Soc. – Rap. Pub. **2**, 07705 (2007)

117. Rios, S., and Lopez, D., "Modified Shack-Hartmann wavefront sensor using an array of super-resolution pupil filters," Opt. Express **17**, 9669-9679 (2009)

118. Tanida, J., et al., "Thin Observation Module by Bound Optics (TOMBO): Concept and experimental verification," Appl. Opt. **40**(11), 1806-1813 (2001)

119. Schonbrun, E., et al., "High throughput fluorescence detection using an integrated zone plate array," Lab Chip **10**, 852-856 (2010)

120. Toprak, E., et al., "Defocused orientation and position imaging (DOPI) of myosin V," Proc. Natl. Acad. Sci. USA **103**, 6495-6499 (2006)

121. Warshaw, D. M., et al., "Myosin conformational states determined by single fluorophore polarization," Proc. Natl. Acad. Sci. USA **95**, 8034-8039 (1998)

122. Bartko, A. P., and Dickson, R. M., "Imaging three-dimensional single molecule orientations," J. Phys. Chem. B. **103**(51), 11237-11241 (1999)

123. Bohmer, M., and Enderlein, J., "Orientation imaging of single molecules by wide-field epifluorescence microscopy," J. Opt. Soc. Am. B **20**, 554-559 (2003)

124. Agrawal, A., et al., "Limits of 3D dipole localization and orientation estimation with application to single-molecule imaging," in Computational Optical Sensing and Imaging, OSA Technical Digest, paper CWA4